Universiteit Leiden
The Netherlands

Nidovirus replication structures : hijacking membranes to support viral RNA synthesis

Knoops, K.

Citation
Knoops, K. (2011, May 10). *Nidovirus replication structures : hijacking membranes to support viral RNA synthesis*. Retrieved from https://hdl.handle.net/1887/17639

Version:	Corrected Publisher’s Version
License:	Licence agreement concerning inclusion of doctoral thesis in the Institutional Repository of the University of Leiden
Downloaded from:	https://hdl.handle.net/1887/17639

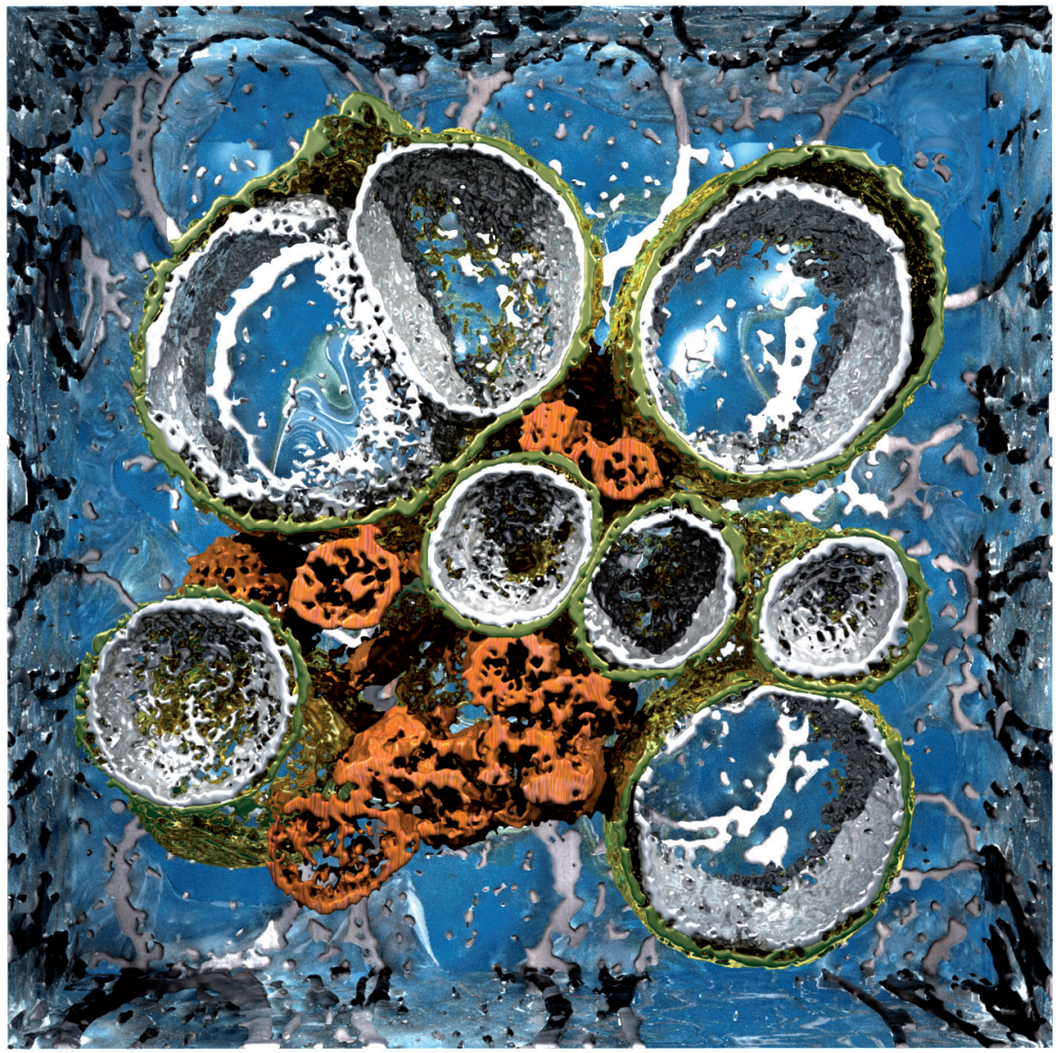
Note: To cite this publication please use the final published version (if applicable).

Nidovirus Replication Structures

Kèvin Knoops

Nidovirus Replication Structures

Hijacking Membranes to Support Viral RNA Synthesis



Kèvin Knoops

Stellingen

behorende bij het proefschrift

Nidovirus Replication Structures:
Hijacking Membranes to Support Viral RNA Synthesis

1. De bevinding dat zowel coronavirussen als arterivirussen een reticulovesiculair netwerk van gemodificeerd endoplasmatisch reticulum induceren, doet vermoeden dat de vorming van dit netwerk een gemeenschappelijke eigenschap van nidovirussen is.
   (Dit proefschrift)

2. Het feit dat membranen het door SARS-CoV en EAV gesynthetiseerde dubbelstrengs RNA omgeven, ondersteunt de hypothese dat het dubbelstrengs RNA wordt beschermd tegen cellulaire afweermechanismen die in het cytosol opereren.
   (Dit proefschrift)

3. De paradoxale ruimtelijke scheiding van het merendeel van het dubbelstrengs RNA en de virale replicase eiwitten in coronavirus- en arterivirusgeïnfecteerde cellen suggereert dat slechts een klein deel van de replicase eiwitten daadwerkelijk actief is in virale RNA synthese.
   (Quinkert et al., Journal of Virology 2005; 79:13594-13605)
   (Dit proefschrift)

4. De vorming en ontwikkeling van het nidovirus-geïnduceerde reticulovesiculaire netwerk is onafhankelijk van het COPII-gemedieerde transport mechanisme maar afhankelijk van voortdurende eiwitsynthese.
   (Dit proefschrift)

5. Het feit dat de aanwezigheid van microsomen de *in vitro* productie van coronavirus nsp3 kan bevorderen, suggereert dat co-translationele translocatie een rol speelt in de membraan-associatie van coronavirus replicase polyproteïnen.
   (Kanjanahaluethai et al., Virology 2007; 361:391-401)

6. Naast het buigen van membranen zijn de replicase eiwitten van sommige positiefstrengige RNA virussen ook in staat eiwitten te rekruteren die de lipidesamenstelling van de door het virus geïnduceerde membraanstructuren veranderen ter bevordering van de virale RNA synthese.
   (Hsu et al., Cell 2010; 141:799-811)

7. Het feit dat duidelijke openingen werden waargenomen in de replicatieblaasjes van het knokkelkoortsvirus is wellicht te verklaren door de wijze van fixatie en laat zien dat preparatie artefacten ook nuttige informatie kunnen opleveren.
   (Welsch et al., Cell Host & Microbe 2009; 5:365-375)

8. De ontwikkeling van Röntgen tomografie maakt het mogelijk om in een relatief korte tijd 3-D reconstructies van intacte cellen te produceren waarbij in de toekomst een resolutie van 5-10 nm te verwachten is.
   (Jiang et al., PNAS 2010; 107:11234-11239)
   (Schneider et al., Nature Methods 2010; 7:985-987)

9. Schaalvergroting leidt tot extreme kwetsbaarheid.
   (Hans van Mierlo, Onder Economen, DDL 31 maart 2001)

10. Omdat Eva en Adam voorafgaand aan het eten van de vrucht van de boom der wijsheid nog niet beschikten over een besef van goed en fout, is de mensheid ten onrechte uit de Tuin van Eden verbannen en zou een correctie op zijn plaats zijn.
    (Genesis, Bijbel; 3:1-15)

11. Omwille van de veiligheid, kosten, efficiëntie en publieke opinie, zou het de voorkeur verdienen om in Nederland Afghaanse politieopleiders te trainen die op hun beurt in Afghanistan politiemensen zullen kunnen opleiden.

12. Omdat de natuur en het kapitalisme beide het recht van de sterkste als uitgangspunt hebben, zijn alle oplossingen die zijn aangedragen voor de verhongerende dieren in de Oostvaardersplassen ook toepasbaar op slecht functionerende bankiers.

Kèvin Knoops

Nidovirus Replication Structures

Hijacking Membranes to Support Viral RNA Synthesis

Kèvin Knoops

Nidovirus Replication Structures
Hijacking Membranes to Support Viral RNA Synthesis
Kèvin Knoops

Ph.D. Thesis Leiden University, 2011

The work presented in this thesis was performed at the Departments of Medical Microbiology and Molecular Cell Biology of Leiden University Medical Center, the Netherlands.

The printing of this thesis was financially supported by the *Stichting tot Bevordering van de Electronenmicroscopie in Nederland* (SEN).

ISBN/EAN: 978-94-6169-062-3
Printed by: Optima Grafische Communicatie, Rotterdam, The Netherlands

Cover: Three-dimensional reconstruction of the reticulovesicular network of modified endoplasmic reticulum derived from a section through a frozen SARS coronavirus-infected Vero E6 cell.

All rights reserved. No part of this thesis may be reproduced or transmitted in any form or by any means without prior written permission of the author.

© Copyright Kèvin Knoops, Grenoble, 2011

Nidovirus Replication Structures

Hijacking Membranes to Support Viral RNA Synthesis

Proefschrift

ter verkrijging van
de graad van Doctor aan de Universiteit Leiden
op gezag van de Rector Magnificus Prof. mr. P.F. van der Heijden
volgens het besluit van het College voor Promoties
te verdedigen op dinsdag 10 mei 2011
klokke 11:15 uur

door

Kèvin Knoops

geboren te Heerlen
in 1980

PROMOTIECOMMISSIE

Promotores: Prof. dr. E.J. Snijder
Prof. dr. ir. A.J. Koster

Co-promotor: Dr. A.M. Mommaas-Kienhuis

Overige leden: Prof. dr. J. Klumperman
Universiteit Utrecht

Dr. F. van Kuppeveld
Radboud Universiteit Nijmegen

Prof. dr. H.J. Tanke

Table of contents

List of abbreviations 7

Chapter 1 General introduction 11

Chapter 2 SARS-Coronavirus replication is supported by a reticulovesicular network of modified endoplasmic reticulum 29
PLoS Biology (2008) 16;6(9):e226

Chapter 3 Integrity of the early secretory pathway promotes, but is not required for SARS-coronavirus RNA synthesis and virus-induced remodeling of endoplasmic reticulum membranes 57
Journal of Virology (2010) 84(2):833-46

Chapter 4 Development and RNA-synthesizing activity of coronavirus replication structures in the absence of protein synthesis 81
Journal of Virology (in press)

Chapter 5 Ultrastructural characterization of arterivirus replication structures: reshaping the endoplasmic reticulum to accommodate viral RNA synthesis 89
Submitted for publication

Chapter 6 General discussion 121

References 135

Summary 151

Samenvatting 155

Curriculum vitae 158

Awards 158

List of publications 159

List of abbreviations

-RNA	Negative-sense RNA
+RNA	Positive-sense RNA
3-D	3-dimensional
^{3}H	Tritium
A	Actin
aa	Amino acid
ActD	Actinomycin D
Arf	ADP-ribosylation factor
Atg	Autophagy-related protein
BHK	Baby hamster kidney
BFA	Brefeldin A
BIG	Brefeldin A-inhibited GEP
BrU	Bromouridine
BrUTP	Bromouridine triphosphate
CCD	Charged coupled device
CEACAM	Carcinoembryonic antigen-related cell adhesion molecules
CF	Cryo fixation
CHX	Cycloheximide
CM	Convoluted membranes
COP	Coat protein complex
CoV	Coronavirus
CPV	Cytopathic vacuole
CTP	Cytidine triphosphate
CVB3	Coksackie virus B3
Cy3	Indocarbocyanine 3
DENV	Dengue virus
DMV	Double-membrane vesicle
DNA	Deoxyribonucleic acid
DNase	Deoxyribonuclease
ds	Double stranded
dsRNA	Double-stranded RNA
E	Envelope protein
EAV	Equine arteritis virus
EDEM	ER degradation enhancing alpha-mannosidase-like protein
EFTEM	Energy-filtered transmission electron microscopy
EGTA	Ethylene glycol tetraacetic acid

EM	Electron microscopy
ER	Endoplasmic reticulum
ERAD	ER-associated protein degradation
ERGIC	ER-Golgi intermediate compartment
ESI	Electron spectroscopic imaging
ET	Electron tomography
eV	Electron volt
Exo	Exonuclease
FHV	Flock house virus
FMDV	Footh-and-mouth-disease virus
FS	Freeze substitution
G	Golgi complex
GEF	Guanine nucleotide exchange factor
GFP	Green fluorescent protein
GTP	Guanosine-5′-triphosphate
HCoV	Human coronavirus
HCV	Hepatitis C virus
HEL	Helicase
HeLa	Henrietta Lacks
HEPES	4-(2-hydroxyethyl)-1-piperazineethanesulfonic acid
Huh	Human hepatoma
IF	Immunofluorescence
IEM	Immunoelectron microscopy
IgG	Immunoglobulin G
IM	Inner membrane
kb	Kilobase
LC3	Light chain 3
M	Membrane protein *or* Mitochondrion
Mab	Monoclonal antibody
MHV	Mouse hepatitis virus
MOI	Multiplicity of infection
MP	Main protease
mRNA	Messenger RNA
MT	Methyl transferase
MVB	Multivesicular body
N	Nucleocapsid protein *or* Nucleus
NaP_i	Sodium phosphate buffer
NC	Nucleocapsid
NS	Non-structural protein

nsp	Non-structural protein
OM	Outer membrane
ORF	Open reading frame
P	RNA primase *or* Phosphorus
PALM	photo-activated localization microscopy
PBS	Phosphate buffered saline
PC	Paracrystalline arrays
PDI	Protein disulfide isomerase
PDM	Product of the difference from the mean
PFA	Paraformaldehyde
p.i.	Post infection
PI4K	Phosphatidylinositol 4-kinase
PLP	Papain-like protease
pp	Polyprotein
PRRSV	Porcine reproductive and respiratory syndrome virus
PUR	Puromycin
PV	Poliovirus
rER	Rough endoplasmic reticulum
RdRp	RNA-dependent RNA polymerase
RF	Replicative form
RFS	Ribosomal frameshift
RI	Replicative intermediate
RNA	Ribonucleic acid
RNase	Ribonuclease
RTC	Replication/transcription complex
RVN	Reticulovesicular network
SARS	Severe acute respiratory syndrome
SARS-CoV	Severe acute respiratory syndrome coronavirus
SDS-PAGE	Sodium dodecyl sulfate polyacrylamide gel electrophoresis
siRNA	Small interfering RNA
SIRT	Simultaneous iterative reconstruction technique
SNARE	Soluble NSF attachment protein receptor
SRP	Signal recognition particle
ss	Single stranded
STED	Stimulated emission depletion
STORM	Stochastic optical reconstruction microscopy
TEM	Transmission electron microscopy
TF	Transcriptive form
TI	Transcriptive intermediate

TIM	Transporter inner membrane
TM	Transmembrane domain
TOM	Transporter outer membrane
TRIS	Tris(hydroxymethyl)aminomethane
TUNEL	Terminal deoxynucleotidyl transferase dUTP nick end labeling
TVC	Tubulovesicular cluster
TX-100	Triton-X 100
UTP	Uridine-5′-triphosphate
V	Smooth walled vesicles
VP	Vesicle packet
WNV	West Nile virus
YFP	Yellow fluorescent protein

CHAPTER 1

General introduction

General Introduction

According to the commonly used biological definitions, viruses cannot be classified as living organisms. The evolution of cellular life was the basis for the diversity of viruses we encounter today. However, viruses are ranked in an extraordinary biological category because they need to invade living cells to "come to life", express their genome, and replicate themselves. Like their host cells, viruses are primarily composed of nucleic acids and proteins, and -depending on the virus family - these macromolecules may be supplemented with lipid membranes and carbohydrates. Virus replication and assembly are supported by the metabolic pathways and infrastructure of the living host cell. The proteins encoded by viral genomes are synthesized by the host cell's translation machinery. Subsequently, the host cell's homeostasis is disrupted and the cell is converted into a factory for new virus particles. Ultimately, the virus-induced reprogramming of cellular metabolism and function may lead to necrosis at the cellular level, disease at the organismal level, and epidemics at the population level.

Virus particles are too small to be seen by the naked eye or to be distinguished by the first light microscopes that were developed in the 17th century. As a result, the causative agents of severe viral diseases like polio, smallpox, yellow fever, rabies, and influenza remained unknown for a long time. Towards the end of the 19th century, filtration experiments by Dimitri Iwanowski [1] and Martinus Beijerinck [2] revealed the existence of infectious entities smaller than the smallest known organisms at that time (bacteria), which led to the hypothesis that viruses were 'living fluids' (*contagium vivum fluidum*). By performing dilution experiments, Friedrich Loeffler ruled out the possibility of a toxin and concluded that viruses must be replicating entities [3]. The 'living fluid' theory of Martinus Beijerinck was finally rejected in 1935 by Wendell Stanley, who crystallized concentrated tobacco mosaic virus and thus demonstrated that viruses have particulate properties [4].

In the early 1930s, Ernst Ruska developed the electron microscope, which for the first time enabled the visualization of structures at nanometer-scale resolution [5,6]. His brother Helmut Ruska used this new instrument to study the unknown agents that cause virus infections and he was amongst the first to document the extensive morphological variety among viruses [7-9]. He also noticed that viruses with similar structures were able to infect different host species and proposed to categorize viruses according to structural criteria, disregarding the clinical syndromes and organic manifestations that they cause [10]. His method of virus identification improved the diagnosis of known viral infections and was also very helpful for the identification and classification of new viruses.

In 1962, Lwoff, Horne, and Tournier proposed to classify viruses using a systematic nomenclature that again was based on the structural properties of the virion [11]. Their primary criterion was the nature of the viral nucleic acid, which can either be DNA or RNA, and single- (ss) or double-stranded (ds). Their next parameter was the symmetry of the protein shell, or coat, that protects the viral genome. The morphology of this so-called nucleocapsid (genome

plus protein coat) varies between virus families, but the vast majority of viruses contain either helical or icosahedral nucleocapsids. Some viruses have more complex nucleocapsid structures and may, in addition to a core with helical and/or icosahedral properties, contain external features such as a protein tail. A large number of viruses contains a lipid membrane, the presence of which was used as the third major criterion in virus nomenclature. The membranes of enveloped viruses contain proteins that direct recognition of a host cell receptor molecule. This triggers fusion of the viral envelope with the host cell's membrane, either at the plasma membrane or following endocytosis of the virus particle, and results in the release of the nucleocapsid into the cytosol. Although the general classification developed by Lwoff and colleagues is still applicable, the introduction of genome sequencing technologies allowed the classification of viruses into orders, families, genera, and species based on the nucleic acid sequence of their genome and phylogenetic principles [12-15]. Nowadays, the International Committee on the Taxonomy of Viruses maintains and refines a universal virus taxonomy, which is primarily based on the features of virus genomes rather than the structural features of the particles.

An important alternative classification scheme was proposed by David Baltimore in 1971 and emphasizes the viral genome expression strategy, in particular the pathway leading to viral mRNA synthesis [16]. As a rule, in cellular gene expression, DNA genes are transcribed into messenger RNAs (mRNAs) which transfer the genetic code for amino acid polymerization to the cell's protein-synthesizing factories, called ribosomes. Like cells, all viruses produce mRNAs for translation into (structural and non-structural) proteins and, because they lack their own ribosomes, viruses completely depend on the host's translational machinery. By placing the universal step of mRNA synthesis and translation in a central position, Baltimore discriminated between the different pathways used by viruses to produce their mRNAs. In general, DNA viruses use pathways resembling those commonly used by their host cells, i.e. from DNA to RNA to protein. RNA viruses, however, with the exception of retroviruses, lack a DNA stage during their replication cycle. The positive-sense ssRNA (+RNA) viruses have genomes that are recognized directly by ribosomes, resulting in viral protein production immediately after infection. For both the negative-sense ssRNA (-RNA) and dsRNA viruses, transcription rather than translation is the first step in the viral replicative cycle, a step carried out by a viral RNA-dependent RNA polymerase that is present in the incoming virus particle.

Positive-stranded RNA viruses

The +RNA viruses are the largest group of viruses known to date and include important human pathogens like poliovirus, hepatitis C virus, dengue virus, and SARS-coronavirus. In biological terms, their replication cycle is unconventional as its key feature is the cytoplasmic replication of a +RNA genome, i.e. an RNA strand which also acts as a messenger RNA. Since this type of RNA-templated RNA synthesis is foreign to the host cell, +RNA viruses encode

their own specialized replicative enzymes. These nonstructural proteins (nsps), collectively referred to as 'replicases', always include an RNA-dependent RNA polymerase (RdRp) that, together with other viral and host proteins and the RNA template, assembles into a membrane-associated replication complex. The molecular interactions within this nucleic acid-protein machinery secure the specificity of viral RNA synthesis [17-21].

Following entry, translation of the genome of mammalian +RNA viruses yields large polyprotein precursors that incorporate the viral nsps and, in specific virus groups, also the structural proteins. These precursors are cleaved by internal proteases to produce the mature nsps [22,23]. Following the membrane association of hydrophobic replicase subunits, which often induces specific membrane alterations, the viral nsps engage in the synthesis of RNA strands that are complementary to the genome (negative-stranded RNAs) and subsequently serve as templates for positive strand RNA synthesis [24]. Genome replication thus results in the formation of dsRNA intermediates, which can be sensed by the cellular innate immune system and thus pose a potential "weak link" during the replication phase of infection. The transformation of host cell membranes into 'viral factories' is believed to be a universal feature of +RNA virus replication [25-27]. Whereas the exact roles of membrane association and modification are still a matter of debate, there are some clear potential benefits. Compartmentalization of specific processes and pathways within membrane boundaries might increase the local concentration of the necessary components. Also, the modified membranes might act as a scaffold for replication, with membrane-associated replicase subunits anchoring other, enzymatic nsps to the structures. Furthermore, removal of the viral genome from the cytosol, and thus preventing access for ribosomes, possibly prevents further translation of the RNA template and might constitute an important switch between genome translation and replication. Finally, shielding of dsRNA intermediates and possibly viral negative-strand RNAs carrying uncapped 5'-triphosphates within the membrane compartments limits their exposure to the host cell's sensors and might prevent the activation of defense mechanisms counteracting viral infection [28-30].

All +RNA viruses hijack intracellular membranes from host cell organelles and studies on different +RNA viruses have implicated different membrane donors in the formation of the structures supporting +RNA virus replication complexes [25-27,31,32]. +RNA viral replicases can create different types of "mini-organelles", and primarily they can be subdivided into small invaginations of the target organelle's cytosolic face and much larger membraneous networks (Fig. 1). Both types of membrane structures are thought to constitute beneficial microenvironments for viral RNA replication, as discussed in the previous paragraph. Recently, the formation, structure, and function of these organelles have become a major focus in +RNA virus research, for which electron microscopy has proven to be an essential tool. Dissection of the architecture and protein/RNA composition of these mini-organelles' has already provided important clues to their structure and possible function. For example, infection with the alphaviruses Semliki Forest virus and Sindbis virus induces cytopathic vacuoles

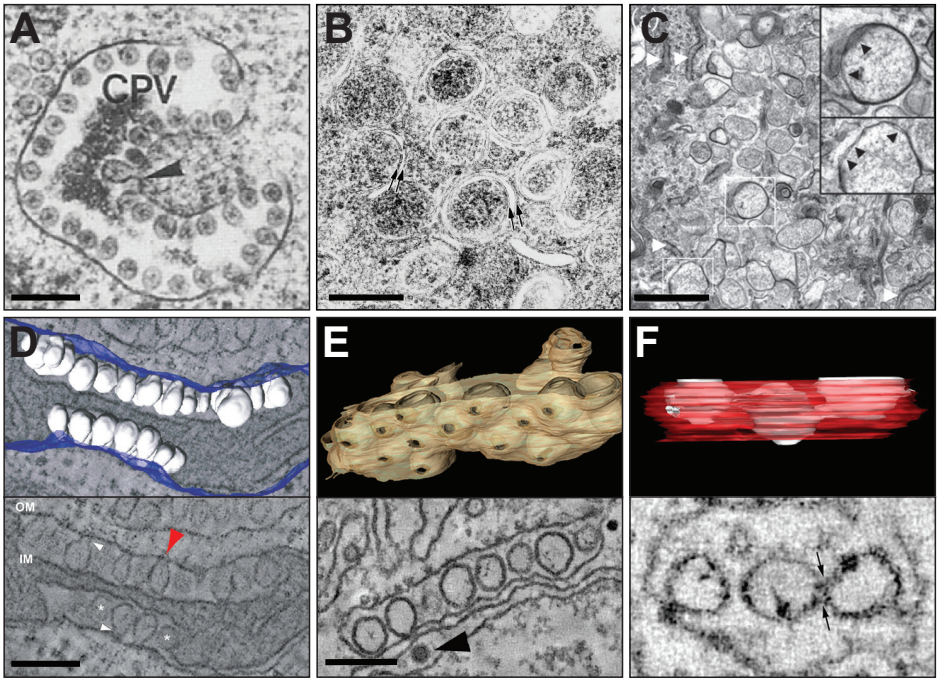


Figure 1. EM images of the membrane modifications that are induced by different +RNA viruses. (A) Semliki Forest virus-infected BHK cell showing spherules at the membrane of cytopathic vacuoles (CPV). The small and large arrowheads indicate connections of the spherule interior with the cytosol and thread-like material attached to the cytosolic base of the spherule, respectively (adapted with permission from [34]). Bar represents 200 nm. (B) Poliovirus-infected HeLa cell showing double-membrane vesicles (arrows) with an electron-lucent inter-membrane lumen after high-pressure freezing (adapted with permission from [49]). Bar represents 200 nm. (C) Huh7.5-C5 cells harboring a Hepatitis C virus subgenomic replicon showed double-membrane vesicles. Arrowheads indicate areas where the two closely apposed membranes are locally separated (adapted with permission from [44]). Bar represents 1 µm. (D) ET reconstruction of a Flock House virus-infected Drosophila DL-1 cell showing spherules (asterisks) in the inner-membrane (IM) space of mitochondria. The white arrowheads point at neck-like connections between spherules and the mitochondrial outer-membrane (OM). The red arrowhead indicates a connection of the spherule interior with the cytosol (adapted with permission from [36]). Bar represents 100 nm. (E) ET analysis of a Dengue virus-infected Huh-7 cell showing vesicles integrated into an ER-derived network. Pores of ~11 nm that connect the vesicles' interiors with the cytosol are directly opposing the site of Dengue virus particle budding (arrowhead; adapted with permission from [38]). Bar represents 200 nm. (F) West Nile virus strain Kunjin virus-infected BHK cell showing vesicles in the lumen of the rough-ER. A neck-like structure that tethers two individual vesicles inside the rough-ER membrane is indicated by the arrows and represented in 3-D by ET surface rendering (adapted with permission from [41]).

that were shown to originate from endosomes and lysosomes and contain large numbers of typical spherular invaginations [33-35] (Fig. 1A). Immunogold labeling showed that the viral polymerase nsP4 is present on the cytosolic surface of the membranes and structural studies suggested that these invaginations are connected to the cytosol via a single opening, with which thread-like electron-dense material was frequently associated. Comparable observa-

tions were made for Flock House virus (FHV), an insect virus belonging to the *Nodaviridae*, which induces similar invaginations, however, at the mitochondrial outer membrane [36,37] (Fig. 1D). Both the FHV polymerase protein A and incorporation of bromouridine triphosphate (BrUTP), a marker for viral RNA synthesis, were found to be associated with the FHV spherules, which strongly suggested that these invaginations are indeed the site of viral RNA synthesis. Like the alphavirus-induced spherules, also the FHV spherules have a channel that connects their interior to the cytosol, thus opening the intriguing possibility of continuous import of necessary components and export of newly synthesized RNA products.

The endoplasmic reticulum (ER) is another cytoplasmic organelle that is favored by many +RNA viruses as scaffold for their replication complex. Invaginations of the ER, called vesicle packets (VPs), were found after infection with different flaviviruses, e.g. Dengue virus [38] (Fig. 1E), Kunjin virus [39,40] and West-Nile virus [41] (Fig. 1F), and were suggested to be the intracellular site of RNA replication. Viral polymerases, newly synthesized RNA, and dsRNA were all found to reside inside these invaginations, which remain connected to the cytosol, as observed for alpha- and nodaviruses. In addition, large clusters of paired membranes, referred to as convoluted membranes (CM) and paracrystalline arrays (PC), were found to be connected to the VPs and part of a network of morphologically different structures. Interestingly, the flavivirus NS2B protein, which is an important co-factor for the NS3 protease, was only found on the CM and PC, which were thus proposed to be the site of flavivirus polyprotein processing [39,42]. In hepatitis C virus (HCV)-infected cells, similar vesicles embedded in clusters of membranes were found and were coined the 'membraneous web' [43-45] (Fig. 1C). This structure is also believed to be derived from the ER and HCV RNA replication is presumed to be associated with it. Isolated membrane fractions were found to contain HCV replicase activity which additionally was resistant to nuclease- and protease treatment, suggesting that HCV replication takes place within vesicles rather than on the surface of the membraneous web [46,47].

The last virus to be discussed in this general overview is poliovirus (PV), which belongs to the *Picornaviridae* and induces membrane alterations that have a similar appearance as those used by nidoviruses, which will be discussed in further detail below. PV induces clusters of single- and double-membrane vesicles (DMVs) ranging from 70 to 500 nm in diameter. Their exact ultrastructure has not been established yet. After high-pressure freezing, they appeared mainly as DMVs (Fig. 1B), but they were observed as an interconnected rosette-like, single-membrane structure after gradient purification [48,49]. In a preliminary model, it was proposed that the formation of the DMVs occurs in an autophagy-like manner during which the replication complex is engulfed by a double membrane [49,50]. Autoradiography and *in situ* hybridization have shown that newly synthesized viral RNA is associated with the cytosolic surface of these virus-induced vesicles and the compact membranes that were found in close contact with the vesicles [51-53]. The PV 2B, 2C, and 3A proteins, which are known to be required for RNA replication, are tightly associated with ER membranes. Secretory pathway

markers were found to co-fractionate with isolated PV replication structures, whereas some ER-resident markers could not be detected on PV vesicles themselves and seemed to be excluded during vesicle formation [49,54]. The drug brefeldin A, which blocks the anterograde transport, inhibits PV replication and, together with the co-purification of secretory pathway proteins, this finding suggested that the COPII-mediated pathway might be responsible for PV vesicle formation. For PV and Coxsackie Virus B3 (CVB3), both members of the enterovirus genus of the picornavirus family, it has now been shown that GBF1, a guanine nucleotide exchange factor of the small Ras-family GTPase Arf1, is required for RNA replication [55,56].

Membranes and their curvature

Membranes are the outer barriers of the cell and, in eukaryotic cells, also define internal organelles, enclosed spaces or compartments that are selectively permeable to ions and organic molecules. Phospholipids are the backbone of biological membranes and typically consist of a hydrophilic phosphate group (head) at one side and hydrophobic long fatty acid hydrocarbon chains (tail) at the other side. In water, phospholipids spontaneously arrange into a bilayer in which the hydrophobic tails are grouped together and the hydrophobic head groups face the aqueous environment. Besides phospholipids, biological membranes contain many transmembrane proteins that are anchored via hydrophobic domains [57]. Most integral membrane and also secretion proteins are made at the ER and contain an N-terminal or trans-membrane signal sequence that, upon translation, directs the ribosome to the ER membrane where membrane protein insertion and secretion protein translocation is facilitated by the Sec61-translocation machinery [58,59]. Once inserted into the ER and properly folded, the proteins follow specific pathways that transport them via vesicles to their final destination within or outside the cell.

The intracellular transport of membranes and their cargo is mediated by vesicles that pinch off from organelles towards the cytosol [60]. This is considered a "positive" membrane bending event and well-known examples are the formation of COPI-, COPII-, and clathrin-coated vesicles [61,62]. In uninfected eukaryotic cells, "negative" membrane bending (*i.e.* away from the cytosol) is only known to occur in multivesicular bodies which are late endosomes that internalize vesicles containing membrane proteins destined for degradation [63]. In addition, negative curvature is used extensively by viruses, not only while assembling virus particles, e.g. during budding into the ER, Golgi, or at the plasma membrane, but apparently also during the formation of the replication vesicles induced by many +RNA viruses [35,36,38,41].

Although the formation of positive curvature inside the cell is relatively well understood, the mechanisms behind the induction of negative curvature remain elusive thus far. Different membrane-bending mechanisms have been described and are categorized in five main divisions [60,64]. First, the phospholipid composition and asymmetric distribution of phospholipids within membranes can induce local curvature. Second, the cytoskeleton interacts with

membrane domains, in particular in the cell's periphery, and is able to "push" the membrane by polymerization or "pull" membrane tubules by motor proteins. Third, proteins with an amphipathic helix are inserted into one leaflet of the membrane bilayer or between the polar headgroups of lipid molecules and induce a positive curvature. Often, these amphipathic helix proteins recruit scaffolding proteins, like clathrin, COPI, and COPII, and their membrane-bending mechanism is considered to be the fourth group. These scaffolding proteins do not have a direct membrane association, but, are linked to membranes through adaptor proteins and mainly stabilize membrane curvature. Last, the structure of integral membrane proteins might influence the shape of membranes, especially if they have the ability to oligomerize. Unfortunately, only a few structures of transmembrane proteins are available and especially their contribution to membrane curvature needs to be studied in more detail.

Although significant advances in the determination of ultrastructure and composition of the membrane alterations induced by most +RNA virus families have been made, still very little is known about the exact mechanisms that underlie the membrane reorganizations that result in viral factories. Also the exact interplay of virus proteins with host cell factors and their recruitment is poorly understood. Nonetheless, interesting observations were made after expressing individual viral proteins or when using replicon systems, i.e. minimized systems that are still capable of replication and often lack expression of structural proteins. In particular, the expression of individual transmembrane subunits of many +RNA viruses can promote the induction of very similar structures like observed in infected cells [48,50,65-68]. Interestingly, it was recently found for FHV that expression of Protein A alone did not induce spherule formation whereas co-expression of the genomic RNA restored the formation of RNA replication-linked spherules [69]. These findings imply that, unlike what was found for many +RNA viruses, the formation of FHV replication organelles not only depend on viral proteins, but also on active RNA replication.

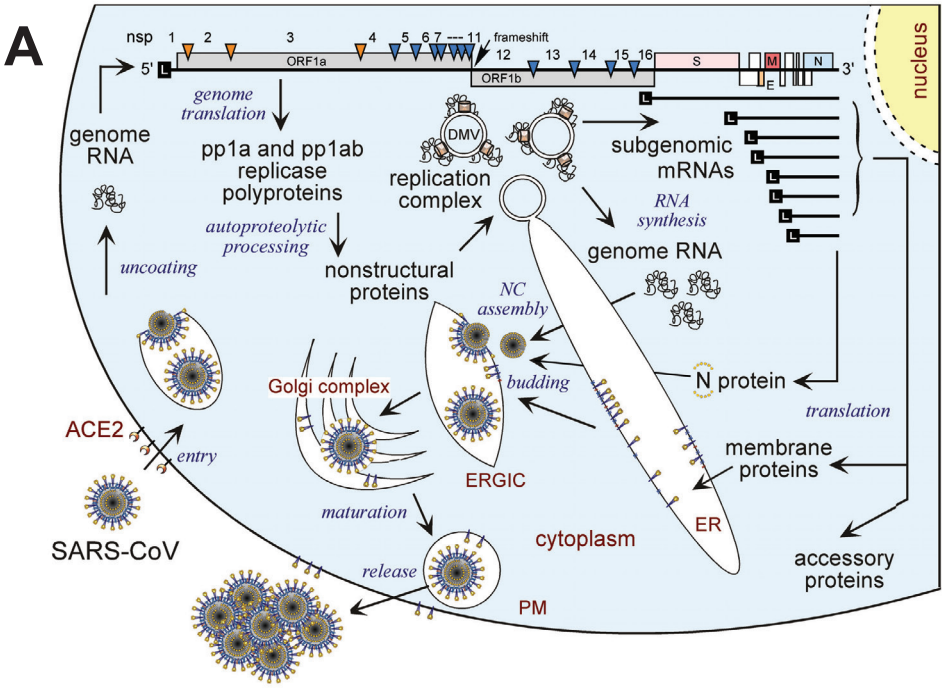
Nidoviruses

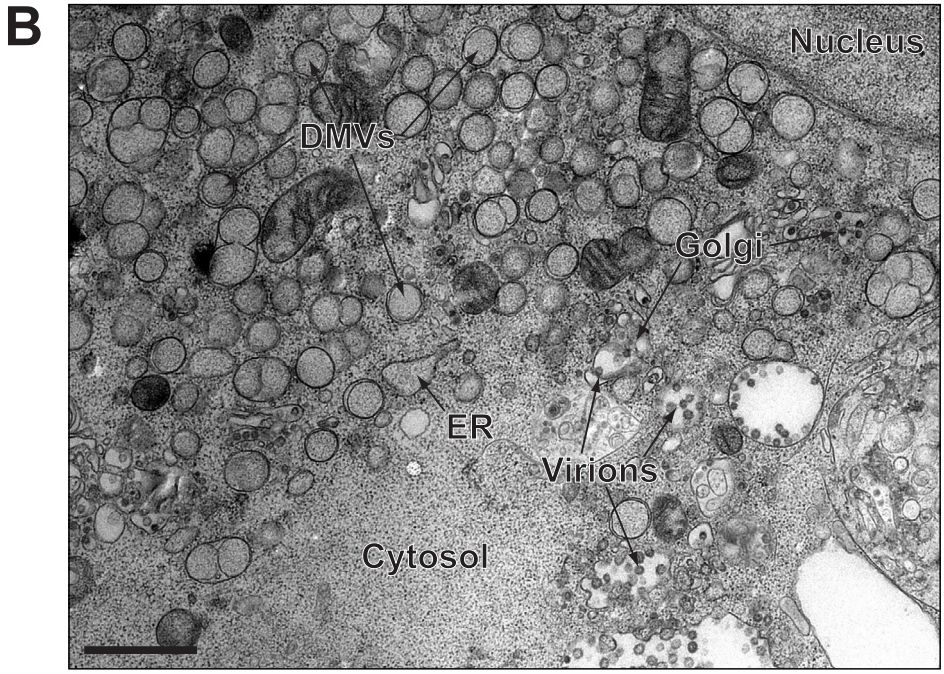
Nidoviruses (corona-, arteri-, and roniviruses) are enveloped +RNA viruses that are united by a number of common features in their replication strategy. The order of the nidoviruses is extremely diverse and their genome size ranges from large (~13 kb) to very large (~31 kb) [13]. They infect a variety of animal hosts, including mammals, birds, fish, and even invertebrates, and several nidoviruses are a major economical burden for the farming industry. Among nidoviruses, only certain coronavirus species infect humans, e.g. HCoV-229E and HCoV-OC43, and these human coronaviruses (HCoV) account for a significant percentage of the common colds during the winter and spring seasons. Because of difficulties in propagating these HCoVs in cell culture, mouse hepatitis virus (MHV) was the best studied coronavirus representative for a long time. This rapidly changed after the outbreak of the Severe Acute Respiratory Syndrome (SARS) in 2003. The causative agent of this respiratory disease, with a relatively high mortality

rate of 9.6%, was found to be a previously unknown coronavirus that subsequently became the best-known and -studied nidovirus [70-72]. Most likely, SARS coronavirus (SARS-CoV) evolved from a bat coronavirus that crossed the species barrier into the human population via civet cats from animal markets [73,74]. A concerted action led by the World Health Organization contained the SARS outbreak within a few months, mainly thanks to extensive contact tracing and quarantining of SARS patients. Nonetheless, recent discoveries of other animal and human coronaviruses, like HCoV-NL63 [75] and HCoV-HKU1 [76], illustrate the fact that more unknown coronaviruses might enter or already circulate in the human population.

Nidoviruses have a polycistronic genome organization and commonly use a characteristic strategy to express their structural and accessory protein genes [77,78] (Fig. 2A). Only the first two open reading frames (ORFs 1a and 1b) of the nidovirus genomic RNA are accessible to ribosomes and their translation yields the nidovirus replicase polyproteins, pp1a and pp1ab. Near the 3′ end of ORF1a, a conserved ribosomal frameshifting mechanism directs a fraction of the translating ribosomes into the -1 reading frame (ORF1b) to produce pp1ab, whereas the remaining ribosomes continue to terminate translation at the ORF1a stop codon, yielding pp1a. This results in a fixed ratio between pp1a and pp1ab, and thus ORF1a- and ORF1b-encoded subunits [79-81]. The remaining genes, encoding the structural and accessory proteins, are located towards the 3′ end of the genome. These downstream ORFs can only be expressed by translation of subgenomic mRNAs, in which they are placed at a 5′-proximal position. Both corona- and arteriviruses produce nested sets of 5-10 subgenomic mRNAs that are 3′-coterminal and additionally contain a common 5′ leader sequence that originates from the 5′ end of the genome [82,83]. Each of the subgenomic mRNAs is produced from a complementary subgenome-length negative-sense RNA, which - in arteri- and coronaviruses - is produced via a mechanism involving discontinuous extension of negative-strand RNA synthesis during which the "leader" and "body" sequences of the subgenomic RNA are joined [84]. Alternatively, negative-strand RNA synthesis can also be continuous, yielding the full-length negative-sense template for genome replication. As a side note, it should be men-

Figure 2. Schematic overview and EM visualization of the nidovirus life cycle, using SARS-CoV as an example. (A) Following entry and release into the cytosol, the +RNA genome is uncoated and translated into two replicase polyproteins (pp1a en pp1ab) from which 16 nsps are released by autoproteolytic cleavage. The nsps assemble into a membrane-bound replication/transcription complex (RTC) that is thought to be associated with double-membrane vesicles (DMVs). The RTC produces negative-stranded RNA that serves as template for genome replication and subgenomic mRNA transcription. The subgenomic mRNAs are translated into the viral structural and accessory proteins. The newly synthesized genome and nucleocapsid proteins (N) assembly into the nucleocapsid (NC) which, at budding sites in the ER-Golgi intermediate compartment (ERGIC), becomes enveloped by a membrane containing the viral envelope proteins. Maturation of the newly assembled virions takes place in the Golgi complex and downstream organelles of the exocytic pathway, until they are ultimately released from the infected cell (adapted with permission from [155]). (B) Electron micrograph showing the accumulation of the typical DMVs in the cytoplasm of a SARS-CoV-infected Vero E6 at 8h p.i. Golgi compartments containing newly assembled virions are in close proximity of the DMVs. Scale bar represents 1 μm.


A
nsp 1 2 3 4 5 6 7 --- 11 frameshift 12 13 14 15 16
5'
ORF1a
ORF1b
S
M
E
N
3'
nucleus
genome translation
genome RNA
pp1a and pp1ab replicase polyproteins
DMV
replication complex
subgenomic mRNAs
RNA synthesis
genome RNA
autoproteolytic processing
uncoating
nonstructural proteins
NC assembly
budding
N protein
translation
Golgi complex
ACE2
entry
SARS-CoV
ERGIC
membrane proteins
maturation
ER
cytoplasm
release
PM
accessory proteins


B
Nucleus
DMVs
Golgi
ER
Virions
Cytosol

tioned that the biological terms 'transcription' and 'replication' formally define the synthesis of RNA from a DNA template and the duplication of a DNA genome, respectively; however, in nidovirus-research these terms are commonly used to describe the synthesis of sg mRNAs and full-length genomes, respectively [77].

Upon translation, the replicase polyproteins are co- and post-translationally processed; hydrophobic transmembrane domains most likely anchor the nascent polyproteins to host cell membranes [65,85-87], and, virus-encoded proteases cleave both pp1a and pp1ab to produce between 13 and 16 mature nsps [23,88]. These nsps contain a variety of functions for RNA synthesis and processing, which are necessary for replication and transcription [89,90]. The majority of these nsps accumulate in the perinuclear region of the infected cell, suggesting that the viral replication/transcription complex (RTC) also resides in this area [91-96]. For both arteriviruses [65,97-99] and coronaviruses [93,100-105], electron microscopy revealed the induction of typical double-membrane structures, which have commonly been referred to as 'double-membrane vesicles' (DMVs) (Fig. 2B). Because the DMVs appeared as round structures in electron micrographs, it was assumed that they were isolated vesicular structures that are not connected to other membraneous compartments. Furthermore, it was unknown whether the inner and outer membranes were completely closed or might have openings, similar to those in the spherular invaginations mentioned above, that would connect the DMV interior with the cytosol. By immune electron microscopy, it was shown that both replicase subunits and viral RNA are associated with arteri- and coronavirus DMVs, strongly suggesting a viral origin and role in RNA synthesis for these unusual structures. This conclusion was further supported by experiments in which expression of just two arterivirus replicase cleavage products, nsp2 and nsp3, was shown to induce DMVs very similar to those observed in infected cells [65,97,106].

The ER was suggested to be the most likely donor of the membranes that carry the nidovirus RTC [97,100,101], although some studies on coronaviruses also suggested a role for late endosomes and autophagosomes [96,107]. The ER is a large cytoplasmic organelle which forms an interconnected network of functionally diverse compartments within the eukaryotic cell [108,109]. The rough ER is involved in both translocation and maturation of proteins, and the smooth ER is mainly engaged in lipid synthesis, signal transduction within the cell, and stress responses. Regardless of the question whether the ER is involved in the formation of DMVs, nidoviruses do need the ER and downstream compartments of the secretory pathway for the production and maturation of viral envelope proteins and as site for virus assembly [110-112].

Electron microscopy of intracellular structures

About 75 years ago, the development of the electron microscope suddenly provided access to a vast area of biological structures that are beyond the resolution of the light microscope.

Consequently, entirely new procedures for biological specimen preparation had to be developed to be able to use the resolving power of this new instrument to its full extent [113-115]. Studies into cellular ultrastructure were performed with the excitement and anticipation that attended the geographical exploration of unknown continents several centuries earlier [116,117]. Cellular organelles and macromolecular components were rapidly discovered and the interests of biologists, physicists, and chemists converged in this new approach to cellular research, which paved the way for the present field of cell biology. For transmission electron microscopy (TEM), ideally specimens should be thin, dry, and contain heavy atoms that diffract electrons. Because the majority of biological samples do not match these criteria, new preparation methods had to be developed, involving fixation, staining, dehydration, and embedding in epoxy resins which can be sectioned into slices thin enough for electrons to penetrate and shape a projection image [118-120]. For that purpose, chemical fixation of cells with aldehydes and/or osmium tetraoxide, followed by a uranyl acetate and/or lead citrate staining, became the standard for stabilization and contrast formation of biological structures.

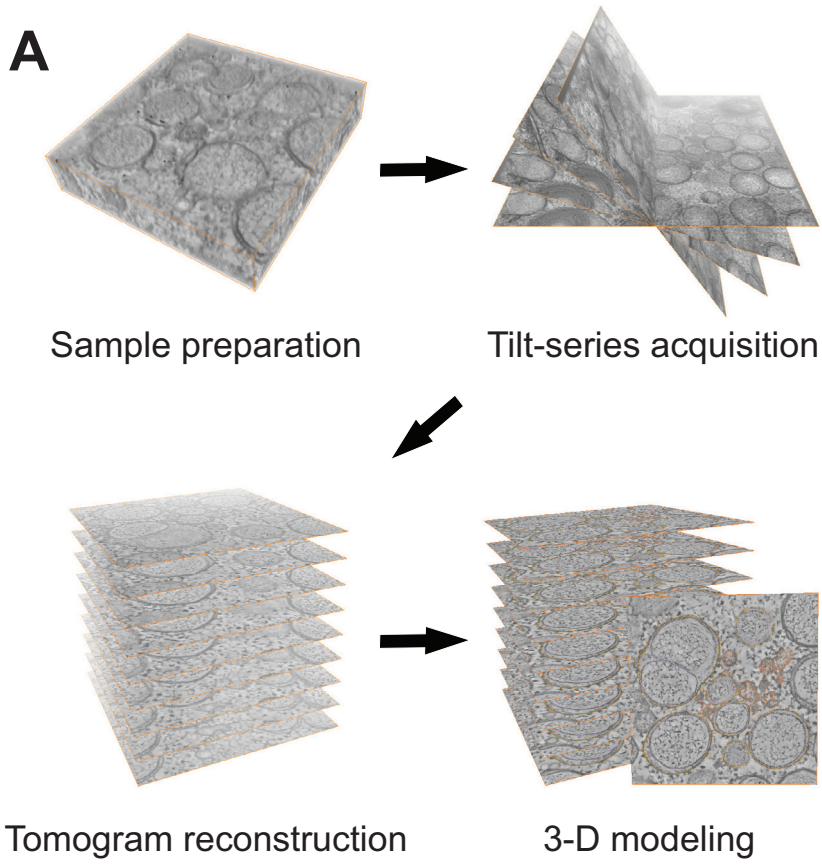
Upon chemical fixation, +RNA virus-induced membrane structures implicated in viral RNA synthesis, in particular those of coronaviruses, were found to be extremely fragile, which seriously hampered their straightforward chemical preparation for ultrastructural studies [49,100,121,122]. Alternative methods were developed that improved the ultrastructural preservation significantly of both cells [123,124] and +RNA virus-induced membrane structures [49,100,121,122]. One such technique, rapid freezing of living biological materials, is a faster immobilization method and has obvious advantages compared to the slow diffusion of fixatives into the specimen that is employed for chemical fixation. In order to properly freeze specimens for TEM, cryo-immobilization needs to be achieved within 5-10 ms: fast enough to turn water into a vitreous state, and thus preventing the damage caused by the formation of crystalline ice. In the studies described in this thesis, two cryo-immobilization methods were applied, plunge-freezing and high-pressure freezing, which rely on different principles to prepare frozen cells [125-128]. With the plunge-freezing technique, monolayers of cells are rapidly immersed in a cryogen, e.g. ethane or propane, with a high freezing rate (~10^{4o}C/sec). The latter property is required to efficiently extract heat from the specimen in order to rapidly reach the temperature of liquid nitrogen, i.e. -196°C. Although plunge-freezing is a relatively easy cryo-fixation method, it only produces well-frozen cells to a depth of ~10 μm below the specimen surface and often results in local ice crystal formation. The second method, high-pressure freezing, involves pressurizing samples to ~2000 bar before the actual freezing process is started, thus preventing ice crystal expansion. With this technique, well-frozen samples with a thickness up to 200 μm can be obtained and the technique even allows the proper freezing and preparation of organ tissue for TEM observation [129,130].

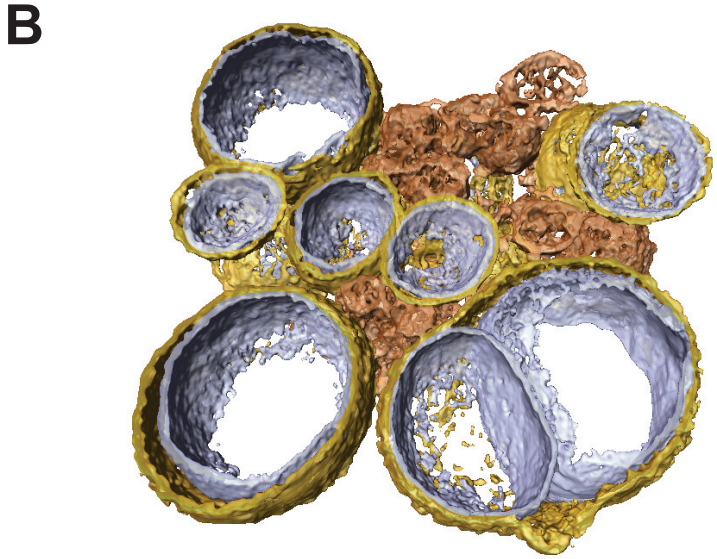
In principle, samples can be subjected to TEM analysis in a frozen, hydrated state, which is believed to resemble the native state as closely as possible [131]. Unfortunately, the

thickness of the average cell prevents its observation *in toto* and only permits imaging of areas that are thin enough for electrons to penetrate without undergoing multi-scattering events. This applies to small bacteria [132-134] or, in the case of cultured mammalian cells, to the cell's periphery [135]. Cryo-sectioning of frozen-hydrated samples is now becoming a popular technique to overcome this thickness limitation [136], but does not circumvent another limiting factor of frozen-hydrated samples, i.e. the very low electron dose that needs to be used in order to avoid radiation damage by the electron beam [137,138]. An alternative method is freeze substitution: frozen cells are subjected to a substitution-fixation step at -90°C, during which water is removed and substituted with organic solvents containing fixatives and contrasting agents [139]. Due to the low temperature, commonly used fixatives and contrasting agents are barely active and will first diffuse into the sample without cross-linking it. Subsequently, the temperature is gradually raised to room temperature to allow proper fixation throughout the specimen. Finally, as in a chemical fixation, the freeze-substituted cells are embedded in an epoxy resin that can be sectioned to yield thin slices for TEM observation.

In conventional 2-dimensional TEM, cells are sectioned into 80-100 nm thick slices from which a projection image is taken inside the electron microscope. Although the sections are relatively thin, they still contain 3-dimensional (3-D) information that cannot be retrieved from a single projection image. If a sample holds a large amount of identical particles distributed with random orientations, a reconstruction can be calculated by the single-particle analysis approach [140-142]. For this method, Euler angles describing their 3-D orientation in space are assigned to individual particles which can then be "back-projected" into a 3-D model. Yet, most macromolecular- and membrane structures inside a cell are not identical and thus not suitable for single-particle analysis. Therefore, a technique has been developed that can extract 3-D information from images derived from tilt series of a specimen [143,144]. For this electron tomography (ET) technique, the sample is tilted inside the microscope, typically from -70° to +70° with a tilt-increment of 1° between each step (Fig. 3A). This results in a dataset containing multiple images from the same object from a different perspective. The introduction of the charged coupled device (CCD) camera, in combination with new automating algorithms for measurement and correction of image shifts and defocus values

Figure 3. Schematic diagram illustrating the sequence of steps involved in obtaining a three-dimensional image by room temperature electron tomography. (A) Following sample fixation and sectioning, slices of cells with a thickness of ~200 nm are overlaid with a suspension of gold particles that act as fiducial markers during the image alignment procedure. Inside the electron microscope, a series of projection images is collected at varying tilt angles around the axis perpendicular to the electron beam, usually ranging from +70° to -70° with a tilt increment of 1°. The tilt-series are then reconstructed into a three-dimensional (3-D) volume (tomogram) which forms the basis of data interpretation. 3-D representation of cellular components can be accomplished by masking and surface rendering of objects in successive sections. (B) Example of a final 3-D surface rendered model showing the SARS-CoV reticulovesicular network of modified ER (see chapter 2).


A
Sample preparation
Tilt-series acquisition
Tomogram reconstruction
3-D modeling


B

resulting from specimen tilting, made the data acquisition more straightforward and less time consuming [145]. After acquisition of the tilt-series, the images are back-projected in Fourier space to finally derive the 3-D architecture of the object in real space [146]. To portray the large and complex datasets which are produced in ET, tomograms are often modeled by 3-D surface rendering. However, it should be stressed that this process is largely based on the subjective interpretation of the researcher (Fig. 3B) and that biological conclusions should therefore preferably be based on the raw tomography data.

ET of cell components is an extremely powerful technique for visualizing the 3-D organization of organelles within the 3-10 nm resolution range and has contributed significantly to our understanding of the cell's architecture. The mitochondrial Baffle model for instance, which defined mitochondrial cristae as simple folds of the mitochondrial inner-membrane, was shown to be inaccurate [147]. In fact, the cristae are highly dynamic structures which, depending on the cell's state, transform from simple tubular to more complex lamellar structures that stay connected to the inner-membrane via small neck-like connections. In another study, ET was applied to address the involvement of the ER in peroxisome biogenesis. Although the traditional hypothesis predicted peroxisomes to be autonomous organelles that multiply by fission, clear membrane connections between the ER and newly formed peroxisomes were found by using ET, which strongly suggested the ER to be involved in peroxisome regeneration [148]. Apart from organelle ultrastructure, the resolution of ET nowadays suffices to study the structure and even dynamics of smaller macromolecular assemblies like the nuclear pore complex [149,150], ribosomes [151-153] and proteasomes [154], in the context of their natural environment.

Outline of this thesis

All +RNA viruses infecting mammalian cells are thought to modify membranes into structures that provide a suitable microenvironment for their RNA synthesis. Although a first impression of the ultrastructure of these compartments has been documented for several nidoviruses [97-99,101-104], the experimental setup always included chemical fixation methods and was therefore prone to preparation artifacts [100]. For the work described in this thesis, state-of-the-art cryo EM techniques were used to analyze the ultrastructure and properties of the nidovirus-induced membrane structures with which replication/transcription complexes are thought to be associated. Our aim was to learn more about the structural and functional interactions within this viral RNA-protein-membrane complex and its relation to host cell components.

In **chapter 2**, cryo-fixation and electron tomography of SARS-coronavirus-infected cells were optimized and combined to analyze the membrane modifications that are induced by virus infection. The chapter provides a general overview of the structural changes in the course of infection. 3-D morphological analysis of the membrane rearrangements

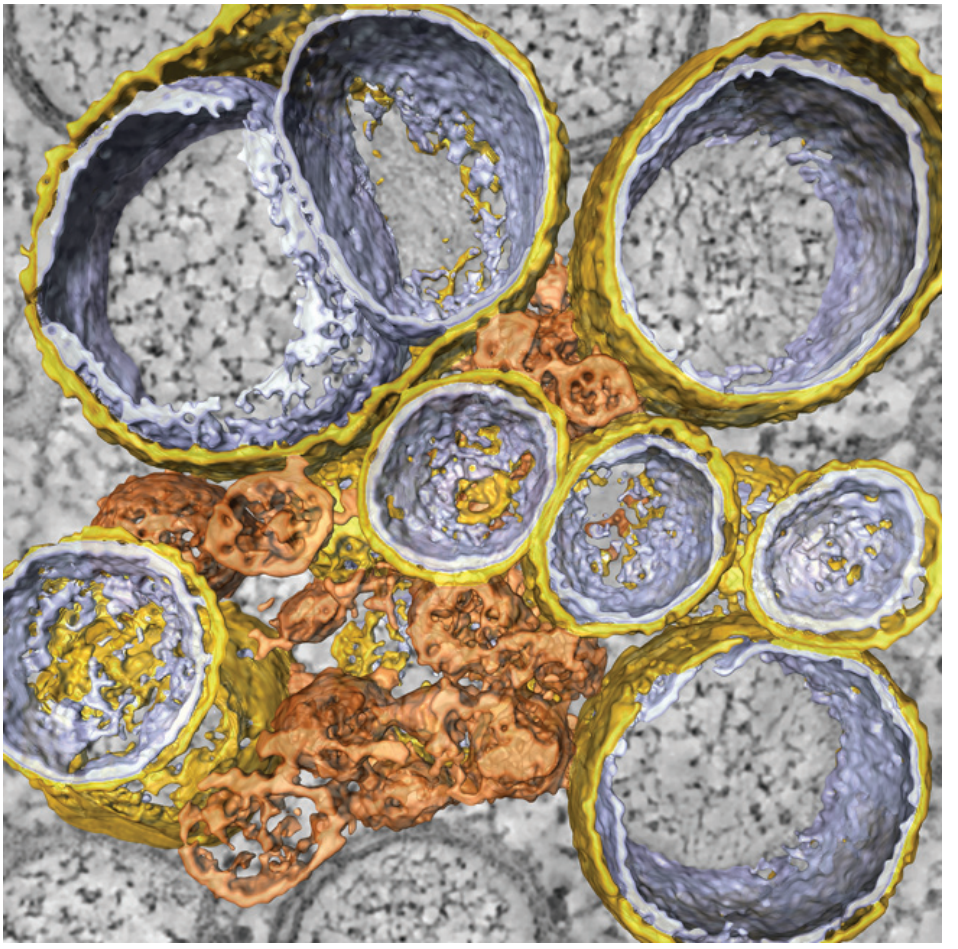
showed that SARS-CoV induces a reticulovesicular network (RVN) which is derived from ER membranes. Immuno-labeling was used to localize various replicase subunits and dsRNA, presumably representing the intermediate stage of viral RNA synthesis, on the different compartments of the RVN.

With the new results of chapter 2 as a starting point, the involvement of the ER and its proteins in SARS-CoV RVN formation was studied in **chapter 3**. Immunofluorescence microscopy was used to study which ER compartments may be associated with SARS-CoV replication. Interestingly, this revealed that the main cellular translocase, Sec61α, extensively co-localized with the membrane-bound nsps and even seemed to be recruited to the sites where these are present. A set of biochemical experiments, including *in vitro* RTC activity assays, demonstrated that the early secretory pathway unlikely plays a major role in RVN morphogenesis or functionality. These results confirmed our previous observation that RVN membranes are derived from rough endoplasmic reticulum (rER).

Chapter 4 describes a set of experiments performed to analyze the requirement for continuous translation in coronavirus RTC activity and RVN expansion. RTC activity was carefully monitored when translation inhibitors were used to block translation at several stages of SARS-CoV and MHV infection. These experiments showed that a low level of RTC activity could be maintained for several hours in the absence of protein synthesis, which suggested that preformed RTCs continue to function under these conditions. Light and electron microscopy were used to demonstrate that translation inhibition interrupts RVN development, suggesting that new viral proteins are required for RVN expansion.

In **chapter 5**, our in-depth ultrastructural study of nidovirus-induced membrane structures was extended to EAV-infected cells, thus allowing the comparison of two distantly related nidoviruses. It was discovered that the induction of an RVN-like structure appears to be a common property of at least two prominent members of the nidovirus order. One striking parallel between the EAV- and SARS-CoV-induced RVNs was the accumulation of double-stranded RNA in the EAV DMV interior, whereas the replicase proteins, including the RNA-dependent RNA polymerase, mainly localized to RVN membranes. Furthermore, semi-permeabilization and nuclease digestion experiments on EAV-infected cells were used to gain support for the observation that openings connecting the DMV interior with the cytosol were rarely observed. This suggests that the DMV interior is not accessible from the cytosol and that protective membranes segregate the double-stranded RNA. Additionally, we explored electron spectroscopic imaging as a novel approach to visualize and quantify the RNA content of individual DMV cores, which in the future might aid to analyze and compare the replication structures of different +RNA viruses in considerable more detail.

Finally, **chapter 6** summarizes the results described in this thesis in a broader perspective and in the context of recent findings for other +RNA replication structures. Moreover, technical approaches that might aid to identify the exact place of nidovirus RNA synthesis are discussed.



CHAPTER 2

SARS-coronavirus replication is supported by a reticulovesicular network of modified endoplasmic reticulum

Kèvin Knoops, Marjolein Kikkert, Sjoerd H.E. van den Worm, Jessika Zevenhoven-Dobbe, Yvonne van der Meer, Abraham J. Koster, A. Mieke Mommaas and Eric J. Snijder

PLoS Biology (2008) 16;6(9):e226
(Image featuring issue cover)
Reprinted with permission

ABSTRACT

Positive-strand RNA viruses, a large group including human pathogens such as SARS-coronavirus (SARS-CoV), replicate in the cytoplasm of infected host cells. Their replication complexes are commonly associated with modified host cell membranes. Membrane structures supporting viral RNA synthesis range from distinct spherular membrane invaginations to more elaborate webs of packed membranes and vesicles. Generally, their ultrastructure, morphogenesis, and exact role in viral replication remain to be defined. Poorly characterized double-membrane vesicles (DMVs) were previously implicated in SARS-CoV RNA synthesis. We have now applied electron tomography of cryofixed infected cells for the three-dimensional imaging of coronavirus-induced membrane alterations at high resolution. Our analysis defines a unique reticulovesicular network of modified endoplasmic reticulum that integrates convoluted membranes, numerous interconnected DMVs (diameter 200–300 nm), and "vesicle packets" apparently arising from DMV merger. The convoluted membranes were most abundantly immunolabeled for viral replicase subunits. However, double-stranded RNA, presumably revealing the site of viral RNA synthesis, mainly localized to the DMV interior. Since we could not discern a connection between DMV interior and cytosol, our analysis raises several questions about the mechanism of DMV formation and the actual site of SARS-CoV RNA synthesis. Our data document the extensive virus-induced reorganization of host cell membranes into a network that is used to organize viral replication and possibly hide replicating RNA from antiviral defense mechanisms. Together with biochemical studies of the viral enzyme complex, our ultrastructural description of this "replication network" will aid to further dissect the early stages of the coronavirus life cycle and its virus-host interactions.

INTRODUCTION

Viruses rely on the host cell's infrastructure and metabolism during essentially all stages of their replication cycle and have therefore adopted strategies to coordinate a variety of molecular interactions in both time and intracellular space. The fact that the replication complexes of positive-strand RNA (+RNA) viruses of eukaryotes are invariably associated with (modified) intracellular membranes appears to be a striking example of such a strategy [24-26,32,36,156-158]. Specific +RNA virus replicase subunits are targeted to the membranes of particular cell organelles that are subsequently modified into characteristic structures with which viral RNA synthesis is associated. The morphogenesis, ultrastructure, and function of these complexes, sometimes referred to as "viral factories," are only beginning to be understood. They may facilitate the concentration of viral macromolecules and provide a membrane-based structural framework for RNA synthesis. Other potential benefits include the possibility to coordinate different steps in the viral life cycle and to delay the induction of host defense mechanisms that can be triggered by the double-stranded RNA (dsRNA) intermediates of +RNA virus replication [28,29,159]. Defining the structure–function relationships that govern the membrane-associated replication of +RNA viruses, a large virus cluster including many important pathogens, will enhance our general understanding of their molecular biology and may have important implications for the development of novel antiviral control strategies.

Following the 2003 outbreak of severe acute respiratory syndrome (SARS; for a review, see [160]), the coronavirus family of +RNA viruses received worldwide attention. In addition to SARS-coronavirus (SARS-CoV), several other novel family members were identified, including two that also infect humans [161]. Coronaviruses, and other members of the nidovirus group, have a polycistronic genome and employ various transcriptional and (post)translational mechanisms to regulate its expression [13,162]). The gene encoding the replicase/transcriptase (commonly referred to as "replicase") comprises about two-thirds of the coronavirus genome, which—at 27–31 kb—is the largest RNA genome known to date. The replicase gene consists of open reading frames (ORFs) 1a and 1b, of which the latter is expressed by a ribosomal frameshift near the 3′ end of ORF1a. Thus, SARS-CoV genome translation yields two polyproteins (pp1a and pp1ab) that are autoproteolytically cleaved into 16 nonstructural proteins (nsp1 to 16; Fig. 1) by proteases residing in nsp3 and nsp5 [93,96,163]. Several of the replicative enzymes of coronaviruses, like an RNA-dependent RNA polymerase (RdRp) and a helicase, are common among +RNA viruses, but they also contain a variety of functions that are rare or absent in other +RNA viruses, including a set of intriguing proteins that are distantly related to cellular RNA processing enzymes [13,83,162]. The complexity of coronavirus RNA synthesis is further highlighted by the fact that it entails not only the production of new genome molecules from full-length negative-strand RNA ("replication"), but also a unique mechanism of discontinuous RNA synthesis to generate subgenome-length negative-strand

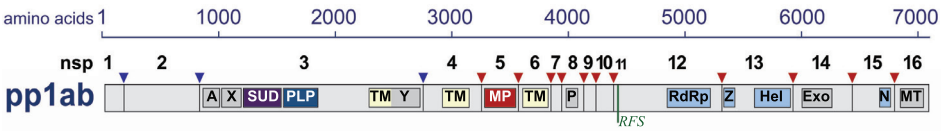


Figure 1. The coronavirus replicase polyprotein. The domain organization and proteolytic processing map of the SARS-CoV replicase polyprotein pp1ab. The replicase cleavage products (nsp1–16) are numbered, and conserved domains are highlighted (blue, conserved across nidoviruses; grey, conserved in coronaviruses). These include transmembrane domains (TM), protease domains (PLP and MP), and (putative) RNA primase (P), helicase (HEL), exonuclease (Exo), endoribonuclease (N), and methyl transferase (MT) activities. For more details, see [13,83]. The delineation of amino acids encoded in ORF1a and ORF1b is indicated as RFS (ribosomal frameshift), and arrows represent sites in pp1ab that are cleaved by the nsp3 papain-like protease (in blue) or the nsp5 main protease (in red).

RNA templates for subgenomic mRNA production ("transcription") [77,78]. The resulting set of subgenomic transcripts (eight in the case of SARS-CoV) serves to express structural and accessory protein genes in the 3′-proximal domain of the genome. Ultimately, new coronavirions are assembled by budding of nucleocapsids into the lumen of pre-Golgi membrane compartments [111,164].

The nidovirus replicase includes several (presumed) multispanning transmembrane proteins that are thought to physically anchor the replication/transcription complex (RTC) to intracellular membranes. In the case of coronaviruses, these domains reside in nsp3, nsp4, and nsp6 (Fig. 1) [85,86]. In the cytoplasm of infected cells, nidoviruses induce the formation of typical paired membranes and double-membrane structures that have commonly been referred to as "double-membrane vesicles" (DMVs) [97,100,103,104]. These structures are mainly found in the perinuclear area of the cell, where—according to immunofluorescence (IF) microscopy studies—de novo–made viral RNA and various replicase subunits colocalize, presumably in the viral RTC [93,94,96,100]. Immunoelectron microscopy (iEM) previously revealed that SARS-CoV nsp3 and nsp13 localize to the outside of DMVs and/or the region between DMVs. Although these proteins also colocalized in part with endoplasmic reticulum (ER) marker proteins [100,101,104], the origin of DMV membranes has remained undecided since other studies have implicated other organelles in the formation of RTCs and DMVs, e.g., late endosomes, autophagosomes, and most recently, the early secretory pathway and potentially also mitochondria [105,107,165-167]. Previous ultrastructural studies may have been hampered by the technical challenge of DMV preservation [100]. In particular, the DMV inner structure is fragile, and loss or collapse of DMV contents likely was a complicating factor. Although the use of cryofixation methods dramatically improved DMV preservation [100], our understanding of the three-dimensional (3-D) organization and origin of DMVs was hampered by the inherent limitations of analyzing "conventional" thin sections (100 nm) by electron microscopy (EM), in particular since the diameter of DMVs was estimated to be between 200 and 350 nm [100].

To develop a 3-D ultrastructural model for the RTC-related membrane alterations in SARS-CoV–infected cells, we have now employed electron tomography (ET; for reviews, see [143,168]). This technique uses a set of two-dimensional (2-D) transmission EM images, recorded at different specimen tilt angles with respect to the primary beam, for calculating a 3-D image (tomogram). Typically, the specimen is tilted over a range of ±65° in small tilt increments (1°), and an image is recorded at each tilt angle. The tomograms of infected cells allowed us to trace DMV membranes and establish previously unnoticed structural connections. In particular, ET revealed that coronavirus DMVs are not isolated vesicles, but instead are integrated into a unique reticulovesicular network of modified ER membranes, which also includes convoluted membranes that were not previously implicated in viral RNA synthesis. Strikingly, the latter structure—and not the DMVs—were primarily immunolabeled using antibodies recognizing viral replicase subunits. In contrast, immunolabeling with an antibody recognizing (presumably viral) dsRNA abundantly labeled the DMV interior. Since we could not discern a connection between the DMV interior and cytosol, our analysis raises several questions about the mechanism of DMV formation and the actual site of SARS-CoV RNA synthesis. The virus-induced "replication network" documented here places the early stages of the viral lifecycle and accompanying virus–host interactions in a new perspective.

RESULTS

SARS-Coronavirus infection induces multiple distinct membrane alterations

Previously, we experienced that, compared to more traditional chemical fixation protocols, the preservation of the fragile coronavirus DMV structures could be significantly improved by using a combination of cryofixation and freeze substitution (FS) [100]. We now further refined the FS protocol, in particular by improving membrane contrast by adding 10% water to the FS medium [169].

Using these optimized conditions to prepare thin sections (100 nm) of SARS-CoV–infected Vero E6 cells, we could detect the first DMVs at 2 h postinfection (h p.i.) and were able to monitor the subsequent development of virus-induced membrane alterations. Early DMVs had sizes ranging from 150 to 300 nm, were distributed throughout the cytoplasm, and were sometimes located in the proximity of small reticular membranes with which, occasionally, they appeared to be connected (Fig. 2A). From 4 h p.i. on, the number of DMVs increased dramatically, and DMV clusters were observed throughout the cell, again frequently accompanied by and sometimes clearly connected to reticular membrane structures (Fig. 2B, arrow). As infection progressed, DMVs became increasingly concentrated in the perinuclear area of the cell (Fig. 2C), in accordance with the available IF microscopy data for various SARS-CoV replicase subunits [94,96,100]. At 7 h p.i., a 100-nm-thick slice through the center of an

infected Vero E6 cell generally contained between 200 and 300 DMVs. Initially, the DMV inner and outer membranes were generally tightly apposed, but occasionally, some luminal space between the two lipid bilayers could be discerned (Fig. 2B, arrowhead). Although similar observations were previously made for different nidoviruses using a variety of chemical and cryofixation protocols, and despite the generally excellent preservation of cellular membranes, the documented fragility of coronavirus DMVs makes it clear that we cannot formally exclude the possibility that these local separations could result from preparation damage.

From 3 h p.i. on, we also observed large assemblies of convoluted membranes (CM), often in close proximity to DMV clusters (Fig. 2D). These structures, with diameters ranging from 0.2 to 2 μm, are probably identical to the "reticular inclusions" that were first observed in cells infected with mouse hepatitis coronavirus (MHV) more than 40 y ago [102] and were later referred to as 'clusters of tubular cisternal elements,' which may have a connection to the ER-Golgi intermediate compartment (ERGIC) [111]. We noticed that the SARS-CoV–induced CM resembled one of the replication-related membrane alterations induced by flaviviruses, which were proposed to be the site of viral genome translation and polyprotein processing [25,39,170]. In some of our images, the SARS-CoV–induced CM appeared to be continuous with both DMV outer membranes (Fig. 2D; inset) and ER cisternae, suggesting a link to the viral RTC also in coronaviruses.

Especially at later stages of SARS-CoV infection (generally beyond 7 h p.i.), we observed packets of single-membrane vesicles surrounded by a common outer membrane, as previously described by Goldsmith et al. [103]. The diameter of these vesicle packets (VPs) ranged from 1 to 5 μm, and they sometimes included more than 25 inner vesicles (Fig. 2E). In terms of size, morphology, electron density, and immunolabeling properties (see below), the vesicles contained in VPs strongly resembled the inner vesicles of DMVs, as seen at earlier time points. During these later stages of infection, the clustered single DMVs (Fig. 2C) gradually disappeared, suggesting their merger into the VPs. The average outer diameter of DMV inner vesicles at 4 h p.i. was 250 ± 50 nm ($n = 99$), whereas later in infection, their average diameter (DMVs and VPs combined) increased to about 300 nm (310 ± 50 nm at 7 h p.i., 300 ± 50 μm at 10 h p.i.).

Our observations define VPs as a third distinct modification of intracellular membranes that is induced by SARS-CoV infection. By 10 h p.i., VPs appeared to have merged into even larger cytoplasmic vacuoles, containing both vesicles as well as significant numbers of budding and completed virions (Fig. 2E). DMVs, CM, and VPs were not observed in mock-infected Vero E6 cells.

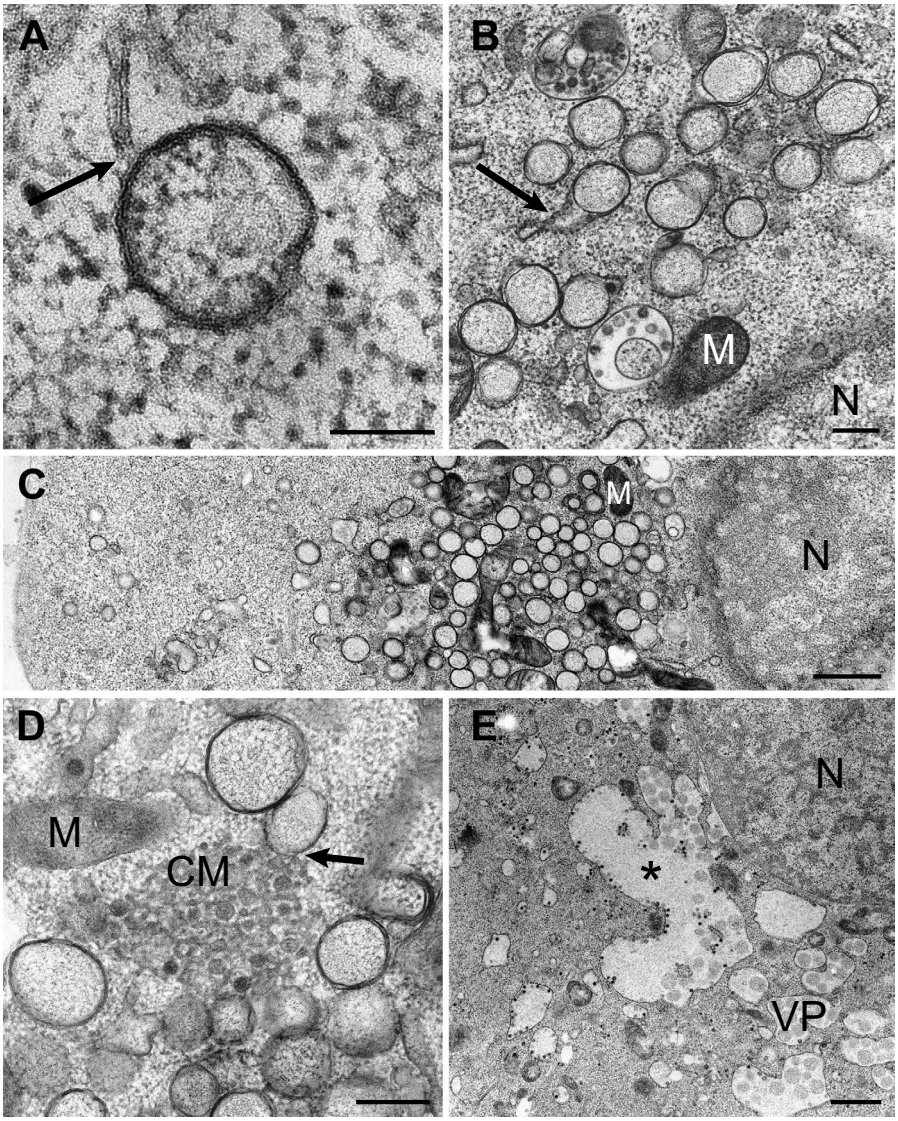


Figure 2. Overview of membrane structures induced by SARS-CoV infection. Electron micrographs of SARS-CoV–infected Vero E6 cells. The cells were cryofixed and freeze substituted at 2 h p.i. (A), 8 h p.i. (B–D), or 10 h p.i. (E). (A) Early DMV as observed in a few sections, showing a connection (arrow) to a reticular membrane. (B) From 4 h p.i. on, clusters of DMVs began to form. Occasionally, connections between DMV outer membranes and reticular membrane structures were observed (arrow). Locally, luminal spacing between the DMV outer and inner membranes could be discerned (arrowhead). (C) As infection progressed, DMVs were concentrated in the perinuclear area (nucleus; N), often with mitochondria (M) lying in between. (D) Example of a cluster of CM, which were often surrounded by groups of DMVs. The structure seems to be continuous with the DMV outer membrane (inset). (E) During the later stages of infection, DMVs appeared to merge into VPs, which developed into large cytoplasmic vacuoles (asterisk) that contained not only single-membrane vesicles (arrowhead pointing to an example), but also (budding) virus particles. Scale bars represent 100 nm (A), 250 nm (B and D), or 1 µm (C and E).

Electron tomography reveals a reticulovesicular network of modified ER membranes in SARS-CoV–infected cells

Although, occasionally, the analysis of "conventional" thin sections suggested CM and DMV outer membranes to be continuous and connected to ER cisternae, a more accurate assessment required an analysis in three dimensions. We therefore employed ET of semi-thick (200 nm) sections of cryofixed, SARS-CoV–infected Vero E6 cells. By using a specimen holder that could also be tilted around a second axis, perpendicular to both electron beam and first tilt axis, we obtained datasets, each consisting of 262 differently tilted 2-D images, which were used to produce a high-resolution reconstruction in three dimensions. Such "dual-axis" tomograms allowed us to visualize and analyze membrane continuities between the respective structures defined in the previous paragraph (as illustrated by Videos S1–S4 and Fig. 3–5). The analysis was performed at 7 h p.i., a time point at which the various membrane alterations were all abundantly present in the absence of advanced cytopathology. Nevertheless, in some cells, infection had progressed more than in others, allowing the visualization of both advanced and earlier stages of infection in the same specimen.

Two major conclusions from this ET analysis were (1) that most or—likely—all coronavirus DMVs are interconnected by their outer membrane and (2) that they are part of an elaborate network that is continuous with the rough ER. As illustrated by the 3-D reconstruction in Fig. 3, for most DMVs, we observed one or multiple thin (~8 nm in diameter), "neck-like" connections of their outer membrane to the outer membranes of other DMVs, to CM, and to cisternae of the rough ER (Fig. 3; insets). For example, in the two tomograms used for Videos S1 and S3, at least one such connection was visible for 77 out of 81 DMVs analyzed, strongly suggesting that for the remaining DMVs, such outer membrane connections existed but fell outside the volume reconstructed using these particular tomograms. Of the 77 DMVs for which at least one outer membrane connection was detected, 38 had a single connection, whereas 27, nine, and three DMVs had two, three, and four connections, respectively. Of these 131 connections, approximately one-half were between the outer membranes of DMVs and the other half were connections to ER or CM membranes, a ratio that was more or less stable when DMVs were differentiated in groups having one, two, or three connections. Consequently, the original concept of "free floating" coronavirus-induced DMVs (i.e., structures surrounded by two, fully detached unit membranes) should be adjusted, and it would appear more appropriate to describe DMVs as single-membrane vesicles confined in the lumen of an ER-connected membrane network. The VPs (Fig. 4 and 5) and the tightly apposed membranes of the CM (Fig. 5C) were found to be integral parts of the same reticulovesicular network. The ET analysis further suggested the presence of fibrous material inside DMV inner vesicles (Fig. 3–5). Although ribosomes were clearly visible on rough ER cisternae and DMV/VP outer membranes (Fig. 4, arrowheads; Video S1), they were not detected on the membranes or in the interior space of the inner vesicles.

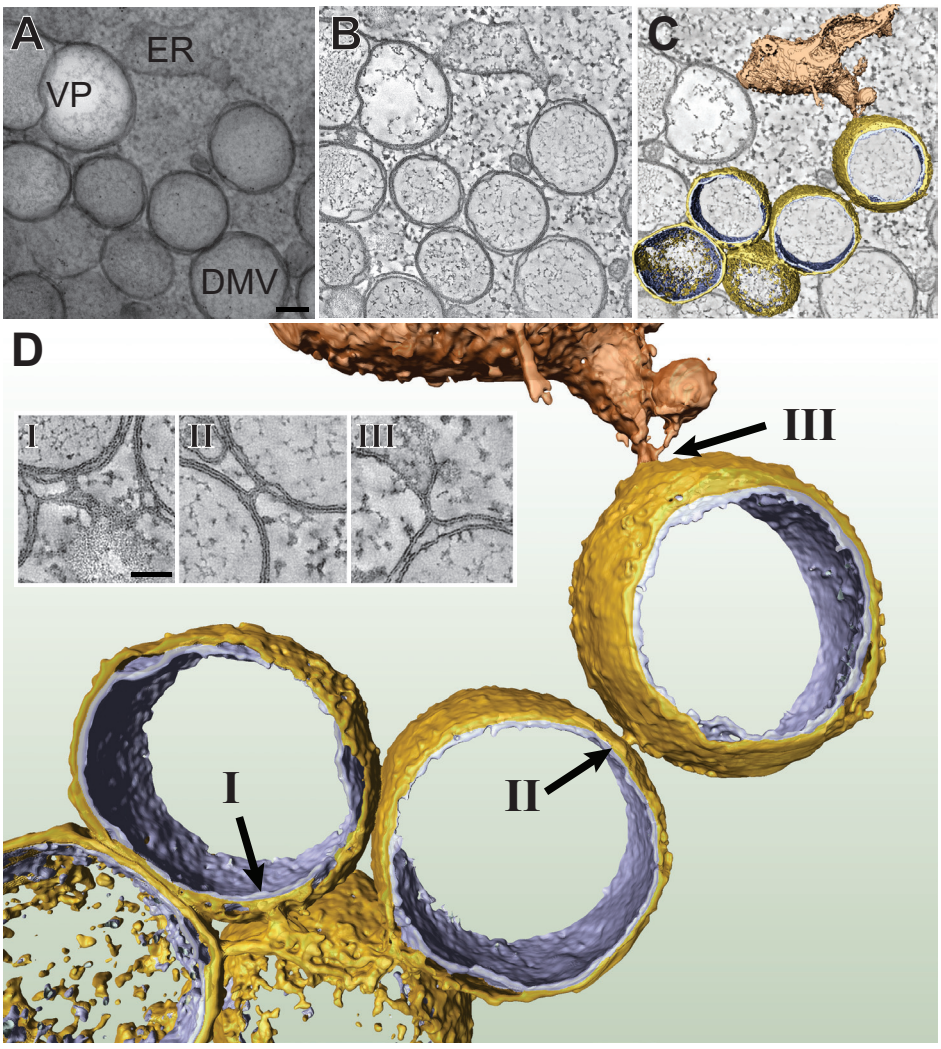


Figure 3. Electron tomography revealing the interconnected nature of SARS-CoV–induced DMVs. The series of images at the top illustrates how a 3-D surface-rendered model was derived by applying ET on a semi-thick section of a SARS-CoV–infected Vero E6 cell cryofixed at 7 h p.i. (A) A 0°-tilt transmission EM image of a 200-nm-thick resin-embedded section showing ER and a cluster of DMVs. The 10-nm gold particles were layered on top of the sections and were used as fiducial markers during subsequent image alignment. Scale bar represents 100 nm. (B) Using the IMOD software package (see Materials and Methods), tomograms were computed from dual-axis tilt series of the 200-nm-thick section shown in (A) (see also Videos S1 and S2). The tomographic slice shown here has a thickness of 1.2 nm. (C) The improved image from (B) following anisotropic diffusion filtering. The optimized signal-to-noise ratio facilitates thresholding and DMV surface rendering. (D) Final 3-D surface-rendered model showing interconnected DMVs (outer membrane, gold; inner membrane, silver) and their connection to an ER stack (depicted in bronze). Arrows (I, II, and III) point to three clearly visible outer membrane continuities, with insets highlighting these connections in corresponding tomographic slices. Scale bar represents 50 nm.

By 7 h p.i., in part of the cells, the formation of VPs had begun (Fig. 4 and 5), for which we could distinguish two different morphologies in our tomograms. In the first type (Fig. 4; Video S3), the membranes of the adjacent inner vesicles were tightly apposed but intact, and there was little luminal space between the inner vesicles and the surrounding outer membrane. In contrast, the outer membrane of the second type of VP appeared more relaxed and generally contained multiple inner vesicles (Fig. 5A; Video S4). Strikingly, instead of the intact inner membranes observed in DMVs and the first type of VP, we observed inner membrane discontinuities for many of the vesicles present in the second type of VP (Fig. 5A), de facto resulting in the fusion of vesicles or in apparent connections with the lumen of the membrane compartment. Interestingly, we also observed virus budding from the outer membranes of the second type of VPs (Fig. 5A and 5B, arrowheads), suggesting the ultimate convergence of RTC-associated membrane structures with compartments involved in virus assembly.

SARS-CoV replicase subunits localize predominantly to convoluted membranes

In order to assess the association of replicase subunits with the various coronavirus-induced membrane structures, we performed iEM experiments on SARS-CoV–infected Vero E6 cells. In view of previously experienced problems to preserve DMV ultrastructure for iEM [100], the FS protocol was further optimized, and samples were embedded in Lowicryl HM20. When using this fixation and embedding protocol, several of our antisera unfortunately no longer recognized their target, restricting our analysis—for the moment—to a relatively small number of replicase subunits. On the other hand, the various SARS-CoV–induced membrane alterations documented in the previous paragraphs could now readily be recognized in iEM samples (Fig. 6). Furthermore, DMV inner structure was preserved, which had proven impossible in previous iEM studies [100].

For samples fixed at 8 h pi, highly specific immunogold labeling results were obtained with antisera [100] recognizing the large nsp3 subunit, which contains one of the viral proteases and is also a presumed transmembrane protein [85,171], the viral main protease nsp5 [23], and the nsp8 putative RNA primase, which has been postulated to be a subunit of the core RdRp complex [172,173]. Protein contrast was enhanced in these FS samples, due to the absence of stained membranes, revealing electron-dense areas between DMVs that were strikingly similar, both in size and localization, to the CM structures documented above (Fig. 6). Remarkably, using all three reactive SARS-CoV antisera, CM were the most abundantly labeled structures. For nsp3 and nsp5, small numbers of gold particles were also found on DMV membranes, but the interior of DMVs (and VPs) was essentially devoid of label (Fig. 6). In the case of nsp8, some labeling of the DMV interior was observed, but again the majority of the label localized between DMVs on the CM structures. In combination with our data from previous IF studies, documenting the colocalization of several key replicative enzymes [100], our iEM data suggest that the CM structures are the major site of SARS-CoV nsp accumulation.

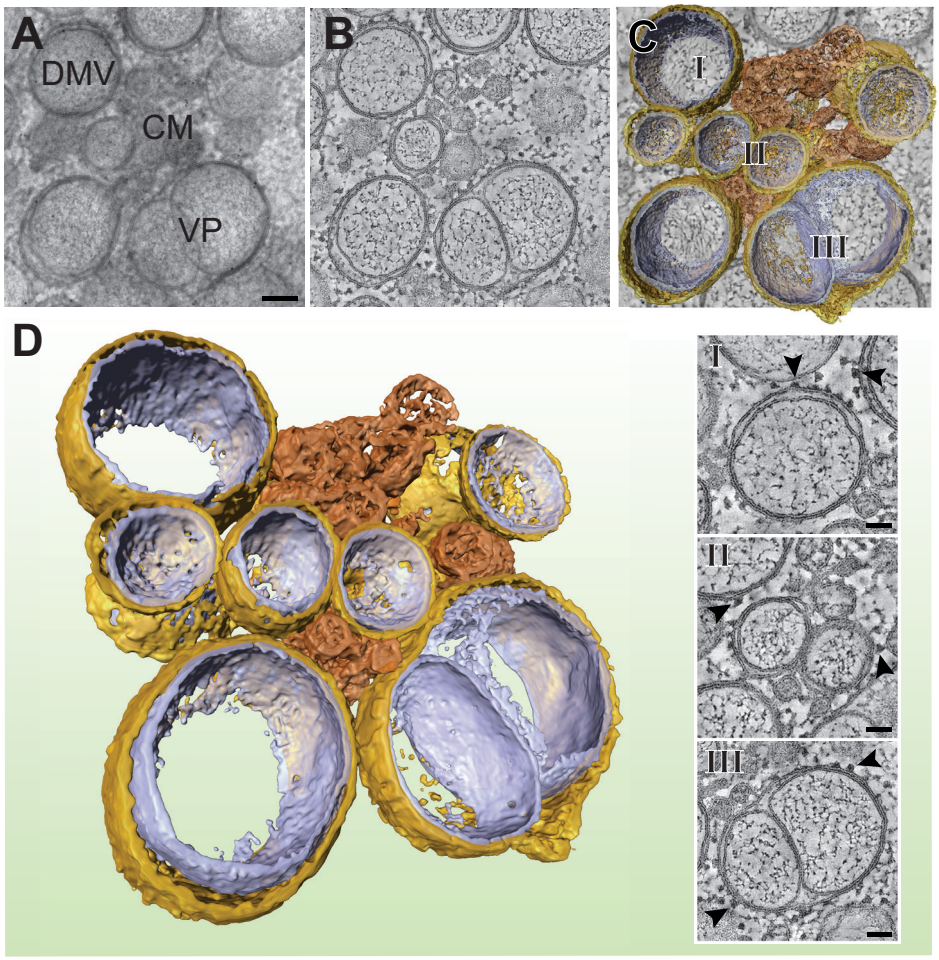


Figure 4. Electron tomography of SARS-CoV–induced CM, DMVs, and VPs. As in Figure 3, (A–C) illustrate how a 3-D surface-rendered model was derived by applying ET on a semi-thick section of a SARS-CoV–infected Vero E6 cell cryofixed at 7 h p.i. Scale bar in (A) represents 100 nm. The type 1 VP present in this image shows an outer membrane that accommodates two tightly apposed inner vesicles with minimal luminal spacing. The insets (I, II, and III) below (C) show tomographic slices that highlight the presence of ribosomes (arrowheads) on DMV and VP outer membranes. Scale bar represents 50 nm. (D) shows the final 3-D surface-rendered model of this cluster of larger and smaller DMVs (outer membrane, gold; inner membrane, silver) of which the outer membranes are connected to the type 1 VP and a CM structure (depicted in bronze).

The interior of coronavirus-induced DMVs labels abundantly for double-stranded RNA

A critical step in the replication of +RNA viruses is the production of a negative-stranded copy of the genome, which is used as a template for genome replication by the viral RdRp.

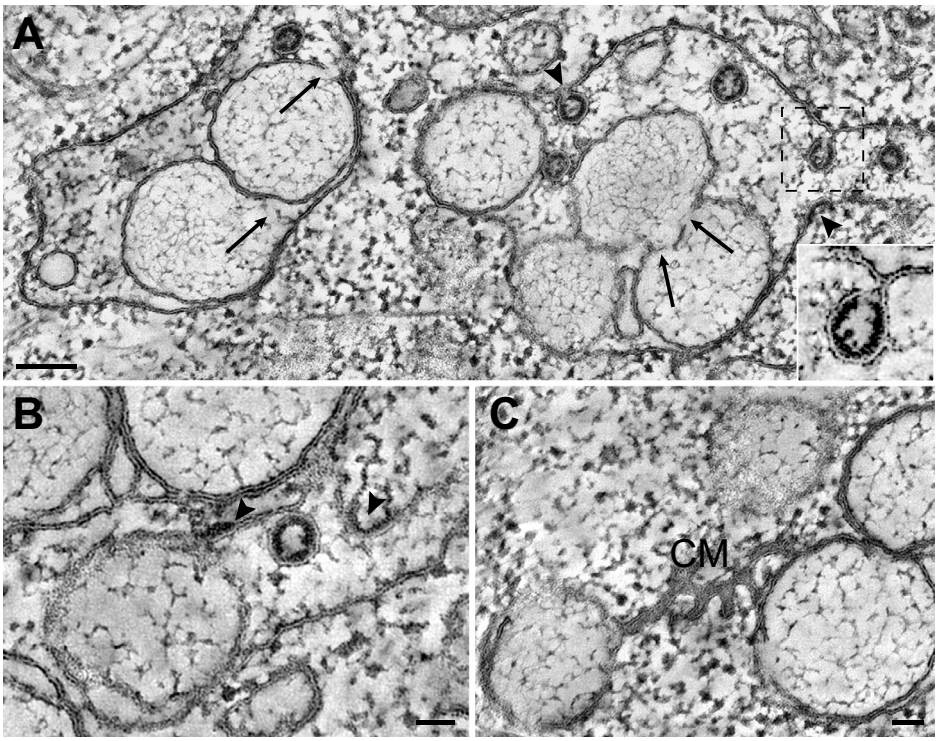


Figure 5. Electron tomography of the SARS-CoV–induced reticulovesicular membrane network at a more advanced stage of development. Gallery of 10-nm-thick digital slices of tomograms (see legend to Figure 3B) from SARS-CoV–infected Vero E6 cells again cryofixed at 7 h p.i., but now selected for cells in which infection had progressed more than in others, allowing the visualization of more advanced stages of development of the virus-induced membrane alterations. (A) VP of the second type, showing a more relaxed outer membrane and several discontinuities (arrows) of inner vesicle membranes. New SARS-CoV particles can be seen budding from a VP outer membrane into the luminal space (arrowheads and inset; the inset shows a slightly tilted image to optimize the view). (B) Initial stage of virus budding from a VP outer membrane: formation of the electron-dense nucleocapsid structure at the cytosolic side of the membrane (arrowheads). (C) Example of a CM structure showing stacked membranes that are continuous with DMV outer membranes. Scale bars represent 100 nm (A) or 50 nm (B and C).

Coronaviruses also generate a set of subgenome-length negative-strand RNAs, which serve as templates for subgenomic mRNA synthesis [77,78]. It is widely assumed that viral negative-strand RNA synthesis leads to the formation of partially and/or completely dsRNA structures, commonly referred to as replicative intermediates (RIs) and replicative forms (RFs) and, in the case of coronavirus subgenomic mRNA production, transcriptive intermediates (TIs) and transcriptive forms (TFs) [174,175]. Whereas RFs/TFs are (nearly) completely double stranded, and may accumulate, e.g., when RNA synthesis ceases and the last positive strand is not released from the negative strand, RIs/TIs are viewed as dynamic multistranded intermediates engaged in positive strand synthesis. They are thought to be only partially double stranded and contain multiple tails of nascent single-stranded RNA produced by the

successive RdRp complexes engaged in copying the negative-strand template (see [175] and references therein).

For a variety of +RNA viruses, the (presumed) dsRNA intermediates of replication have been visualized in situ by using antibodies recognizing dsRNA [39,176-178]. In particular, monoclonal antibody J2 [179], recognizing RNA duplexes larger than 40 base pairs, was reported to be a useful tool in recent IF studies [178,179]. We here used the J2 antibody in IF and EM studies, resulting in a highly specific labeling of SARS-CoV–infected cells, whereas mock-infected cells were essentially devoid of signal (Fig. 7A). Even before immunodetection of nsps was feasible, the first IF signal for dsRNA could already be detected (at 2–3 h p.i.) as small but very bright foci throughout the cell (Fig. 7A). By 4 h p.i., the distribution of dsRNA-containing foci generally mirrored that of nsp3, nsp5 (unpublished data), and nsp8 (Fig. 7B). However, high-resolution confocal microscopy (Fig. 7C and 7D) revealed that the overlap was far from complete, and frequently, multiple dsRNA foci appeared to surround an area that labeled for replicase. Later in infection, the labeling for both dsRNA and nsps was mainly concentrated in the perinuclear region (Fig. 7E). Whereas different nsps colocalized to a large extent (Fig. 7E, bottom row), this was less obvious when the labeling for dsRNA and replicase subunits was compared.

In subsequent iEM experiments, the J2 antibody was found to retain its reactivity for dsRNA in sections of cells that had been embedded in Lowicryl, following the FS procedure described above. An abundant and highly specific labeling for dsRNA was observed on the interior of SARS-CoV–induced DMVs (Fig. 8), with some additional label being present in the vicinity of DMVs where CM were frequently observed during our studies (Fig. 8B). Also, type 1 and type 2 VPs were positive for dsRNA (Fig. 8C), whereas (budding) virions present in these structures were always negative. Thus, our data revealed the accumulation of dsRNA, presumably of viral origin (see Discussion), in the interior vesicles of DMVs and VPs, and also suggested that the fibrous material observed in our ET analysis (Fig. 3–5 and Videos S1 and S3) may consist (in part) of viral nucleic acids.

DISCUSSION

Hijacking cellular membranes to facilitate coronavirus RNA synthesis

The functional dissection of the multi-enzyme complexes that drive +RNA virus replication and transcription is essential for our understanding of the molecular biology of this important group of pathogens. Presumably, the membrane structures used to compartmentalize RTCs provide a suitable scaffold for viral RNA synthesis facilitate the organization of the viral replication cycle, and aid in evading or delaying antiviral host cell responses, including those that can be triggered by viral dsRNA [25,27,159,165,180]. The "replication structures" induced

in cells infected with +RNA viruses can range from distinct spherular membrane invaginations to elaborate networks of CM and single- or double-membrane vesicles (for a recent review, see [26]). The first 3-D ultrastructural analysis of a replication structure of the spherular type was recently reported by Kopek et al. [36]. In an ET-based study, the replicase and RNA synthesis of flock house virus were found to be confined to spherular invaginations of the mitochondrial outer membrane. This "viral mini-organelle" was reported to be connected to the cytosol by a neck-like channel with a diameter of about 10 nm. This connection is assumed to be both sufficient and essential for the import of, e.g., nucleotides into replication spherules and for export of viral RNA products, which need to be released into the cytosol for translation and packaging.

We have now employed ET to analyze the replication structures of SARS-CoV, a prominent member of the coronavirus group which—at about 7,000 amino acids—encodes the largest known +RNA virus replicase [13]. DMVs had previously been observed in cells infected with coronaviruses and related nidoviruses [97,100,101,103,104], and the precise origin of their membranes had remained debated. They were generally assumed to be "free floating" vesicles associated with viral RNA synthesis. However, our present ET analysis has revealed that they form a unique reticulovesicular membrane network (Fig. 9) with which both viral replicase subunits and dsRNA are associated (Fig. 6–8). The network is continuous with the rough ER and contains in its lumen numerous "inner vesicles," which stand out for their relatively large size (200–300-nm diameter), their number (several hundred, possibly more than 1,000 vesicles per cell), and for the fact that they label abundantly for dsRNA. Remarkably, however, their interior does not appear to be connected to the cytosol (see also below). The fact that the average diameter of the SARS-CoV–induced DMVs (250–300 nm) exceeds the maximal thickness (~200 nm) of the sections that could be used for ET made it generally impossible to visualize their entire perimeter. However, the number of inter-DMV connections that could be observed in the reconstructed volume (at least one for 95% of the DMVs analyzed, with more than half of those having multiple connections) justifies the conclusion that they form an integrated network and makes it highly unlikely that free DMVs exist (Fig. 3–5). VPs and CM structures are also an integral part of the network (Fig. 3–5 and 9), and in particular, the latter structures appear to be a major site of immunolabeling for SARS-CoV nsps. Essentially similar observations were made for cells infected with a second coronavirus, MHV (unpublished data). Our studies identify the ER as the source for a virus-induced membrane network that integrates CM, DMVs, and VPs, although the (additional) involvement of the ERGIC remains a possibility [111]. In combination with biochemical studies, the ultrastructural description of this network is important to take our understanding of coronavirus RTC structure and function to the next level.

Finally, our analysis of cells at more advanced stages of SARS-CoV infection (Fig. 5) opens the intriguing possibility that the membrane network involved in virus replication is continuous (or merges) with membranes involved in virus assembly. For MHV, based on

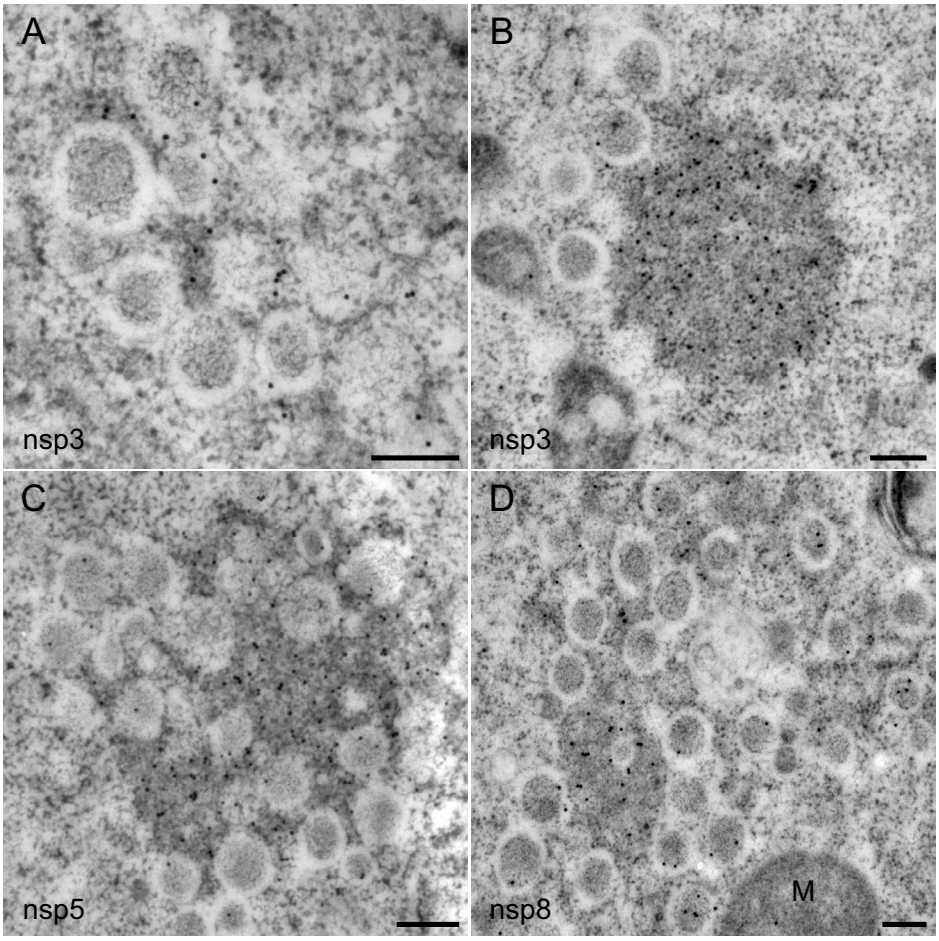


Figure 6. Immunogold EM of the SARS-CoV replicase in infected cells. SARS-CoV–infected Vero E6 cells were cryofixed at 8 h p.i. and processed for FS and IEM using rabbit antisera (see Materials and Methods). In all images, 15-nm colloidal gold particles conjugated to protein A were used for detection of primary antibodies. (A and B) Labeling for SARS-CoV nsp3 was mainly found on the electron-dense areas between DMVs, presumably representing CM as most clearly visible in (B). (C) Immunolabeling for SARS-CoV nsp5 (the viral main protease), which was essentially similar to that for nsp3. (D) When using an antiserum recognizing SARS-CoV nsp8 (the putative viral primase), the majority of label was again present on CM. However, a small fraction of the nsp8 signal was reproducibly found on the interior of DMVs. Scale bars represent 250 nm.

IF microscopy studies using the nsp13 helicase and viral membrane (M) protein as markers for RTCs and virus assembly sites [111], respectively, such a connection was previously proposed [181], but could not be corroborated in our studies using the same protein markers in SARS-CoV–infected cells [100]. According to the data presented in this study, the bulk of the labeling for nsps is found on the CM structures (Fig. 6), not on DMVs, which would explain the minimal overlap between the nsp labeling and that for the M protein [100]. Furthermore,

it cannot be excluded that merger of type 2 VPs and compartments involved in virus budding is a relatively rare event that could result from general cytopathology and/or fusion of different membrane compartments. Notably, in some of the larger VPs (e.g., see Fig. 2E), a kind of polarity was observed, with budding and mature virions mostly on one side and the

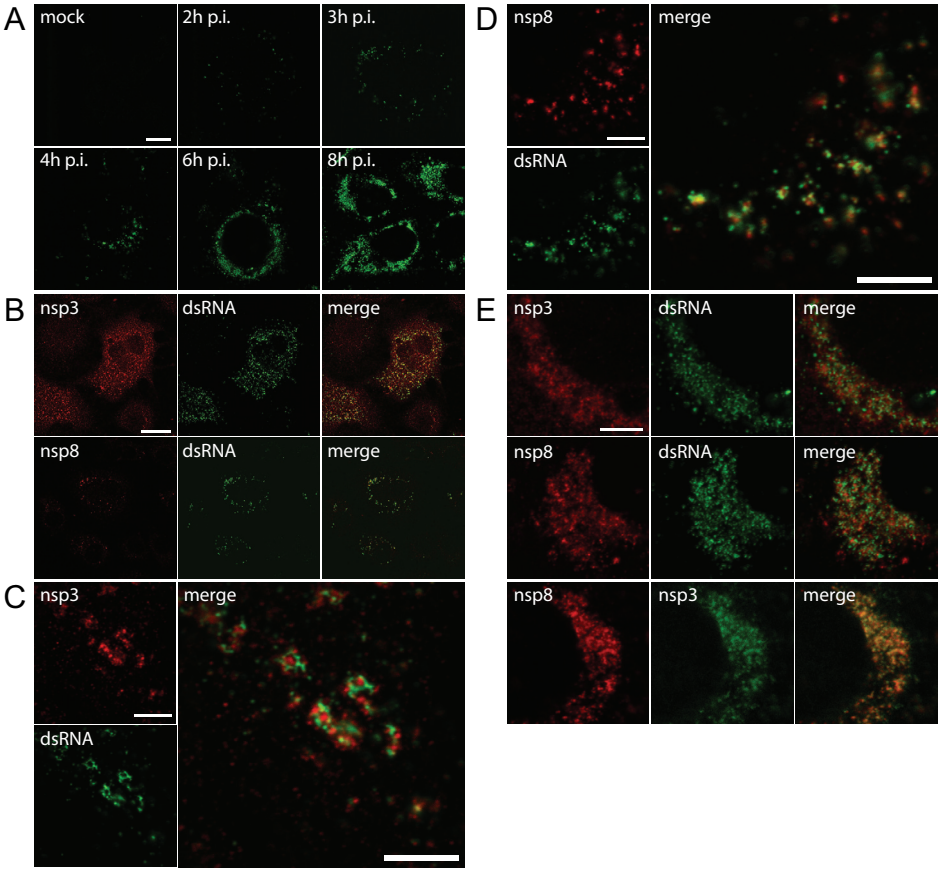


Figure 7. Detection of dsRNA in SARS-CoV–infected cells. SARS-CoV–infected Vero E6 cells were fixed at various time points after infection and processed for IF assays using rabbit antisera recognizing different replicase subunits and a mouse monoclonal antibody specific for dsRNA. Imaging was done using a confocal laser scanning microscope. (A) Time-course experiment showing the development of dsRNA signal, which could be detected as early as 2 h p.i. Later in infection, the initially punctate cytoplasmic staining developed into a number of densely labeled areas close to the nucleus. (B) Dual-labeling IF assays using antisera recognizing dsRNA and either nsp3 or nsp8. The early signals for dsRNA and both nsps (here shown at 3 h p.i.) were found in close proximity of each other and partially overlapped. (C) High-resolution images of dual-labeling experiments for nsp3 and dsRNA early in infection (4 h p.i.), with the enlarged merged image illustrating that these signals were largely separated. (D) See (C), but now a dual-labeling experiment for nsp8 and dsRNA was performed. (E) High-resolution images of dual-labeling experiments for nsp3, nsp8, and dsRNA later in infection (6 h p.i.). Whereas the two nsps colocalized to a large extent (bottom row), this was less obvious when the labeling for dsRNA and replicase subunits was compared. Scale bars represent 10 μm (A), 25 μm (B), or 5 μm (C–E).

inner vesicles of (former) DMVs on the other, as if two previously "dedicated compartments" recently merged into a larger vesicle. Although the juxtaposition and functional connection of compartments involved in genome replication, encapsidation, and assembly remains a fascinating idea, a thorough quantitative analysis of SARS-CoV assembly is beyond the scope of this paper and would require the collection of extensive datasets, in particular around the peak time of virus assembly (10–12 h p.i.).

The enigma of the double membrane

By analogy with the replication-associated "membrane spherules" of several other +RNA viruses [34,36], it was anticipated that the DMV interior would be connected to the cytosol, thus allowing import of (macro)molecules required for RNA synthesis and export of RNA products, e.g., for translation and packaging. However, our tomograms revealed a sealed DMV inner membrane and an uninterrupted outer membrane that was clearly continuous with other membrane structures. The two tomograms that were the basis for Fig. 3 and 4 and Videos S1 and S3 were scrutinized for discontinuities of DMV inner and/or outer membranes, with the expectation of finding at least one such connection per vesicle when DMV interior and cytosol would indeed be continuous. Neck-like connections between the outer membranes of different DMVs were readily discerned (see above; Fig. 3), and the quality of our images also allowed the high-resolution visualization of, e.g., membrane necks of budding virions (Fig. 5). However, for the vast majority of DMVs, an extensive search for a repetitive pattern showing a neck, channel, or other type of structure connecting DMV interior and cytosol remained negative. For only one out of 78 DMVs visible in Videos S1 and S3, an aligned gap of both inner and outer membrane could be detected (Fig. 10A). Furthermore, in three other DMV profiles, the inner membrane was locally disrupted (Fig. 10B–D), but since these sites also showed local separation of the two leaflets of the bilayer, we consider it likely that these interruptions were fixation or processing artifacts. Given the previously documented fragility of the DMV inner membrane in particular, this would not be surprising, and this property may also be related to the puzzling inner membrane discontinuities observed for type 2 VPs late in infection (Fig. 5 and Video S4). However, for the vast majority of DMVs in our images, the inner membrane was found to be uninterrupted, and thus, the DMV interior appears not connected to the cytosol.

In view of the resolution provided by our tomograms, we are confident that we would have readily detected connections to the cytosol with a diameter (8–10 nm) in the range previously described for other +RNA virus replication structures [34,36]. Thus, our data suggest that—at least at the moment of fixation—DMV inner membranes form closed vesicles and their morphogenesis has now become one of the major unresolved issues. It should be stressed that we cannot exclude the possibility that proteinaceous pores or transporters may be present in DMV membranes, since similar complexes (e.g., the translocon) have

not been recognized in situ in EM/ET studies yet. However, despite the fact that the large coronavirus proteome was recently found to include several unexpected and unprecedented functions, proposing the existence of such a channel would seem highly speculative at this moment. Three coronavirus replicase subunits (nsp3, nsp4, and nsp6) contain hydrophobic domains that are each predicted to traverse the membrane multiple times [85,86,182]. Their properties have not been characterized in detail, but the recent phenotypic characterization

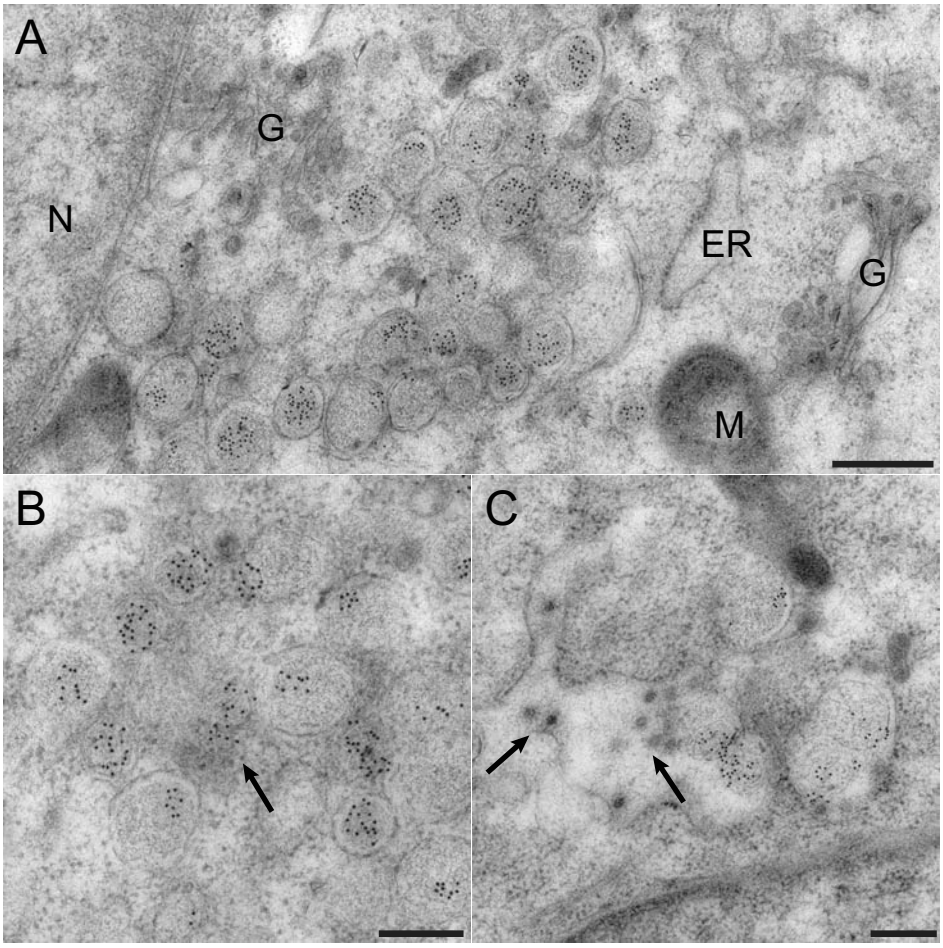


Figure 8. Immunogold EM reveals abundant dsRNA labeling on the interior of SARS-CoV–induced DMVs. SARS-CoV–infected Vero E6 cells were high-pressure frozen and processed for FS and IEM using a monoclonal antibody specific for dsRNA. In all images, 10-nm gold particles conjugated to protein A were used for detection of primary antibodies. (A) Overview of a SARS-CoV–infected cell at 7 h p.i., documenting the specificity of the dsRNA labeling and the abundant amount of label present on DMVs. G, Golgi complex; N, nucleus; M, mitochondria. (B) Cluster of abundantly labeled DMVs with additional labeling present in the area between the vesicles (arrow). (C) Type 2 VP showing abundant labeling for dsRNA on the interior of the inner vesicles. In addition, newly assembled virus particles can be seen in the lumen of the compartment (arrows). Scale bars represent 500 nm (A) or 250 nm (B and C).

of a temperature-sensitive MHV mutant with a lesion in nsp4 revealed a dramatic reduction of DMV formation at the restrictive temperature, thus clearly implicating this protein in the formation of the reticulovesicular network documented in this study [166]. Still, apart from the question whether the transmembrane nsps are able to form membrane-spanning channels or recruit host proteins capable of forming such a connection, other conceptual problems would remain. For example, the alignment of the channels spanning the inner and outer membranes would appear to be a requirement, much like it has been proposed for the sophisticated TOM and TIM complexes engaged in import across mitochondrial outer and inner membranes [183,184]. Moreover, the transport across membranes of a large, negatively charged RNA molecule like the approximately 30-kb coronavirus genome poses a challenge that in biology appears to be met only by the nuclear pore complex.

In addition to the recent data on MHV nsp4 [166], results obtained with the distantly related arteriviruses indicate that the (predicted) membrane-spanning nsps of nidoviruses are likely to play a critical role in inducing membrane alterations. It was shown that the expression of two such arterivirus nsps sufficed to induce paired membranes and DMVs similar to those found upon virus infection [65,97,106]. Most likely, these subunits are first inserted into "regular" ER membranes, which may thus also be the site of early viral RNA synthesis. When replication leads to a rapid increase of replicase expression, the accumulating transmembrane nsps may induce membrane pairing and curvature, due to, e.g., their specific structural features, oligomerization, or recruitment of cellular factors involved in membrane bending. The notion that inner and outer bilayer may be "physically associated", due, for example, to interacting luminal domains of protein partners present in the two membranes, is supported by the fact that the two membranes remain tightly associated just up to the point where narrow neck-like connections protrude to the outer membrane of other vesicles or compartments (Fig. 3). Apparently, at later time points after infection when DMVs merge into the larger vesicle packets, the inner membranes are able to more and more detach from the outer membrane. Interestingly, during our recent (unpublished) studies using the drug brefeldin A, which interferes with vesicular transport and de facto results in fusion of Golgi complex and ER into one large, dilated compartment, similar observations could be made much earlier in infection. This would suggest that the interaction between the two membranes eventually weakens, possibly in particular when the outer membrane network becomes dilated due to cytopathology and/or merger of multiple vesicles.

Presumably, membrane pairing is followed by the wrapping of membrane cisternae around cytosolic constituents and leads to the membrane fission event that is needed to explain the sealed DMV inner membrane. However, despite the presence of several hundred DMVs in infected cells and despite the extensive EM analysis of hundreds of cells in the course of this study, we were unable to find morphological profiles that seemed obvious examples of an actual DMV-forming fission event. Although some smaller DMVs were sometimes observed (Video S3), the average dimensions of their inner compartments (200–300 nm in diameter)

should have made the detection of nascent DMV structures straightforward. Arguably, DMV formation might be very rapid, and thus rarely captured, or obscured in, e.g., the complex architecture of the CM structure, where smaller DMVs were sometimes apparent (Fig. 4 and Video S3). Alternatively, the conspicuous absence of ribosomes from DMV inner membranes lends some credibility to a scenario involving a preformed inner vesicle derived from another membrane source.

The observed narrow neck-like connections in the network (Fig. 3) and the fact that many DMVs were found to have multiple (up to four) of such outer membrane connections with other DMVs, CM, or ER also leaves the possibility that additional fusion and fission events may occur during the formation or maturation of the network, which would obviously hamper the analysis of the initial DMV forming event. The future identification of inhibitory drugs or dominant-negative mutants of viral or host proteins involved in this step may facilitate the visualization of this crucial intermediate stage in DMV morphogenesis.

Comparison with other +RNA virus replication complexes

In infected cells, several other groups of +RNA viruses induce membrane alterations that differ from the spherular membrane invaginations described, e.g., for nodaviruses [36] and alphaviruses [34]. In the case of picornaviruses (for a recent review, see [26]), the pioneering work of the Bienz laboratory demonstrated that poliovirus RNA replication occurs on the cytosolic surface of ER-derived vesicles [54], which aggregate into rosette-like structures [156]. However, the first detectable negative-stranded RNA of poliovirus is associated with regular ER cisternae, which may thus be the initial site of RNA synthesis [185]. Other studies revealed that poliovirus-induced vesicles may have a double membrane [49] and implicated the autophagic pathway in their formation [186]. A similar hypothesis was launched to explain MHV DMV formation [105]. Despite a convincing link between overall MHV replication and the expression of a host protein with a critical function in autophagy (Apg5), the "autophagy hypothesis" was contradicted by IF studies using autophagosomal marker proteins [100,101].

Our studies may in fact have uncovered a closer parallel to the membranes with which the replication complexes of flaviviruses are associated. Ultrastructural studies of cells infected with Kunjin virus have defined various characteristic membrane structures, which were implicated in viral RNA synthesis on the basis of immunolabeling and biochemical studies ([39]; for reviews, see [25,26,157]). These structures include "convoluted membranes" and "vesicle packets," terms that we have chosen to adopt in our study, without wanting to imply a direct ultrastructural or functional similarity. Whereas the flavivirus CM have been implicated in replicase polyprotein synthesis and processing, the VPs were proposed to be the site of viral RNA synthesis, in particular because they could be immunolabeled for replicase subunits, dsRNA, and de novo–synthesized viral RNA that had been metabolically labeled by bromouridine (BrU) incorporation [25]. A key premise, however, in the current model proposed

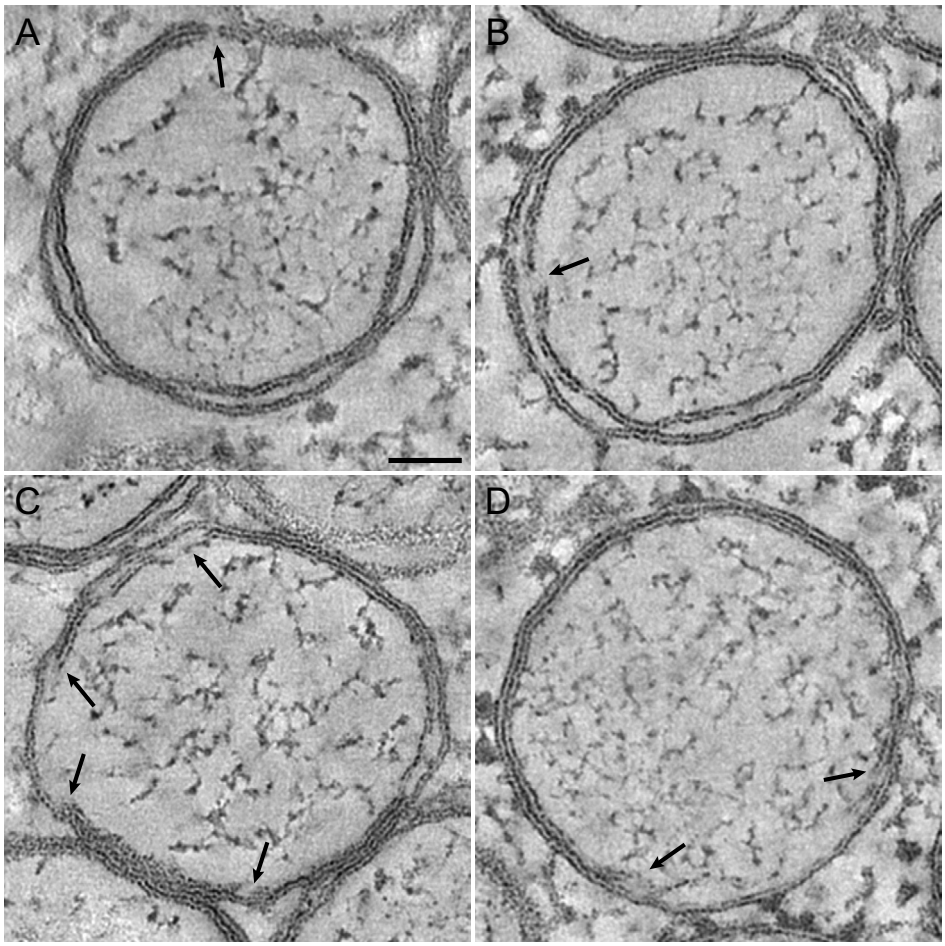


Figure 9. Electron tomography-based model of the network of modified ER membranes that supports SARS-CoV RNA synthesis. A model showing the SARS-CoV–induced reticulovesicular network of modified membranes with which both viral replicase subunits and dsRNA are associated. Time post infection increases from left to right. The various interconnected membrane structures documented in this study are depicted. The CM, the outer membranes of DMVs and VPs, and—ultimately—membrane compartments used for virus budding were all found to be continuous with the rough ER, as underlined by the presence of ribosomes on each of these components. DMV inner membranes and the interior of the vesicles, which contained as yet undefined "fibrous material," were devoid of ribosomes but labeled abundantly for dsRNA. Ultimately, the network appears to connect membrane structures involved in SARS-CoV RNA synthesis to sites at which the assembly of new virions occurs and may thus contribute to the organization of successive stages in the viral life cycle in both time and space.

for flaviviruses [25,47,187] is the idea that—as in the case of viruses employing spherular replication compartments (see above; [36])—the interior of the vesicles enclosed in the VPs are connected to the cytosol.

For the DMVs induced by coronaviruses and other nidoviruses, a similar hypothesis was among the previously formulated models [97], but—as explained above—in our SARS-CoV

tomograms, an open connection between DMV interior and cytosol could not be discerned. Recent biochemical studies on the in vitro activity of SARS-CoV RTCs, which were associated with membrane fractions prepared from infected cells, revealed that a detergent treatment is required to render the viral RNA synthesizing complex susceptible to digestion with proteases or nucleases [188]. Thus, the isolated RTC appears to be protected by at least one membrane, a conclusion also drawn from similar biochemical studies on flavivirus RTCs, leading to an alternative model [42] in which flavivirus VPs would be "topologically similar" to coronavirus VPs and consist of a closed inner vesicle surrounded by an outer membrane that is continuous with CM and ER. If a future ET analysis of flavivirus replication structures were to confirm this similarity, we would essentially be faced with the same question for both virus groups [42]: if RNA synthesis would indeed occur inside closed DMVs or VPs, how then are import and export across the double membrane achieved?

Pinpointing the active site of SARS-CoV RNA synthesis

The presence of both viral nsps and dsRNA on the SARS-CoV–induced membrane network strongly suggests its involvement in viral replication and transcription. However, the apparent separation in immunolabeling studies (Fig. 6–8) between the bulk of the nsps and most of the dsRNA emphasizes the need to pinpoint the active coronavirus RTC. In particular the exact role in viral RNA synthesis of the DMV inner vesicle, its "fibrous content," and its abundant labeling for dsRNA are intriguing. Extensive proteolytic processing of replicase polyproteins pp1a and pp1ab (Fig. 1) is assumed to be a critical posttranslational step in the activation of coronavirus replicative enzyme functions. It is also a complicating factor in immunolabeling studies since antibodies will commonly recognize both mature cleavage products and larger processing intermediates. Moreover, immunolabeling will merely reveal the site of accumulation of specific antigens, not necessarily their site of synthesis.

The fact that most of the label for SARS-CoV nsps was present on CM may seem incompatible with the presence of most of the dsRNA signal on DMVs. If, however, as proposed for flaviviruses, the coronavirus CM would be the site of polyprotein synthesis and processing, abundant labeling of this region could be expected, in particular for the two viral proteases, nsp3 and nsp5, that were detected on the CM in this study. The labeling observed for the putative nsp8 primase differed slightly, with some label consistently being present on the DMV interior (Fig. 6D). The nsp8 subunit possesses a secondary RNA polymerase activity and has been postulated to be part of the core enzyme complex of the virus [172,173]. Additional antisera, in particular targeting the viral key enzymes encoded in ORF1b (Fig. 1), are currently being generated to increase our possibilities for detection of subunits of the multicomponent SARS-CoV RTC. Also, the search for suitable antibodies against cellular marker proteins continues, which could aid in defining the interaction with the host cell's secretory pathway in more detail.

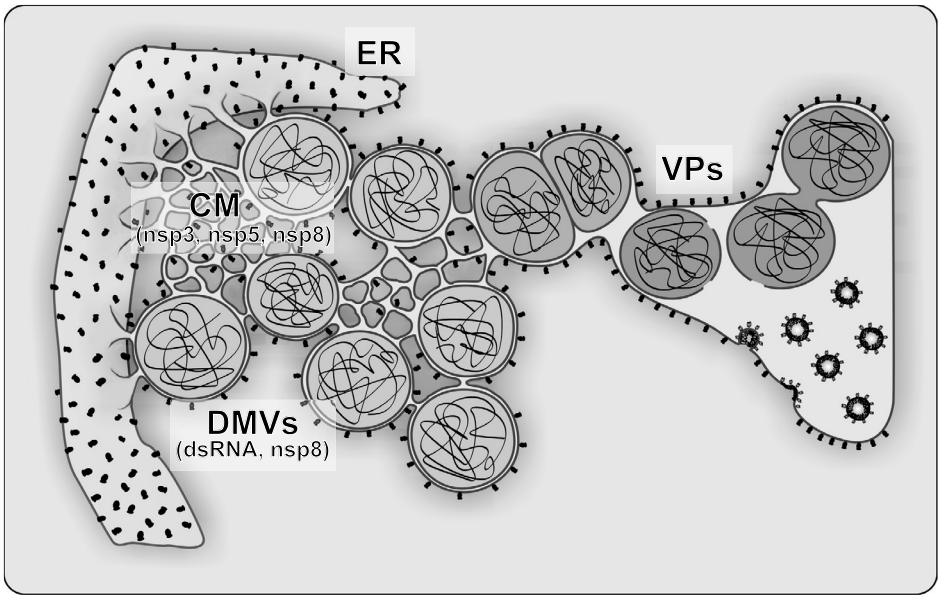


Figure 10. In-depth analysis of discontinuities in the membranes of SARS-CoV–induced DMVs. See the legend to Figure 3 for details. A total of 78 DMVs in the two tomograms that were the basis for Figure 3A and 3B and Videos S1 and S2 were scrutinized for discontinuities of DMV inner and/or outer membranes that might reveal a connection between the DMV interior and the cytoplasm. However, an extensive search for a repetitive pattern showing a neck, channel, or other type of structure connecting the DMV interior and cytoplasm remained negative. One out of 78 DMVs (A; arrow) showed a small, aligned gap of both inner and outer membrane. In three other DMV profiles (B–D; arrows), the inner membrane was locally disrupted, but the separation of the two leaflets of the bilayer made it likely that these discontinuities were artifacts that had occurred during fixation and processing of the fragile DMV inner structure. The scale bar represents 50 nm.

As recently concluded for hepatitis C virus [47], a huge excess of nonstructural proteins may be produced in virus-infected cells, with only a fraction of these molecules actively participating in viral RNA synthesis at any point in time. Likewise, the labeling for dsRNA, although widely considered a marker for +RNA virus RTCs [25,177,178], does not formally pinpoint RTC activity. Clearly, molecules inside active RTCs may be among the dsRNA strands recognized, as is strongly suggested by colocalization of dsRNA and newly made viral RNA following BrU pulse labeling [189]. On the other hand, however, it is likely that part of the signal, a part that may in fact vary between different viruses, represents dsRNA molecules that are no longer actively engaged in viral RNA synthesis. In this context, it is noteworthy that the calculations on the number of active replication complexes in hepatitis C virus replicon cell lines (less than 100; [47]) are not easily reconciled with the much larger number of discrete foci detected in such cells when labeling with the J2 anti-dsRNA monoclonal antibody [178]. Given these considerations, it would be most straightforward to localize the site of activity of the SARS-CoV RTC early in infection, using ultrastructural studies that are combined with

pulse labeling of viral RNA synthesis using BrU [189] or radioisotope-labeled nucleosides [51], or by transfecting the corresponding nucleoside triphosphates. Experiments to explore whether it is technically feasible to combine such an approach with the cryo-EM and FS fixation protocols required for SARS-CoV DMV preservation are in progress. In our opinion, previous iEM studies using BrU labeling of MHV-infected cells [104] cannot be considered conclusive in view of the obvious loss during fixation of the DMV inner vesicles, and possibly also the CM. Nevertheless, the BrU labeling detected by these authors on DMV outer membranes and surrounding structures suggests that at least part of the newly made RNA was cytosolic after a 1-h labeling interval.

In conclusion, a scenario in which part, or even most, of the SARS-CoV dsRNA signal represents molecules that are not present in active RTCs (Fig. 7 and 8) cannot be ruled out at present. In this alternative scenario, the active complex might, for example, localize to the CM, where small amounts of dsRNA labeling and the bulk of the viral nsps were detected. The subsequent formation of DMVs could then even be postulated to constitute an elegant mechanism to conceal viral RNA and aid in the evasion of dsRNA-triggered antiviral host responses. A variety of recent studies have made clear that coronaviruses are capable of interacting and interfering with the innate immune system at multiple levels, likely also depending on the cell type involved (for a recent review, see [190]). Both SARS-CoV and MHV [191-193] were found to counteract the induction of interferon via cytoplasmic pattern recognition receptors that can sense the presence of viral dsRNA [28,29] and possibly also viral negative-strand RNAs carrying uncapped 5′-triphosphates [30]. Further analysis of the structure, interactions, and function of the coronavirus RTC may reveal to which extent this property should be attributed to the unusual network of modified membranes with which coronavirus RNA synthesis appears to be associated.

MATERIALS AND METHODS

Virus, cells, and antisera

SARS-CoV strain Frankfurt-1 (kindly provided by Dr. H. F. Rabenau and Dr. H. W. Doerr [Johann-Wolfgang-Goethe-Universität, Frankfurt am Main, Germany]; [163]) was used to infect Vero E6 cells. All work with live SARS-CoV was performed inside biosafety cabinets in the biosafety level 3 facility at Leiden University Medical Center. A multiplicity of infection of 10 was used in all experiments, and infection rates were routinely confirmed in IF assays. A panel of rabbit antisera against the SARS-CoV replicase, including the nsp3, nsp5, and nsp8 subunits, was described previously [100]. A mouse monoclonal antibody J2 [179], which is specific for dsRNA, was purchased from Scicons.

Electron microscopy

For ultrastructural morphological investigations, SARS-CoV–infected Vero E6 cells were pre-fixed (for biosafety reasons) overnight with 3% paraformaldehyde in 0.1 M PHEM buffer (60 mM piperazide-1,4-bis[2-ethanesulfonic acid], 25 mM HEPES, 2 mM $MgCl_2$, 10 mM EGTA) at various time points after infection. For cryofixation, cell monolayers adhered to Thermanox coverslips (Nunc) were plunged into liquid ethane. Freeze substitution was performed at −90°C in an automated freeze-substitution system (Leica) using an FS medium consisting of 90% acetone and 10% water, containing 1% osmium tetroxide and 0.5% uranyl acetate. After washing with pure acetone at room temperature, the samples were embedded in epoxy LX-112 resin. Thin sections were contrasted with uranyl acetate and lead hydroxide, and subsequently viewed at 80 keV with a Philips CM-10 transmission electron microscope.

For iEM, infected cell monolayers were cryofixed by either plunging them into liquid ethane or by high-pressure freezing using a Leica EM PACT2. The freeze substitution was performed using anhydrous acetone containing 0.25% glutaraldehyde and 0.1% uranyl acetate. After washing with ethanol, samples were infiltrated with Lowicryl HM20 and polymerized under UV light at −50°C. Thin sections were labeled with specific antisera [100], which were detected with protein A-gold particles (10 or 15 nm). A bridging rabbit–anti-mouse IgG antibody (DakoCytomation) was used for mouse monoclonal antibodies. Grids were contrasted with uranyl acetate and lead hydroxide, and subsequently viewed with a Philips CM-10 transmission electron microscope.

When quantifying DMVs per infected cell, thin sections were cut in the direction parallel to the substrate, and the slice producing the largest nuclear diameter was analyzed, since this plane was generally found to contain the largest number of DMVs. Electron micrographs (between 20 and 100) covering the entire cross-section of the cell were recorded, and to facilitate counting, these were digitally merged to produce a single image representing a 100-nm-thick plane through the center of the infected cell. Merged images were analyzed with Zoomify software. Only DMVs for which the surrounding bilayers could be readily distinguished were counted, and their diameter was measured using ImageJ software (http://rsb.info.nih.gov/ij/).

Electron tomography

Freeze-substituted infected cell samples, processed for morphological investigation as described above, were used to cut 200-nm-thick sections. To facilitate the image alignment that is required for the subsequent image reconstruction step, a suspension of 10-nm gold particles was layered on top of the sections as fiducial markers. For dual-axis tomography, two single-axis tilt series were recorded of the specimens with an FEI T12 transmission electron microscope operating at an acceleration voltage of 120 keV. Per single-axis tilt series, 131

images were recorded at 1° tilt increments between −65° and 65°. Automated tomography acquisition software was used (Xplore 3D; FEI Company). Images were acquired with a cooled slow-scan charge-coupled device (CCD) camera (4k Eagle; FEI Company) with 4,096 × 4,096 pixels and were recorded by binning 2. The electron microscope magnification was 18,500×, corresponding to a pixel size of 1.2 nm at the specimen level. To enable dual-axis tomography, the specimens were rotated 90° around the *z*-axis using a dual-axis tilt tomography holder (Fishione; model 2040). To compute the electron tomogram, the dual-axis tilt series were aligned by means of the fiducial markers using the IMOD software package [194]. The size of the voxels in the tomograms corresponds to 1.2 nm. Full datasets have been deposited in the Cell Centered Database (http://ccdb.ucsd.edu; [195]) under accession numbers 6020–6023, respectively, containing the datasets of the tomograms shown in Videos S1, S3, and S4, and a Zoomify image showing a high-resolution cross-section of an entire SARS-CoV–infected cell.

The 3-D surface-rendered reconstructions of viral structures and adjacent cellular features were processed using AMIRA Visualization Package (TSG Europe) by surface rendering and thresholding. During this process, some volumes were denoised using the nonlinear anisotropic diffusion filtering [196]. Denoised volumes were used only for producing the surface-rendered masks. Final analyses and representations were done using undenoised data (either masked or unmasked).

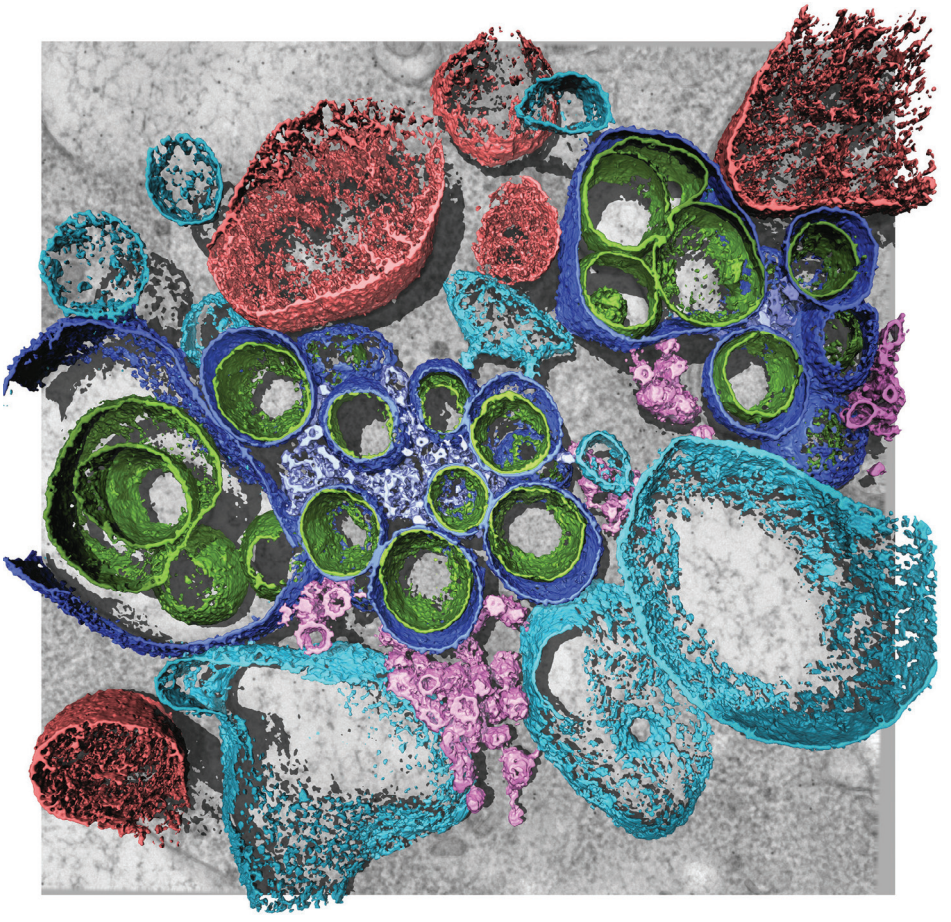
Immunofluorescence microscopy

Infected cells on glass coverslips were fixed with 3% paraformaldehyde in PBS at various time points after infection and were processed for IF microscopy essentially as described previously [95]. Following permeabilization, single- or dual-labeling IF assays were carried out with rabbit antisera and/or mouse monoclonal antibodies, which were detected using indocarbocyanine (Cy3)-conjugated donkey anti-rabbit immunoglobulin (Ig) and Alexa Fluor 488-conjugated goat anti-mouse Ig secondary antibodies, respectively (Molecular Probes). For dual-labeling experiments with two rabbit antisera recognizing different SARS-CoV nonstructural proteins, the anti-nsp3 antibodies were directly coupled to Alexa Fluor 488, as described previously [100].

Samples were examined with a Zeiss Axioskop 2 fluorescence microscope (equipped with the appropriate filter sets, a digital Axiocam HRc camera, and Zeiss Axiovision 4.2 software) (Carl Zeis, Microimaging) or with a Leica SP5 confocal laser scanning microscope, using a pinhole size of 1 airy unit (for both channels) to give optical sections with a theoretical thickness of 236 nm. Images were minimally optimized for contrast and brightness using Adobe Photoshop CS2.

ACKNOWLEDGMENTS

For helpful discussions and support, we thank many of our colleagues at LUMC, in particular, Montserrat Bárcena, Martijn van Hemert, Henk Koerten, Roman Koning, Hans van Leeuwen, Danny Nedialkova, Willy Spaan, Cindy Swett Tapia, and Aartjan te Velthuis. We gratefully acknowledge the skillful assistance of Ronald Limpens and Jos Onderwater in protocol development.



CHAPTER 3

Integrity of the early secretory pathway promotes, but is not required for severe acute respiratory syndrome coronavirus RNA synthesis and virus-induced remodeling of endoplasmic reticulum membranes

Kèvin Knoops, Cindy Swett-Tapia, Sjoerd H.E. van den Worm, Aartjan J.W. te Velthuis, Abraham J. Koster, A. Mieke Mommaas, Eric J. Snijder, and Marjolein Kikkert

Journal of Virology (2010) 84:833-46
(Image featuring issue cover)
Reprinted with permission

ABSTRACT

To accommodate its RNA synthesis in the infected cell, severe acute respiratory syndrome coronavirus (SARS-CoV) induces a cytoplasmic reticulovesicular network (RVN) that is derived from endoplasmic reticulum (ER) membranes. We set out to investigate how the early secretory pathway interacts with the RVN and the viral replication/transcription complex (RTC) that is anchored to it. When the secretory pathway was disrupted by brefeldin A (BFA) treatment at the start of infection, RVN formation and viral RTC activity were not blocked and continued up to 11 h postinfection, although RNA synthesis was reduced by ca. 80%. In vitro RTC assays, using membrane fractions from infected cells, demonstrated that BFA does not directly interfere with the activity of the viral RNA-synthesizing enzymes. Confocal microscopy studies showed that early secretory pathway components are not associated with SARS-CoV-induced replication sites, although our studies revealed that infection induces a remarkable redistribution of the translocon subunit Sec61α. Ultrastructural studies, including electron tomography, revealed that the formation of the RVN and all its previously documented features can occur in the presence of BFA, despite differences in the volume and morphology of the network. We therefore conclude that early secretory pathway proteins do not play a direct role in RVN morphogenesis or the functionality of the SARS-CoV RTC. The BFA-induced disruption of ER integrity and functionality probably affects the overall quality of the membrane scaffold that is needed to support the viral RTC and/or the availability of specific host factors, which in turn compromises viral RNA synthesis.

INTRODUCTION

In eukaryotic cells, the RNA replication of plus-stranded RNA (+RNA) viruses occurs exclusively in the cytoplasm and is inextricably associated with modified host membranes. Depending on the virus group, membrane modifications can range from small invaginations in the (outer) membrane of the target organelle to multiple, physically connected membrane compartments, including vesicular and reticular structures (for reviews, see references [25-27,32]). The microenvironment created in this manner presumably benefits the activities of the viral replication complex. The membrane structures probably promote efficient RNA synthesis by concentrating the molecular players and likely also shield the viral machinery from host defense mechanisms recognizing viral proteins and/or intermediates of viral RNA synthesis. Little is known about the morphogenesis, activities, and maintenance of these viral RNA factories. Their structural and functional dissection will enhance our understanding of +RNA virus replication strategies and may reveal new opportunities for antiviral strategies.

Among +RNA viruses, coronaviruses are unique for their exceptionally large polycistronic genome of ~30 kb (for a recent review, see reference [197]). The large open reading frames (ORFs) 1a and 1ab are translated from the genomic mRNA, yielding the replicase precursor polyproteins pp1a and pp1ab, whereas downstream ORFs, encoding structural and "accessory" proteins, are expressed from a nested set of subgenomic mRNAs. Two or three proteinases encoded in ORF1a process pp1a and pp1ab into 15 or 16 nonstructural protein subunits (nsp's), most of which are known or presumed to be functionally associated with the viral replication/transcription complex (RTC) that drives the production of new genomes and subgenomic mRNAs [13]. Three nsp's (3, 4, and 6) contain multiple membrane-spanning domains and are likely involved in the modification of intracellular membranes into the unusual membrane structures to which the coronavirus RTC is anchored [86,100,101,104].

Following the 2003 severe acute respiratory syndrome (SARS) outbreak (for a review, see reference [160]), SARS coronavirus (SARS-CoV) has rapidly become one of the best-studied members of the coronavirus family. Like mouse hepatitis coronavirus (MHV) [104], SARS-CoV replication induces cytoplasmic membrane alterations, with the most conspicuous structures being large numbers of double-membrane vesicles (DMVs) with diameters of 250 to 300 nm [100,103]. The modified membranes are concentrated in the perinuclear area of the infected cell and label for a variety of coronavirus RTC subunits [93,96,100]. Using electron tomography (ET), we recently established that SARS-CoV DMVs are not free-floating vesicles but instead are interconnected through their outer membranes via narrow necklike connections and can thus be described as single-membrane vesicles surrounded by a common outer membrane [198]. In fact, these interconnected DMVs are part of a membraneous reticulovesicular network (RVN) that also includes convoluted membranes (CM) and is physically connected to the endoplasmic reticulum (ER). Ribosomes can be found on both CM and DMV outer membranes. Late in infection, the interconnected DMVs transform into so-called

vesicle packets (VPs), in which multiple inner vesicles are surrounded by a more dilated outer membrane. Frequently, virus particles can be seen budding from VP outer membranes into the lumen. The interior of DMV inner vesicles labels extensively for dsRNA, presumably representing intermediates of viral replication and transcription. However, the bulk of various replicase proteins (nsp3, nsp5, and nsp8) localizes to the CM, and not to DMVs [198]. In addition, even with the resolution of ET, visible connections between the double-stranded RNA (dsRNA)-containing interior of DMVs and the cytoplasm were not detected, raising a number of questions regarding RVN morphogenesis, function, and the exact position and orientation of the RTC in relation to the modified membranes [198].

Besides viral transmembrane nsp's, cellular pathways or factors likely play a role in the morphogenesis and/or function of membrane structures associated with +RNA virus replication, which was in particular investigated for various picornaviruses. Picornavirus "replication vesicles" usually are of nonuniform shape and size (ranging from 70 to 400 nm), appear to have a double membrane, and lack obvious connections to the cytosol [25,27,50,51,121,199,200]. Again, the ER appears to be the primary source for vesicle formation, although cellular ER proteins are excluded from these structures, except for several secretory pathway markers [50,54]. Late in infection, also markers of other organelles, such as lysosomes and the Golgi complex, can be found in these picornavirus-induced structures [25,49]. Although not yet addressed with the resolution of ET, the available light and electron microscopy data suggest that these picornavirus-induced membrane structures may resemble the coronavirus-induced RVN [49,50,121,200].

The connection between picornavirus replication vesicles, RNA synthesis, and the early secretory pathway has been investigated in considerable detail. It was proposed that vesicle formation is triggered by the assembly of COPII coats, which direct vesicular transport from the ER to the ER-Golgi intermediate compartment (ERGIC) [54]. The involvement of the COPI coat complex was investigated by using the drug brefeldin A (BFA), which forms stable trimeric complexes with one of three guanine nucleotide exchange factors (GEFs)—GBF1, BIG1, or BIG2—and an ADP-ribosylation factor (Arf) belonging to a family of small GTPases. As a result, Arf cannot be activated to recruit subunits of the COPI complex to the membrane, which in turn blocks COPI-mediated vesicular transport between ERGIC and the Golgi complex and retrograde transport between the Golgi complex and the ER [201-204]. Picornaviruses display highly variable sensitivity to BFA treatment. For example, poliovirus and echovirus 11 replication is completely blocked by BFA [200,205-207], whereas other family members are partially sensitive or not sensitive at all [121,200,208]. The nonsensitive picornaviruses do not seem to require or recruit COPI, whereas the replication complexes of sensitive viruses clearly associate with COPI-coated membranes and depend on COPI function, which is reflected in a strong sensitivity to BFA [200]. Poliovirus protein 3A appears to hijack GBF1, which also inhibits secretory pathway function [55,209-211]. In support of these findings, the sensitivity of poliovirus replication to BFA can in part be overcome by GBF1 overexpression [55]. Protein

3CD recruits BIG1 and BIG2, possibly with similar effects [55]. As also suggested by in vitro experiments in which BFA was added, the COPI machinery is likely involved in the replication process itself but is not a key player in vesicle biogenesis [205,212].

Two recent studies have addressed the involvement of the early secretory pathway in coronavirus infection. Oostra et al. disrupted COPII-driven protein export from the ER and found that this impaired MHV replication [86]. Verheije et al. [167] then analyzed the effect of BFA treatment and GBF1/Arf knockdown and again noticed a significant reduction in MHV replication. However, the relation between MHV replication and the processes targeted by BFA treatment seemed to be of a very different nature than the intimate involvement of GEFs and Arfs in the replication of BFA-sensitive picornaviruses. Whereas the latter are completely blocked by the presence of the drug, MHV replication was merely inhibited, and virus-induced membrane alterations could still be observed. Furthermore, no significant colocalization was observed between the MHV replicase, represented by nsp8, and any of the BFA targets, which is in strong contrast to the results obtained for the above-mentioned picornaviruses.

The present study addresses the relation between SARS-CoV RNA synthesis and the host cell's early secretory pathway. The addition of BFA to SARS-CoV-infected cells early in infection inhibited RVN formation and viral RNA synthesis, but the drug did not completely block viral RNA synthesis, which continued for up to 10 h. In vitro RTC assays were used to exclude the possibility that the drug might directly affect the activity of SARS-CoV key enzymes. By confocal microscopy, we compared the subcellular localization of the SARS-CoV RVN to that of early secretory pathway factors and other ER markers. Although none of the secretory pathway markers colocalized with the RVN, infection induced a remarkable redistribution of the translocon subunit Sec61α. Ultrastructural studies, including ET, revealed that a reduced level of RVN formation can be maintained in the presence of BFA, suggesting that it is unlikely that the early secretory pathway is intimately involved in coronavirus replication.

RESULTS

SARS-CoV replication is inhibited, but not abrogated, by BFA treatment

Before treating SARS-CoV-infected cells with BFA, the drug was titrated to establish the dose to use (range tested, 1 to 12 μg/ml). By IF microscopy 6 μg of BFA/ml was found to suffice to completely disperse the Golgi complex in all cells. TUNEL assays did not show apoptosis at this BFA concentration and also MTS cell viability assays did not reveal adverse effects of this drug concentration during treatment for up to 10 h, the maximum incubation time used in our experiments.

Vero-E6 cells were infected with SARS-CoV (MOI of 10) and, upon removal of the inoculum at 1 h p.i., medium containing BFA was given to the cells. Subsequently, viral RNA synthesis

was monitored at different time points after infection by performing 1-h metabolic labeling with [^{3}H]uridine. ActD was added to inhibit cellular transcription. Tritium incorporation into RNA was measured by scintillation counting and, as illustrated in Fig. 1A, SARS-CoV RNA synthesis was considerably affected, but certainly not blocked by BFA treatment. Compared to the untreated control, ca. 20% of residual activity was measured throughout infection. Essentially similar data were obtained using a second cell line, mouse L cells expressing the human ACE2 receptor used by SARS-CoV (data not shown). In line with these metabolic labeling data, a hybridization analysis of viral RNA produced in the presence of BFA confirmed that at 9 h p.i. both genome and subgenomic mRNAs had accumulated to ca. 20% of the amount

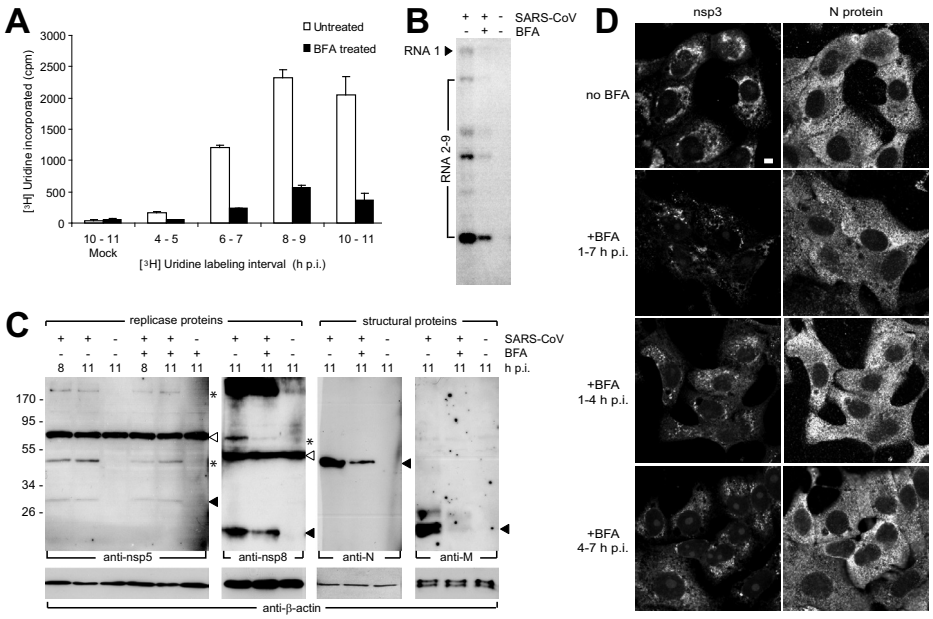


Figure 1. SARS-CoV replication is inhibited, but not abrogated, by BFA treatment. SARS-CoV-infected Vero-E6 cells were BFA treated or mock treated from 1 h p.i. until the time of harvesting or fixation. (A) Viral RNA synthesis at different time points p.i. in the presence or absence of BFA. At 1 h prior to metabolic labeling of viral RNA synthesis, cells were given 10 µg of ActD/ml to inhibit host cell transcription. After a 1-h [^{3}H]uridine labeling in the presence of ActD, cells were harvested and incorporation of radiolabel was measured by scintillation counting. (B) Hybridization analysis to compare the viral RNA content (genome and subgenomic mRNAs) from infected control cells and BFA-treated infected cells lysed at 9 h p.i. RNA isolated from uninfected cells was included as a negative control. (C) Western blot showing the accumulation of SARS-CoV nsp5, nsp8, nucleocapsid (N), and membrane (M) protein (indicated by the respective black arrowheads) in the presence or absence of BFA. β-Actin was included as a loading control (lower panels). The asterisks indicate possible SARS-CoV replicase processing intermediates, and the white arrowheads indicate nonspecific bands that were also detected in mock-infected cell lysates. (D) IF assays showing nsp3 and N protein accumulation in SARS-CoV-infected cells that were fixed at 7 h p.i and BFA treated for the indicated time intervals. Bar represents 5 µm.

observed in the untreated control (Fig. 1B), indicating that replication and transcription were equally affected by the presence of the drug.

To assess the effect of BFA treatment on viral protein synthesis, cell extracts were analyzed by Western blotting (Fig. 1C). A clear reduction in the amount of the structural proteins M and N, expressed from subgenomic mRNAs 8 and 9, was observed, but nsp levels seemed to be only moderately affected. Although we cannot formally exclude major stability differences between nsp's and structural proteins, these observations suggest that—under normal conditions—there is an excess of genome molecules and that part of these may not be engaged in translation.

IF microscopy revealed that the effect of BFA, when present from 1 to 7 h p.i., can differ substantially between individual infected cells. Most of the cells showed reduced signal for nsp3 and N protein and a more punctate and dispersed nsp3 labeling pattern compared to the dense perinuclear staining in untreated control cells (Fig. 1D, compare the top four panels). However, in some cells the difference with untreated cells was barely detectable (not shown). When analyzed at 7 h p.i., the overall effect of BFA treatment from 1 to 4 h p.i. was similar, i.e., the labeling was more punctate and dispersed, although compared to samples treated 1 to 7 h p.i. the reduction of the signal was less obvious (Fig. 1D). The sustained effects observed at 7 h p.i. after 1 to 4 h p.i. treatment may be explained by the observation that after removal of the drug, the secretory pathway of Vero-E6 cells needed several hours to recover from BFA treatment (data not shown). When BFA was added later in infection (at 4 h p.i.), the staining was generally more indistinguishable from that in untreated control cells at 7 h p.i. (Fig. 1D). This implies that in particular the early phase of SARS-CoV replication is likely to be sensitive to the effects of BFA treatment.

BFA does not inhibit the RNA-synthesizing enzymes of the SARS-CoV RTC

To investigate the possibility that BFA might inhibit one of the many enzyme functions of the SARS-CoV RTC, we made use of an in vitro RTC assay recently developed in our laboratory. The assay is based on isolation of membrane fractions and the associated RTCs from infected cells and in vitro RTC activity is measured on the basis of incorporation of [α-^{32}P]CTP into viral RNA products [188]. BFA was added to this type of assay at the same concentration (6 µg/ml) as that used for the *in vivo* experiments, and the RTC activity was measured 40 and 100 min into the reaction. At these time points, we could not establish a negative influence of BFA on RTC activity (Fig. 2), indicating that the observed reduction of viral RNA synthesis *in vivo* was probably not due to the direct inhibition of viral RNA-synthesizing enzymes by the presence of the drug.

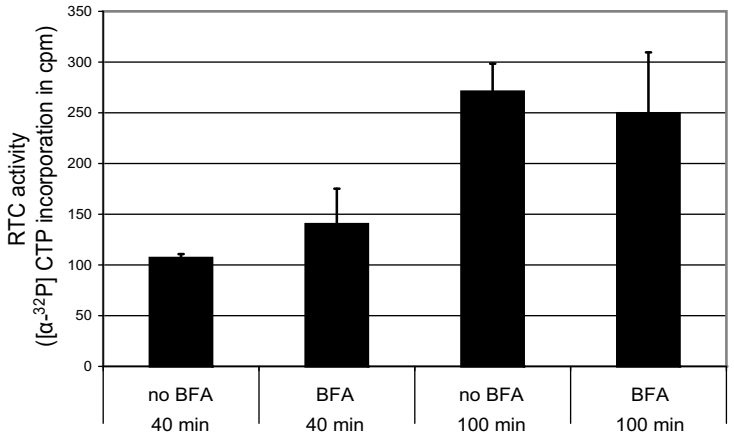


Figure 2. BFA does not inhibit the RNA-synthesizing enzymes of the SARS-CoV RTC. Using membrane fractions isolated from SARS-CoV-infected cells, an in vitro RNA synthesis assay [188] was performed to assess the effect of BFA on SARS-CoV RTC activity. The incorporation of [α-^{32}P]CTP into viral RNA products was allowed to continue for 40 or 100 min, either with or without 6 μg of BFA/ml being present in the reaction. No significant inhibition of RTC activity by BFA was observed

Early secretory pathway factors, including those targeted by BFA, do not colocalize with the SARS-CoV replicase

In contrast to observations made for certain picornaviruses, BFA did not completely block SARS-CoV virus replication and had no direct effect on the *in vitro* activity of isolated RTCs, as described above. We subsequently sought to determine whether the proteins targeted by BFA or other early secretory pathway factors would colocalize with the SARS-CoV replicase, possibly revealing their involvement in RVN formation or RTC function. This was assessed by using confocal laser scanning microscopy (Fig. 3A to C), which was supplemented with quantifications of colocalization levels of SARS-CoV replicase subunit nsp3 and a variety of cellular marker proteins (Fig. 3D; see also Materials and Methods and the figure legend). nsp3 was previously shown to colocalize with the majority of replicase subunits, including several of the key enzymes of the viral RTC [100,198].

We first analyzed the colocalization of nsp3 and resident ER proteins not involved in vesicular trafficking. Earlier studies have reported that the luminal ER PDI partially colocalizes with the SARS-CoV replicase [94], which was confirmed in the present study (Fig. 3A and D). As a negative control for colocalization, we used the Golgi marker Giantin, which indeed did not colocalize (3A and D), in line with previous reports that SARS-CoV nsp's and Golgi markers are separated in the cell [94].

Various other ER markers showed a generally very limited colocalization with nsp3 (data not shown), but the labeling for one marker protein strikingly overlapped with the SARS-CoV replicase. This protein is Sec61α, a key subunit of the translocon that is involved in the

docking of ribosomes on the ER and translocation of the nascent polypeptide chain into the lumen. In uninfected cells, Sec61α labeling was dispersed throughout the cytoplasm (Fig. 3B), but upon SARS-CoV infection the protein became concentrated around the nucleus and colocalized extensively with the characteristic perinuclear labeling pattern of the SARS-CoV replicase (Fig. 3B and D). To exclude that the Sec61α antiserum cross-reacted with any of the viral nsp's, which could also have explained our observation, we checked its specificity by Western blot analysis. In both uninfected and SARS-CoV-infected Vero-E6 cell lysates, the serum recognized only a single protein species of ~40 kDa, the reported molecular mass of Sec61α ([213]; data not shown). This makes cross-reaction with viral proteins unlikely, and we therefore believe that in infected cells Sec61α may indeed be recruited to the SARS-CoV-induced RVN.

No similar recruitment to the SARS-CoV RVN was observed for any of the ER-associated secretory pathway markers that were tested. In fact, neither the COPII coat subunit Sec13 nor the COPI-associated proteins GBF1 and Arf1, which are targeted by BFA treatment, showed any colocalization with SARS-CoV nsp3 (Fig. 3C and D). Colocalization with Arf1 was tested by the transfection of infected cells with a plasmid expressing a YFP-tagged Q71L mutant of Arf1 [214,215]. This mutant has increased affinity for GTP, which prolongs its active and membrane-associated state, in contrast to wild-type Arf1 that continuously shuttles between cytosol and membranes [215]. Expression of this mutant protein facilitated the colocalization analysis of Arf1 and nsp3, but no overlap was observed (Fig. 3C and D). Also wild-type Arf1 and the inactive T31N Arf1 mutant, which is predominantly present in the cytosol [216], did not colocalize with nsp3 (data not shown). Finally, we included syntaxin 5, an essential t-SNARE protein of the ER and *cis*-Golgi involved in vesicular transport between these compartments [217], but also this early secretory pathway marker did not colocalize with SARS-CoV nsp3 (Fig. 3C and D). We therefore conclude that early secretory pathway factors, including those targeted by BFA, are not abundantly associated with the SARS-CoV-induced RVN.

BFA treatment appears to accelerate RVN maturation

Since we concluded that it is unlikely that cellular targets of BFA are directly involved in SARS-CoV replication, we sought to find another explanation for the effect of the drug. BFA disrupts the early secretory pathway and causes massive rearrangements of intracellular membrane compartments, including the ER that is the membrane donor of the SARS-CoV-induced RVN. We therefore analyzed the development and morphology of the RVN during BFA treatment. SARS-CoV-infected Vero-E6 cells were again given BFA at 1 h p.i. and were fixed and processed for EM analysis at 4, 7, or 11 h p.i. The presence of dilated ER [218,219] and tubulovesicular clusters [220], documented effects of BFA treatment in sensitive cells, was apparent in both infected samples and mock-infected controls (Fig. 4E to H and J). When we compared the morphology of the RVN in the presence or absence of BFA, the early stage

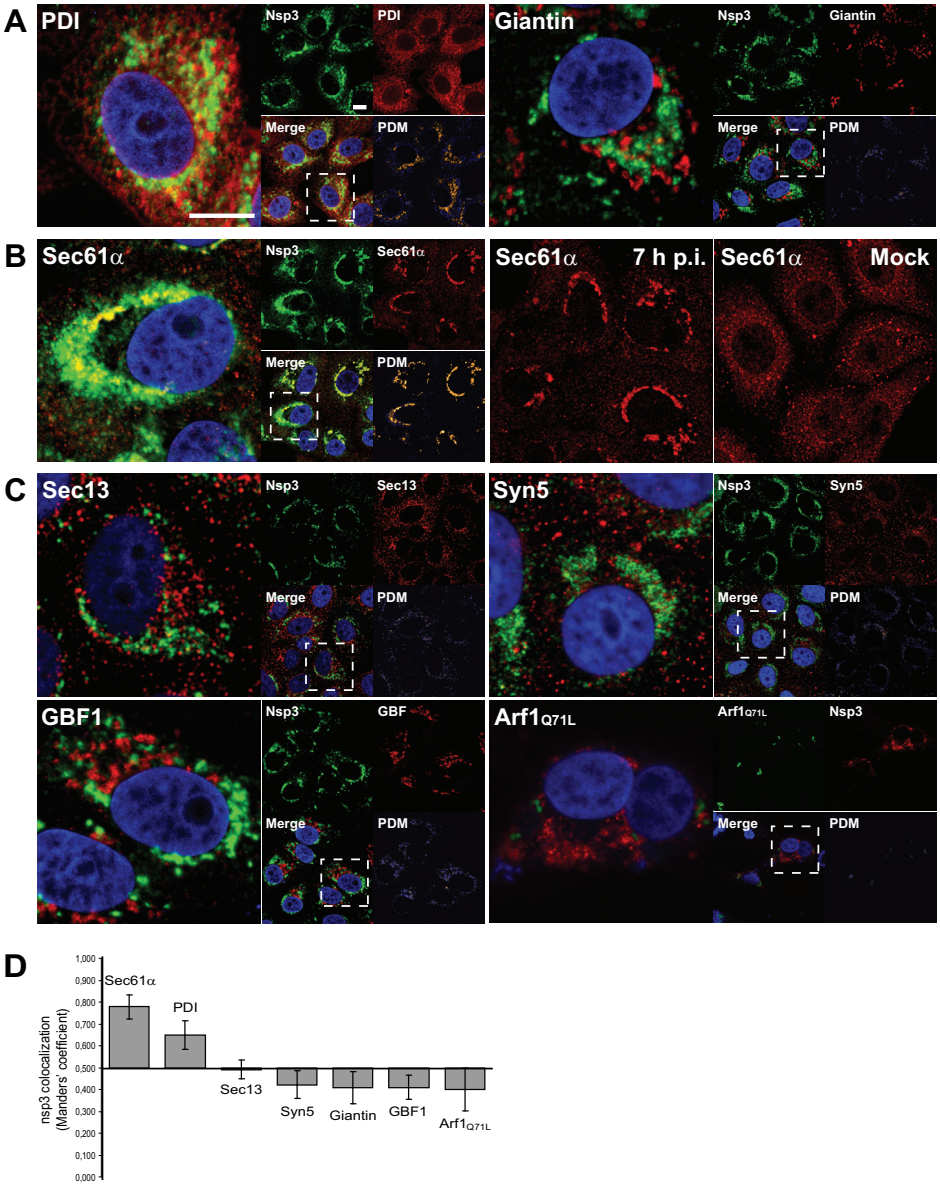

A
PDI
Nsp3
PDI
Merge
PDM
Giantin
Nsp3
Giantin
Merge
PDM
B
Sec61α
Nsp3
Sec61α
Merge
PDM
Sec61α
7 h p.i.
Sec61α
Mock
C
Sec13
Nsp3
Sec13
Merge
PDM
Syn5
Nsp3
Syn5
Merge
PDM
GBF1
Nsp3
GBF
Merge
PDM
Arf1Q71L
Arf1Q71L
Nsp3
Merge
PDM
D
nsp3 colocalization (Manders' coefficient)
1,000
0,900
0,800
0,700
0,600
0,500
0,400
0,300
0,200
0,100
0,000
Sec61α
PDI
Sec13
Syn5
Giantin
GBF1
Arf1Q71L

Figure 3. Early secretory pathway factors are not directly associated with the SARS-CoV-induced RVN. Colocalization analysis of the SARS-CoV replicase and a variety of cellular marker proteins by indirect confocal microscopy. SARS-CoV-infected Vero-E6 cells were fixed at 7 h p.i. and processed for IF assays. A cytomegalovirus (CMV) promoter-containing expression vector for YFP-tagged $Arf1_{Q71L}$ was transfected to visualize this Arf mutant. The subpanels marked PDM (lower right corner of each set in panels A to C) show the product of the differences from the mean (PDM) [232], a method for colocalization analysis in which positive values (displayed in yellow) represent signal in both channels, whereas negative values (blue) represent signal in only one of the channels. Bars represent 10 μm. (A) As positive and negative controls for colocalization, the ER resident protein PDI and Golgi marker Giantin were included, respectively. As reported previously, PDI labeling partially overlapped with the replicase, whereas Giantin showed no colocalization. (B) Redistribution of Sec61α, a major component of the translocon, upon SARS-CoV infection. The double labeling on the left shows the extensive overlap of the signal for nsp3 and Sec61α in the perinuclear area of SARS-CoV-infected cells. The two panels on the right illustrate the virus-induced redistribution of Sec61α, which normally shows a typical reticular labeling pattern throughout the cytoplasm. (C) Colocalization analysis for a number of important early secretory pathway markers, including factors targeted by BFA treatment. Colocalization with SARS-CoV nsp3 was not observed for Sec13, Syntaxin 5 (Syn5), GBF1, and Arf1. (D) Graph showing the average Manders' overlap coefficients of the host proteins used in this analysis and SARS-CoV nsp3 (n = 18 cells per pair). By definition, Manders' overlap coefficients range from 0 to 1, representing full separation and complete colocalization of signals, respectively. We interpreted values greater than 0.5 as indicative of (a certain level of) colocalization and values less than 0.5 as indicative of a lack of colocalization.

of infection (4 h p.i.) did not show striking differences, since regular DMVs were also observed in BFA-treated cells, often adjacent to typically swollen ER stacks (compare Fig. 4B and F). However, by 7 h p.i. the effect of BFA treatment had become very pronounced. Whereas we predominantly observed DMVs in untreated cells (Fig. 4C and I), BFA-treated cells mainly contained VPs, multiple inner vesicles sharing a dilated outer membrane, which usually becomes the dominant structure only later in infection [198] (Fig. 4G and J [compare with Fig. 4D]). Moreover, the luminal space between the inner vesicle and outer membranes of the VPs and remaining DMVs was often markedly increased compared to the structures in untreated cells, an observation reminiscent of what can be seen at later stages of infection in the absence of BFA treatment (e.g., see Fig. 4D, top left [see also below]). Therefore, we conclude that the drug apparently expedites the maturation of delimited though interconnected DMVs into VPs and thus accelerates the morphological maturation of the RVN, as observed during regular SARS-CoV infection.

Clearly, the swollen ER induced by BFA treatment and RVN were integrated at 7 h p.i. and later time points of infection (arrows in Fig. 4G and H); this was probably due to the fusion of the two structures. By 11 h p.i., many large VPs were seen, both in untreated and in BFA-treated infected cells (Fig. 4D and H). Also, in both samples virus budding into RVN membranes or nearby compartments was apparent at 7 and 11 h p.i. (Fig. 4C and D and G to I). Examination of photo mosaics representing complete cross-sections of BFA-treated, infected cells showed that they contain many intracellular virions. However, in contrast to untreated infected cells, these were not observed near the plasma-membrane or outside the cells (data not shown), which was not unexpected since a functional exocytic pathway is

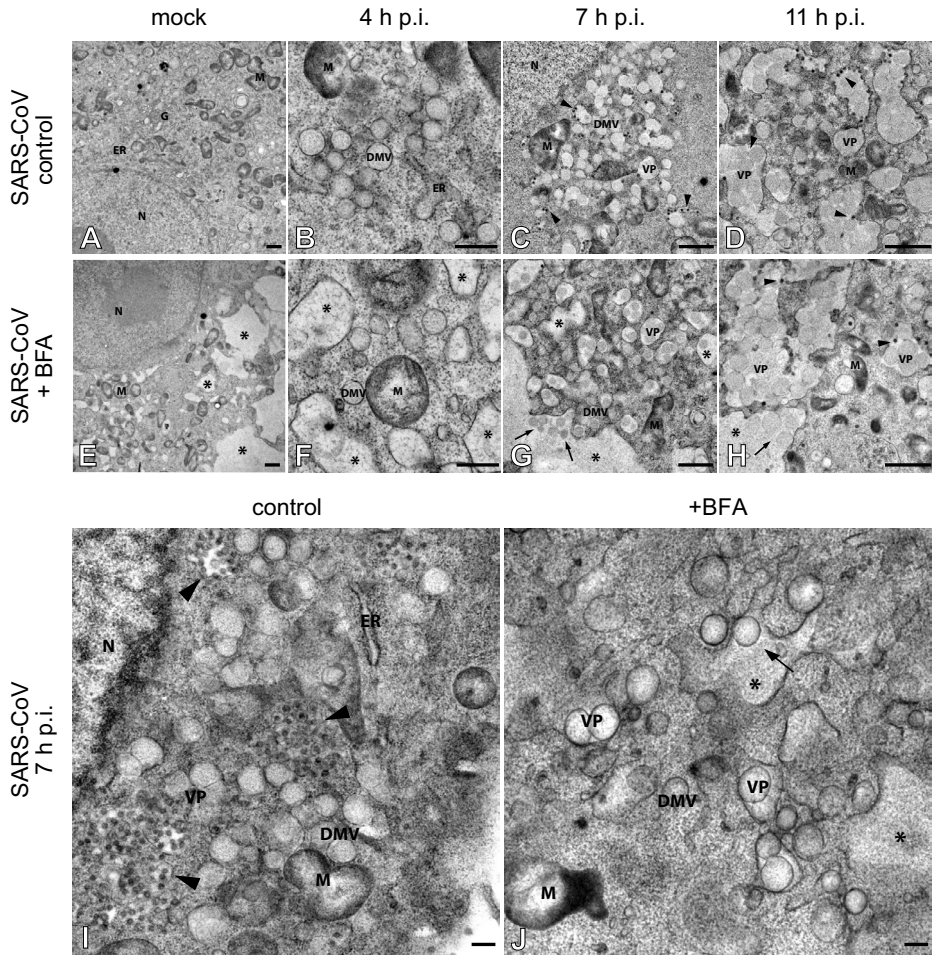


Figure 4. BFA treatment appears to accelerate RVN maturation. Transmission EM analysis of the influence of BFA treatment on the morphogenesis of the SARS-CoV-induced RVN. Vero-E6 cells were mock infected (A and E) or SARS-CoV infected (B to D, F to H, I, and J) and were either not treated (A to D, and I) or treated with BFA (E to H and J) starting at 1 h p.i. Samples were processed for electron microscopy by cryofixation and freeze substitution as described in Materials and Methods. In all BFA-treated samples (E to H and J), the collapse of the Golgi complex and its merger with the ER resulted in the absence of Golgi stacks and the formation of large vacuoles (E to H and J; indicated by asterisks). Untreated SARS-CoV-infected cells showed the normal clusters of DMVs at 4 h p.i. (B), which gradually transformed into VPs from 7 h p.i. on (C, D, and I). When BFA was present, small DMV clusters were observed in close proximity of swollen ER at 4 h p.i. (F). By 7 h p.i., VPs had become the most prominent component of the RVN and seemed to merge with the dilated ER-Golgi vacuoles, which is a striking difference from the control cells (G and J, indicated by arrows). At 11 h p.i., many large VPs were seen, both in untreated and in BFA-treated cells (Fig. 3D and H). Virus particles were observed budding from VP outer membranes (indicated by arrowheads) in both untreated and BFA-treated cells. Panels I and J show higher-magnification examples of Vero-E6 cells fixed at 7 h p.i., with or without BFA treatment. Abbreviations: ER, endoplasmic reticulum; G, Golgi apparatus; M, mitochondrion; DMV, double membrane vesicle; VP, vesicle packet. Bars represent 500 nm (A, C to E, and G to H) or 250 nm (B, F, and I to J).

known to be required for coronavirus maturation and release. Plaque assays using medium harvested from BFA-treated SARS-CoV-infected cells confirmed the very limited release of infectious progeny.

The same photo mosaics allowed us to accurately assess the effect of BFA treatment on the number of inner vesicles (either in individual DMVs or in VPs) present at 7 and 11 h p.i. We counted a total of 15 untreated and 15 BFA-treated infected cells for both time points and calculated the average number of inner vesicles per μm^2 of cytoplasm. As illustrated by Fig. 5A, BFA treatment caused a major reduction in the number of vesicles: ca. 9 and 20% of the normal number were counted at 7 and 11 h p.i., respectively. We next sought to determine whether, despite their altered morphology and reduced number, the vesicles in BFA-treated cells still labeled for dsRNA, as described for regular infection samples [198]. Indeed, both IF microscopy and immuno-electron microscopy confirmed the presence of dsRNA in the vesicles in BFA-treated cells (Fig. 5). IF analysis revealed a higher degree of clustering of the labeling after BFA treatment (compare Fig. 5B and C), which matched the larger number of VPs in these samples described above (Fig. 4). Immuno-electron microscopy showed that in BFA-treated cells dsRNA was still concentrated within the inner vesicles of VPs (Fig. 5D), as well as in vesicles inside dilated ER membranes (Fig. 5E). Although the exact significance of the dsRNA labeling inside SARS-CoV vesicles remains to be elucidated, our joint observations suggest that the primary difference induced by BFA is the accelerated maturation of the RVN, which may well contribute to the drop in RNA synthesis observed upon drug treatment.

Electron tomography confirms the general integrity of the SARS-CoV-induced RVN upon BFA treatment

The EM analysis presented in Fig. 4 revealed interesting differences in RVN morphogenesis in the presence of BFA, particularly at 7 h p.i. (Fig. 4C and G). However, as described previously [198], various aspects of the three-dimensional organization of the RVN can only be properly discerned by ET. These include the structure of the CM, the narrow connections between DMVs and between DMVs and the ER, and the integrity of inner vesicle membranes. Therefore, ET was applied to BFA-treated samples fixed at 7 h p.i. (Fig. 6 and 7; see also Videos S1 and S2 in the supplemental material). Untreated control samples were included in all ET experiments and were processed for conventional EM to confirm the overall quality of infection experiments. The images in Fig. 4I and J were derived from the same experiment as used for the ET analysis shown in Fig. 6 and 7. An extensive ET analysis of untreated samples was described in a prior publication from our laboratory [198]. Analysis of BFA-treated samples by ET revealed that the presence of the drug did not affect the necklike connections between DMVs and between DMVs and ER (Fig. 6D [closeups I and II], Video S2 in the supplemental material, and Fig. 7). The appearance of the CM compartment of the RVN, the intertwined membranes that are most abundantly labeled for viral nsp's [198], was also unchanged after

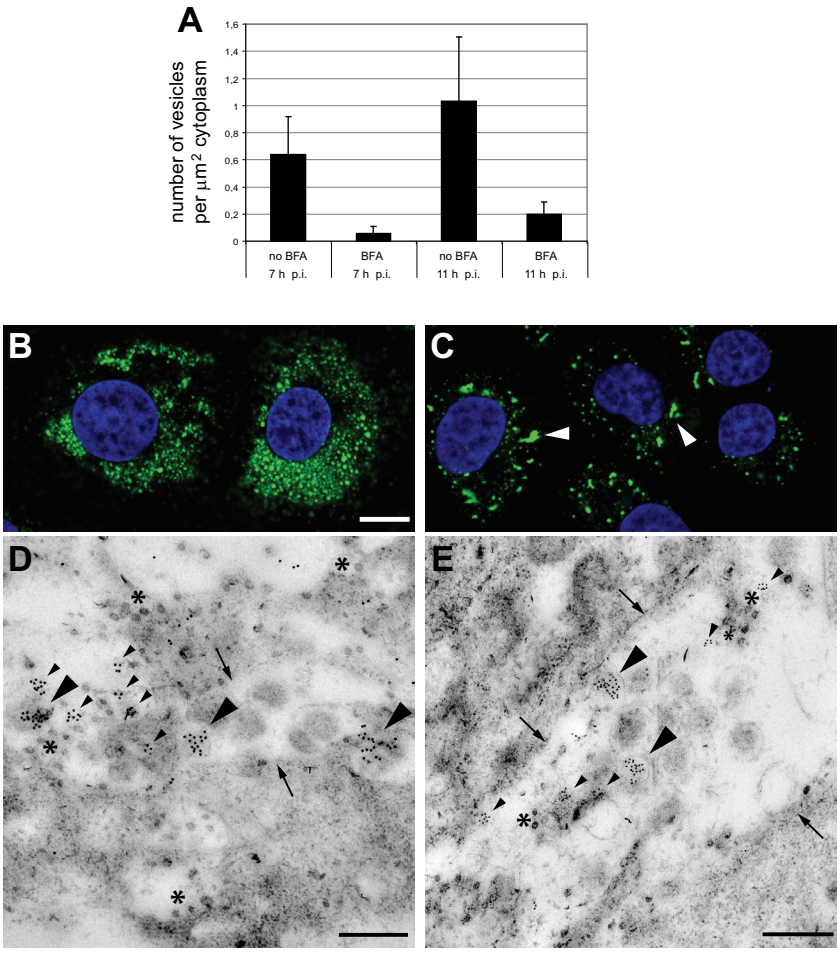


Figure 5. BFA treatment affects RVN morphogenesis and volume, but vesicles still contain dsRNA. (A) Thin sections of SARS-CoV-infected cells were cut in the direction parallel to the substrate and, for each condition (with or without BFA; 7 or 11 h p.i.), the RVN inner vesicles in DMVs or VPs were counted. For this purpose, images covering a complete slice through the center of the cell were stitched into large mosaics to facilitate the analysis. Per sample, 15 cells were analyzed. The graph represents the average number of SARS-CoV-induced vesicles per µm^2 of cytoplasm and illustrates how BFA treatment reduces the number of vesicles to ca. 9 and 20% at 7 and 11 h p.i., respectively. (B and C) SARS-CoV-infected cells were BFA treated (C) or left untreated (B), fixed at 11 h p.i., and processed for IF assays with a MAb specific for dsRNA. Imaging was done by using a confocal laser scanning microscope. Although both treated and untreated cells contained dsRNA products, the labeling seemed less intense in BFA-treated cells (C) compared to untreated cells (B). Also, the distribution of dsRNA was clearly different in BFA-treated samples, which contained fewer and larger clusters of label (C; arrowheads). Bars, 5 µm. (D and E) SARS-CoV-infected Vero-E6 cells were treated with BFA from 1 h p.i. until fixation at 11 h p.i. Immunogold labeling was performed with an antibody recognizing dsRNA. Two representative micrographs are shown. Large arrowheads indicate dsRNA labeling inside DMV inner vesicles; smaller arrowheads point to clusters of labeling not obviously associated with vesicles. Arrows indicate outer membranes of the large VPs that are characteristic of BFA-treated SARS-CoV-infected samples (see also Fig. 4G and H). Asterisks indicate examples of virus particles. Bars represent 500 nm.

BFA treatment (Fig. 6D, closeups I and II). As in untreated controls [198], ribosomes were associated with the outer membranes of the RVN upon BFA treatment (Fig. 6D, closeups I to III). The accelerated development of VPs, two or more inner vesicles sharing an outer membrane, was confirmed when BFA-treated cells and untreated controls were compared at 7 h p.i. (Fig. 6A to D, closeup III). The integrity of the inner vesicles quite often seemed disrupted and peculiar vesicle fusions were observed, resulting in complicated vesicular structures that seemed to have partially single and partially double membranes (Fig. 6A to D, closeup III; Video S2 in the supplemental material; and Fig. 7). Similar observations, although possibly with a lower frequency, were previously made late in the infection of non-BFA-treated cells [198]. However, the meaning of these membrane disruptions is unclear, particularly in view of the documented extreme fragility of the inner vesicles, which might even be enhanced upon BFA treatment. The outer membranes, on the other hand, seemed intact and unchanged.

In contrast to the tightly apposed DMV and type 1 VP membranes found in untreated SARS-CoV-infected cells [198], increased luminal space between the inner and outer membranes of VPs and particularly also DMVs was observed after BFA treatment (Fig. 6A to D, closeups I and II; Video S2 in the supplemental material; and Fig. 7). This implies that the treatment apparently disrupts the (unidentified) mechanism that is responsible for the close apposition of inner and outer membranes. An additional striking observation (Fig. 6A and B and Fig. 7) was the fact that the increased luminal space of many DMVs was not obvious at the side of the vesicle that faced the center of a DMV cluster, which is often adjacent to CM (Fig. 6, closeups I and II). This illustrates how the detailed analysis of the RVN under alternative conditions, like BFA treatment, may reveal additional structural features (see also the Discussion).

DISCUSSION

Our recent detailed analysis of the ultrastructure of the SARS-CoV-induced RVN revealed that the ER is the organelle from which this presumed scaffold for the coronavirus RTC arises [198]. A logical next step was to investigate the relation between the morphogenesis and functionality of the RVN and the host cell's secretory pathway, for which the ER is the general starting point and membrane source. We utilized the commonly used drug BFA to disrupt the COPI pathway that directs vesicular transport between ER and Golgi complex and observed a more or less consistent 80% decrease of SARS-CoV RNA synthesis throughout infection (Fig. 1). Although this is a sizeable reduction, the effect of BFA treatment on the replication of certain picornaviruses, which appear intimately associated with and dependent on early secretory pathway factors, was found to be much more severe, rendering RNA synthesis essentially undetectable [200,207]. Our data on the effect of BFA treatment on SARS-CoV protein synthesis (Fig. 1C and D) and in vitro RTC activity (Fig. 2), the lack of colocalization between replicase and important secretory pathway factors (Fig. 3), and RVN morphogenesis

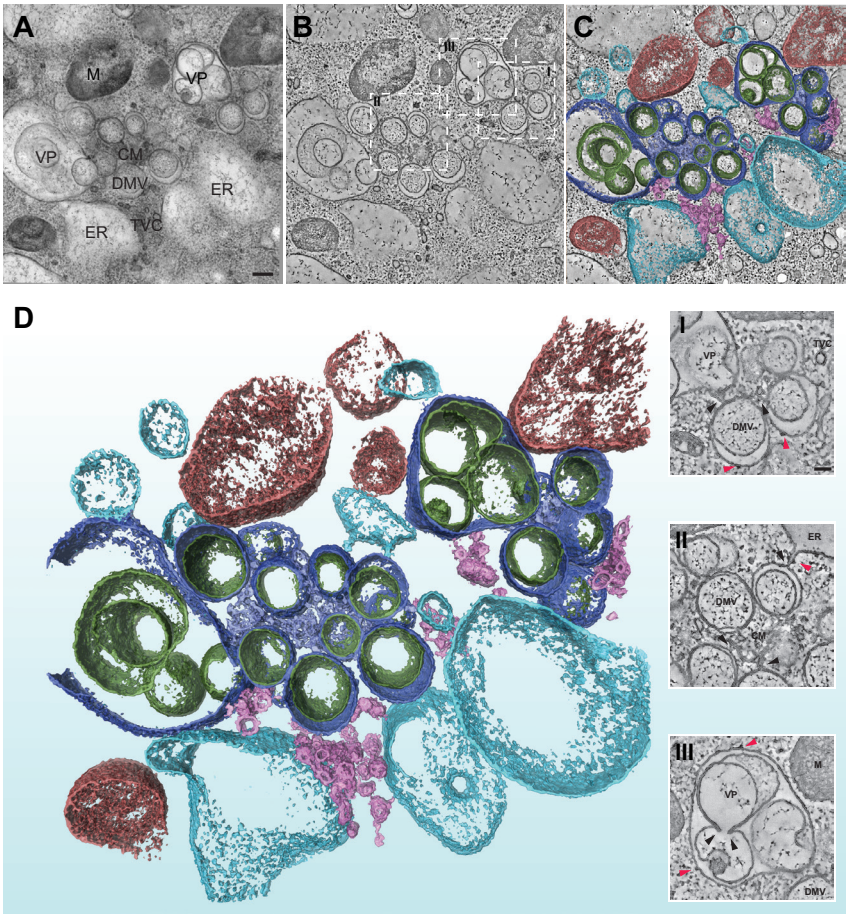


Figure 6. ET confirms the general integrity of the SARS-CoV-induced RVN upon BFA treatment. ET was applied for the three-dimensional analysis of the RVN in BFA-treated cells cryofixed at 7 h p.i. The top three panels illustrate how a three-dimensional surface-rendered model was derived by applying ET to a semi-thick section of a SARS-CoV-infected Vero-E6 cell, which had been treated with BFA from 1 to 7 h p.i. (A) A 0°-tilt transmission EM image of a 200-nm-thick resin-embedded section showing part of a SARS-CoV RVN after BFA treatment. Scale bar, 250 nm. (B) Using the IMOD software package, tomograms were computed from dual-axis tilt series of the 200-nm-thick section shown in panel A. The tomographic slice shown was taken from the central plane of the section and represents a thickness of 1.2 nm. The dashed squares mark the insets shown below in panel D. (C) The improved image from panel B after anisotropic diffusion filtering. The optimized signal-to-noise ratio facilitates masking, thresholding, and surface rendering. (D) Final three-dimensional surface-rendered model showing the RVN against a background of mitochondria (M, red), dilated ER and tubulo-vesicular clusters (both resulting from BFA treatment; depicted in light blue and pink, respectively). Furthermore, all substructures normally encountered in the SARS-CoV-induced RVN were observed after BFA treatment, including DMVs and VPs (outer membranes, dark blue; inner membranes, dark green) and CM (depicted in lavender). The insets (I, II, and III) show tilted tomographic slices taken from panel B and highlight RVN membrane connections between DMVs, between ER and DMVs, and between CM and DMVs (black arrowheads). Ribosomes attached to the cytosolic face of RVN membranes or ER are indicated with red arrowheads. Scale bar represents 100 nm. For abbreviation definitions, see Fig. 4. TVC, tubulovesicular cluster [220].

in the presence of BFA (Fig. 4 and 5) are also consistent with the conclusion that the drug cannot abrogate either RTC function or RVN formation to a similar extent as reported for BFA-sensitive picornaviruses. Apparently, all critical steps in the early stages of viral replication can proceed in the presence of BFA, suggesting that the early secretory pathway does not directly participate in or contribute to these steps. Although the integrity of the ER and the secretory pathway clearly promote RVN formation and SARS-CoV RTC function, the data presented here argue against a direct connection or functional dependence.

Coronaviruses versus picornaviruses: a different relationship with the secretory pathway

Picornaviruses may subvert the cell's secretory system without direct consequences, since they do not need this pathway for the production or release of viral progeny. In fact, they have been postulated to use this strategy to avoid certain host defense mechanisms [221,222]. In contrast, coronaviruses, as well as many other enveloped viruses, rely on the secretory pathway for virus assembly, maturation, and release. The interaction of viral proteins with GEFs such as GBF1 or BIG1 and BIG2, affecting Arf function and thereby disrupting secretory pathway functionality, may therefore be a property that is rare or lacking in viruses such as coronaviruses that depend on the secretory pathway for the release of their progeny.

For the most part, our results corroborate and extend the data of an MHV study recently published by Verheije et al. [167]. Instead of directly analyzing viral RNA synthesis, these authors measured the impact of BFA treatment by using a recombinant MHV that expresses luciferase from a subgenomic mRNA. They also utilized small interfering RNA (siRNA) knockdown of GBF1 and Arf1 in MHV-infected cells, which profoundly affected MHV replication. In contrast, knockdown of BIG1 or BIG2 did not inhibit MHV. In our opinion, this confirms that the normal functionality of ER and the early secretory pathway promotes efficient coronavirus replication but that the integrity of the downstream secretory pathway (beyond *cis*-Golgi), which is regulated by BIG1 and BIG2, is much less important. Nonetheless, the MHV nsp's tested also did not convincingly colocalize with GBF1 or Arf1 [167]. Although, in our opinion, the study by Verheije et al. insufficiently discriminates between the viral RTC itself and the modified membranes that presumably carry the viral enzyme complex, it was concluded that BFA treatment did not prevent MHV RTC formation, since both reduced numbers of DMVs and inhibition of reporter gene expression were observed. They then postulated that BFA treatment, or the depletion of Arf1 or GBF1, should in some other way interfere with replication, resulting in reduced *de novo* formation of viral replication complexes. Since these authors did not observe colocalization of GBF1 or Arf1 with MHV nsp's, they proposed that downstream effectors of Arf1 may be involved in MHV RNA replication. However, association with αγCOPI, a subunit of the COPI coat complex, was not observed, nor was colocalization detected with another obvious downstream effector of Arf1, phospholipase D. Finally, it

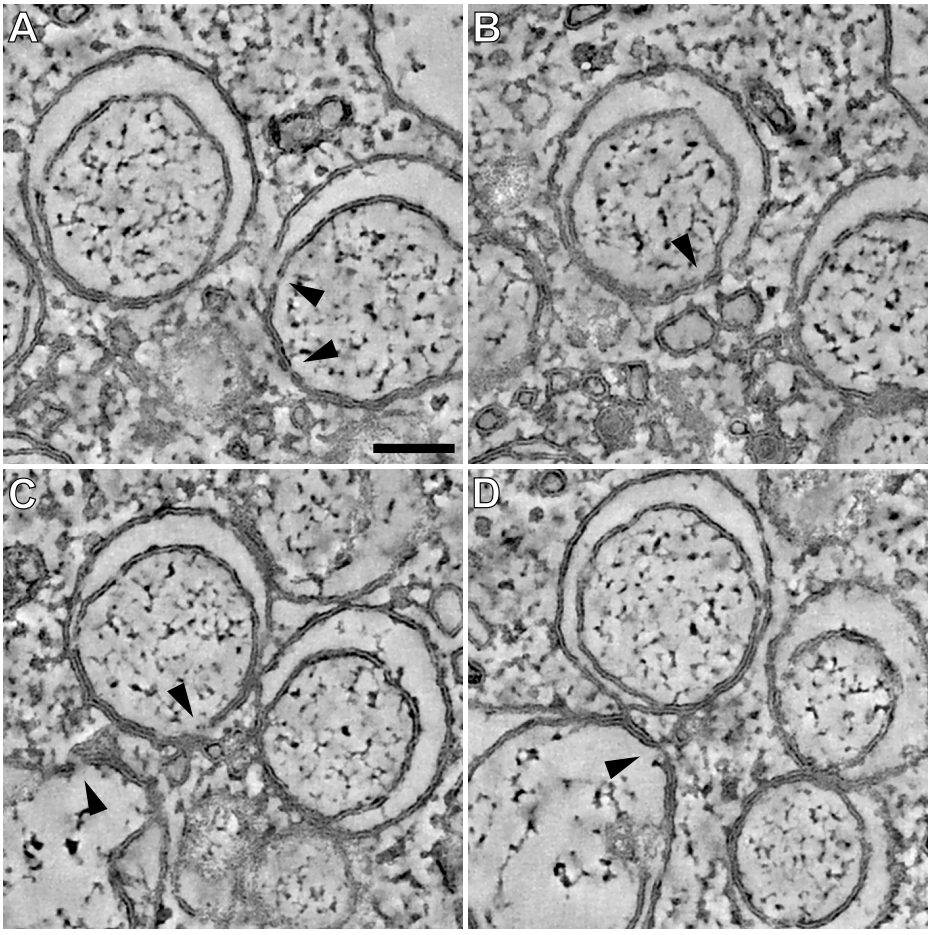


Figure 7. In-depth analysis of RVN membrane discontinuities after BFA treatment. The tomograms that were used for our ultrastructural analysis of RVN membranes in BFA-treated cells were scrutinized for openings that connect the DMV interior with the cytosol. (A to D) Examples of membrane discontinuities observed in our specimens (arrowheads), including a number that were present on the side of the vesicle facing the CM (e.g., in panels A and C), where double membranes remained tightly apposed. We doubt whether these discontinuities could be associated with viral RNA trafficking between vesicle interior and cytosol and consider it more likely that they may be artifacts resulting from the previously documented fragility of the RVN, which may actually be promoted by BFA treatment. Panels A to D also illustrate the separation of DMV inner and outer membranes during BFA treatment. However, the increased luminal space was generally lacking at the side of the DMV that faces the CM, where the two membranes remained tightly apposed. Panel D also shows an example of a necklike connection between the outer membranes of two DMVs. Bar represents 100 nm.

was hypothesized that the role of GBF1-mediated Arf1 activation in MHV replication may be the delivery of membranes to the ER through retrograde vesicular transport, which is inhibited after BFA treatment or knockdown of GBF1 or Arf1 [167]. Whereas normally there is a regulated stream of membrane delivery from ER to the Golgi complex and back through

anterograde and retrograde transport, respectively, BFA treatment induces the collapse of the Golgi complex and its merger with the ER. In this way, Golgi membranes could in fact become available for inclusion in the RVN. Indeed, we observed that the colocalization of the Golgi marker Giantin and SARS-CoV nsp3 slightly increased upon BFA treatment, going from a negative correlation in untreated cells (0.386 ± 0.02, equaling no significant colocalization; Fig. 3A) to a slightly positive correlation in BFA-treated cells (0.514 ± 0.04, indicating minimal colocalization, data not shown). This suggests that Golgi membranes may indeed end up in the RVN in the presence of BFA, although it remains unclear whether their inclusion actually promotes RVN formation or RTC function.

At present, we can only speculate on the mechanism(s) behind the indirect effect of BFA treatment on SARS-CoV replication. Clearly, viral replication may be hampered by structural changes of RVN elements (e.g., the reduced number of vesicles; Fig. 5A) and accelerated maturation of the network (VP formation). The first effect may be explained by the general influence of BFA treatment on ER integrity. Much of the ER becomes dilated soon after the start of BFA treatment [218,219], as also observed in the present study (Fig. 3F). Our unpublished data obtained with equine arteritis virus, a distant relative of SARS-CoV in the order *Nidovirales*, support the hypothesis that DMV morphogenesis commences with the formation of paired membranes, which are likely held together by protein-protein interactions. We do not yet have comparable information for SARS-CoV, but it is clear that the formation of paired membranes may be affected when the ER is dilated due to BFA treatment.

Separation of inner and outer membranes after BFA treatment

The changes in RVN morphology upon BFA treatment are intriguing, since the drug seems to speed up the normally observed maturation of the structure and thereby possibly also its deterioration near the end stage of infection. The expedited maturation is best illustrated by the accelerated appearance of VPs, although their significance for coronavirus replication has remained elusive thus far (Fig. 4). BFA treatment apparently disrupts or prevents membrane pairing, leading to separation of membranes that are normally tightly apposed. This may in fact reflect the mechanism leading to VP formation during normal infection. DMV outer membranes are continuous with each other and, when the interaction between inner and outer membranes would weaken, the necklike connection between DMVs may open up, resulting in VP formation. Possibly, SARS-CoV infection and BFA treatment affect ER integrity in a comparable manner. Indeed, in the absence of BFA, large VPs with extensive "empty volume" were observed late in infection [198], resembling the dilated ER membranes now found in BFA-treated samples (Fig. 4D, large VPs on left side). Moreover, Verheije et al. reported decreased secretion of a reporter protein from MHV-infected cells [167]. Thus, although at least a certain level of secretory pathway functionality is required for the transport of progeny virions, RVN formation and maturation may somehow mimic the effects of BFA treatment on

the ER and early secretory pathway. This effect may be intrinsic to the transmembrane nsp's that induce RVN formation.

The increased luminal space between the RVN membranes that we observed in BFA-treated cells also relates to the unresolved issue of possible RNA transport between DMV interior and cytoplasm. Whereas dsRNA labeling in +RNA virus-infected cells is commonly taken to indicate the site of viral RNA synthesis, RNA products must reach the cytoplasm to be translated and/or packaged. Although, using ET methods, we previously scrutinized DMVs for the presence of a connection to the cytoplasm [198], these were not detected, leaving the question of the localization of the exact site of coronavirus RNA synthesis wide open.

The fact that BFA treatment can induce separation of inner and outer membranes (Fig. 6A to C, closeups I and II) strengthens the notion that the inner membrane indeed is a distinct vesicular structure. The interaction between inner and outer membrane appeared to be stronger at the DMV side that faces the CM (Fig. 6), resulting in striking images of DMVs in which the luminal space was asymmetrically distributed. Using our electron tomograms, the part of the DMV surface where membranes remained apposed was again scrutinized for connections to the cytosol. Fig. 7 shows closeups of a number of membrane discontinuities, but we do not believe that these should be considered equivalent to the openings previously described for replication structures of other +RNA viruses [36,38]. We doubt whether these discontinuities could be associated with viral RNA trafficking and consider it more likely that they may be artifacts resulting from the previously documented fragility of the RVN, which may actually be promoted by BFA treatment. Consequently, the question of whether RNA synthesis indeed occurs inside DMVs, as suggested by the abundant presence of dsRNA, and the possibility of RNA transport across double membranes [198], remain intriguing and highly relevant topics for further research. In this context, it was interesting that a quantitative correlation seemed to exist between the reduction of viral RNA synthesis and the decrease of vesicle numbers upon BFA treatment (Fig. 1A and 5A). Moreover, in untreated cells both viral RNA synthesis and DMV numbers approximately doubled between 7 and 11 h p.i. (Fig. 1A and 5A), a correlation that even appears to hold up in the presence of BFA. Although these observations could be taken to support the hypothesis that RNA synthesis indeed occurs inside DMVs, they may on the other hand also be accommodated in models proposing that DMV formation is a cellular response to viral replication or a viral strategy to avoid antiviral host responses [198]. According to the latter hypothesis, DMVs would essentially function as "garbage bags" to hide excess viral dsRNA from the cytosolic sensors of the innate immune system, while viral RNA synthesis would take place in association with another RVN component, for example, the CM that appear to be the primary site of nsp accumulation [198]. In any case, our analysis, for the first time, revealed a correlation between RTC activity and DMV number, strengthening the connection between viral RNA synthesis and the coronavirus-induced RVN.

Which host factors are involved in SARS-CoV replication?

Various markers of the early secretory pathway such as Sec13, syntaxin 5, GBF1, and Arf1 do not seem to localize to the SARS-CoV-induced RVN (Fig. 3) and therefore are unlikely to play a prominent role in its morphogenesis or function. On the other hand, ER proteins that are associated with the RVN are PDI and Sec61α, which normally have prominent functions in the translocation and modification of proteins synthesized in association with the ER. Considering the presence of ribosomes on the RVN outer membrane and in CM, we speculate that viral protein synthesis may take place at these sites, as was also proposed for the CM induced by flavivirus infection [25]. Our data suggest that cellular factors, such as PDI and Sec61α, may therefore be recruited to the network, which could also hamper cellular protein synthesis.

For both picornaviruses and the coronavirus MHV, previous studies addressed the possibility of a link between virally induced DMVs and the autophagic pathway, the only cellular mechanism that is also associated with double membrane structures. Thus far, however, contradictory data sets have been described that either confirm or reject the hypothesis for the same or similar picorna- or coronaviruses [50,96,100,186,223-226]. Now that we conclude that also the early secretory pathway is unlikely to be directly involved in SARS-CoV RVN formation or RTC function, it remains to be established which cellular factors do play a prominent role during the earliest stages of coronavirus replication. In addition to our observations here regarding Sec61α redistribution upon infection, recent *in vitro* studies have shown that an (as-yet-unidentified) cytosolic host factor is essential for *in vitro* activity of the SARS-CoV RTC [188]. Besides the secretory and autophagic pathways, the reticulon family of membrane curvature-inducing ER proteins [227] was implicated in picornavirus replication [228], and their role in the life cycle of other +RNA viruses, including coronaviruses, should be investigated. Also, systematic large-scale approaches, such as the use of siRNA libraries, will be important in the quest for host factors and pathways involved in +RNA virus replication.

MATERIALS AND METHODS

Virus, cell culture, antisera, and cellular markers

SARS-CoV strain Frankfurt-1 was used to infect Vero-E6 cells (multiplicity of infection [MOI] of 10) as described previously [94]. All work with live SARS-CoV was performed inside biosafety cabinets in the biosafety level 3 facility at Leiden University Medical Center. Polyclonal rabbit antisera recognizing SARS-CoV nsp3, nsp5, and nsp8 and M protein have been described previously [100]. A rabbit antiserum against the N protein was raised as described previously [100] using a recombinant full-length N protein as antigen. Mouse monoclonal antibody (MAb) J2 [179] recognizing dsRNA was purchased from Scicons (Hungary). To visualize host

cell marker proteins, a variety of antibodies and yellow fluorescent protein (YFP)-tagged proteins were used. Mouse MAbs recognizing protein disulfide isomerase (PDI) [229], Giantin (G1/133; Alexis Biochemicals), GBF1 (BD Transduction Labs), and Sec13 [230] were used. Mouse MAb against human β-actin (clone AC74) was obtained from Sigma-Aldrich, and rabbit anti-human sec61α was purchased from Upstate. Rabbit anti-syntaxin 5 was kindly provided by Matsuo Tagaya (Tokyo, Japan), and expression constructs encoding wtArf1, $Arf1_{T31N}$, and $Arf1_{Q71L}$ [214] were kindly made available by Guillermo Romero (Pittsburg, PA). Transfections in combination with SARS-CoV infections were done as described before [94]. TUNEL assay kits were from Roche (In Situ Cell Death Detection kit TMR Red), and a kit for MTS assays was obtained from Promega.

Metabolic labeling of viral RNA synthesis and RNA hybridization analysis

At different time points after infection, in the presence or absence of BFA, infected cells were given 10 μg of actinomycin D (ActD; Sigma-Aldrich)/ml for 1 h to block cellular transcription. Subsequently, viral RNA synthesis was labeled for 1 h using medium containing 73 μCi of [^{3}H] uridine and 10 μg of ActD/ml. For RNA isolation, cells were washed with phosphate-buffered saline (PBS) and lysed for 5 min in a buffer containing 20 mM Tris-HCl (pH 7.6), 150 mM NaCl, 0.5% deoxycholine, 1.0% Nonidet P-40, 0.1% sodium dodecyl sulfate, and 1.25 U of DNase I (Invitrogen)/ml. Lysates were mixed with an equal volume of 100 mM Tris-HCl (pH 8), 500 mM LiCl, 10 mM EDTA (pH 8), 5 mM dithiothreitol, and 5% lithium dodecyl sulfate containing 100 μg of proteinase K/ml, followed by incubation for 10 min at 37°C. Aliquots (5 μl), equaling approximately 1,500 cells, were spotted in duplicate on Whatman filter paper. After precipitation by washing with TCA-P (5% TCA, 100 mM $Na_4P_2O_7$, 95 mM NaH_2PO_4) and drying, the incorporation of [^{3}H]uridine was measured in a Beckman liquid scintillation counter (LS6500 IC). Alternatively, intracellular RNA was isolated by phenol extraction and ethanol precipitation, separated in a formaldehyde-agarose gel, and hybridized to a ^{32}P-labeled oligonucleotide probe complementary to the 3′ end of the genome, as described previously [100].

SDS-PAGE and Western blotting

Cells were lysed in Laemmli sample buffer [231], boiled, separated in SDS-10% PAGE gels, and electroblotted onto polyvinylidene difluoride membrane according to standard protocols. Blots were blocked with 5% skimmed milk and 0.02% Tween 20 in PBS prior to incubation with antisera dilutions. Between antibody incubations, blots were washed with 0.5% skimmed milk and 0.02% Tween 20 in PBS and before ECL-Plus chemiluminescence detection (GE Healthcare) washing was done with PBS containing 0.02% Tween 20.

IF microscopy

Infected cells on glass coverslips were fixed with 3% paraformaldehyde at the indicated time points postinfection (p.i.) and processed for immunofluorescence (IF) microscopy essentially as described by van der Meer et al. [95]. As before, an Alexa 488-coupled SARS-CoV nsp3 antiserum was used to visualize the viral replicase. After permeabilization, single- or dual-labeling IF assays were carried out with rabbit antisera and/or mouse monoclonal antibodies, which were detected by using indocarbocyanine (Cy3)-conjugated donkey anti-rabbit immunoglobulin and Alexa Fluor 488-conjugated goat anti-mouse immunoglobulin secondary antibodies, respectively (Molecular Probes/Invitrogen). Samples were examined with a Leica SP5 confocal laser scanning microscope, using a pinhole size of 1 airy unit. Images were optimized and analyzed for colocalization with the WCIF version of ImageJ (http://www.uhnresearch.ca/facilities/wcif/imagej/). The product of the differences from the mean (PDM) images and the Manders' overlap coefficients were calculated as described by Li et al. [232].

In vitro RNA synthesis assay

In vitro assays to measure the RTC activity of membrane fractions isolated from infected cells (10 h p.i.) were performed as described previously [188]. Activity was measured on the basis of [α-^{32}P]CTP incorporation into RNA products. Assays were done in the presence or absence of 6 μg of BFA/ml and were terminated after 40 or 100 min. Subsequently, RNA was isolated by acid-phenol extraction and isopropanol precipitation. Reaction products were separated on 1% denaturing formaldehyde agarose gels and visualized by using a Typhoon variable mode imager (GE Healthcare, Chalfont St. Giles, United Kingdom). Phosphorimager data were analyzed and quantified by using ImageQuant TL software (GE Healthcare).

Electron microscopy

For ultrastructural morphological investigations, SARS-CoV-infected Vero-E6 cells, with or without BFA treatment, were prepared as described before [198]. After prefixation, cryofixation by plunging into liquid ethane, and freeze substitution, the samples were embedded in epoxy LX-112 resin. Thin sections (100 nm) were viewed with a FEI Tecnai 12 Biotwin transmission electron microscope operating at 120 keV.

DMVs were quantified in the cell slice showing the largest nuclear diameter as described before [198]. Briefly, electron micrographs covering the entire cross-section of the cell were recorded and digitally merged to produce an image composition representing a 100-nm-thick plane through the center of the cell. Merged images were analyzed using ImageJ software (http://rsb.info.nih.gov/ij/). Examples of representative images used for DMV counting have

been deposited in the Cell Centered Database (http://ccdb.ucsd.edu) under the accession numbers 6935 to 6938.

For immuno-electron microscopy, infected cell monolayers were prefixed, cryofixed by high-pressure freezing using a Leica EM PACT2, and freeze substituted using anhydrous acetone containing 0.2% uranyl acetate. After being washed with ethanol, the samples were infiltrated with Lowicryl HM20 and polymerized under UV light at –50°C. Thin sections were labeled with anti-dsRNA mouse MAb J2 [179], a bridging rabbit- anti-mouse IgG antibody (Dako Cytomation) and protein A-gold particles (10 or 15 nm). Grids were contrasted with uranyl acetate and lead hydroxide.

Electron tomography

Freeze-substituted cell samples, processed for morphological investigation as described above, were used to cut 200-nm-thick sections. Then, 10-nm gold particles were layered on top of the sections as fiducial markers. For dual-axis tomography, two single-axis tilt series were recorded with a FEI T12 transmission EM operating at 120 keV. Per single-axis tilt series, 141 images were recorded with 1° tilt increments by using automated tomography acquisition software (Xplore 3D; FEI Company). Images were acquired with a cooled slow-scan charge-coupled device camera (4k Eagle; FEI Company). To obtain electron tomograms, the dual-axis tilt series were aligned by means of the fiducial markers and processed by using the IMOD software package [194]. The size of the voxels in the tomogram corresponds to 1.2 nm. The full data set has been deposited in the Cell Centered Database (http://ccdb.ucsd.edu) under accession number 6939. Three-dimensional surface-rendered reconstructions of the RVN and adjacent cellular features were produced using the AMIRA visualization package (TSG Europe) by masking structures of interest and subsequent thresholding. For this process, volumes were denoised by using nonlinear anisotropic diffusion filtering [196]. Videos were made with QuickTime Pro (http://www.apple.com/quicktime).

ACKNOWLEDGMENTS

We are very grateful to Mitsuo Tagaya (Tokyo, Japan) and Wanjin Hong (Singapore) for providing the antibodies against syntaxin 5 and Sec13, respectively. Arf1 expression constructs were kindly provided by Guillermo Romero (Pittsburgh). We thank Frank van Kuppeveld (Nijmegen, The Netherlands) for the antiserum against GBF1 and for numerous helpful discussions. We thank Helene Verheije, Xander de Haan, and Peter Rottier (Utrecht, The Netherlands) for sharing unpublished data and stimulating discussions. Finally, we acknowledge the input of Martijn van Hemert and the technical assistance of our coworkers Yvonne van der Meer (IF microscopy) and Raimond Ravelli and Joke van der Meer (whole-cell mosaics).

CHAPTER 4

Development and RNA-synthesizing activity of coronavirus replication structures in the absence of protein synthesis

Sjoerd H.E. van den Worm, Kèvin Knoops, Jessika C. Zevenhoven-Dobbe, Corrine Beugeling, Yvonne van der Meer, A. Mieke Mommaas, and Eric J. Snijder

Journal of Virology (in press)

ABSTRACT

The RNA replication and transcription complex of coronaviruses is associated with an elaborate reticulovesicular network (RVN) of modified endoplasmic reticulum. Using cycloheximide and puromycin, we have studied the effect of translation inhibition on the RNA synthesis of severe acute respiratory syndrome coronavirus and mouse hepatitis virus. Both inhibitors prevented the usual exponential increase in viral RNA synthesis, with immunofluorescence and electron microscopy indicating that RVN development came to a standstill. Nevertheless, limited RNA synthesis was supported, implying that continued translation is not an absolute requirement and suggesting a direct link between RVN formation and accumulation of coronavirus proteins.

Coronaviruses have a positive-strand, approximately 30-kb RNA genome of which the 5' two-thirds encode two large replicase polyproteins (pp1a and pp1ab) that are autoproteolytically cleaved to produce 15 or 16 mature nonstructural proteins (nsps; [13,23,83]). The majority of nsps assemble into the viral replication and transcription complex (RTC), which includes the viral RNA-dependent RNA polymerase (nsp12; [233]). The 3'-proximal part of the coronavirus genome encodes structural and accessory proteins, which are expressed from a nested set of subgenomic mRNAs [78,197,234].

Coronavirus infection induces elaborate membrane structures [104,198,235] that presumably serve as RTC scaffold, a common feature among positive-strand RNA viruses [45,197,199,236-238]. This reticulovesicular membrane network (RVN) is derived from and continuous with the endoplasmic reticulum (ER; [198]), and includes convoluted membranes (CM) and a large number of unusual double-membrane vesicles (DMVs). The exact role in viral RNA synthesis of different RVN subdomains remains to be elucidated. Both viral nsps and double-stranded (ds) RNA are associated with the RVN, but –surprisingly- they barely colocalize: whereas the bulk of viral replicase proteins is CM-associated, dsRNA is mainly found inside DMVs [198].

In this study, we have addressed the relation between coronavirus mRNA translation, RNA synthesis, and RVN development. Previously, the RNA synthesis of mouse hepatitis virus (MHV) was reported to decrease almost instantly after addition of the translation inhibitor cycloheximide (CHX; [239]). It was suggested that the MHV RTC is structurally labile or contains an unstable protein factor. In a severe acute repiratory syndrome coronavirus (SARS-CoV) *in vitro* RTC activity assay neither CHX nor the alternative translation inhibitor puromycin (PUR) directly affected RNA synthesis [188]. To explore the impact of translation inhibition in more detail, we have now combined biochemical and cell biological approaches to analyze the effect of CHX and PUR treatment in MHV- and SARS-CoV-infected cells.

The effect of translation inhibition by CHX or PUR was first measured by metabolic labeling of viral RNA synthesis in infected cells, essentially as previously described [240]. MHV-infected 17Clone-1 cells and SARS-CoV-infected Vero-E6 cells were compared, while taking into account the different infection kinetics of these two viruses. For each inhibitor, a dose was chosen that gave complete translation inhibition within 30 minutes after addition to the culture medium, which was verified by metabolic labeling of cellular protein synthesis (Fig. 1A). Cellular transcription was inhibited by using actinomycin D and viral RNA synthesis was measured at different time points after translation inhibition by labeling with [^{3}H]uridine for 1 hour.

SARS-CoV RNA synthesis became measurable at 5 h p.i. and peaked around 9 h p.i. (Fig. 1B). In agreement with previous reports [239], MHV RNA synthesis peaked around 7 h p.i. (Fig. 1C). Addition of CHX or PUR at 4 h p.i. blocked RNA synthesis of both viruses, immediately for SARS-CoV and somewhat more slowly for MHV (Fig. 1B and C), which may reflect stability differences between the RTCs of the two viruses. For both coronaviruses studied here, the inhibitory ef-

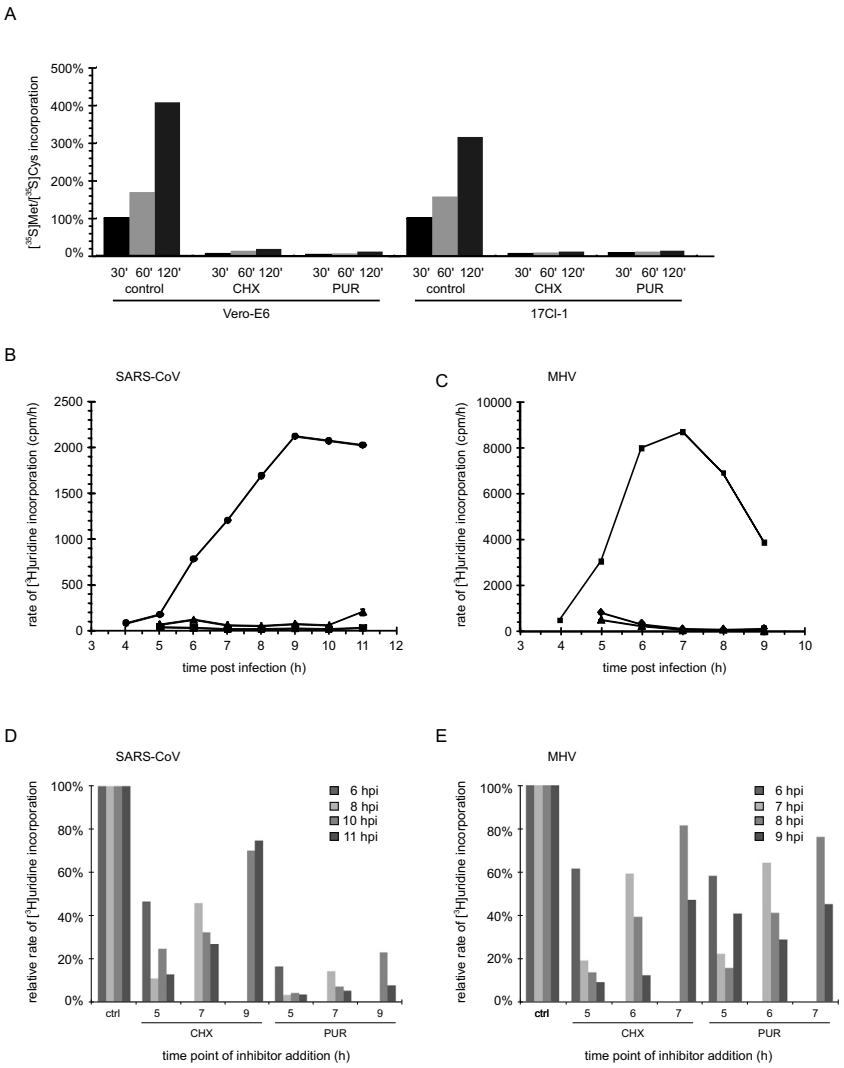


Figure 1. Translation inhibition affects the rate of coronavirus RNA synthesis. (A) Translation inhibition by CHX or PUR in Vero-E6 cells (100 µg/ml CHX; 1 mg/ml PUR) and 17Clone-1 cells (100 µg/ml of both inhibitors). Protein synthesis was measured for 30-120 minutes after the simultaneous addition of ^{35}S-labeled methionine/cysteine and inhibitor. (B-E) Time course of SARS-CoV (B, D) and MHV (C, E) RNA synthesis in Vero-E6 and 17Clone-1 cells, respectively, labeled with [^{3}H]uridine for 1 h prior to lysis in the presence or absence (control, ●) of the translation inhibitors CHX (▲;100 µg/ml) or PUR (■;1 mg/ml). Labeling was performed as described previously [240] and incorporation was quantified by liquid scintillation counting of aliquots of cell lysates corresponding to ~3,500 cells. Cellular transcription was inhibited by giving 10 µg/ml of actinomycin D 1 h prior to labeling. CHX or PUR was added at 4 h p.i. to SARS-CoV infected Vero-E6 cells (B) or MHV-infected 17Clone-1 cells (C) and viral RNA synthesis was measured each hour for the duration of the experiment. Subsequently, the effect of varying the time point of translation inhibition was studied by treating SARS-CoV-infected Vero-E6 cells with CHX or PUR at 5, 7, or 9 h p.i. (D) and MHV-infected 17Clone-1 cells at 5, 6, or 7 h p.i. (E), after which RNA synthesis was measured for 1 h at the indicated time points. The average of two experiments is shown.

fect of early PUR addition on viral RNA synthesis was similar to that of CHX. However, when the inhibitors were added at later time points a difference became apparent. In the first hour of PUR treatment, SARS-CoV RNA synthesis dropped below 20% and subsequently declined to background levels (Fig. 1D). In the presence of CHX, however, RNA synthesis diminished rapidly to about 50%, but then decreased only slowly during the hours that followed. For MHV, the latter trend was observed when using either translation inhibitor (Fig. 1E), thus resulting in a less pronounced inhibition by CHX treatment than previously reported [239] and in longer lasting residual viral RNA synthesis. In the case of SARS-CoV, the different inhibition profiles obtained with CHX and PUR suggest that the effect of the latter drug extends beyond the dissociation of ribosomes. Whereas CHX essentially 'freezes' translating ribosomes on their mRNA, PUR treatment results in polysome disruption and affects the morphology of the ER [241], which may hamper RVN formation or function and –consequently– RNA synthesis. Recent studies using the drug brefeldin A, also suggested a direct link between the integrity of the secretory pathway, RVN formation, and viral RTC activity [167,240]. Although the specific combination of cell lines and drugs used here may have influenced our analysis to a certain extent, our data do indicate that a limited level of coronavirus RTC activity can be maintained for several hours in the absence of *de novo* protein synthesis.

Next, for both SARS-CoV- and MHV-infected cells, we analyzed the distribution and accumulation of nonstructural proteins and viral RNA by performing dual immunofluorescence (IF) microscopy as described previously [198,240]. We employed rabbit antisera recognizing the trans-membrane replicase subunit nsp4 and a mouse monoclonal antibody labeling double-stranded RNA, with the latter presumably representing the replicative intermediates of the viral RNA. Although variable between individual cells, on average the number of small nsp4- and dsRNA-containing foci present at 4 h p.i. remained essentially the same during subsequent CHX or PUR treatment, in contrast to the significant proliferation of the signal observed in untreated control cells (Fig. 2). Still, in SARS-CoV-infected cells the customary development of the early, small foci into a perinuclear collection of larger foci was not prevented by translation inhibition (Fig. 2A). In MHV-infected cells, such a migration to the perinuclear area did not occur during CHX- or PUR-treatment (Fig. 2B). In addition, when cultures infected with SARS-CoV or MHV at a multiplicity of infection of 1 were given translation inhibitors early in infection (4 or 2 h p.i.), the percentage of IF-positive cells essentially remained stable for the next 3 h (Fig. 2C). In the same time frame (4-7 or 2-5 h p.i., respectively), the number of positive cells tripled in untreated control cultures infected with SARS-CoV or MHV. In terms of RVN development, these IF data suggested that translation inhibition leads to a "*status quo*", with complexes formed prior to drug treatment remaining stable and, according to the metabolic labeling data, able to sustain a modest level of viral RNA synthesis (Fig. 1).

Recently, the morphogenesis and ultrastructure of the SARS-CoV-induced RVN were documented in detail using transmission electron microscopy (TEM) and electron tomography [198]. Using TEM, we now compared RVN ultrastructure in SARS-CoV-infected Vero cells fixed

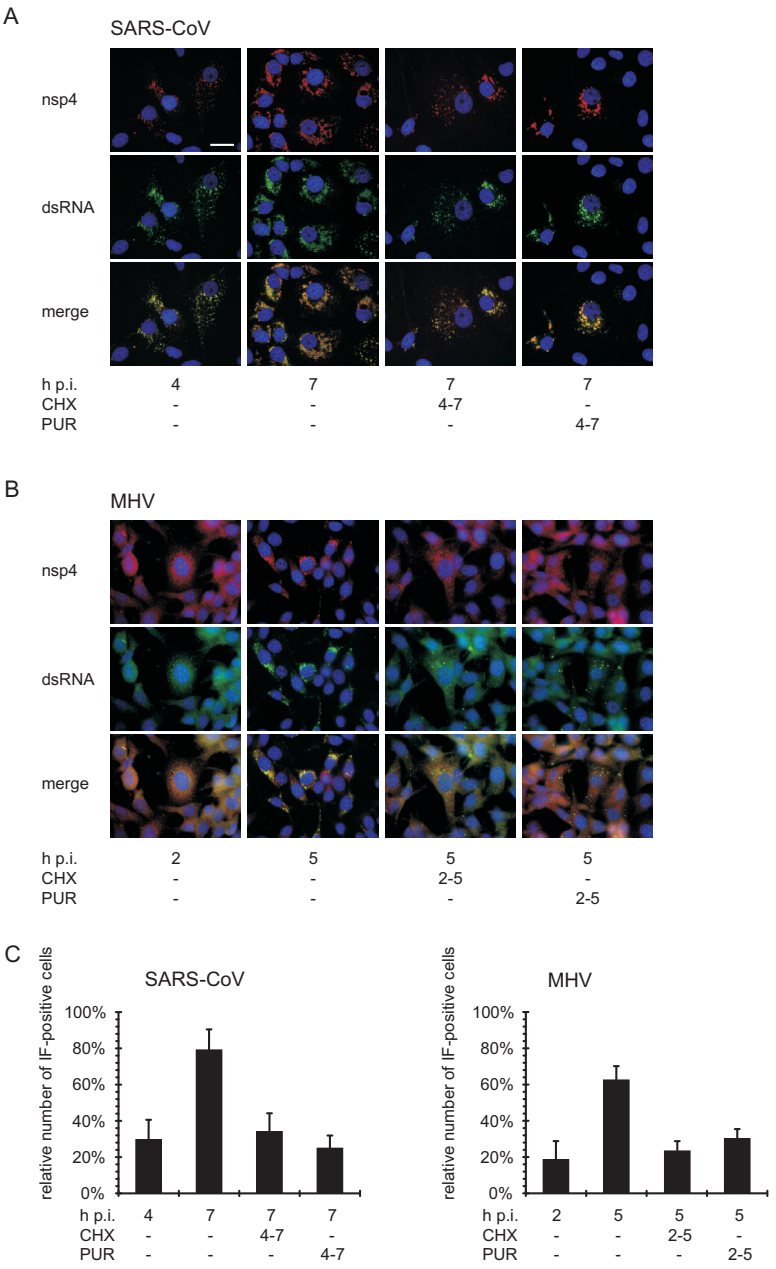


Figure 2. Subcellular localization of nsp4 and dsRNA following translation inhibition. SARS-CoV-infected Vero-E6 cells (A) and MHV-infected 17Clone-1 cells (B) were treated with CHX or PUR from 4 to 7 h p.i. (SARS-CoV) or 2 to 5 h p.i. (MHV). Cells were then fixed and analyzed using dual labeling IF microscopy for nsp4 (red) and dsRNA (green). Nuclei were visualized using Hoechst 33258 staining (blue). Bar represents 25 µm. (C) Microscopic images containing between 300 and 450 cells were analyzed for nsp4 and dsRNA labeling, and scored 'IF positive' when either of these was visible. The average and SEM of all cells per sample is shown.

at either 4 or 7 h p.i., including cultures that had been treated with either CHX or PUR from 4 to 7 h p.i. (Fig. 3). Whereas CHX-treated and untreated mock-infected cells were morphologically indistinguishable, PUR-treatment resulted in the previously described strong reduction of polysome numbers and an increase of tubular ER (data not shown; [241]). Between 4 and 7 h p.i., the RVN developed from mostly clusters of individual DMVs into the vesicle packets (VPs) that are typical of the later stages of infection (Fig. 3A-B; [198]). Following CHX or PUR treatment, RVN development was significantly hampered and only rarely did single DMVs transform into the larger VPs (Fig. 3C-D). In line with the IF data presented in Fig. 2, however, translation inhibition did not induce degradation of virus-induced membrane structures, which likely continued to support limited viral RNA synthesis (Fig. 1).

Next, a quantitative DMV analysis was performed by cutting thin EM sections in a plane parallel with the cell monolayer and counting inner vesicles present in DMVs and VPs. As

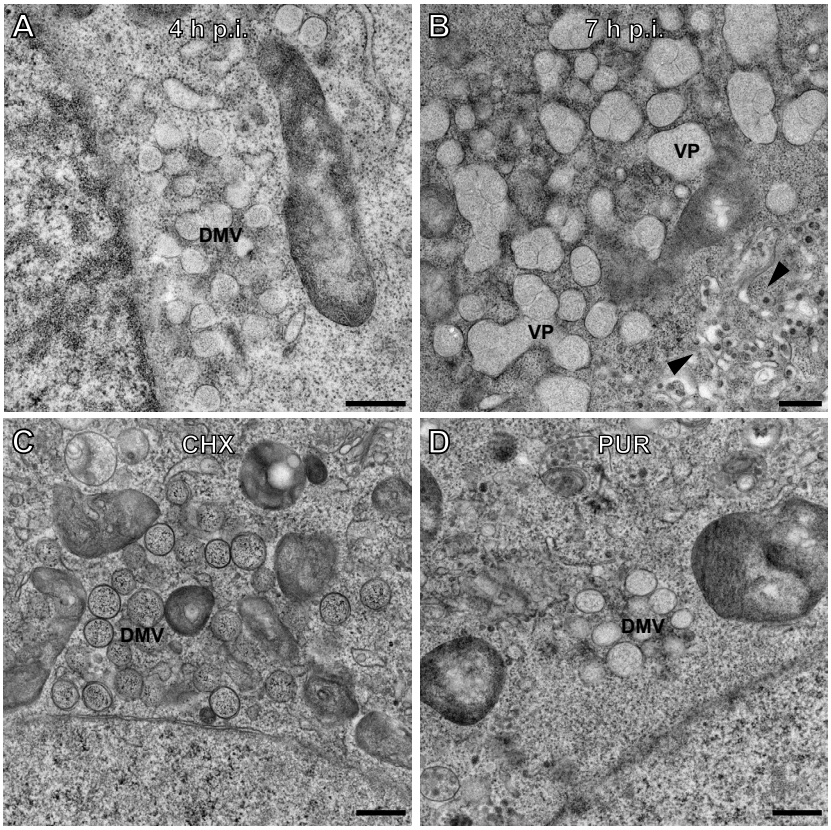


Figure 3. Development of SARS-CoV double-membrane vesicles into vesicle packets is hampered when translation is inhibited. Electron micrographs of SARS-CoV-infected Vero-E6 cells showing (A) normal development of double-membrane vesicles (DMVs) at 4 h p.i. and (B) vesicle packets (VPs) at 7 h p.i. Treatment with CHX (C) or PUR (D) starting at 4 h p.i. prevented the customary development of the virus-induced RVN, resulting in the prolonged presence of DMV clusters and a lack of VPs at 7 h p.i. Bars represent 500 nm.

described previously [240], counting was facilitated by stitching electron micrographs covering a complete slice through the center of the cell into large mosaics each composed of 25 to 100 images. Per condition, 32 cells from three independent experiments were analyzed to calculate the average number of SARS-CoV-induced vesicles per μm^2 of cytoplasm. Unfortunately, the analysis was hampered by the fact that DMVs are still relatively rare at 4 h p.i. (i.e. cells may be infected but random EM images may not reveal any DMVs; see also Fig. 2). Also the relative asynchronicity of infection between cells in the same culture contributed to significant variation in DMV counts. Still, as documented previously [198], average DMV numbers clearly increased between 4 and 7 h p.i. Upon translation inhibition with either CHX or PUR, this trend was clearly lacking (Fig. 4), suggesting a direct connection between RVN development and the accumulation of coronavirus proteins.

Taken together, our data suggest that the coronavirus RVN-forming membrane alterations, which are likely triggered by the synthesis of increasing amounts of trans-membrane proteins like nsp3, nsp4, and nsp6, contribute to the efficiency of the replicative cycle, rather than being the mere consequence of cellular responses to infection. Our study of RNA synthesis and RVN development early in infection revealed that coronavirus RTCs (i) are stable even when viral protein synthesis is stalled (ii) remain capable of limited but sustained RNA synthesis under these conditions, and (iii) can be active in the absence of RVN expansion, although it is clear that the normal development of replication structures likely contributes to the rapid increase in viral RNA synthesis that is typical of the exponential phase of infection.

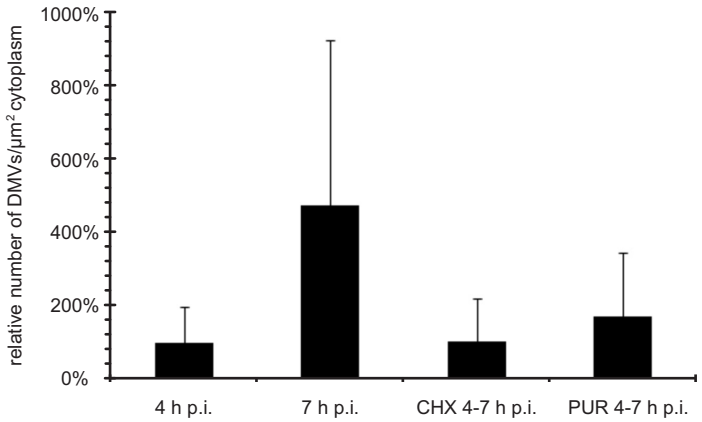


Figure 4. The number of RVN inner vesicles is stable when translation is inhibited. Thin sections of SARS-CoV-infected Vero-E6 cells were used to count RVN inner vesicles in DMVs or VPs. For this purpose, images covering a complete slice through the center of the cell were stitched into large mosaics to facilitate the analysis. Per condition, 32 cells from three independent experiments were analyzed. The graph shows the average number of inner vesicles per square micrometer of cytoplasm and illustrates how translation inhibition by either CHX or PUR prevented expansion of the number of inner vesicles as it normally occurs between 4 and 7 h p.i. DMVs were never observed in mock-infected cells. Error bars represent the standard deviation of the averages from the three independent experiments.

CHAPTER 5

Ultrastructural characterization of arterivirus replication structures: reshaping the endoplasmic reticulum to accommodate viral RNA synthesis

Kèvin Knoops, Montserrat Bárcena, Ronald W.A.L. Limpens, Abraham J. Koster, A. Mieke Mommaas, and Eric J. Snijder

Submitted for publication

ABSTRACT

Virus-induced membrane structures support the assembly and function of positive-stranded RNA virus replication complexes. The replicase proteins of arteriviruses are associated with unusual double-membrane vesicles (DMVs; diameter ~100 nm), which were previously proposed to derive from endoplasmic reticulum (ER). Using advanced electron microscopic techniques, including electron tomography and electron spectroscopic imaging, we have now performed an in-depth ultrastructural analysis of cells infected with the prototypic arterivirus equine arteritis virus (EAV). We established that the outer membranes of EAV-induced DMVs are interconnected with each other and the ER, thus forming a reticulovesicular network (RVN) that – to a certain extent – resembles membrane structures accommodating the RNA synthesis of the very distantly related SARS-coronavirus. A clear and striking parallel between coronavirus and arterivirus DMVs is the accumulation in their interior cavity of double-stranded RNA, the presumed intermediate of viral RNA synthesis. However, openings connecting DMV interior and cytosol were only rarely observed, and likely represent fixation or staining artifacts. Also semi-permeabilization and nuclease digestion experiments suggest that the interior of EAV-induced DMVs is inaccessible from the cytosol, implying that the double-stranded RNA is compartmentalized by membranes. As a novel approach to visualize and quantify the RNA content of viral replication structures, we explored electron spectroscopic imaging of DMVs, which revealed the presence of an RNA amount equaling up to a few dozen copies of the EAV genome. Despite significant morphological differences, including a ~2.5-fold larger diameter of coronavirus-induced DMVs, our analysis establishes that RVN formation is a common property of cells infected with members of the order *Nidovirales*, which includes both arteri- and coronaviruses. Finally, we visualized a peculiar network of EAV nucleocapsid protein-containing protein sheets and tubules, which appears intertwined with the RVN. This potential intermediate in nucleocapsid formation suggests that arterivirus RNA synthesis and virion assembly are coordinated in intracellular space.

INTRODUCTION

Lipid membranes define the boundaries of all important cellular organelles like mitochondria, endoplasmic reticulum (ER), and the Golgi complex. They are also indispensable for the biochemical functions performed by these highly specialized micro-compartments, which require both structural support and physical separation from the cytosol. Along the same lines, in the infected cell, all positive-stranded RNA (+RNA) viruses characterized to date induce the formation of dedicated membrane structures to support the cytoplasmic replication of their RNA genome [25,27,32,242]. Apparently, the formation of these membranous compartments offers important functional and/or strategic benefits for the viral RNA-synthesizing machinery.

For a number of +RNA viruses, the continuous improvement of cryo-fixation methods and the advent of electron tomography (ET) have made important contributions to the visualization of their replication structures by offering better preservation [49,100,121,122], higher resolution imaging, and the possibility of three-dimensional (3-D) ultrastructural analysis [36,38,41,198]. Furthermore, immuno-electron microscopy (iEM) has been used to investigate the presence of viral replicase subunits, host cell markers, and viral RNA products in +RNA virus replication structures. The combination of these technical approaches established that the specific association of replicase proteins and newly synthesized viral RNA with these membrane compartments is a common feature of all +RNA virus models studied to date.

Recent ET-based studies provided valuable information about the 3-D ultrastructure of the replication structures formed by *e.g.* the nodavirus Flock house virus [36], severe acute respiratory syndrome-coronavirus (SARS-CoV) [198], and Dengue and West Nile flaviviruses [38,41]. Flock house virus generates small spherular invaginations of the mitochondrial outer membrane [36,37], similar to those induced by alphaviruses in endosomal and lysosomal membranes [34]. Electron tomography of flavivirus infected cells demonstrated similar invaginations, but in this case ER membranes serve as platform for the biogenesis of the replication complex [38,41]. Moreover, flaviviruses induce a network of additional membrane structures that has been implicated in organizing the different stages of the replicative cycle in space and time [25,38,41,42,45,187]. The accumulation of different membrane structures, whose respective functional importance remains to be investigated, was also documented for picornaviruses [49-51,121,156] and coronaviruses [101-104,198,235]. Members of the latter family induce typical double-membrane vesicles (DMVs) and also convoluted membranes (CM) that ET revealed to be part of a reticulovesicular network (RVN) of modified ER that is continuous with its membrane donor [198,235].

The interior of the invaginations induced by noda-, alpha- and flaviviruses was reported to be connected to the cytosol by a single orifice, which was postulated to be used for the import of building blocks and the export of viral RNA products. Using antibodies recognizing double-stranded RNA (dsRNA), the presumed intermediate of viral RNA synthesis, it was

found that these molecules are present in the interior of the spherules [38,39,243]. When the RNA synthesis of several +RNA viruses was pulse-labeled with 5' brominated nucleosides, iEM detection showed that label was present both inside the compartments and in the cytosol surrounding the replication structures [36,97,104,244], possibly due to RNA transport within the labeling time window used.

In contrast, convincing evidence for a connection to the cytosol was not obtained when SARS-CoV-induced DMVs were analyzed in detail by ET [198,240], a finding difficult to reconcile with the accumulation of dsRNA inside these structures and the *in vitro* biochemical properties of isolated replication and transcription complexes (RTCs) [188]. The latter study clearly suggested that genome replication and subgenomic RNA synthesis occur inside protective membrane structures [188], implying the need for a transport mechanism to deliver newly synthesized viral RNA to the cytosolic ribosomes and virus assembly sites.

Arteriviruses are very distant relatives of coronaviruses. In spite of important differences in terms of genome size, virion structure, and various other biological features [13], the two families have been united in the order *Nidovirales* based on conservation of important replicase domains and striking similarities in genome organization and expression. Also arterivirus-infected cells are characterized by the accumulation of double membrane sheets and DMVs [95,97], but the average diameter of the latter is about three times smaller than those induced by coronaviruses (300 versus 100 nm) and CM have not been observed. The biochemistry and molecular biology of the replication machinery of the arterivirus prototype equine arteritis virus (EAV) have been studied extensively in our laboratory [245,246]. The 5'-terminal open reading frames (ORFs) 1a and 1b in the 12.7-kb EAV genome encode the replicase polyproteins pp1a (1727 aa) and pp1ab (3175 aa), with the latter being a C-terminally extended version of the former that is derived from a ribosomal frameshifting mechanism. Three ORF1a-encoded protease domains mediate cleavage of the replicase polyproteins into at least thirteen individual nonstructural proteins (nsps), which mostly accumulate in the perinuclear region of the infected cell. The key enzymes of the arterivirus RTC, and also the most conserved replicase functions among nidoviruses, are encoded in ORF1b and include an RNA-dependent RNA-polymerase (RdRp; nsp9) and helicase (HEL, nsp10). The ORF1a-encoded subunits nsp2, nsp3, and nsp5 contain trans-membrane regions that are believed to anchor the RTC to intracellular membranes and transform them into DMVs [65]. Expression of nsp2 and nsp3 induces the formation of very similar membrane structures and these proteins were therefore proposed to direct membrane pairing and vesicle formation [65,106]. As in the case of MHV [104], *de novo* made EAV RNA was found both associated with DMVs and in the surrounding cytosol [97].

Given the many unanswered questions regarding nidovirus RTCs and their supportive membranes, and in view of the major differences observed between coronavirus- and arterivirus-induced structures, we have now extended our ultrastructural analysis to EAV-infected cells. An additional advantage is that these samples can be processed for cryofixa-

tion without the need for a chemical prefixation, a biosafety prerequisite when working with SARS-CoV-infected cells. From a general point of view, cryo-immobilization is faster and has shown to provide better morphology and improved membrane contrast in a large variety of specimens [123]. Using direct cryofixation (CF) and a combination of advanced microscopy techniques, we have now performed an in-depth characterization of EAV-infected cells and established some striking parallels between arteri- and coronaviruses. For example, ET revealed that also the EAV-induced DMVs are connected with each other and integrated into a RVN of modified ER. Again co-localization of replicase products and dsRNA was limited, with the latter being present mainly inside DMVs whereas the nsps mainly localized to the membranes of the RVN. Semi-permeabilization experiments suggested that the interior of the dsRNA-containing vesicles is not accessible from the cytosol and that these structures thus appear to segregate the viral RNA. Finally, we explored electron spectroscopic imaging (ESI) to visualize and quantitate the RNA content of individual replication vesicles, and show that this technique may constitute a novel tool to study +RNA virus replication structures.

RESULTS

Time course analysis of replicase and dsRNA accumulation reveals minimal co-localization between viral enzymes and RNA

To investigate the accumulation of viral replicase and RNA, and to establish the most relevant time points for ultrastructural studies, we first studied EAV-infected Vero E6 cells using confocal immunofluorescence microscopy. In particular, we included an anti-dsRNA monoclonal antibody, an antiserum recognizing the nsp3 transmembrane protein, and a new rabbit antiserum recognizing the EAV RNA-dependent RNA polymerase (RdRp; [247]), a core subunit of the viral RTC. Cells were fixed at various time points after infection and immunolabeled (Fig. 1) to establish the time point at which the first signal appeared, its subcellular distribution, and the extent of colocalization of the different arterivirus markers used. Mock-infected control cells were used to confirm the high specificity of each of the three antibodies (Fig. 1A-C; left panels).

The first foci labeling for nsp3, nsp9, or dsRNA could be detected in the perinuclear area of infected cells by 3 h p.i. (data not shown) and by 4 h p.i. most cells were positive (Fig. 1A-C). Using cells fixed every hour from 0 to 15 h p.i., we measured labeling intensities and calculated averages per time point (Fig. 1D; Supplemental Fig. 1). In line with previous metabolic labeling experiments of viral RNA synthesis using [^{3}H]uridine, the 4 h p.i. time point was found to mark the start of an exponential increase of the amount of both dsRNA and EAV replicase (Fig. 1D). Both signals reached a plateau around 9 h p.i. and then slowly declined

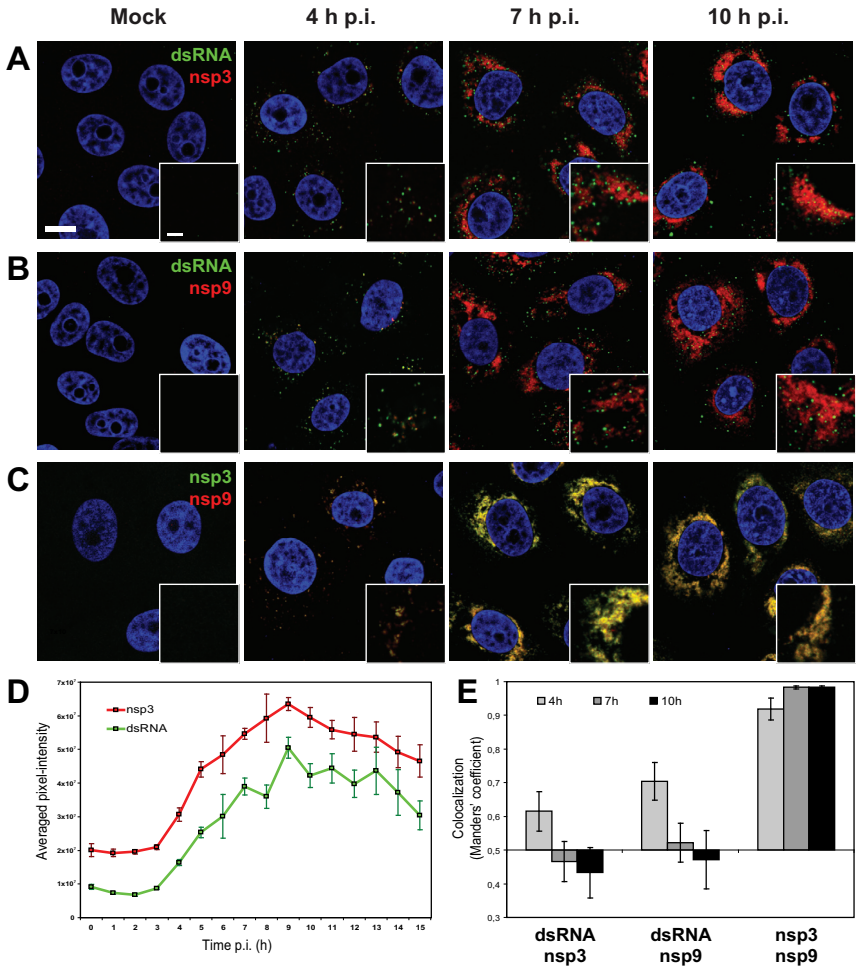


Figure 1. Immunofluorescence analysis of EAV-infected cells. EAV-infected Vero E6 cells were fixed at various time points after infection and processed for IF assays using rabbit antisera recognizing different replicase subunits and a mouse monoclonal antibody specific for dsRNA. Imaging was done using a confocal laser scanning microscope and quantification of labeling intensity was carried out using wide field fluorescence microscopy images. Scale bars represent 10 µm and 2.5 µm (insets). (A-C) Time-course dual-labeling IF assays for (A) dsRNA/nsp3, (B) dsRNA/nsp9, and (C) nsp3/nsp9. At 4 h p.i., the early signals for dsRNA and both nsps were found in close proximity of each other and partially overlapped. At later time points (here shown at 7 and 10 h p.i.), colocalization of dsRNA and either nsp was much less obvious, whereas the signals of nsp3 and nsp9 still colocalized almost completely. (D) Graph showing the total pixel intensities from images acquired from EAV-infected cells that were fixed every hour between 0 and 15 h p.i. The nsp3 and dsRNA signals were quantified from 5 low magnification images, taken with a 40x objective and each containing about 75 cells. For both nsp3 and dsRNA, the intensity of the signals started to increase exponentially between 3 and 4 h p.i. and peaked at 9 h p.i. (E) Graph showing the averaged Manders' overlap coefficients for dsRNA, nsp3, and nsp9, at 4, 7, and 10 h p.i. (n=25 cells per condition). By definition, Manders' overlap coefficients range from 0 to 1, representing full separation and complete co-localization of signals, respectively. We interpreted values above 0.5 as indicative of (a certain level of) co-localization, and values below 0.5 as indicative for a lack of co-localization.

during the final phase of infection (maximum titers of viral progeny were reached by 15 h p.i.; data not shown).

In particular between 4 and 7 h p.i., the labeling for nsp3, nsp9, and dsRNA became much more pronounced. Replicase subunits nsp3 and nsp9 accumulated in a dense perinuclear ring, whereas dsRNA labeling remained restricted to the same distinct foci observed at 4 h p.i. Compared to the latter time point, the number of dsRNA-positive foci had increased by 7 and 10 h p.i., although the labeling intensity of the individual foci was quite comparable (Fig. 1A-B; insets). The most striking observation was the fact that the co-localization of viral RdRp and dsRNA, two presumed key markers of active RTCs, was very limited (Fig. 1B), even during the early phase of infection, a finding resembling the previously observed separation between the bulk of viral replicase and dsRNA in SARS-CoV-infected cells [198]. Co-localization of nsps and dsRNA was quantified at three different time points by calculating the Manders' overlap coefficient (Fig. 1E; [232,248]) for each double labeling. By definition, its value ranges from 0 (full separation) to 1 (complete colocalization), and values above 0.5 are generally taken to signify (a certain level of) colocalization. Whereas overlap measurements for dsRNA and replicase, in particular nsp9, exceeded this threshold by 4 h p.i., values at later time points were around or even below 0.5. On the other hand, from the earliest moment of detection onward, the labeling patterns for nsp3 and nsp9 approached complete colocalization (Fig. 1E).

Our analysis established that in terms of viral replicase and dsRNA accumulation, and therefore likely also for the development of viral replication structures, the most relevant window for a detailed analysis is from 4 to 10 h p.i. Moreover, our data suggested an intriguing separation of the sites at which EAV replicase and dsRNA accumulate. This is obvious late(r) in infection, following abundant nsp synthesis from the rapidly accumulating genomic RNA, but essentially also applies at 4 h p.i. At that time point, both markers localized close to each other, but only a limited number of double-positive foci could be discerned (Fig. 1A-B).

High-pressure cryo-fixation reveals a compact core structure in EAV DMVs

Previous EM studies of EAV-infected cells identified paired membranes and DMVs as the most prominent virus-induced membrane structures, and the ER as the most likely platform for their generation [65,97]. In many electron micrographs in these older studies, the DMV interior was (largely) electron-lucent and, as experienced during our recent characterization of SARS-CoV-induced replication structures [100,198,240], these membrane structures may be fragile and their optimal preservation may be a technical challenge. In the case of SARS-CoV samples, biosafety considerations dictated a paraformaldehyde-based pre-fixation prior to CF and freeze substitution (FS). EAV-infected cells could be subjected to CF methods directly (i.e. without pre-fixation), which is generally believed to minimize fixation artifacts. Therefore, we explored and compared three different fixation techniques to deduce a suitable preservation protocol for EAV replication structures: chemical fixation with glutaraldehyde, CF by

plunge-freezing, and high-pressure freezing (HPF). As described in Material and Methods, all samples were stained, dehydrated, and embedded in an epoxy resin and 100-nm thin sections were used for an EM analysis at 80 keV.

In 7 h p.i. samples, all fixation protocols revealed the presence of typical EAV DMVs (Fig. 2A-C), which were not found in mock-infected cells. Although the tightly apposed double membranes could be recognized in each of the three specimens, membrane contrast was clearly superior in cryo-fixed cells, thus facilitating the straightforward visualization of both bilayers (Fig. 2B-C; insets). Chemical fixation suggested that the DMV interior consists of a web of undefined filaments (Fig. 2A), whereas DMVs in plunge-frozen samples had a more granular interior (Fig. 2B), similar to what was previously observed for SARS-CoV DMVs [100]. Although plunge-freezing is generally considered to be an adequate CF procedure, samples are prone to local freeze damage due to ice crystal formation. High-pressure freezing, *i.e.* limiting ice-crystal expansion by pressurizing samples to ~2000 bar prior to freezing, is believed to minimize this problem [129,130]. When using an HPF protocol, we indeed noticed that the overall ultrastructural preservation of EAV-infected cells was significantly improved compared to plunge-frozen samples, resulting in a denser cytoplasm due to the lack of segregation artifacts (compare Fig. 2B and 2C). In the plunge-frozen samples membrane contrast may be more appealing to the untrained eye, due to the more "empty" appearance of the surrounding intracellular space, but this effect is probably caused by the ice crystal-driven deformation of the cytosol. Interestingly, only in HPF samples the DMV interior was visualized as an electron-dense, roughly spherical mass, which was separated from the inner DMV membrane by an electron-lucent "halo", with the exception of one side of the structure touching the inner DMV membrane. This compact core structure (diameter 30-100 nm; Fig. 2C) was never observed in cells that had either been chemically fixed or plunge-frozen (Fig. 2A-B).

In summary, the overall morphology of both cellular organelles and EAV replication structures appeared improved by the use of CF without pre-fixation. Each of the three fixation methods tested could visualize the double membranes of the EAV-induced structures, but the ultrastructural details of the DMV core were different for each technique. We cannot formally exclude the possibility that the striking electron-dense DMV cores revealed upon HPF (Fig. 2C) are an artifact. However, the general consensus that HPF is the most advanced EM preservation technique and our own ultrastructural comparisons (Fig. 2) provided a clear basis to use the HPF protocol in our subsequent EM experiments.

EAV replicates in association with a reticulovesicular network of modified endoplasmic reticulum

Previously, in conventional transmission EM studies, the outer membrane of EAV DMVs was occasionally found to be continuous with ER membranes [65,97]. Because these connections

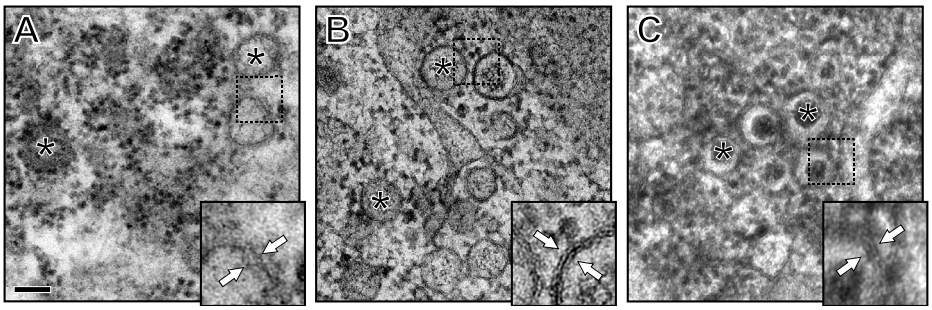


Figure 2. Comparison of DMV morphology after different fixation procedures. EAV-infected Vero E6 cells were fixed at 7 h p.i. using different fixation methods to assess the most suitable preservation protocol for the EAV-induced membrane structures. Asterisks indicate the interior of selected DMVs. Scale bar represents 100 nm. (A) Chemical fixation with 1.5% glutaraldehyde and, subsequently, 1% osmium tetroxide in 0.1 M sodium cacodylate buffer. The contrast of DMV membranes is relatively poor and the double membranes are difficult to discern. The DMV interior shows an undefined appearance. (B) Cryo-fixation by plunge freezing followed by FS in 1% osmium tetroxide, 0.5% uranyl acetate, and 10% H_2O in acetone. The lipid bilayers of DMVs are recognizable and the DMV interior has a more granular appearance. As a result of ice crystal formation, the cytosol surrounding the DMV cluster contained electron-lucent areas. (C) Cryo-fixation by HPF, followed by FS in 2% osmiumtetraoxide, 1% glutaraldehyde, and 10% H_2O in acetone. Overall, membrane-contrast was high and the cytosol was free of freezing artifacts. The interior of DMVs prepared by HPF was visualized as an electron-dense core that is surrounded by an electron-lucent halo.

were only rarely observed, this morphology was postulated to represent an intermediate stage of DMV formation, after which outer membrane fission would occur to release a separate vesicular structure that is bound by a double membrane [97]. For coronaviruses, using electron tomography (ET)-based 3-D reconstruction, we could recently show that DMV outer membranes are connected with each other and with the ER. Accordingly, coronavirus DMVs were concluded to be integrated into a reticulovesicular network that also includes convoluted membranes [198]. ET was now applied to EAV-infected cells (Fig. 3-5) to evaluate the presence of a similar network of structures.

EAV-infected Vero E6 cells were high-pressure frozen at 4, 7, and 10 h p.i. and samples were freeze-substituted and embedded in an epoxy resin. Serial 200-nm thick sections were cut to analyze the EAV replication structures in successive sections cut from the same cell. This approach was particularly useful when searching for replication structures in early samples (4 h p.i.), when only small DMV clusters were present (Fig. 3A). This technique also allowed us to produce tomograms from the same relative position, i.e. the central region of replication compartments, in samples fixed at different time points after infection. At 4 h p.i., clusters of DMVs were distributed throughout the cytoplasm (Fig. 3B; depicted in brown). They were often observed in close proximity of ER cisternae (Fig. 3B; beige) and, occasionally, near bundles of actin filaments (Fig. 3B; purple). By 7 h p.i., the number of vesicles per cluster had dramatically increased (Fig. 3C-D) and the dimensions of the replication compartments extended beyond the volume of our tomograms (2.5 x 2.5 x 0.2 µm). Nevertheless, our data offered a unique 3-D view of the central space of the EAV replication structures.

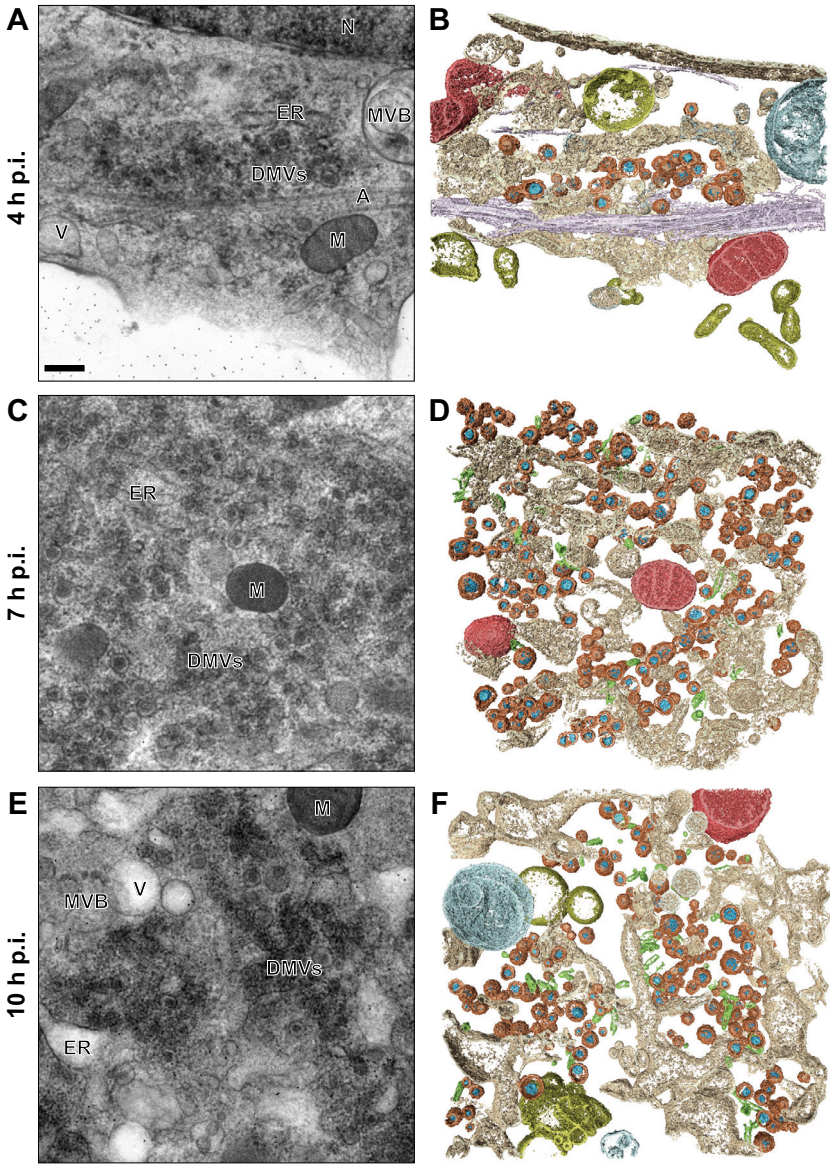


Figure 3. Electron tomography of cytoplasmic areas containing EAV-induced DMVs. EAV-infected Vero E6 cells were high-pressure frozen at (A-B) 4, (C-D) 7, and (E-F) at 10 h p.i. and processed for dual-axis electron tomography to obtain 3-D reconstructions of relevant cytoplasmic areas. Scale bar represents 250 nm. (A,C,E) The left panels show the 0°-tilt transmission EM images of 200-nm-thick resin-embedded sections. 10-nm gold particles were layered on top of the section and were used as fiducial markers during the tomogram alignment. (B,D,F) The right panels show the 3-D surface rendered models of the tomograms that were derived from the left panels. The models illustrate the cytoplasmic content near the vesicles and the clustering of DMVs. Along with DMVs (brown), cores (blue), ER (beige), EAV sheets (green), mitochondria (M; red), smooth walled vesicles (V; yellow), multivesicular body (MVB; blue-grey), and actin filaments (A; purple) are depicted.

By 7 h p.i., in addition to the developing virus-induced membrane compartments, unusual tubular structures (Fig. 3D-F; depicted in green; Video S1) were observed in their immediate vicinity. These tubules were described previously in arterivirus-infected cells [249-251] and were proposed to be induced by the virus infection. Specifically, their formation was found to be linked to the expression of the viral nucleocapsid (N) protein [112], which rapidly increases from 7 h p.i. onwards. Since it was previously established that the arterivirus N protein is not required for viral RNA synthesis [252], we will discuss these tubules separately in one of the next paragraphs (see also Fig. 8). Besides the tubules, cytoskeleton elements, and abundant ER cisternae, mitochondria were frequently observed in close proximity of DMVs (Fig. 3; depicted in red). By 10 h p.i., the ER of EAV-infected Vero E6 cells had become dilated, which appeared to promote the dispersal of both DMVs and tubules (Fig. 3E-F).

A detailed analysis (Fig. 4; Video S1) of HPF-derived membrane structures revealed both important differences (in addition to DMV diameter) and striking similarities with coronavirus replication structures. The outer membranes of EAV DMVs are continuous with rough ER membranes (Fig. 4B and 4F), each other (Fig. 4C), or paired membrane structures (Fig. 4D). These connections were sometimes hard to visualize in HPF samples, due to the lower membrane contrast, but they were readily observed when ET was applied to plunge-frozen EAV infected Vero-E6 cells (Video S2). Typically, these membrane continuities consist of tightly apposed membranes, similar to those previously described for coronaviruses [198,235]. However, the large CM clusters found in coronavirus-infected cells were not observed in the case of EAV infection. The presence of ribosomes on the cytosolic face of EAV DMVs (Fig. 4E; arrows) strongly suggested that their outer membranes are indeed derived from rough ER. Occasionally, both cytosolic surfaces of curved double-membrane sheets (similar to those shown in Fig. 4D) were found to be decorated with ribosomes (data not shown).

For DMVs that were entirely or largely included in the volume of our tomograms, we measured their maximum diameter. Throughout infection, both the average DMV diameter (92±21, 94±20, and 94±27 nm at 4, 7, and 10 h p.i., respectively) and the DMV size distribution were essentially constant (Fig. 5). Also the average diameter of DMV cores did not differ significantly between the time points analyzed (52±14, 49±14, and 51±18 nm at 4, 7, and 10 h p.i., respectively). The diameters of DMV core and entire DMV appeared to be directly correlated (Fig. 5B, 5D, and 5F), with larger DMVs containing a relatively larger electron-lucent "halo-like" space between DMV inner membrane and electron-dense core (Fig. 4A). In all DMVs, at least one side of the core structure touched the inner membrane, although fibrillar structures crossing to the other side of the DMV's inner vesicle were also seen (see e.g. Fig. 4B and 4E).

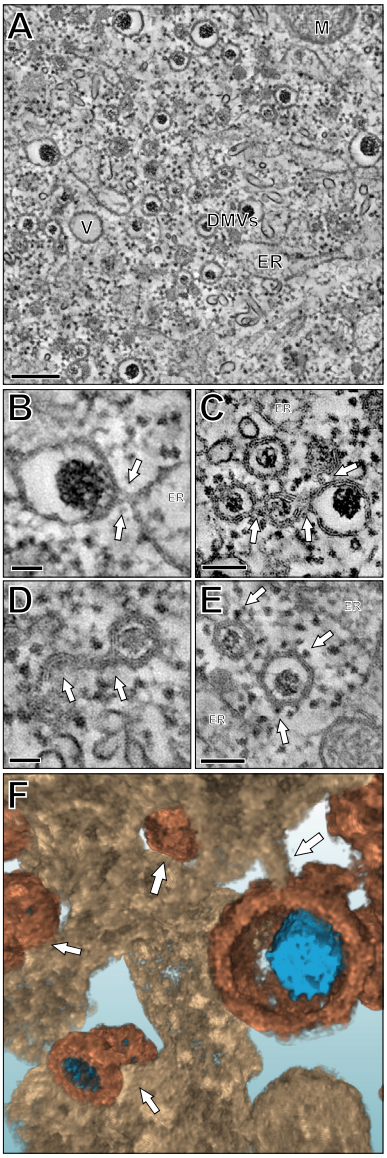


Figure 4. Electron tomography of the EAV-induced reticulovesicular membrane network. EAV-infected Vero E6 cells were high-pressure frozen at 8 h p.i. and processed for dual-axis electron tomography to obtain 3-D reconstructions. (A) A 5-nm thin digital slice running through the middle of the reconstructed tomogram showing DMVs in the vicinity of the ER, smooth-membrane vesicles (V), and mitochondria (M). Scale bar represent 500 nm. (B-E) Close-ups from the tomogram shown in panel A. The arrows indicate connections of DMV outer membranes with the ER (B), other DMVs (C), and curved double-membrane structures (D). Ribosomes were found to decorate the surface of the outer DMV membrane (E; arrows). Scale bars represent 50 nm (B, D) and 100 nm (C, E). (F) Direct-volume rendered reconstruction from a small part of the tomogram shown in panel A highlighting DMVs (brown), DMV cores (blue), and the ER (beige). The arrows point to several neck-like structures that connected the DMV outer-membrane with the ER (see also Video 1).

EAV DMV cores contain both dsRNA and replicative enzymes

Subsequently, iEM was used to confirm the association of the viral replication machinery with the network of EAV-induced double-membrane structures described in the previous paragraph (Fig. 6). Previously, DMV membranes were found to modestly label for nsp2 and nsp3 [97], the two membrane proteins that suffice to induce double-membrane structures [65]. In specimens prepared according to our new FS protocol, DMV membranes again labeled for nsp3 and also the tightly apposed membranes in their vicinity contained a substantial amount of label (Fig. 6A). A similar pattern was obtained using an antiserum recognizing the nsp7-8 region (Fig. 6B), which recognizes a large number of replicase processing intermediates [253], including the abundant nsp5-8 and nsp5-7 products that contain a major hydrophobic domain in the form of nsp5. Newly produced antisera also allowed the immuno-detection of two of the ORF1b-encoded viral enzymes, the nsp9 RdRp (Fig. 6C) and the nsp11 endoribonuclease (Fig. 6D), which both were abundantly associated with DMV membranes and surrounding membrane structures. Only small amounts of label appeared to be present on the interior of DMVs (Fig. 6B-D; black arrows). Together, these data indicated that both membrane-modifying and enzymatic subunits of the EAV replicase are associated with the virus-induced membrane network, but that only a small fraction of these proteins is associated with the electron dense DMV core.

To analyze the RNA component of RTCs as well, we labeled the sections for dsRNA (Fig. 6E). As in the case of SARS-CoV-infected cells [10], the dsRNA labeling in EAV-infected cells

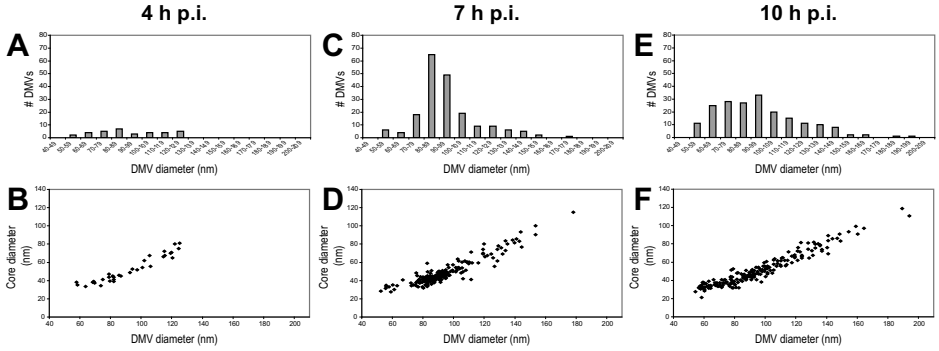


Figure 5. Size distribution of EAV-induced DMVs and their cores. All DMVs within the tomograms shown in Fig. 3 were delimited *in silico*, counted, and measured in the x and y direction to derived average diameters of complete DMV and DMV core. If the equator of an individual DMV was present within the tomogram volume, a sub-volume of 250 (x) by 250 (y) by 10 (z) pixels was extracted from the central part of the DMV and merged into a single image representing a 12-nm thin section through the middle of the DMV. (A,C,E) DMV numbers from tomograms acquired at 4, 7, and 10 h p.i. were plotted against the average (x,y)-diameter, determined as described above. (B,D,F) Graph showing the correlation between the average (x,y)-diameter of individual DMVs (x-axis) and the corresponding averaged (x,y)-diameter of the DMV cores (y-axis).

was almost exclusively associated with the interior of the DMVs (Fig. 6E; black arrows). At first glance, some of the label appeared to localize outside the DMV core (Fig. 6E), but in these cases ET analysis of serial sections revealed an association with the contents of "obscured DMVs" that had been cut tangentially and, for the most part, resided in an adjacent section (data not shown). Thus, in addition to containing small amounts of different replicase subunits, EAV DMV cores were found to be the primary site of dsRNA accumulation.

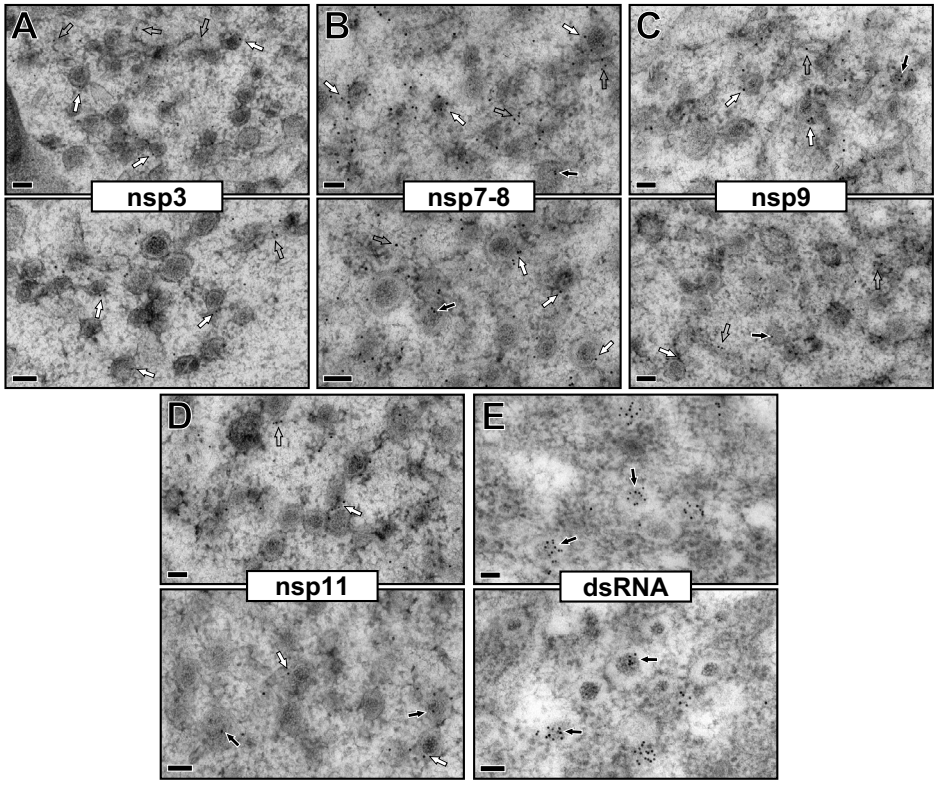


Figure 6. Immuno-gold EM of EAV replicase and dsRNA in infected cells. EAV-infected Vero E6 cells (7 h p.i.) were high-pressure frozen and processed for FS and iIEM (see Materials and Methods). In all labelings, 10-nm colloidal gold particles conjugated to protein A were used for detections of the primary antibodies. Scale bars represent 100 nm. (A-D) Immuno-labeling with antisera recognizing different EAV replicase subunits, respectively, nsp3 (transmembrane protein), nsp7-8 (which is present in several trans-membrane protein containing replicase cleavage products, nsp9 (the EAV RdRp), and nsp11 (the EAV endoribonuclease). Label was predominantly found on DMV membranes (white arrows) and surrounding membranes (transparent arrows) and occasionally on DMV cores (black arrows). (E) Immuno-labeling for dsRNA, showing extensive clustering of label on DMV cores (black arrows).

EAV DMVs are closed compartments that protect double-stranded RNA from RNAse digestion

As outlined in the introduction, several +RNA virus replication structures have been characterized as spherular membrane invaginations whose interior is connected to the cytosol. On the other hand, in spite of an extensive ET analysis, such connections could not be identified in the case of the SARS-CoV-induced DMVs [198]. We therefore scrutinized EAV-induced DMVs (n=888; from five different tomograms representing four different time points after infection) for the presence of membrane discontinuities (diameter > 4 nm) that might constitute a connection to the cytosol. For at least 91% of these vesicles both membranes appeared to be fully intact, but some of the larger vesicles showed membrane discontinuities that could be interpreted as connections to the cytosol (Supplemental Fig. 2A-D). On the other hand, the fact that similar openings were occasionally detected in the membranes of host cell organelles like the ER (Supplemental Fig. 2E-F) suggests they are more likely explained by technical issues like membrane fragility, freeze damage, and/or staining artifacts.

As an alternative approach to probe whether the interior cavity of EAV DMVs constitutes a closed, dsRNA-containing compartment, we employed semi-permeabilization of infected cells with saponin in combination with nuclease digestion. EAV infected Vero E6 cells were fixed at 7 h p.i. in NaPi-buffer containing 3% paraformaldehyde (PFA), a procedure previously reported to prevent permeabilization of the plasma membrane [254,255]. Subsequently, cells were semi-permeabilized with increasing concentrations of the mild detergent saponin, which at low concentrations only affects the plasma membrane. Next, semi-permeabilized cells were incubated for 1 h with mouse monoclonal antibodies recognizing the cytosolic protein β-tubulin (Fig. 7A), the luminal ER marker PDI (Fig. 7B), or dsRNA (Fig. 7C). At the same time, these specimens were co-stained with a polyclonal rabbit antiserum recognizing the cytosolic C-terminal domain of EAV nsp3 (Fig. 7A-C). After extensive washing, cells were again fixed with 3% PFA and then fully permeabilized with 0.1% Triton X-100 (TX-100). Finally, cells were incubated with fluorescent anti-mouse IgG and anti-rabbit IgG conjugates, to reveal whether primary antibodies have bound to their target when the cells were in the semi-permeabilized state. Cells were analyzed with a confocal laser scanning microscope. Non-permeabilized cells and cells that were fully permeabilized with TX-100 right away served as negative and positive controls, respectively.

Contrary to our expectations, but possibly due to the infection process, the plasma membrane of the PFA-fixed, non-permeabilized cells was found to be quite leaky. Abundant labeling for cytosolic β-tubulin and the cytosolic domain of EAV nsp3 could be observed (Fig. 7A), although the use of higher concentrations of saponin (or the TX-100 used as positive control) did enhance the labeling intensity. This technical complication did not prevent an analysis of dsRNA-containing membrane structures since in cells not treated with saponin the membrane of an intracellular compartment like the ER had apparently remained intact.

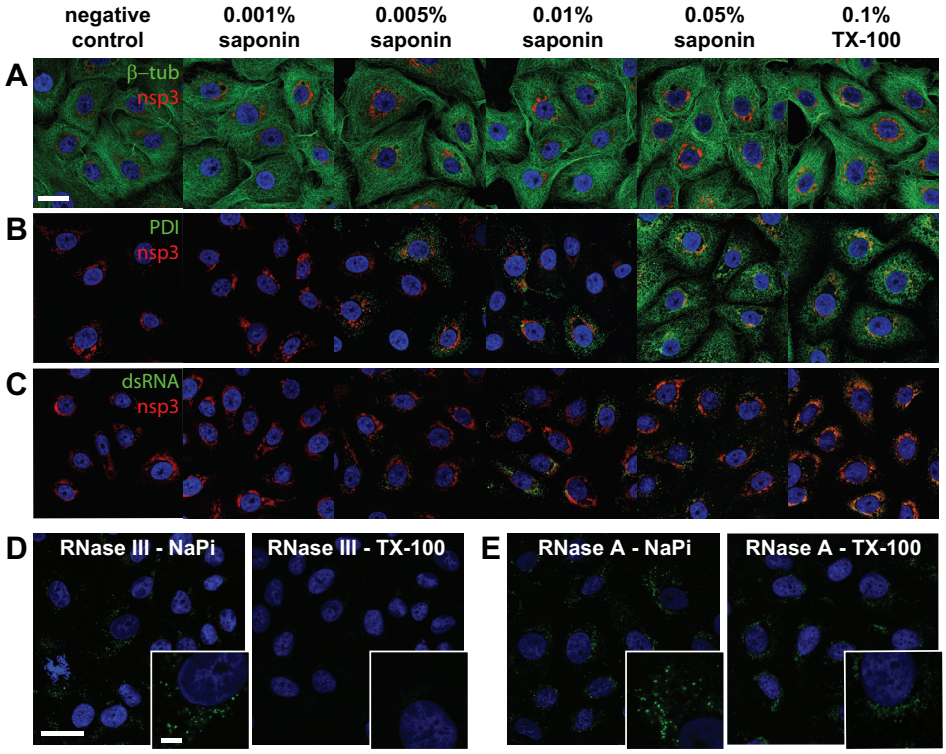


Figure 7. Accessibility of dsRNA in semi-permeabilized infected cells EAV-infected cells were fixed at 7 h p.i. in NaPi-buffer containing 3% paraformaldehyde. This fixation was previously reported to leave the plasma membrane intact [254], although in our experiments considerable permeabilization was observed, possibly as a side-effect of infection. Scale bars represent 25 µm and 5 µm (insets). (A-C) In order to determine whether antigens are accessible from the cytosol, infected cells were semi-permeabilized with increasing concentrations of saponin. Untreated and fully TX-100-permeablilized cells served as negative and positive controls, respectively. After detergent treatment, cells were simultaneously incubated with mouse- and rabbit antisera recognizing (A) β-tubulin/nsp3, (B) PDI/nsp3, or, (C) dsRNA/nsp3. After washing, cells were fully permeabilized with TX-100 and incubated with fluorescent anti-rabbit (cy3) and anti-mouse (Alexa488) secondary antibodies. (A) Labeling for the cytosolic markers β-tubulin and nsp3, which revealed plasma membrane permeability without detergent treatment, although further permeabilization did improve signal intensity. (B) Labeling for the luminal ER protein PDI required treatment with at least 0.05% saponin for 10 min, indicating that this detergent concentration was needed to permeabilize the ER membrane. (C) As in the case of PDI, also labeling for dsRNA required a 10-min treatment with 0.05% saponin, suggesting that the dsRNA is protected by cytoplasmic membranes and not directly accessible from the cytosol. (D-E) Paraformaldehyde-fixed EAV-infected cells were left untreated or permeabilized with TX-100. Subsequently, samples were incubated with RNase III or RNase A, which specifically degrade dsRNA and ssRNA, respectively. Next, cells were again fixed with 3% PFA to prevent further RNase activity and permeabilized with 0.1% TX-100 to allow immuno-labeling of any remaining dsRNA. (D) Whereas cells not treated with detergent still labeled for dsRNA after RNAse III digestion, this signal was lost upon prior permeablization with TX-100, indicating that cytoplasmic membranes protect dsRNA from nuclease activity. (E) When cells were treated with RNase A rather than RNAse III, dsRNA was detected in both untreated and TX-100-permeabilized cells. Although the labeling intensity was slightly reduced in the latter, this control experiment corroborated the specificity of the RNase III treatment used in panel D.

PDI labeling could not be detected unless at least 0.005% saponin was used (Fig. 7B) and, as expected on the basis of our ET-analysis, also the labeling for dsRNA became visible only after treatment with that same saponin concentration (Fig. 7C). The latter result suggested that EAV DMVs are closed structures, or at least compartments not accessible to molecules with the dimensions of immunoglobulins (about 14 by 10 by 4.5 nm; [256]).

To confirm the above findings, we tested whether the dsRNA in the not saponin-treated, but leaky cells was protected against the activity of *E. coli* RNase III, a 26-kDa nuclease specific for dsRNA. Indeed, dsRNA was still detectable in these cells after a 2-h RNAse III treatment, whereas all signal was lost in control cells permeabilized with 0.1% TX-100 (Fig. 7D). As a specificity control, treatment with bovine pancreatic RNAse A (14 kDa) was used and found to have no effect on the dsRNA labeling in either semi- or fully permeabilized cells (Fig. 7E). Together with our ET analysis, these results strongly suggest that EAV-induced DMVs are closed compartments, or at least lack the connections to the cytosol with a diameter in the order of 10 nm, as they were observed for the replication compartments of various other groups of +RNA viruses [36,38].

EAV-induced cytosolic tubules contain the viral nucleocapsid protein

In our tomograms of EAV-infected cells fixed at 7 h p.i. or later (Fig. 3 and 4), we observed tubular structures in close proximity of DMVs. As discussed above, previous arterivirus studies suggested that these tubules contain the viral N protein. In particular, Wieringa and co-workers described the absence of the tubule formation in cells transfected with RNA of an EAV mutant lacking a functional N protein gene [112]. Nonetheless, EAV N protein overexpression, in the absence of infection, did not induce similar tubules, suggesting a requirement for additional infection-related factors.

To further analyze the origin and ultrastructure of the EAV-induced tubules, immunofluorescence microscopy was used to establish that N protein expression and tubule formation indeed coincide. Vero E6 cells fixed at various time points after infection were double-labeled for nsp3 and N, and analyzed by laser scanning confocal microscopy (Fig. 8A). At 4 h p.i., nsp3 signal was visible in most of the infected cells, however, N protein was not yet detectable in any of them (Fig. 8A). At 7 h p.i., the N protein-labeling intensities varied between cells, probably reflecting a certain asynchronicity of infection. As documented previously [252], in cells still containing little N protein, the signal overlapped with nsp3, a marker for the replication structures (Fig. 8A). Cells in which infection was more advanced (Fig. 8A) also showed N protein accumulation in the rest of the cytoplasm, where the protein may be present in soluble form or as part of newly assembled virions.

With our iEM protocols, the EAV-induced tubules were clearly visible and immuno-gold labeling showed that the tubules contain N protein (Fig. 8B-C; black arrows), whereas a small fraction was found in close association with DMV membranes (Fig. 8B; white arrows). Next,

we analyzed the tubules in 8 h p.i. tomograms and found that they are actually sheets that locally curve into tubules (Fig. 8D-E; black arrows; Video S1). Compared to the clearly visible DMV and host cell membranes, the ultrastructure of the sheets was different and always

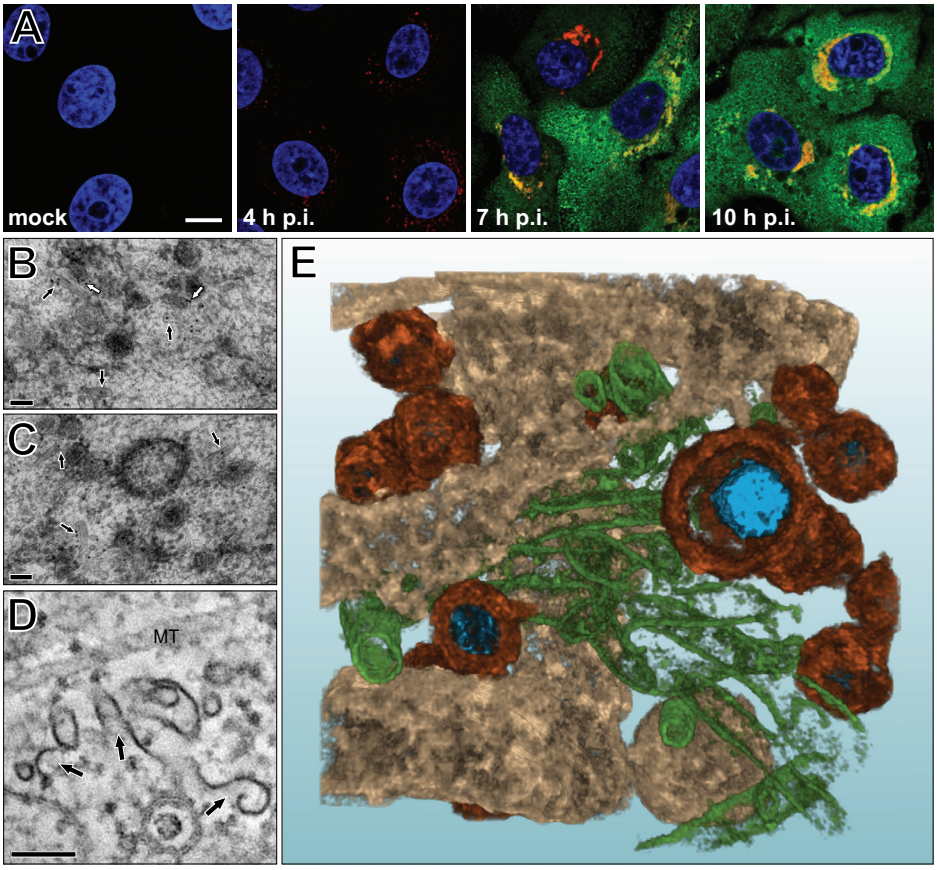


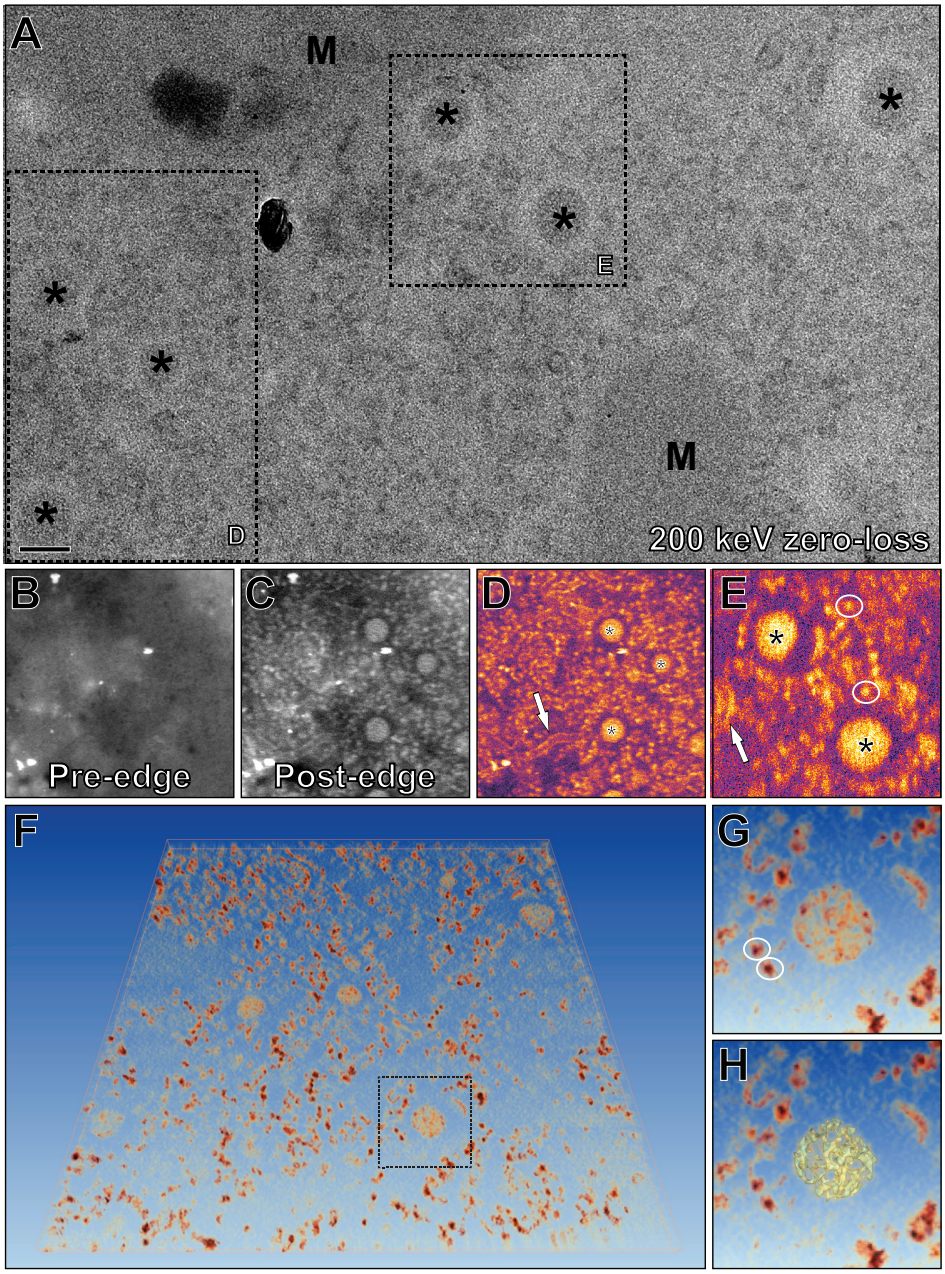
Figure 8. Nucleocapsid-protein containing structures are intertwined with EAV-induced replication structures. (A) EAV-infected Vero E6 cells were fixed at various time points after infection, processed for IF microscopy using a dual labeling for nsp3 and N protein, and analyzed by confocal laser scanning microscopy. By 4 h p.i., nsp3 signal was visible in most of the infected cells, but N protein was not yet detectable. Although the intensity varied between cells, N protein signal became detectable in most cells by 7 h p.i. and partially overlapped with nsp3 signal. By 10 h p.i., N protein had become distributed throughout the cytoplasm of infected cells. Scale bar represents 10 µm. (B-C) EAV-infected Vero E6 cells were high-pressure frozen at 8 h p.i., processed for FS, and immuno gold-labeled for the N protein. The majority of the label was found to be associated with EAV-induced tubular structures (black arrows) and DMVs (white arrows). Scale bars represent 100 nm. (D) EAV-infected Vero E6 cells were high-pressure frozen at 8 h p.i. and processed for dual-axis electron tomography (see also Fig. 4). This 5-nm thin slice illustrates the relatively high electron density of the EAV-induced sheets and tubules when compared to *e.g.* a microtubule (MT) present in the same section. Arrows indicate local openings in tubules and curved protein sheets. Scale bar represent 100 nm. (E) 3-D ET reconstruction illustrating the distribution and architecture of the EAV tubules (depicted in green) and their proximity to the DMVs (depicted in brown; with cores depicted in blue and the ER in beige).

showed a single electron-dense layer rather than the well-known bilayer profile of a lipid membrane. This strongly suggested that these structures, which are closely associated with the EAV-induced RVN, constitute protein sheets and tubules rather than membranes (Fig. 8E).

Visualization and quantification of the RNA content of DMV cores by electron spectroscopic imaging

Few quantitative data are available on the RNA and protein content of +RNA virus replication structures [36,38,47,244]. Using replicon cell lines and a combination of biochemical techniques, Quinkert et al. [47] concluded that hepatitis C virus establishes about 100 replication complexes per cell, requiring (at best) only a few percent of the available nonstructural proteins. For FHV replication structures, Kopek and coworkers [36] quantified the RNA and protein content biochemically and related these measurements to the number of spherules per cell (estimated to be 20,000 ± 11,000). They derived an overall estimate of the RTC composition, but these biochemical approaches do not allow the analysis of individual replication structures. In a first attempt to address this issue, we applied the EM-based method of electron spectroscopic imaging (ESI) to the EAV-induced DMVs. This EM technique is based on imaging only with inelastically scattered electrons that suffer a specific energy loss as a result of collisions with electrons in the specimen [257]. The magnitude of this energy loss is element-specific and can be used to derive a so-called elemental map that reveals the concentration of a given element in the specimen. Recently, ESI has been successfully applied to biological samples, for example to visualize the distribution of nucleic acids and proteins within the cell's nucleus based on the signals for phosphorus and nitrogen, respectively [258-260].

Based on our dsRNA labeling (Fig. 6E), we expected DMV cores to contain large amounts of RNA and, thus, phosphorus (P), an element with a relatively low abundance in the protein component of ribonucleoprotein complexes [259]. Thus, we explored whether ESI could be used to visualize DMV cores and assess their RNA content on the basis of the P signal. EAV-infected cells were high-pressure frozen at 8 h p.i. and freeze-substituted in acetone containing 1% glutaraldehyde. Contrasting agents were omitted to prevent background signal in our elemental maps and, because of the very low contrast in these unstained specimens, 60-nm thick sections were first scrutinized for the presence of EAV DMVs using an EM running at 80 keV. After image acquisition at different magnifications from an area rich in DMVs, the grid was transferred to a 200-keV EM equipped with a post-column electron image filter. The 80-keV images were used to retrieve the area of interest and a zero-loss image at 200 keV was acquired, based only on electrons not encountering any collisions (Fig. 9A). Although the contrast was very low, DMVs were easily recognized by their cores, which were clearly visible in these images (Fig. 9A; asterisks). Next, P maps were acquired by calculating the ratio between the pre- (Fig. 9B) and post-edge images (Fig. 9C), which reflect the electrons that encountered background scattering and phosphorus-specific scattering, respectively (see Materials and


A
M
M
D
E
200 keV zero-loss
B
Pre-edge
C
Post-edge
D
E
F
G
H

Methods for more details). In these P maps, DMV cores were easily distinguishable (Fig. 9D-E; asterisks) and were found to indeed contain a large amount of P. Surprisingly, also the characteristic N protein-containing tubules showed up in the P-maps (Fig. 9D-E; arrows).

Since the average EAV DMV core diameter of about 50 nm was close to the thickness of our sections (60 nm), most cores were not entirely included in our sections and spherical caps of variable size were missing. Therefore, to estimate the RNA content of individual DMV cores, we measured the P signal of those cores that contained a clear electron-lucent halo and thus contained most or all of the original core volume (see the cores marked with an asterisk in Fig. 9D-E). Ribosomes, which were clearly visible in the cytosol (Fig. 9G; circles) were used to calibrate the P measurements on the basis of their known RNA content [258,259]. After correction for background signal, the P measurements of 11 DMV cores were compared to the averaged P signal measured for 25 ribosomes, each containing 7,128 nucleotides of ribosomal RNA [261]. Our calculations indicated that these 11 cores contained 0.9 to $3.5*10^5$ P atoms, with an average of $1.7*10^5$, the equivalent of about 13 EAV genomes. In order to visualize the P distribution within the DMV cores, we acquired electron spectroscopic tomograms to derive 3-D P maps (Fig. 9F-H; Video S3; [258]). This revealed thread-like structures that did not appear to extend into the cytosol (Fig. 9G-H). The ESI ET analysis revealed that, compared to DMV cores, the density of the P signal was higher in ribosomes (Fig. 9F), suggesting that ribosomal RNAs are packed more densely than the RNA within the EAV-induced DMVs. Clearly, a more extensive structural characterization of DMV cores is required, including ESI experiments targeting their protein content, but in any case the first application of ESI to nidovirus-infected cells established the potential of this novel tool to investigate both structure and composition of +RNA viral replication structures.

Figure 9. Visualization of RNA inside EAV-induced DMVs by electron spectroscopy imaging-based phosphorus mapping. EAV-infected cells (8 h p.i.) were high-pressure frozen and freeze-substituted. Contrast-rich maps of DMV-containing areas in 75-nm thin sections were made at 80 keV to subsequently retrieve the same areas in a microscope running at 200 keV (when significantly less contrast can be obtained). Scale bar represents 100 nm. (A) 200 keV zero-loss image showing part of the EAV-infected cytoplasm containing DMV cores (asterisks) and mitochondria (M). Phosphorus elemental maps were obtained by acquisition of pre- (B) and post-edge images (C) at 120 and 157 eV electron loss, respectively, with a 15 eV slid-with. Phosphorus maps (D-E) were derived from the highlighted areas in panel A by calculating the ratio between the pre- and post-edge intensities, which clearly revealed the P content of DMV cores (asterisks), ribosomes (encircled), and EAV N protein-containing tubules (arrows). (F) An ESI tomogram was recorded at the P energy edge and direct volume rendering was used to visualize the P content in 3-D. (G) Besides the abundant ribosomes (encircled), the cores of EAV-induced DMVs were clearly visible. (H) DMV core high-lighted with an isosurface, suggesting a thread-like ultrastructure of the RNA content inside.

DISCUSSION

Reshaping the endoplasmic reticulum to accommodate arterivirus RNA synthesis

The in-depth dissection of ultrastructural changes in infected cells is an important starting point for understanding how +RNA viruses use and modify cellular infrastructure to create an environment that is optimally suited for their genome replication and gene expression. Ultrastructural studies can define a spatial and temporal framework to integrate cell biological and biochemical data from infected systems and thus contribute significantly to our overall understanding of the replicative cycle of +RNA viruses. The analysis of the biogenesis and function of +RNA virus replication structures is critical to assess parallels and differences between virus families and may reveal opportunities to develop novel antiviral strategies.

SARS-CoV and mouse hepatitis virus (MHV) are the best-studied coronavirus models and the ultrastructure of cells infected with these viruses has been investigated in some detail [100-104,198,235,262]. The only ET analysis of coronavirus replication structures thus far, i.e. that of SARS-CoV, established that DMVs are not isolated membrane vesicles but are part of a reticulovesicular network (RVN) that is continuous with CM and the ER membrane donor [198]. It should be mentioned that, over the years, a number of – at times contradictory – reports implicated alternative cellular organelles in coronavirus RNA synthesis, including endosomes, autophagosomes, and specific subcompartments of the secretory pathway [105,107,167,226,263]. Whereas the CM seemed to contain the bulk of the replicase proteins [198,235], dsRNA was found inside DMVs, thus revealing a paradoxical localization difference between the coronavirus replicase and the dsRNA it produces [198].

In the present study, the combination of HPF and ET was used to define the 3-D architecture of an EAV-induced RVN of modified ER, which includes much smaller but again interconnected DMVs with an electron-dense inner core structure (Fig. 2 and 4). Despite the ~2.5-fold smaller size of arterivirus-induced DMVs and the apparent absence of CM, striking parallels were observed with coronavirus replication structures [198,240]. These included the general DMV morphology, the presence of ribosomes on DMV outer membranes (Fig. 4C-E), the connectivity of DMV outer membranes with each other and the rough ER (Fig. 4), and their immuno-labeling properties, in particular the abundant presence of signal for dsRNA (Fig. 6). The finding that all DMVs have neck-like connections with the ER confirms previous observations during conventional EM studies [97], which were the basis for the hypothesis that these ER-connected DMVs represent an intermediate stage in the formation of fully detached DMVs. However, our present ET data strongly suggest that such a membrane fission event does not occur (Fig. 4E, Video S2), a conclusion supported in particular by our ET analysis in which each DMV outer membrane was found to have at least one connection to another RVN membrane structure. Arteriviruses thus appear to belong to the +RNA virus

groups that induce an elaborate network of modified ER membranes, as also documented for coronaviruses [198], flaviviruses [38,41], hepatitis C virus [45], and picornaviruses [156]. By 10 h p.i., the ER of EAV-infected Vero E6 cells became dilated, as also documented for the late stages of SARS-CoV infection in the same cell line [198]. The densely concentrated DMV clusters dispersed into smaller clusters that stayed in close proximity of ER membranes and EAV-induced tubules (Fig. 3E-F). The morphology of individual DMVs at 10 h p.i. seemed indistinguishable from those found at earlier time points. Contrary to the late stages of SARS-CoV infection, we did not observe the formation of "vesicles packets", dilated outer membrane sacs containing of up to a few dozen DMV inner vesicles [198].

As previously reported for picornaviruses [49,121], the use of HPF can dramatically alter the appearance of viral replication structures like DMVs. In the case of EAV, the use of HPF had a major impact on the appearance of DMVs (Fig. 2), which were found to contain an electron-dense core that was not observed after conventional chemical fixation or plunge freezing. By iEM, we established that the labeling for dsRNA (Fig. 6E) as well as some labeling for the viral RdRp (Fig. 6C) were associated with these cores, although the vast majority of the RdRp labeling was found on the surrounding RVN membranes. All EAV replicase subunits that could be analyzed by iEM in this study were associated with both DMV membranes and the other interconnected membranes structures of the RVN. Strikingly, convoluted membranes like those previously found to carry large amounts of coronavirus nsps [198,235] were not observed upon infection with EAV. Clearly, the large evolutionary distance between the two nidovirus subgroups and their respective replicase subunits involved in intracellular membrane modification leaves ample space to explain such differences, *e.g.* on the basis of the specific characteristics and expression levels of their trans-membrane nsps. For EAV, in the absence of virus replication, expression of nsp2 and nsp3 induces the formation of DMV-like structures [65,106], which appear to lack the typical content observed in DMVs from cryo-fixed infected cells (data not shown). A similar "surrogate system" to study coronavirus-induced replication structures remains to be developed.

Pinpointing the active site of nidovirus RNA synthesis

When it comes to finding the exact site of nidovirus RNA synthesis in infected cells, and the specific structure(s) with which the active RTC is associated, it will be imperative to differentiate between, on the one hand, the abundantly produced replicase proteins, their subcellular localization, and the various membrane structures they appear to induce, and on the other hand the actual RNA synthesizing enzyme complexes, whose localization remains unknown thus far and whose number may be just as restricted as previously estimated for some other +RNA viruses. Obviously, also nidovirus replicase proteins may be "overexpressed" and in particular the numerous nsps encoded by coronaviruses [13,23,197] have been postulated to interact with cellular factors and pathways in the context of a variety of functions other than

viral RNA synthesis *per se*. In fact, the number of (potential) nsp-based coronavirus virus-host interactions and domains known to be nonessential for RNA synthesis has rapidly increased over the past years. Thus, it is clear that the overall nidovirus nsp localization in the infected cell is unlikely to reflect the position and abundance of active RTCs, in particular when the replicase subunit analyzed is known to be dispensable for viral RNA synthesis [67,68]. The same reasoning may in fact apply to part of the induced membrane structures, which may either serve other viral functions or be the mere consequence of nsp or RNA accumulation in the course of infection. Finally, as discussed previously for coronaviruses [198] and now enhanced by the strikingly similar results obtained for EAV DMVs in this study: it is tempting to propose that the widely used antibody labeling for dsRNA indeed reflects the site of active viral RNA synthesis, but this assumption remains to be supported by approaches allowing the *in situ* analysis of viral RNA synthesis in a much shorter time frame than the many hours of infection during which dsRNA signal is allowed to accumulate in most studies. In this context, the technical possibilities of the ESI approach introduced in this study certainly merit further exploration (see below).

Our previous *in vitro* activity assays with EAV and SARS-CoV RTCs isolated from infected cells [188,247] showed that their RNA-synthesizing activity depended on the presence of intact membranes. Upon detergent treatment, EAV RTCs became susceptible to nuclease and protease digestion. Although these experiments did not provide information about the exact architecture of the protective membranes, they strongly suggested compartmentalization of the RTC. In the present study, the accessibility of dsRNA was investigated *in situ* by nuclease treatment and antibody labeling of semi-permeabilized EAV-infected cells (Fig. 7). Also these results supported our ET-based conclusions that the interior of the majority of DMVs is not connected to the cytosol and encloses the dsRNA. These experiments do not eliminate the possible existence of small openings, not permitting entry of RNase III or immunoglobulin molecules, or alternative transport mechanisms, but it is tempting to speculate that RNA synthesis indeed occurs inside DMVs, in particular because dsRNA was not detected elsewhere in the cytosol of infected cells after semi-permeabilization (Fig. 7C). Quantitative ET analysis of EAV-induced DMVs during the first phase of infection clearly showed that the number of vesicles increased rapidly, in particular between 4 and 7 h p.i., but that the average DMV and core diameter remained more or less the same throughout infection (Fig. 5). Thus, DMVs are apparently primed to develop to a relatively uniform size, although -at present- the mechanism of inner vesicle formation remains as obscure as it is for coronaviruses [198]. The same applies to the question of how RNA is exported to the cytosol, for translation and packaging, if the DMV cores would indeed constitute the site of viral RNA synthesis. An alternative model could involve RNA synthesis in a closed DMV compartment followed by disruption of the membrane to release RNA products, although neither cores devoid of membranes nor cytosolic dsRNA labeling were detected in our EM studies. Finally, it should be stipulated that direct evidence for RNA synthesis inside arteri- or coronavirus-induced DMVs remains to be

obtained, and that the induction of these structures by 'simple replicase overexpression' or in the context of cellular antiviral responses remain to be excluded.

ESI as a novel approach to dissecting +RNA viral replication structures

To our knowledge, our study is the first to use ESI for the analysis of +RNA virus replication structures. Making use of the high P content of RNA, compared to proteins, and with lipids being extracted during the FS procedure, the technique was found to provide both ultrastructural and quantitative information about DMV cores. Although our analysis must have underestimated the amount of RNA for some of the cores, of which spherical caps were lost during the sectioning of our specimens, the 11 DMV cores analyzed were found to have an average P content that is equivalent to about a dozen RNA molecules of the size of the EAV genome (12.7 kb). Future experiments will be aimed at confirming the viral nature of these molecules, which formally remains to be proven. Clearly, ESI will not be able to distinguish positive- from negative-stranded RNA, and also the question whether nidovirus genome replication and subgenomic RNA synthesis occur in the same complexes remains to be studied in more detail. Most importantly, however, we will first need to distinguish between viral RNA synthesis occurring directly in the cores of nidovirus-induced DMVs on the one hand, and the accumulation of RNA produced elsewhere in the cell on the other hand. To this end, metabolic RNA labeling experiments, using short pulse-labelings with radiolabeled or chemically modified nucleosides (or nucleotide triphosphates), will be required. Also the biochemical characterization of the RVN and its components, either *in situ* or following their isolation from infected cells, should be expanded to obtain additional information on the composition and function of these virus-induced membrane structures. In addition to the possibilities for RNA and protein quantitation by ESI [259], we now also gained the first structural information about the interior of DMV cores (Fig. 9F-H; Video S2), although it is clearly too early to speculate about its internal organization in any detail. In the future, it will be worthwhile to explore the use of a combination of different elemental maps to analyze and compare the replication structures of different +RNA viruses in considerable detail.

A structural connection between the arterivirus-induced RVN and nucleocapsid assembly?

In addition to the ultrastructure of the EAV-induced RVN, our analysis also documented the previously observed N protein-containing structures in unprecedented detail. During the central stage of infection (7 to 10 h p.i.), this network of sheets and tubules rapidly expands and becomes intertwined with the components of the RVN (Fig. 3 and 8). Our EM analysis strongly suggests the absence of lipid membranes in these structures and revealed (putative) protein sheets whose local curvature appears to give rise to the tubular structures (Fig. 8D).

Immuno-labeling directly confirmed the presence of N protein in these tubules (Fig. 8B-C). Interestingly, the electron density of the tubules in our tomograms was significantly higher than the density of structures known to be solely composed of proteins, like microtubules (Fig. 8D). Previous studies of Wieringa and co-workers [112] indicated that tubule formation depends on both infection/replication and the synthesis of the EAV N protein, *i.e*. N protein expression itself does not induce tubule formation. The fact that the tubules were clearly visible in our ESI P maps could well reflect the presence of RNA. Formally, P signal could also be derived from the reported phosphorylation of the N protein (at an unknown number of residues; [264,265]), but this explanation may be considered less likely since a hyper-phosphorylated protein domain like the C-terminal region of RNA polymerase II remained undetectable in a recent ESI study [259]. Arterivirus assembly has not been studied in much detail so far. Budding of pre-assembled nucleocapsid structures has been reported to occur at smooth intracellular membranes [250,266,267]. Particularly intriguing EM observations were made by Wada and co-workers (Fig3G-H in [250]), who documented tubules (average diameter 42 nm) extending from the cytosol into virions that were in the process of budding. Recent cryo EM studies on the structure of the porcine arterivirus PRRSV describe the core of that virion as a double-layered, hollow structure with an average diameter of 39 nm [268]. This diameter is remarkably close to the average tubule diameter for EAV-induced tubules reported by Wada et al. [250] and our own measurements in this study: 42.8+4.6 nm (n=50). Clearly these N protein-containing sheets and tubules need to be investigated in more detail, but assuming they constitute a complex of viral RNA and N protein, and given their proximity to the RVN, they may represent a key step in arterivirus nucleocapsid formation and, thus, an important structural intermediate in the pathway from genome synthesis to virion assembly. Also studies with other +RNA virus suggest the existence of mechanisms to organize different stages of the replicative cycle, from genome translation to virus assembly, in intracellular space [25,38,269]. The in-depth analysis of such "viral factories" [157,242] is a technically challenging research area, but recent pioneering ultrastructural studies illustrate how technical advances like ET and, now, ESI may provide new insights into the morphogenesis, structure, and function of these structures that are key to +RNA virus replication and evolution.

MATERIALS AND METHODS

Virus, cells, and antisera

A cell-culture adapted derivative of the EAV Bucyrus isolate [270] was used to infect monolayers of Vero E6 cells grown in Dulbecco's modified Eagle's medium supplemented with 10% fetal calf serum. A multiplicity of infection of 10 and incubation temperature of 39.5°C were

used in all EAV infection experiments, and infection rates were routinely confirmed in IF assays. Rabbit antisera recognizing different EAV replicase subunits were described previously, including antisera against nsp3 [97], nsp7-8 [88], nsp9 [247]. A novel nsp11 rabbit antiserum was produced using previously described immunization protocols [88] and purified recombinant nsp11 as antigen. Monoclonal antibodies against the EAV N protein [271] and dsRNA (MAb J2 [177,179]) were documented previously.

Immunofluorescence microscopy

Infected cells grown on glass coverslips were fixed with 3% paraformaldehyde in PBS at various time points after infection and were processed for IF microscopy essentially as described previously [95]. Following permeabilization, single- or dual-labeling IF assays were carried out with rabbit antisera and/or mouse monoclonal antibodies, which were detected using appropriate indocarbocyanine (Cy3)-conjugated donkey anti-rabbit immunoglobulin (Ig) and Alexa Fluor 488 (Al488)-conjugated goat anti-mouse Ig secondary antibodies, respectively (Molecular Probes). To allow dual-labeling experiments with the nsp3 serum and a second rabbit antiserum recognizing a different nsp, an IgG fraction was isolated from the anti-nsp3 antiserum for direct coupling to Alexa Fluor 488, as described previously [100]. Specimens were examined with a Zeiss Axioskop 2 fluorescence microscope (equipped with the appropriate filter sets, a digital Axiocam HRc camera, and Zeiss Axiovision 4.2 software) (Carl Zeis, Microimaging) or with a Leica SP5 confocal laser scanning microscope, using a pinhole size of 1 airy unit. Images were optimized and analyzed for co-localization with the WCIF version of ImageJ (http://www.uhnresearch.ca/facilities/wcif/imagej/). The Manders' overlap coefficients were calculated as described by Li and co-workers [232].

Electron microscopy

For ultrastructural morphological investigations, EAV–infected Vero E6 cells were fixed at various time points after infection. The procedures that were used for either chemical fixation or CF by plunge-freezing have been described before [100,198]. When HPF was applied, cell monolayers adhered to sapphire discs (Leica) were frozen using a Leica EM PACT2 high pressure freezer. Freeze substitution was carried out in an automated FS system (Leica) using a medium consisting of 2% osmium tetroxide, 1% glutaraldehyde and 10% H_2O in acetone. Samples were kept at –90°C for 9 h, after which the temperature was raised with 23.33°C/h to -20°C, at which temperature samples were kept for 1 h. Subsequently, the temperature was raised with 20°C/h to 0°C, and samples were kept at this temperature for 1 h. After washing with pure acetone at 0°C and room temperature, the samples were embedded in epoxy LX-112 resin. Thin sections were contrasted with uranyl acetate and lead citrate, and subsequently viewed at 80 keV with a FEI T12 transmission electron microscope.

For iEM, infected cell monolayers were cryo fixed by HPF as above, but FS was performed in anhydrous acetone containing 0.25% glutaraldehyde and 0.1% uranyl acetate for the nsp and N protein labelings, and 0.2% uranyl acetate and 1% methanol for the dsRNA labeling. For the dsRNA labeling, a prefixation with 3% paraformaldehyde in 0.1 M PHEM buffer (60 mM piperazide-1,4-bis[2-ethanesulfonic acid], 25 mM HEPES, 2 mM $MgCl_2$, 10 mM EGTA) was used, as this was found to improve the labeling efficiency. During the FS step, samples were kept at −90°C for 72 h, after which the temperature was raised with 23.33°C/h to -20°C, at which temperature samples were kept for 1 h. Subsequently, the temperature was lowered with 20°C/h to -50°C. After washing with ethanol, samples were infiltrated with Lowicryl HM20 and polymerized under UV light at −50°C. Thin sections were labeled with the different primary antisera, which were detected with 10-nm protein A-gold particles. A bridging rabbit-anti-mouse IgG antibody (DakoCytomation) was used when the primary antibody was a mouse monoclonal antibody. Grids were contrasted with uranyl acetate and lead citrate and subsequently viewed in a FEI T12 transmission electron microscope at 80 keV.

Electron tomography

Freeze-substituted infected cell samples, processed for morphological investigation by HPF as described above, were used to cut 200-nm-thick sections. Serial sections were placed side-by-side on formvar/carbon coated grids containing only 8 parallel bars, thus allowing analysis of the same cell in successive sections. To facilitate the image alignment required for tomogram production, a suspension of 10-nm gold particles was layered on top of the sections as fiducial markers. For dual-axis tomography, two single-axis tilt series were recorded with an FEI T12 transmission electron microscope operating at 120 keV. Per single-axis tilt series, 131 images were recorded at 1° increments between tilt angles of −65° to +65°. Automated tomography acquisition software was used (SerialEM) [272]. Images were acquired with a cooled slow-scan charge-coupled device (CCD) camera (4k Eagle; FEI Company) with 4,096 × 4,096 pixels and were recorded in 2x2 binned mode. The electron microscope magnification was 18,500×, corresponding to a pixel size of 1.2 nm at the specimen level. For dual-axis tomography, the specimens were rotated 90° around the *z*-axis using a dual-axis tilt tomography holder (Fishione; model 2040). For tomogram computation, dual-axis tilt series were aligned using the fiducial markers and the IMOD software package [194].

The 3-D surface-rendered reconstructions of virus-induced structures and adjacent cellular features were processed using AMIRA Visualization Package (TSG Europe) by surface rendering and thresholding. During this process, volumes were denoised using the nonlinear anisotropic diffusion filtering [196]. Denoised volumes were used only for producing the surface-rendered masks. Final analyses and representations were done using the original data. To facilitate DMV quantification and size measurements in the tomograms, the central position of each DMV was marked in 3-D in the slice in which it had its largest diameter. By

combining IMOD and Linux scripts, sub-volumes of 250x250x10 pixels containing 10 sections around the DMV equator were extracted and binned 10 times in the z direction to obtain a 12 nm thick slice. To calculate size averages for DMVs and cores, the diameters in both the x and y directions were measured and averaged using the ImageJ software.

Analysis of semi-permeabilized EAV-infected cells

EAV-infected cells were rinsed twice at 39.5°C with NaP_i-buffer (100 mM NaP_i, pH 7) containing 0.9 mM $CaCl_2$ and 0.5 mM $MgCl_2$. Fixation was performed with 3% PFA in NaP_i-buffer which should prevent membrane permeabilization [254]. To determine the saponin concentration needed for full permeabilization of the plasma membrane without affecting the membranes of intracellular organelles, cells were treated for 10 min with different concentrations of saponin ranging from 0.001 to 0.5%. Cells not treated with saponin or fully permeabilized with Triton-X 100 (TX-100) right away were used as negative and positive controls, respectively, to assess membrane permeabilization and labeling efficiency. After the (mock) detergent treatment and extensive washing with PBS containing glycine, cells were incubated for 1 h at 37°C with a rabbit antiserum recognizing nsp3 and a monoclonal antibody recognizing either beta-tubulin, PDI, or dsRNA. Cells were then washed with PBS/glycine and fully permeabilized with 0.1% TX-100 in PBS for 10 minutes. After washing, cells were incubated with Cy3 Alexa488 secondary antibodies against rabbit and mice IgG, respectively, and confocal IF microscopy was performed as outlined above.

To analyze the susceptibility of dsRNA to RNase III digestion, fixed EAV-infected cells were left untreated or were fully permeabilized with 0.1% TX100 in PBS for 10 min. After washing, cells were incubated for 2 h (37°C) with 2 units/ml of RNase III or RNase A (both from Ambion), as described by Weber et al. [177]. After washing, the cells were fixed for a second time, using 3% PFA in PBS, to block all further RNase activity. Samples were washed again, treated with 0.1% TX100 in PBS for 10 min, and processed for dsRNA IF labeling as described above.

Electron spectroscopic imaging

EAV-infected cells were high-pressure frozen at 8 h p.i. and freeze-substituted in 1% glutaraldehyde in acetone. 60-nm thin sections were cut and inspected in an FEI T12 electron microscope to identify cytoplasmic areas that contained DMVs. Images at different magnification were acquired at 80 keV, with the aim to retrieve the same area after transferring the specimen to a FEI F20 electron microscope running at 200 keV, which was equipped with a post-column electron image filter (Gatan). Because of the significant contrast reduction at 200 keV, zero loss images of the same cytoplasmic areas were recorded to obtain overview images. Next, pre- and post-edge images were acquired at an energy loss of 120 and 157 eV, respectively, with a slid-width of 15 eV [257]. To improve the signal-to-noise ratio, we averaged 5 images

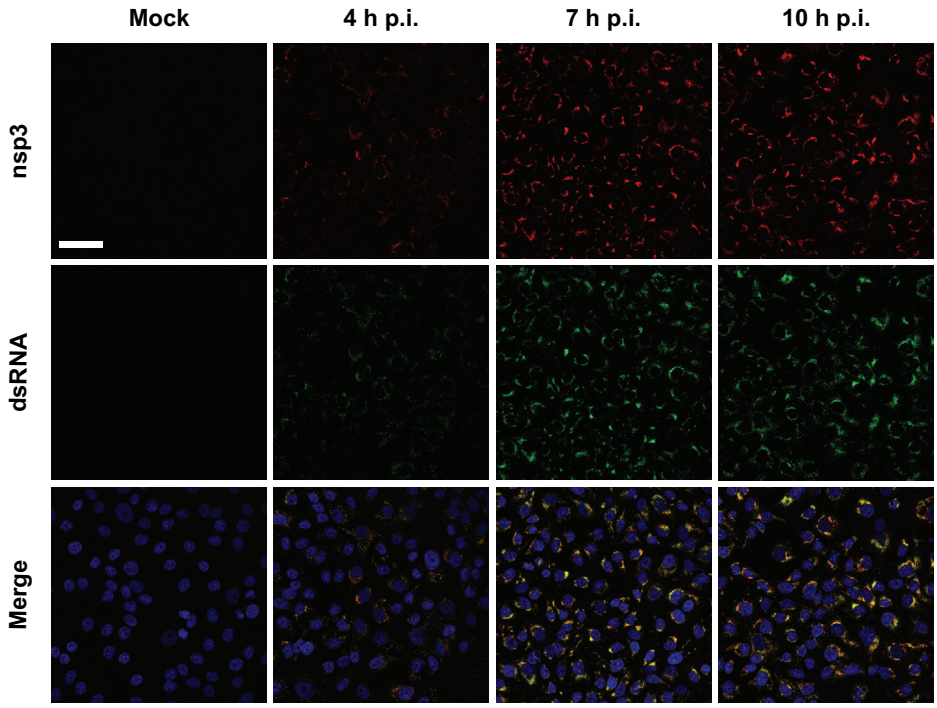
recorded with an exposure time of 1 min each. Phosphorus maps were calculated based on the ratio between the averaged pre- and post-edge images (Digital Micrograph™; Gatan). To estimate the P content of individual DMV cores, the averaged P signal of 25 ribosomes was used for calibration. After correction for background intensities, measurements were correlated to 7,128 P atoms in a mammalian ribosome [261]. This signal was then compared to the P signal in DMV cores, which was also corrected for background noise. While performing these measurements, only cores surrounded by a clear halo were included, which were likely to be complete and reside in the middle of the section.

To facilitate the image alignment required for ESI tomogram production, 10-nm gold particles were layered on top of the 75-nm sections as fiducial markers. For ESI tomography, a pre-edge and a post-edge single-axis tilt series were recorded with an FEI F20 transmission electron microscope operating at 200 keV, using the EFTEM tomography software (Gatan). A total of 64 images were recorded at 2° increments between tilt angles of –63° to +63°. Per tilt angle, 5 images were acquired with a cooled slow-scan charge-coupled device (CCD) camera (2k GIF; Gatan) in 2x2 binned mode and averaged to obtain a better signal-to-noise ratio. The electron microscope magnification was 19,000×, corresponding to a pixel size of 2.7 nm at the specimen level. For ESI tomogram computation, the pre-edge tilt series was aligned using the fiducial markers and the IMOD software package [194]. These alignments were then transferred to jump ratio tilt series, where the gold markers are not visible, and a reconstruction was computed using 25 iterations of the simultaneous iterative reconstruction technique (SIRT) algorithm implemented in IMOD [194]. The 3-D surface-rendered reconstructions of virus-induced structures and adjacent cellular features were processed by surface rendering and thresholding using the AMIRA Visualization Package (TSG Europe).

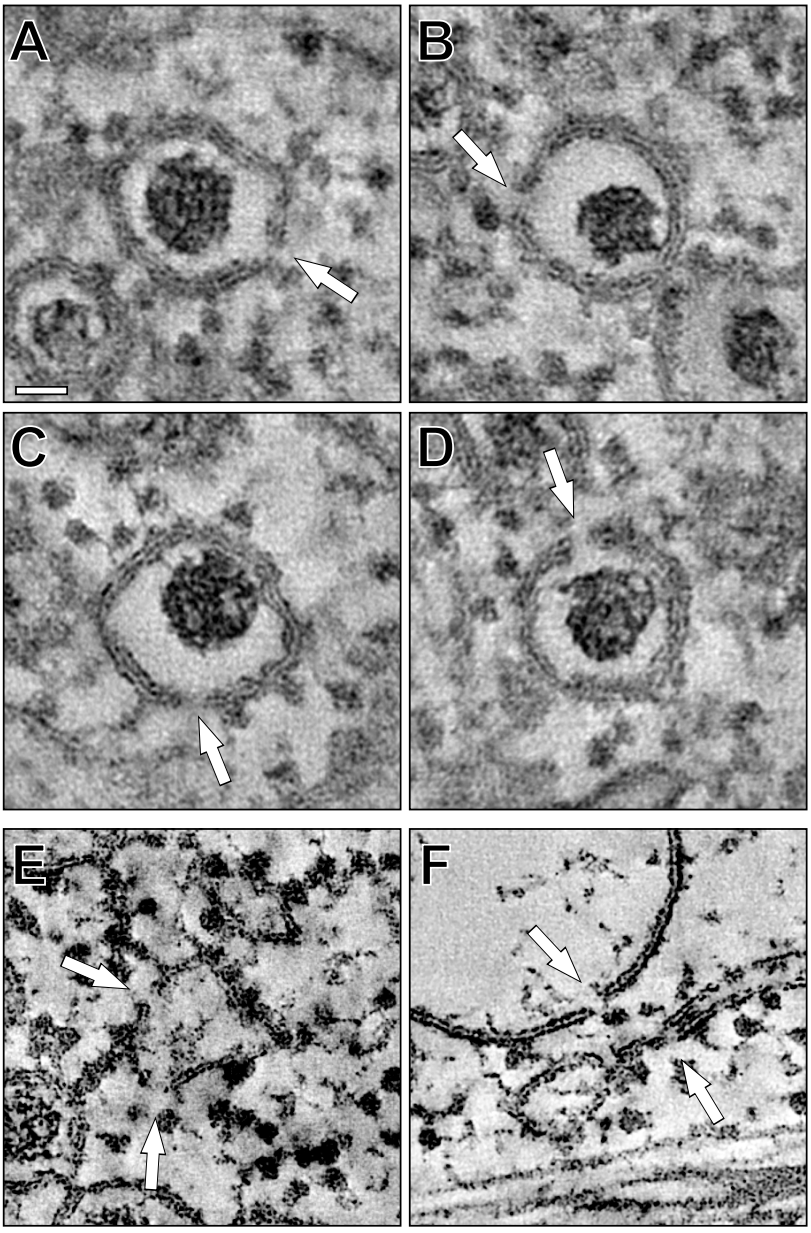
ACKNOWLEDGMENTS

For skillful technical assistance, helpful discussions, and support we thank our (former) LUMC colleagues Danny Nedialkova, Jolanda Liefhebber, Nisha Verweij, Frank Faas, Yvonne van der Meer, Martijn van Hemert, Aartjan te Velthuis and Marjolein Kikkert. We gratefully acknowledge the collaboration and assistance of Dr. Richard Leapman and Dr. Maria Aronova (NIH, Bethesda, MD, USA) with the ESI analysis, and of Vincent Richard (Gatan) with the ESI-tomography data collection.

SUPPLEMENTARY FIGURES



Supplemental Fig. S1. Immunofluorescence microscopy overview images of EAV-infected cells. Representative low-magnification images of EAV-infected Vero E6 cells that were fixed every hour between 0 and 15 h p.i. (here shown for 0, 4, 7, and 10 h p.i.) and processed for dual labeling IF microscopy (nsp3 and dsRNA). Imaging was done using a wide field fluorescence microscope with a 40x objective. For the calculations of labeling intensities presented in Fig. 1D, for each time point the total pixel intensities in 5 low magnification images, each containing about 75 cells, were averaged. The scale bar represents 25 µm.



Supplemental Figure S2. In-depth analysis of discontinuities in the membranes of EAV–induced DMVs. The tomograms that were used for our ultrastructural analysis of RVN membranes in EAV-infected cells were scrutinized for openings that connect the DMV interior with the cytosol. (A to D) Examples of DMV membrane discontinuities observed in our HPF specimens (arrows). (F-E) Similar discontinuities were occasionally observed in membranes of other cytoplasmic organelles (arrows). Consequently, there is considerable doubt whether the DMV membrane discontinuities of this type, observed for only 9 percent of the almost 900 DMVs in our tomograms, represent true connections between cytosol and DMV interior rather than fixation and/or staining artifacts. The scale bar represents 25 nm.

CHAPTER 6

General discussion

DISCUSSION

The reticulovesicular replication network

The distantly related nidoviruses SARS-CoV and EAV both modify the endoplasmic reticulum (ER) into a reticulovesicular network (RVN) with which their RNA synthesis is thought to be associated. By using electron tomography (ET; chapters 2 and 5) to study the replication structures of two distantly related nidoviruses, we discovered that the previously documented double-membrane vesicles (DMVs) induced by infection with both viruses are continuous with each other and the ER via narrow membrane connections, often just 8 nm in diameter. Although these narrow connections at first glance may seem rather insignificant, their discovery refined our view of nidovirus-host interactions during replication. An ER-origin of replication vesicles was previously suggested for both coronaviruses [94,100,101] and arteriviruses [65,97], however, the fact that the DMVs of both virus families are connected and thus form a membraneous network was not known. The discovery of nidovirus-induced RVNs not only supported the notion that these viruses use the ER as membrane donor for RVN formation, but also implied that nidovirus replication maintains a close physical relationship with the ER throughout infection. In particular, this was demonstrated by two studies using drugs that affect the morphology and function of the ER, brefeldin A (BFA; chapter 3) and the translation inhibitors puromycin (PUR) and cycloheximide (CHX; chapter 4). BFA treatment, which triggered dilation of the ER, resulted in a faster transformation of DMVs into vesicle packets and affected DMV formation and RTC function [240]. The blockage of DMV formation by PUR treatment would seem a likely result of protein translation inhibition; however, the rapid reduction of RNA synthesis by preformed complexes cannot be solely attributed to translation inhibition because this drastic effect was not observed after translation inhibition with CHX, a difference that might be explained by the fact that PUR induces much more pronounced changes of ER morphology (Chapter 4).

Coronavirus DMVs were first described in ultrastructural studies of cells infected with mouse hepatitis virus (MHV) [102,262]. Next to DMVs, diverse membrane clusters were observed, which were named tubular bodies and reticular inclusions [102]. Recently, iEM studies have shown that the tubular bodies contain the structural envelope (E) protein, which likely induces the tubular morphology when it accumulates in the cell [235]. Also upon SARS-CoV-infection, a second membrane structure was observed in close proximity of the first detectable DMVs from 2 h p.i. on (Chapter 2). We chose to name this structure "convoluted membranes" (CM) by analogy to similar structures induced by flavivirus infection, which were proposed to be the site of viral genome translation and polyprotein processing [39,170]. ET and iEM on SARS-CoV-infected cells showed that SARS-CoV CMs are composed of membranes that connect the ER and DMV outer membranes and contain the majority of the nsp species for which iEM could be performed (Chapter 2). Similar results have recently been published for MHV

using iEM and showed that several nsps as well as the structural nucleocapsid (N) protein are present on DMVs as well as CMs, but not on other MHV-induced structures like the tubular bodies [235]. In contrast to our observations for SARS-CoV, these authors did not observe continuities between DMVs and CM, which is likely explained by the use of conventional 2-D TEM rather than ET. For SARS-CoV, these membrane connections were only discovered when using ET, while in 2-D TEM they were not apparent. Additionally, it was claimed that the CMs appeared only after DMV formation and are therefore unlikely to be a precursor structure of DMVs [235]. However, in our ET studies, from the earliest moment of detection onwards, the DMVs induced by both SARS-CoV (Chapter 2) and MHV (Knoops et al., unpublished data; Fig. 1) were accompanied by the reticular CM structures. Theoretically, these contradicting results may be explained by differences between the host cells used in these two studies (HeLa-CEACAM versus Vero E6), although no clear differences were observed in any aspect of RVN structure or development when comparing different cell lines infected with MHV (Knoops et al., unpublished data). It is also possible, and perhaps more likely, that early in infection the small CM structures remained invisible to Ulasli and co-workers in their 2-D analysis and were only detected at later time points when they had become larger. Besides the structures described by Ulasli et al., we observed vesicle packets (VPs) in MHV-infected Vero E6 cells (Knoops, unpublished data; Fig. 1C), the same type of structures that became very pronounced late in SARS-CoV infection (Chapter 2).

Made from the ER

Both arteriviruses [65,106] and coronaviruses [85,87,182] encode three non-structural proteins (nsps) that contain hydrophobic domains and presumably anchor the RTC to cellular membranes. In support of the conclusion that the nidovirus-induced RVN is derived from rough ER (rER), ribosomes were found to abundantly decorate its outer membranes (Chapters 2 and 5) and co-localization was observed of the main protein of the cellular Sec61-translocon channel co-localized and SARS-CoV nsps (Chapter 3). Ribosomes dock to the translocon in ER membranes while being engaged in the co-translational insertion of trans-membrane (TM) and secretory proteins. While translation is on-going, the nascent polypeptide chain leaves the ribosomal exit tunnel and is scanned for signal and/or TM sequences by the signal recognition particle (SRP). Upon SRP binding, the entire complex (i.e. ribosome, nascent chain, and SRP) is targeted to the SRP-receptor in the ER membrane, where translation continues with the nascent chain entering the translocon channel [59]. However, when a TM sequence is specific for the SRP-independent pathway, the nascent protein is first completed in the cytosol where it is kept in an unfolded conformation by cytosolic chaperones [273]. In mammalian cells, protein translocation is almost exclusively co-translational and it remains unclear how the unfolded proteins are targeted to the ER, although insertion into the membrane seems to be facilitated by the Sec61/Sec62/Sec63 complex [274]. For now, it is unclear whether

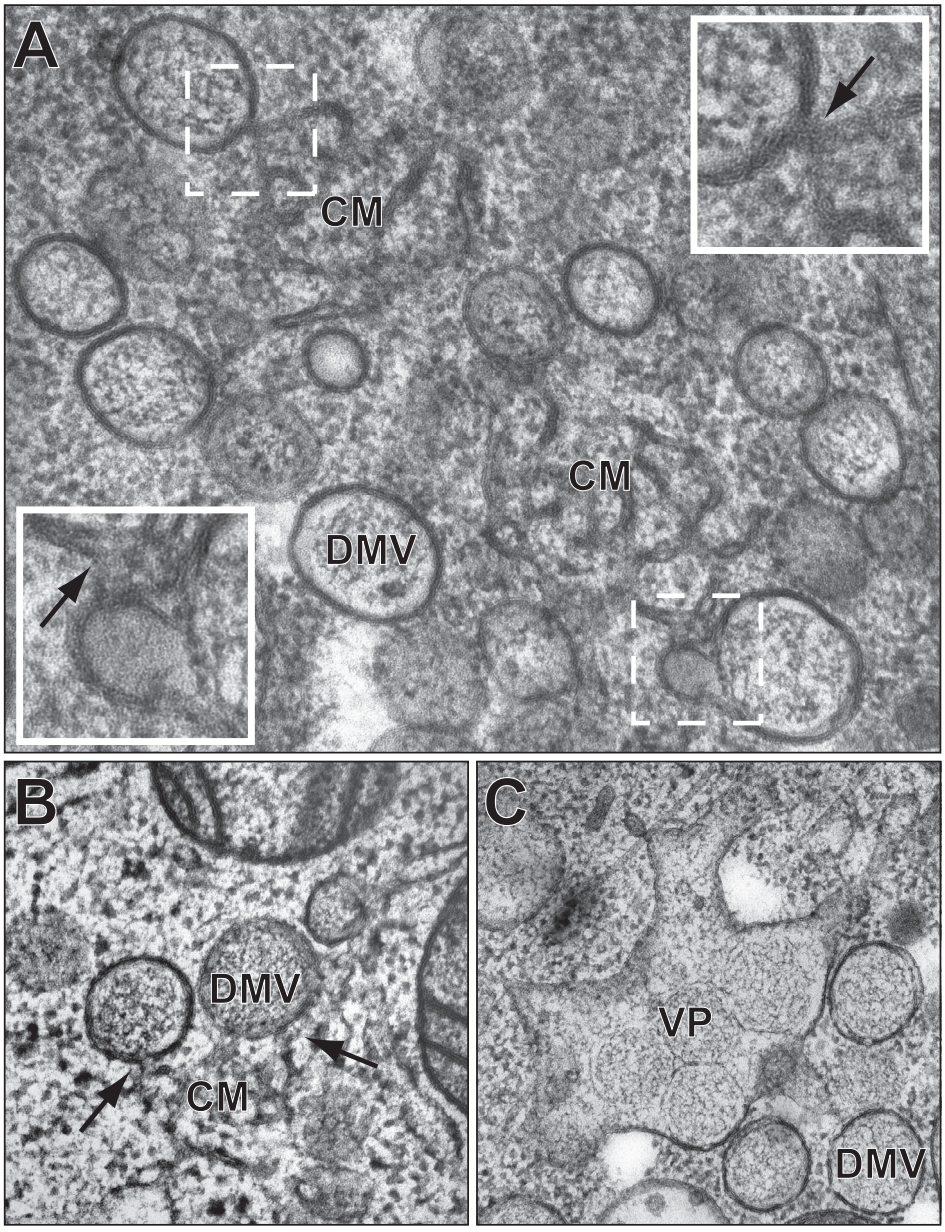


Figure 1. EM images of the membrane modifications that are induced by Mouse Hepatitis Virus. Vero E6 cells containing the CEACAM1-receptor were infected with MHV-A59, cryo-fixed by plunge-freezing and processed for TEM analysis as described earlier (Chapters 2 and 3). (A) At 8 h p.i., clusters of DMVs were visible in the cytoplasm and were often accompanied by clusters of convoluted membranes (CM). The arrows in the insets show the connections of DMVs with CM structures that were readily visible in our TEM-images. (B) In a time-course experiment, the first MHV-induced DMVs were detected at 4 h p.i. and, also at this early time-point, were connected with CM membranes (arrows). (C) Besides DMVs, also vesicle packets (VP) were occasionally found at 8 h p.i. in which multiple inner-vesicles shared the same outer membrane.

membrane insertion of the nidovirus transmembrane replicase subunits occurs co- or post-translationally, although the efficient integration of MHV nsp3 in microsomes suggested the involvement of an SRP-dependent ER-translocation mechanism [85]. If the SRP pathway indeed directs the nascent replicase polyprotein towards ER membranes, this would be the first step in which its template, the viral genome, would become physically associated with the ER membrane via translating ribosomes [275]. Multiple ribosomes would translate ORF1a or ORF1ab, simultaneously producing polyproteins and thus securing the membrane asso-

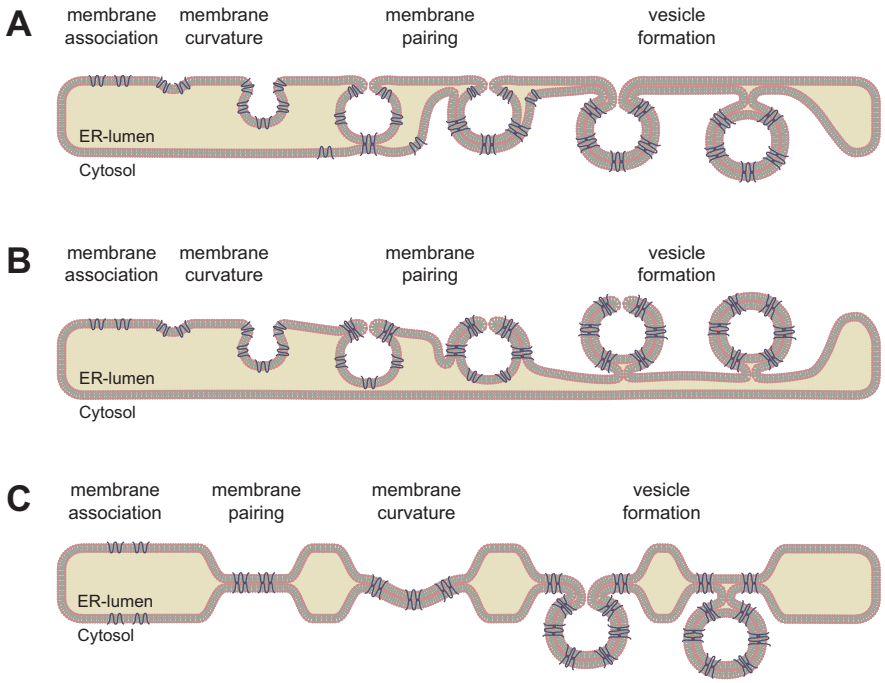


Figure 2. Models for the formation of DMVs from ER membranes. (A) Double-budding mechanism. After association of the replicase polyproteins with ER-membranes, the ORF1A-encoded membrane domains induce a negative curvature towards the ER-lumen, thus creating an invagination into the ER. Membrane-pairing occurs by luminal interaction of replicase proteins situated on the membranes of the invagination and the opposing ER-membrane, and results in a wrapping event towards a double-membrane vesicle. In this model, one membrane-fission event at the orifice of the invagination would be necessary to explain the morphology of the connected DMV as was observed after infection with either EAV or SARS-CoV. (B) Single-budding mechanism. Similar to the double-budding mechanism, with the exception that membrane-pairing would not occur with the membrane opposing the invagination, but with the membranes surrounding the orifice. In this model, the neck-like connection of the DMV with the ER can be explained without any fussion result, although fission would be a necessity for complete closure of the DMV. (C) Protrusion model. After association of the replicase with ER-membranes, the ORF1A-encoded membrane-domains first induce membrane-pairing which afterwards results in membrane-bending. Like in the double-budding mechanism, one membrane-fission event at the orifice of the invagination would be necessary to explain the morphology of the connected DMV. Especially in this model, it is unclear what influences the direction of membrane-bending. (Figure adapted and adjusted from [97])

ciation of the genome with the ER via the ribosome-translocon interaction, potentially until the genome switches from acting as template for translation to being a template for minus-strand RNA synthesis. The mechanism of membrane-association by polyribosome formation was discovered during translation of the poliovirus genome, supporting the theory that this mechanism indeed is used in some RNA virus systems [276,277]. After SARS-CoV infection, we found that Sec61α resides almost exclusively within the RVN and therefore likely plays a major role in the insertion of replicase TM domains into the ER membrane (Chapter 3). However, upon translation of coronavirus subgenomic mRNAs, also various structural and accessory transmembrane proteins need to be inserted into the ER-membrane, a step likely utilizing the same translocation-machinery. Thus, by rearranging the host's ER into a system which associates the RTC with the translation/translocation machinery, nidoviruses may have created the perfect system to couple RNA synthesis and the multi-step pathway leading to virus assembly.

After membrane insertion, nidovirus replicase transmembrane-domains are thought to not only constitute a membrane anchor for the RTC but also to induce membrane pairing at the luminal interface by "zipping" the two opposing ER membranes together, thus minimizing the luminal space between the membranes of DMVs and CM [65,106]. The transmembrane domains expressed from ORF1a and the expression level of the nsps that contain them may have a profound effect on the membranes in which they are inserted and are believed to induce curvature. For EAV, it was shown that the first two transmembrane replicase subunits, nsp2 and nsp3, are capable of inducing characteristic double membranes and DMVs when expressed together in the absence of any other nsps or viral RNA synthesis [65]. Two models have been proposed to explain the formation of arterivirus DMVs from ER membranes [97]. According to the "double-budding mechanism" model, the replicase proteins would first induce a negative curvature in the ER membrane and, after membrane fission, this would give rise to a vesicle within the ER lumen (Fig. 2A). Subsequently, luminal replicase TM domains in the ER and the membrane of this vesicle would interact to induce positive curvature and induce a second budding event, this time towards the cytosol, which after a second membrane fission event would result in a detached vesicle with a double membrane. In summary, in this model two opposing budding events would follow each other, while the switch from inducing negative to positive curvature would be driven by luminal interactions of replicase subunits. Similar to the double budding mechanism proposed by Pedersen et al., membrane pairing could also occur by oligomerization of proteins positioned in the membrane region surrounding the orifice (Fig. 2B). In this model, the neck-like connections between DMVs and the ER composed of two membranes, similar to what was observed in electron tomography, can be explained without any membrane fusion event, although membrane fusion at the orifice would still be a necessity for complete closure of the DMV. The alternative "protrusion-and-detachment" model operates in a similar way; however, the interaction of replicase subunits in opposing membranes, resulting in the formation of tightly-paired

membranes, would now precede the membrane-bending and -fission events that ultimately would create a sealed DMV (Fig. 2C). In this model, it remains unclear what determines the beginning and direction of curvature. The tomograms that were obtained from both SARS-CoV- and EAV-infected cells mainly showed paired-membrane structures like those proposed in the "protrusion-and-detachment" model. Vesicles within the ER that do not show the paired-membrane morphology, as proposed in the "double-budding mechanism", were only observed in the SARS-CoV VPs, which were detected only late in infection and might result from dilating ER and dissociation of membrane protein interactions. The detachment of DMVs from the ER was not observed for the nidoviruses studied in this thesis (chapter 2 and 5) and thus suggests that the last fission event, which is part of both models, does not occur. Alternatively, an initial fission event, creating a fully detached DMV, could be followed by fusion of DMV outer membranes to generate the RVN. Still, it remains unclear how the trans-membrane subunits of the replicase induce membrane pairing and curvature, and at which stage cellular proteins might be involved. It was recently found [106] that a cluster of four conserved cysteine residues in a luminal domain of EAV nsp3 is essential for DMV formation and that their replacement is lethal to the virus when evaluated in a reverse genetics system. Although experimental evidence is still lacking, it is tempting to speculate that these cysteine residues are responsible for membrane pairing by e.g. forming disulfide bridges or a tertiary structure element like a zinc finger domain. Interestingly, a mutant nsp2-nsp3 polyprotein containing an engineered N-glycosylation site in this cysteine-containing loop appeared to retain the ability to pair and curve membranes but hardly induced closed DMV structures, a defect likely due to steric hindrance by the sugar group. When this mutation was tested by reverse genetics, EAV replication was not detected until this nsp3 mutant pseudo-reverted and lost the signal for N-glycosylation [106].

Particularly in the case of coronaviruses, the CM structures that extensively labeled for the replicase proteins did not have the characteristic vesicular morphology and comparison of their 2D projection-pattern with *in silico*-generated templates of different cubic-membrane organizations revealed a 3-D gyroid-based cubic membrane architecture [103,278]. The formation of these geometrical and crystalloid membrane conformations is normally induced by a high concentration of transmembrane proteins with the ability to self-interact [279]. Unfortunately, a surrogate system to study these membrane modifications, e.g. expressing only the trans-membrane nsps of coronaviruses, has not yet been developed. Such a system might provide valuable clues about the mechanism and chronology of CM and DMV formation. Moreover, reconstitution experiments involving isolated nidovirus trans-membrane nsps and "empty" proteoliposomes, as well as insertion of nsps into translocon-containing microsomes during *in vitro* translation could provide useful information about the exact type of curvature that these proteins can induce [280] and the question whether they need host factors to do so.

Recently, it was suggested that depletion of LC3, which is a marker protein for autophagosomes, inhibits MHV replication to a certain extent (*i.e.* a 4-fold reduction of virus-driven protein expression was measured) [263]. Autophagy was previously implicated in coronavirus replication because some light microscopy studies reported that LC3 co-localizes with SARS-CoV [96,226] and MHV replicase proteins [263], although other studies could not confirm these observations [100,281]. This may in part be explained by the use of transiently expressed GFP-LC3 fusion proteins, which were found to not co-localize with nsps and seemed to be excluded from the virus-induced membrane structures, whereas endogenous LC3 appears to co-localize partly with coronavirus replicase proteins [263]. An in-depth colocalization analysis, including iEM, is clearly required to determine if and where LC3 is indeed present in RVN membranes. The light microscopy study of Reggiori et al [263] showed a certain level of LC3 co-localization with MHV nsp2 and nsp3, which were suggested to reflect the localization of DMVs. However, since CM, much more than DMVs, are the structures that contain the largest amounts of replicase proteins, it is likely that any co-localization between LC3 and coronavirus replicase will be concentrated in the CMs. It was also suggested that Atg5 knockdown, which results in autophagy-deficient cells, impaired DMV formation after MHV-infection [105], but this result was contradicted in a follow-up study showing that Atg5 knockdown does not have an effect on DMV formation and that autophagy is not required for replication [226]. This was again confirmed by Reggiori and co-workers, who showed that also the essential autophagy protein Atg7 is dispensible for MHV replication [263]. In the same paper, it was also claimed that the MHV-induced RVN, besides LC3, contains EDEM1 and OS-9, which both are part of the ER-associated protein degradation (ERAD) machinery [263]. These proteins are normally located in the ER-lumen and target misfolded proteins for ubiquitination and subsequent degradation by cytosolic proteasomes, a process also involving the sec61-translocon for "dislocation" across the ER membrane [282]. In contrast to their proposed role in the Sec61-mediated dislocation pathway however, it was suggested in a structural study that EDEM1-containing smooth-membrane vesicles might pinch off from the ER and would subsequently be exported into the autophagy-lysosomal pathway [283]. Whereas the authors of the latter paper suggested that this is an alternative way to remove misfolded proteins from the ER, Cali and co-workers [284], who introduced the term "EDEMosomes" for these small vesicles, interpreted the observed phenomena as a way to downregulate the amounts of ERAD chaperones such as EDEM1 and OS-9 themselves, in order to prevent unnecessary degradation of newly synthesized proteins in the ER. Subsequently, it was claimed that these EDEMosomes form the scaffold for the formation of MHV-induced replication-associated membranes [263], although it remains entirely unclear how this would be achieved. In particular, it is difficult to envision how 200 to 300-nm double-membrane structures that are decorated with ribosomes [198] would arise from 150-nm smooth single-membrane vesicles that are stuffed with protein cargo. In-depth ultrastructural and biochemical studies will be needed to test the viability of the EDEMosome hypothesis.

For a complete understanding of the cellular pathways that nidoviruses use for induction of their replication membranes, it will be important to identify the specific host proteins and mechanisms involved. Recently, it was shown that both flavi- and enterovirus RTCs are able to recruit phospholipid-modifying enzymes, e.g. phosphatidylinositol 4-kinases (PI4K), and change the lipid composition of their replication membranes which seems essential for viral replication [285,286]. Furthermore, the enterovirus polymerase seems to specifically bind phosphatidylinositol-4-phosphate lipids which might be a key feature in the membrane association of the RTC and subsequent viral RNA synthesis [286]. It will be highly informative to understand whether also nidoviruses influence the lipid environment of the RVN, which viral and host proteins might be involved in this process, and what their exact rolein RVN formation might be.

Place of nidovirus RNA synthesis: *Concealed*

Optimization of the cryo-fixation protocols for electron microscopy analysis greatly improved the preservation of the morphology of nidovirus-induced membrane rearrangements, in particular the DMV interior (Chapters 2 and 5). Upon cryo-fixation, the interior of both SARS-CoV- and EAV-induced DMVs appeared to be packed with a granular substance after plunge-freezing and, for EAV, contained an electron-dense core with surrounding halo after high-pressure freezing (HPF). Similar internal structures were observed after HPF of cells infected with members of the picornavirus family, e.g. poliovirus [49]. As observed for EAV (Chapter 5), the interior of DMVs induced by Foot-and-mouth disease virus (FMDV) contained electron-dense cores upon HPF, which were not seen after conventional chemical fixation [121]. Also for flaviviruses, it was shown that the ultrastructure of the replication vesicles differs between samples prepared by chemical versus cryo fixation [38]. Whereas chemically fixed Dengue virus-infected cells contained spherular ER invaginations, resembling those proposed in the first step of the "double budding" model, cryo-fixation revealed a DMV morphology in which the inner and outer membranes are tightly apposed.

Compared with conventional chemical fixation, which resulted in empty DMVs [100,104], the cryo-EM protocols are less prone to fixation artifacts, thus significantly improving ultrastructure and resolution. Next, these improved protocols were adapted for iEM and made it easier to distinguish between the different components of the RVN on the basis of their morphology (Chapters 2, 3, and 5). A clear difference in the localization and amount of labeling of RVN components was found when iEM was performed with antibodies directed against nsps and dsRNA. Large amounts of replicase proteins that would not contain TM domains after their proteolytic release, like the SARS-CoV main protease (nsp5) and primase (nsp8), and the EAV polymerase (nsp9) and endoribonuclease (nsp11), were found associated with the double membranes of the RVN. These findings suggest these membranes to be the scaffold for the enzymatically active replicase proteins, however, the dsRNA, which is thought to

represent the key nucleic-acid intermediate of viral RNA synthesis, was mainly found inside the apparently sealed DMVs and co-localized only with a small fraction of the nsps (chapter 2 and 5).

This apparent paradox could be explained if only a fraction of the replicase proteins inside the infected cell is actively engaged in RNA synthesis, as postulated for other RNA viruses [47]. Still, it remains unclear where exactly RNA synthesis occurs. Membranes that were isolated from infected cells and retained active RTCs, were used to investigate the synthesis of genomic RNA and subgenomic mRNAs *in vitro* [188,247]. In these studies, it was shown that RTC activity was insensitive to nuclease and protease digestion, and only became sensitive after detergent treatment. These experiments strongly suggested that RTC activity is somehow protected by membranes, although no information was obtained about the exact nature of these membrane compartments. When dsRNA accessibility was investigated *in situ* by nuclease treatment and antibody labeling of semi-permeabilized EAV-infected cells, a similar result was obtained supporting the observation obtained by tomography that the majority of dsRNA is enclosed within membranes (chapter 5).

The *in vitro* and *in situ* data make it tempting to speculate that DMVs are indeed the place of RNA synthesis. However, ET showed that the vast majority of DMVs did not have clear openings connecting their interior with the cytosol (Chapters 2, 3 and 5), in contrast to what was observed when ET was employed for other +RNA viruses [36,38,41]. If the nidovirus-induced vesicles are indeed sealed, this poses the question of how import of nucleotides into the vesicles and export of RNA products out of the vesicles is organized. In the *in vitro* system, only the genomic RNA remained membrane-associated whereas the subgenomic mRNAs were released [188,247]. Attempts have been made to detect newly made viral RNA products by iEM [97,104], but these remained largely inconclusive due to RVN fragility and preparation artifacts, labeling efficiency and the possibility that RNA products may be transported to another location within the labeling timeframe.

iEM is a popular technique to locate the products of viral RNA synthesis products *in situ* on cell sections, however, a few disadvantages inherent to the technique must be taken into account. In iEM, a specific first antibody is used to detect the target which is then visualized using a second antibody containing a gold particle. This indirect labeling method is not only prone to background labeling, in particular if antigens have a low labeling intensity, but it also has a limited lateral resolution of ~30 nm. Therefore, it will reveal the localization of the target with an uncertainty that might e.g. make the difference between being inside, outside or on the membrane of DMVs [287]. Furthermore, antibodies will only bind to the surface that became exposed by sectioning of the specimen and, thus, projection-images can show gold particles superimposed on structures which in fact do not contain the target.

One approach to locate products of viral RNA synthesis is the use of an antibody highly specific for dsRNA [177,179], which in turn can be detected with immuno-gold particles (Chapter 2, 3 and 5). However, apart from the question whether the labeled RNA product was

part of an active complex at the time of fixation, it is as yet unclear whether all dsRNA detected upon +RNA virus infection indeed represents viral RNA, and therefore other methods should be used to confidently localize the active RTC. Detection of virus-specific sequences with complementary oligonucleotide probes, combined with immuno-gold detection, may be an option but these probes should be designed carefully to discriminate between the different cellular and viral RNAs that are present in the infected cell. For detection of active RTCs, the viral negative-stranded RNA would preferably have to be targeted, which has a higher chance of being part of a complex that is actively engaged in viral RNA synthesis. On the other hand, negative-stranded RNAs are underrepresented and can hybridize to an excess of complementary positive-stranded RNA molecules, thus complicating the detection of these molecules in iEM. To improve the specificity of iEM detection of negative-stranded RNA sequences, padlock probes could be used which are detected by the rolling-circle amplification method. Briefly, padlock probes are oligonucleotides containing two target-complementary ends which become circularized by DNA ligation after hybridizing to a target DNA [288] or RNA sequence [289]. Besides the high labeling-specificity, a major advantage of this method is that the rolling circle amplification increases the signal of the probe [290,291]. Interestingly, methods are also being developed that will allow detection of proteins in complex with DNA/RNA via padlock-probes [292] and might thus be explored in the future to locate nsps on template RNAs.

Ultrastructural studies have been combined with metabolic labeling of viral RNA synthesis using labeled uridine [51,189] or uridine-triphosphate (UTP) [97,104] and are possibly the most straightforward approaches to localize the active site of RTC. Labeled uridine crosses the cell-membrane efficiently and is metabolized to uridine triphosphate (UTP) which can be incorporated in newly synthesized RNA, with actinomycin D treatment ensuring that most of the RNA made is indeed viral RNA. Labeled UTP itself cannot cross the plasma membrane and needs to be transfected or micro-injected in order to reach the viral RTC. Many different forms of labeled uridine and UTP are available and Bienz and co-workers were among the first to use radiolabeled (tritiated) uridine in ultrastructural studies to localize the active poliovirus RTC by autoradiography [51]. Although this method is highly specific, the large silver-grain size identifies the radioactive spot with a low lateral resolution and the relatively long exposure times (weeks to several months) may be considered cumbersome. Nowadays, halogenated uridine or UTP are used more often and, if incorporated in newly made RNA, can subsequently be detected with an anti-bromo-UTP (BrUTP) monoclonal antibody by iEM. Apart from the iEM complications described above, the BrUTP labeling times needed for the BrUTP to efficiently enter the cell after transfection and to be incorporated into a detectable amount of RNA products likely exceeds the timeframe needed for RNA products to be transported to another location. Furthermore, the variety of labeling efficiency might prevent a synchronized labeling of different cells in a culture and thus microinjection of infected cells would probably be a more useful, alternative approach. Ideally, labeling times

of 5 to 15 minutes should be achieved, which are more realistic given the estimated rate of viral RNA synthesis. However, they also make the detection of the incorporated halogenated-uridine more difficult. Electron spectroscopic imaging (ESI) in combination with ET might be used as a more sensitive alternative to conventional iEM detection with an antibody. During transmission EM, electrons interact with the sample by means of inelastic and/or elastic scattering. Inelastically scattered electrons decrease image quality, however, by using ESI one can specifically detect inelastically scattered electrons that suffered a specific energy loss due to their interaction with the specimen [257]. The energy loss is characteristic for the element that induced it and therefore, by filtering out electrons with an energy loss in a specific range, it is possible to map different atoms in the specimen. ESI is a well-established technique in materials sciences, but its application to biological samples is relatively novel. Especially in combination with ET, the sensitivity of electron spectroscopic imaging has the potential to detect halogenated-uridine labeled viral RNAs inside thin sections.

The results obtained by the experiments described above would be valuable to address the question where exactly viral RNA synthesis takes place. However, given the fact that DMVs may contain large amounts of dsRNA, it would be straightforward to first investigate by biochemical methods whether the dsRNA indeed is viral RNA and thus represents intermediates of replication/transcription. Apart from the latter question, it is very likely that all of the UTP-labeling methods summarized above will initially detect these dsRNA structures because these structures are the first product of the viral polymerase. If short-pulse UTP labeling can be performed, fluorescence microscopy might be vital to gain information about the dynamics of the RTC. Detection of incorporated nucleotides is less prone to background signal in the permeabilized cells used for fluorescence microscopy than on cell sections for iEM. Especially, in combination with semi-permeabilization and RNA digestion (Chapter 5), it could be determined whether newly synthesized RNAs are produced inside or outside DMVs. The very specific padlocking method could then be used to determine the ratios of different viral RNAs that are present in the cytosol or within DMVs.

Furthermore, the *in vitro* replication/transcription system which was developed for EAV [247], might be studied by cryo-electron microscopy in more detail. As demonstrated before [293], it is possible to monitor the membrane-bound replication complex in real time by expressing a recombinant virus expressing GFP fused to one of the replicase subunits. In the same way, cells or even cell fractions that are first observed by *in vivo* or *in vitro* fluorescence microscopy could afterwards be used for electron microscopy to record high-resolution structural information [294]. This approach has recently stimulated a new development for which a (cryo-)electron microscope was equipped with an integrated laser scanning fluorescence microscope, and the detection of fluorescent signal and correlation with EM was done inside this integrated light- and electron microscope (iLEM) [295]. The development of iLEM is relatively new and in the future the technique may be combined with novel fluorescence microscopy techniques that have a superior localization resolution, e.g. STED,

PALM and STORM [296-298]. These super-resolution imaging techniques allow single particle localization of fluorescently labeled probes at a resolution of just tenths of nanometers and, also without being integrated in the iLEM, might play a significant role in the dissection of nidovirus replication in the future.

Final remarks

Thanks to the introduction of ET in +RNA virus replication research, detailed structural information is becoming available with respect to the replication structures that are induced in infected cells. The detailed dissection of the structural changes inside these cells allows us to begin to understand how viruses use and modify cellular components to build an infrastructure that is optimal for their replication. Overall, ultrastructural studies can establish an important framework that places biochemical data in the context of the cell and time course of infection. In this way, they will significantly contribute to our "bigger picture" of +RNA virus replication and will reveal the parallels and differences between virus orders, families, and species, which ultimately can be explained by the diversity of virus genotypes.

In this thesis, I set out to investigate the ultrastructural changes in the host cytoplasm upon infection with nidoviruses. Two prominent members of the coronavirus and arterivirus families, SARS-CoV and EAV, were chosen as models and both were found to induce similar networks of interconnected vesicles made from ER membranes. The in-depth structural dissection of these two nidovirus reticulovesicular networks revealed both common features and striking differences between these distantly related nidovirus families. Our RVN descriptions can now be used as a basis for future research, addressing e.g. the formation and function of these membrane structures and exploring the potential to use this knowledge for the development of antiviral strategies. Apart from providing answers to fundamental ultrastructural questions, the analysis of nidovirus RVN architecture also uncovered new research questions, e.g. the precise location of nidovirus replication/transcription and the mechanism involved in RNA transport from the cytosol into DMVs and/or vice versa. The lack of conventional methods to address these problems will stimulate additional technical advances, which will contribute higher-resolution information that will undoubtedly help to answer these pertinent questions.

References

1. Iwanowski DJ (1892) Concerning the mosaic disease of the tobacco plant. St. Petersb. Acad.Imp. Sci. Bul. 35: 67-70.
2. Beijerinck MW (1898) Over een contagium vivum fluidum als oorzaak van de vlekziekte der tabaksbladen. Versl. Gew. Verg. Wiss. en Natuurk. Afd., Kon. Aka. Wetensch. Amst. 7: 229-35.
3. Loeffler F, Frosch P (1898) Berichte der Kommission zur Erforschung der Maul- und Klauenseuche bei dem Institut für Infektionskrankheiten in Berlin. Centralb.l f. Bakteriol. I. Abt. 23: 371–391.
4. Stanley WM (1935) Isolation of a crystalline protein possessing the properties of tobacco-mosaic virus. Science 81: 644-645.
5. Knoll M, Ruska E (1932) Das Elektronenmikroskop. Z. Physik 78: 318-339.
6. Ruska E (1980) The early development of electron lenses and electron microscopy. Microsc Acta Suppl: 1-140.
7. von Borries B, Ruska E, Ruska H (1938) Bakterien und Virus in übermikroskopischer Aufnahme. Klin. Wochenschr. 17: 921-925.
8. Kausche G, Pfankuch E, Ruska H (1939) Die Sichtbarmachung von pflanzlichem Virus im Übermikroskop. Naturwissenschaften 27: 292-99.
9. Ruska H, von Borries B, Ruska E (1940) Die Bedeutung der Übermikroskopie für die Virusforschung. Arch. ges. Virusforsch. 1: 155-69.
10. Ruska H (1943) Versuch zu einer Ordnung der Virusarten. Arch. ges. Virusforsch. 2: 480-98.
11. Lwoff A, Horne R, Tournier P (1962) A system of viruses. Cold Spring Harb. Symp. Quant. Biol 27: 51-55.
12. Goldbach R (1987) Genome similarities between plant and animal RNA viruses. Microbiol. Sci 4: 197-202.
13. Gorbalenya A, Enjuanes L, Ziebuhr J, Snijder E (2006) Nidovirales: Evolving the largest RNA virus genome. Virus Res. 117: 17-37.
14. Gorbalenya A, Koonin E, Donchenko A, Blinov V (1989) Two related superfamilies of putative helicases involved in replication, recombination, repair and expression of DNA and RNA genomes. Nucleic Acids Res. 17: 4713-4730.
15. Strauss J, Strauss E (1988) Evolution of RNA viruses. Annu.Rev.Microbiol. 42: 657-683.
16. Baltimore D (1971) Expression of animal virus genomes. Bacteriol.Rev. 35: 235-241.
17. Beerens N, Selisko B, Ricagno S, Imbert I, van der ZL, et al. (2007) De novo initiation of RNA synthesis by the arterivirus RNA-dependent RNA polymerase. J.Virol. 81: 8384-8395.
18. Butcher SJ, Grimes JM, Makeyev EV, Bamford DH, Stuart DI (2001) A mechanism for initiating RNA-dependent RNA polymerization. Nature 410: 235-240.
19. Filomatori CV, Lodeiro MF, Alvarez DE, Samsa MM, Pietrasanta L, et al. (2006) A 5′ RNA element promotes dengue virus RNA synthesis on a circular genome. Genes Dev 20: 2238-2249.
20. Oh JW, Ito T, Lai MM (1999) A recombinant hepatitis C virus RNA-dependent RNA polymerase capable of copying the full-length viral RNA. J. Virol 73: 7694-7702.
21. Paul A, van Boom J, Filippov D, Wimmer E (1998) Protein-primed RNA synthesis by purified poliovirus RNA polymerase. Nature 393: 280-284.
22. Gorbalenya A, Snijder E (1996) Viral cysteine proteases. Persp.Drug Discov.Design 6: 64-86.
23. Ziebuhr J, Snijder E, Gorbalenya A (2000) Virus-encoded proteinases and proteolytic processing in the *Nidovirales*. J.Gen.Virol. 81: 853-879.

24. Ahlquist P (2006) Parallels among positive-strand RNA viruses, reverse-transcribing viruses and double-stranded RNA viruses. Nat Rev Micro 4: 371-382.
25. Mackenzie J (2005) Wrapping things up about virus RNA replication. Traffic 6: 967-977.
26. Netherton CM, Brooks E, Wileman T (2007) A guide to viral inclusions, membrane rearrangements, factories, and viroplasm produced during virus replication. Adv.Virus Res. 70: 101-182.
27. Salonen A, Ahola T, Kaariainen L (2004) Viral RNA replication in association with cellular membranes. Curr.Top.Microbiol.Immunol. 285: 139-173.
28. Garcia-Sastre A, Biron C (2006) Type 1 interferons and the virus-host relationship: a lesson in detente. Science 312: 879-882.
29. Haller O, Kochs G, Weber F (2006) The interferon response circuit: induction and suppression by pathogenic viruses. Virology 344: 119-130.
30. Hornung V, Ellegast J, Kim S, Brzozka K, Jung A, et al. (2006) 5'-Triphosphate RNA is the ligand for RIG-I. Science 314: 994-997.
31. den Boon JA, Ahlquist P (2010) Organelle-like membrane compartmentalization of positive-strand RNA virus replication factories. Annu. Rev. Microbiol 64: 241-256.
32. Miller S, Krijnse Locker J (2008) Modification of intracellular membrane structures for virus replication. Nat.Rev.Microbiol. 6: 363-374.
33. Friedman R, Levin J, Grimley P, Berezesky I (1972) Membrane-associated replication complex in arbovirus infection. J.Virol. 10: 504-515.
34. Froshauer S, Kartenbeck J, Helenius A (1988) Alphavirus RNA replicase is located on the cytoplasmic surface of endosomes and lysosomes. J.Cell Biol. 107: 2075-2086.
35. Kujala P, Ikäheimonen A, Ehsani N, Vihinen H, Auvinen P, et al. (2001) Biogenesis of the Semliki Forest virus RNA replication complex. J. Virol 75: 3873-3884.
36. Kopek B, Perkins G, Miller D, Ellisman M, Ahlquist P (2007) Three-dimensional analysis of a viral RNA replication complex reveals a virus-induced mini-organelle. PLoS Biol. 5: e220.
37. Miller DJ, Schwartz MD, Ahlquist P (2001) Flock house virus RNA replicates on outer mitochondrial membranes in Drosophila cells. J. Virol 75: 11664-11676.
38. Welsch S, Miller S, Romero-Brey I, Merz A, Bleck CKE, et al. (2009) Composition and three-dimensional architecture of the dengue virus replication and assembly sites. Cell Host Microbe 5: 365-375.
39. Westaway E, Mackenzie J, Kenney M, Jones M, Khromykh A (1997) Ultrastructure of Kunjin virus-infected cells: colocalization of NS1 and NS3 with double-stranded RNA, and of NS2b with NS3, in virus-induced membrane structures. J.Virol. 71: 6650-6661.
40. Westaway EG, Mackenzie JM, Khromykh AA (2003) Kunjin RNA replication and applications of Kunjin replicons. Adv. Virus Res 59: 99-140.
41. Gillespie LK, Hoenen A, Morgan G, Mackenzie JM (2010) The endoplasmic reticulum provides the membrane platform for biogenesis of the flavivirus replication complex. J. Virol 84: 10438-10447.
42. Uchil P, Satchidanandam V (2003) Architecture of the flaviviral replication complex. J.Biol.Chem. 278: 24388-24398.
43. Egger D, Wölk B, Gosert R, Bianchi L, Blum HE, et al. (2002) Expression of hepatitis C virus proteins induces distinct membrane alterations including a candidate viral replication complex. J. Virol 76: 5974-5984.
44. Ferraris P, Blanchard E, Roingeard P (2010) Ultrastructural and biochemical analyses of hepatitis C virus-associated host cell membranes. J. Gen. Virol 91: 2230-2237.
45. Gosert R, Egger D, Lohmann V, Bartenschlager R, Blum H, et al. (2003) Identification of the hepatitis C virus RNA replication complex in Huh-7 cells harboring subgenomic replicons. J.Virol. 77: 5487-5492.

46. El-Hage N, Luo G (2003) Replication of hepatitis C virus RNA occurs in a membrane-bound replication complex containing nonstructural viral proteins and RNA. J. Gen. Virol 84: 2761-2769.
47. Quinkert D, Bartenschlager R, Lohmann V (2005) Quantitative analysis of the hepatitis C virus replication complex. J.Virol. 79: 13594-13605.
48. Bienz K, Egger D, Rasser Y, Bossart W (1983) Intracellular distribution of poliovirus proteins and the induction of virus-specific cytoplasmic structures. Virology 131: 39-48.
49. Schlegel A, Giddings TJ, Ladinsky M, Kirkegaard K (1996) Cellular origin and ultrastructure of membranes induced during poliovirus infection. J.Virol. 70: 6576-6588.
50. Suhy D, Giddings T, Kirkegaard K (2000) Remodeling the endoplasmic reticulum by poliovirus infection and by individual viral proteins: an autophagy-like origin for virus-induced vesicles. J.Virol. 74: 8953-8965.
51. Bienz K, Egger D, Pasamontes L (1987) Association of polioviral proteins of the P2 genomic region with the viral replication complex and virus-induced membrane synthesis as visualized by electron microscopic immunocytochemistry and autoradiography. Virology 160: 220-226.
52. Bienz K, Egger D, Troxler M, Pasamontes L (1990) Structural organization of poliovirus RNA replication is mediated by viral proteins of the P2 genomic region. J.Virol. 64: 1156-1163.
53. Troxler M, Egger D, Pfister T, Bienz K (1992) Intracellular localization of poliovirus RNA by in situ hybridization at the ultrastructural level using single-stranded riboprobes. Virology 191: 687-697.
54. Rust R, Landmann L, Gosert R, Tang B, Hong W, et al. (2001) Cellular COPII proteins are involved in production of the vesicles that form the poliovirus replication complex. J.Virol. 75: 9808-9818.
55. Belov G, tan-Bonnet N, Kovtunovych G, Jackson C, Lippincott-Schwartz J, et al. (2007) Hijacking components of the cellular secretory pathway for replication of poliovirus RNA. J.Virol. 81: 558-567.
56. Lanke KHW, van der Schaar HM, Belov GA, Feng Q, Duijsings D, et al. (2009) GBF1, a guanine nucleotide exchange factor for Arf, is crucial for coxsackievirus B3 RNA replication. J. Virol 83: 11940-11949.
57. White SH, von Heijne G (2005) Transmembrane helices before, during, and after insertion. Curr. Opin. Struct. Biol 15: 378-386.
58. Mandon EC, Trueman SF, Gilmore R (2009) Translocation of proteins through the Sec61 and SecYEG channels. Curr. Opin. Cell Biol 21: 501-507.
59. Rapoport TA (2007) Protein translocation across the eukaryotic endoplasmic reticulum and bacterial plasma membranes. Nature 450: 663-669.
60. McMahon HT, Gallop JL (2005) Membrane curvature and mechanisms of dynamic cell membrane remodelling. Nature 438: 590-596.
61. Bonifacino JS, Lippincott-Schwartz J (2003) Coat proteins: shaping membrane transport. Nat. Rev. Mol. Cell Biol 4: 409-414.
62. Rothman JE, Wieland FT (1996) Protein sorting by transport vesicles. Science 272: 227-234.
63. Matsuo H, Chevallier J, Mayran N, Le Blanc I, Ferguson C, et al. (2004) Role of LBPA and Alix in multivesicular liposome formation and endosome organization. Science 303: 531-534.
64. Zimmerberg J, Kozlov MM (2006) How proteins produce cellular membrane curvature. Nat Rev Mol Cell Biol 7: 9-19.
65. Snijder E, van Tol H, Roos N, Pedersen K (2001) Non-structural proteins 2 and 3 interact to modify host cell membranes during the formation of the arterivirus replication complex. J.Gen.Virol. 82: 985-994.
66. Barco A, Carrasco L (1995) A human virus protein, poliovirus protein 2BC, induces membrane proliferation and blocks the exocytic pathway in the yeast *Saccharomyces cerevisiae*. EMBO J. 14: 3349-3364.

67. Mackenzie JM, Khromykh AA, Jones MK, Westaway EG (1998) Subcellular localization and some biochemical properties of the flavivirus Kunjin nonstructural proteins NS2A and NS4A. Virology 245: 203-215.
68. Miller S, Kastner S, Krijnse-Locker J, Bühler S, Bartenschlager R (2007) The non-structural protein 4A of dengue virus is an integral membrane protein inducing membrane alterations in a 2K-regulated manner. J. Biol. Chem 282: 8873-8882.
69. Kopek BG, Settles EW, Friesen PD, Ahlquist P (2010) Nodavirus-induced Membrane Rearrangement in Replication Complex Assembly Requires Replicase Protein A, RNA Templates, and Polymerase Activity. J Virol. 84:12492-503.
70. Drosten C, Gunther S, Preiser W, van der Werf S, Brodt H, et al. (2003) Identification of a novel coronavirus in patients with severe acute respiratory syndrome. N.Engl.J.Med. 348: 1967-1976.
71. Ksiazek T, Erdman D, Goldsmith C, Zaki S, Peret T, et al. (2003) A novel coronavirus associated with severe acute respiratory syndrome. N.Engl.J.Med. 348: 1953-1966.
72. Peiris J, Lai S, Poon L, Guan Y, Yam L, et al. (2003) Coronavirus as a possible cause of severe acute respiratory syndrome. Lancet 361: 1319-1325.
73. Lau SKP, Woo PCY, Li KSM, Huang Y, Tsoi H, et al. (2005) Severe acute respiratory syndrome coronavirus-like virus in Chinese horseshoe bats. Proc. Natl. Acad. Sci. U.S.A 102: 14040-14045.
74. Li W, Shi Z, Yu M, Ren W, Smith C, et al. (2005) Bats are natural reservoirs of SARS-like coronaviruses. Science 310: 676-679.
75. van der Hoek L, Pyrc K, Jebbink M, Vermeulen-Oost W, Berkhout R, et al. (2004) Identification of a new human coronavirus. Nat.Med. 10: 368-373.
76. Woo PCY, Lau SKP, Chu C, Chan K, Tsoi H, et al. (2005) Characterization and complete genome sequence of a novel coronavirus, coronavirus HKU1, from patients with pneumonia. J. Virol 79: 884-895.
77. Pasternak A, Spaan W, Snijder E (2006) Nidovirus transcription: how to make sense..? J.Gen.Virol. 87: 1403-1421.
78. Sawicki S, Sawicki D, Siddell S (2007) A contemporary view of coronavirus transcription. J.Virol. 81: 20-29.
79. Brierley I (1995) Ribosomal frameshifting on viral RNAs. J.Gen.Virol. 76: 1885-1892.
80. Brierley I, Digard P, Inglis S (1989) Characterization of an efficient coronavirus ribosomal frameshifting signal - Requirement for an RNA pseudoknot. Cell 57: 537-547.
81. Brierley I, Dos Ramos F (2006) Programmed ribosomal frameshifting in HIV-1 and the SARS-CoV. Virus Res. 119: 29-42.
82. Cavanagh D (1997) Nidovirales: a new order comprising Coronaviridae and Arteriviridae. Arch.Virol. 142: 629-633.
83. Snijder E, Bredenbeek P, Dobbe J, Thiel V, Ziebuhr J, et al. (2003) Unique and conserved features of genome and proteome of SARS-coronavirus, an early split-off from the coronavirus group 2 lineage. J.Mol.Biol. 331: 991-1004.
84. Sawicki S, Sawicki D (1995) Coronaviruses use discontinuous extension for synthesis of subgenome-length negative strands. Adv.Exp.Med.Biol. 380: 499-506.
85. Kanjanahaluethai A, Chen Z, Jukneliene D, Baker S (2007) Membrane topology of murine coronavirus replicase nonstructural protein 3. Virology 361: 391-401.
86. Oostra M, Te Lintelo E, Deijs M, Verheije M, Rottier P, et al. (2007) Localization and membrane topology of the coronavirus nonstructural protein 4: involvement of the early secretory pathway in replication. J.Virol. 81: 13876-13888.

87. Oostra M, Hagemeijer MC, van Gent M, Bekker CPJ, te Lintelo EG, et al. (2008) Topology and Membrane Anchoring of the Coronavirus Replication Complex: Not All Hydrophobic Domains of nsp3 and nsp6 Are Membrane Spanning. J. Virol. 82: 12392-12405.
88. Snijder E, Wassenaar A, Spaan W (1994) Proteolytic processing of the replicase ORF1a protein of equine arteritis virus. J.Virol. 68: 5755-5764.
89. Snijder E, Meulenberg J (1998) The molecular biology of arteriviruses. J.Gen.Virol. 79: 961-979.
90. Ziebuhr J (2005) The coronavirus replicase. Curr. Top. Microbiol. Immunol 287: 57-94.
91. Brockway S, Clay C, Lu X, Denison M (2003) Characterization of the expression, intracellular localization, and replication complex association of the putative mouse hepatitis virus RNA-dependent RNA polymerase. J.Virol. 77: 10515-10527.
92. Brockway S, Lu X, Peters T, Dermody T, Denison M (2004) Intracellular localization and protein interactions of the gene 1 protein p28 during mouse hepatitis virus replication. J.Virol. 78: 11551-11562.
93. Harcourt B, Jukneliene D, Kanjanahaluethai A, Bechill J, Severson K, et al. (2004) Identification of severe acute respiratory syndrome coronavirus replicase products and characterization of papain-like protease activity. J.Virol. 78: 13600-13612.
94. Ivanov K, Thiel V, Dobbe J, van der Meer Y, Snijder E, et al. (2004) Multiple enzymatic activities associated with Severe acute respiratory syndrome coronavirus helicase. J.Virol. 78: 5619-5632.
95. van der Meer Y, van Tol H, Krijnse Locker J, Snijder E (1998) ORF1a-encoded replicase subunits are involved in the membrane association of the arterivirus replication complex. J.Virol. 72: 6689-6698.
96. Prentice E, McAuliffe J, Lu X, Subbarao K, Denison M (2004) Identification and characterization of severe acute respiratory syndrome coronavirus replicase proteins. J.Virol. 78: 9977-9986.
97. Pedersen K, van der Meer Y, Roos N, Snijder E (1999) Open reading frame 1a-encoded subunits of the arterivirus replicase induce endoplasmic reticulum-derived double-membrane vesicles which carry the viral replication complex. J.Virol. 73: 2016-2026.
98. Breese S, McCollum W (1970) Electron microscopic characterization of equine arteritis virus. Proceedings of the 2nd International Conference on Equine Infectious Diseases. Basel: S. Karger. pp. 133-139.
99. Wood O, Tauraso N, Liebhaber H (1970) Electron microscopic study of tissue cultures infected with simian haemorrhagic fever virus. J.Gen.Virol. 7: 129-136.
100. Snijder E, van der Meer Y, Zevenhoven-Dobbe J, Onderwater J, van der Meulen J, et al. (2006) Ultrastructure and origin of membrane vesicles associated with the severe acute respiratory syndrome coronavirus replication complex. J.Virol. 80: 5927-5940.
101. Stertz S, Reichelt M, Spiegel M, Kuri T, Mart¡nez-Sobrido L, et al. (2007) The intracellular sites of early replication and budding of SARS-coronavirus. Virology 361: 304-315.
102. David-Ferreira J, Manaker R (1965) An electron microscope study of the development of a mouse hepatitis virus in tissue culture cells. J.Cell Biol. 24: 57-78.
103. Goldsmith C, Tatti K, Ksiazek T, Rollin P, Comer J, et al. (2004) Ultrastructural characterization of SARS coronavirus. Emerging Infect.Dis. 10: 320-326.
104. Gosert R, Kanjanahaluethai A, Egger D, Bienz K, Baker S (2002) RNA replication of mouse hepatitis virus takes place at double-membrane vesicles. J.Virol. 76: 3697-3708.
105. Prentice E, Jerome W, Yoshimori T, Mizushima N, Denison M (2004) Coronavirus replication complex formation utilizes components of cellular autophagy. J.Biol.Chem. 279: 10136-10141.
106. Posthuma C, Pedersen K, Lu Z, Joosten R, Roos N, et al. (2008) Formation of the arterivirus replication/transcription complex: a key role for nonstructural protein 3 in the remodeling of intracellular membranes. J.Virol. 82: 4480-4491.

107. van der Meer Y, Snijder E, Dobbe J, Schleich S, Denison M, et al. (1999) Localization of mouse hepatitis virus nonstructural proteins and RNA synthesis indicates a role for late endosomes in viral replication. J.Virol. 73: 7641-7657.
108. Shibata Y, Voeltz GK, Rapoport TA (2006) Rough sheets and smooth tubules. Cell 126: 435-439.
109. Voeltz GK, Rolls MM, Rapoport TA (2002) Structural organization of the endoplasmic reticulum. EMBO Rep 3: 944-950.
110. Griffiths G, Rottier P (1992) Cell biology of viruses that assemble along the biosynthetic pathway. Semin. Cell Biol 3: 367-381.
111. Krijnse Locker J, Ericsson M, Rottier P, Griffiths G (1994) Characterization of the budding compartment of mouse hepatitis virus: evidence that transport from RER to the Golgi complex requires only one vesicular transport step. J.Cell Biol. 124: 55-70.
112. Wieringa R, de Vries A, van der Meulen J, Godeke G, Onderwater J, et al. (2004) Structural protein requirements in equine arteritis virus assembly. J.Virol. 78: 13019-13027.
113. Dales S, Eggers H, Tamm I, Palade G (1965) Electron microscopic study of the formation of poliovirus. Virology 26: 379-389.
114. Palade GE (1953) An electron microscope study of the mitochondrial structure. J. Histochem. Cytochem. 1: 188-211.
115. Porter KR, Claude A, Fullam EF (1945) A Study of Tissue Culture Cells by Electron Microscopy. J. Exp. Med 81: 233-246.
116. Fawcett D (1981) The Cell. 2e ed. Philadelphia: W B Saunders Co.
117. Marincola E (2009) Don Fawcett (1917–2009): Unlocking Nature's Closely Guarded Secrets. PLoS Biol 7. doi:10.1371/journal.pbio.1000183
118. Massey BW (1953) Ultra-Thin Sectioning for Electron Microscopy. Biotech. and histochem. 28: 19-26.
119. Newman SB, Borysko E, Swerdlow M (1949) New Sectioning Techniques for Light and Electron Microscopy. Science 110: 66-68.
120. Palade GE (1952) A study of fixation for electron microscopy. J. Exp. Med 95: 285-298.
121. Monaghan P, Cook H, Jackson T, Ryan M, Wileman T (2004) The ultrastructure of the developing replication site in foot-and-mouth disease virus-infected BHK-38 cells. J. Gen. Virol 85: 933-946.
122. Sosinsky GE, Crum J, Jones YZ, Lanman J, Smarr B, et al. (2008) The combination of chemical fixation procedures with high pressure freezing and freeze substitution preserves highly labile tissue ultrastructure for electron tomography applications. J. Struct. Biol 161: 359-371.
123. Murk JLAN, Posthuma G, Koster AJ, Geuze HJ, Verkleij AJ, et al. (2003) Influence of aldehyde fixation on the morphology of endosomes and lysosomes: quantitative analysis and electron tomography. J Microsc 212: 81-90.
124. Studer D, Humbel BM, Chiquet M (2008) Electron microscopy of high pressure frozen samples: bridging the gap between cellular ultrastructure and atomic resolution. Histochem. Cell Biol 130: 877-889.
125. Dahl R, Staehelin LA (1989) High-pressure freezing for the preservation of biological structure: theory and practice. J Electron Microsc Tech 13: 165-174.
126. Gilkey J, Staehelin LA (1986) Advances in ultrarapid freezing for the preservation of cellular ultrastructure. J. Electron Microsc. Tech. 3: 177-210.
127. McDonald K (1999) High-pressure freezing for preservation of high resolution fine structure and antigenicity for immunolabeling. Methods Mol. Biol 117: 77-97.
128. von Schack ML, Fakan S, Villiger W, Müller M (1993) Cryofixation and cryosubstitution: a useful alternative in the analyses of cellular fine structure. Eur J Histochem 37: 5-18.

129. Sartori N, Richter K, Dubochet J (1993) Vitrification depth can be increased more than 10-fold by high-pressure freezing. J. Microsc. 172: 55-61.
130. Studer D, Michel M, Wohlwend M, Hunziker EB, Buschmann MD (1995) Vitrification of articular cartilage by high-pressure freezing. J Microsc 179: 321-332.
131. Dubochet J, Adrian M, Chang JJ, Homo JC, Lepault J, et al. (1988) Cryo-electron microscopy of vitrified specimens. Q. Rev. Biophys 21: 129-228.
132. Briegel A, Ortega DR, Tocheva EI, Wuichet K, Li Z, et al. (2009) Universal architecture of bacterial chemoreceptor arrays. Proc. Natl. Acad. Sci. U.S.A 106: 17181-17186.
133. Kürner J, Frangakis AS, Baumeister W (2005) Cryo-electron tomography reveals the cytoskeletal structure of Spiroplasma melliferum. Science 307: 436-438.
134. Scheffel A, Gruska M, Faivre D, Linaroudis A, Plitzko JM, et al. (2006) An acidic protein aligns magnetosomes along a filamentous structure in magnetotactic bacteria. Nature 440: 110-114.
135. Koning RI, Zovko S, Bárcena M, Oostergetel GT, Koerten HK, et al. (2008) Cryo electron tomography of vitrified fibroblasts: microtubule plus ends in situ. J. Struct. Biol 161: 459-468.
136. Al-Amoudi A, Chang J, Leforestier A, McDowall A, Salamin LM, et al. (2004) Cryo-electron microscopy of vitreous sections. EMBO J 23: 3583-3588.
137. Dubochet J, Chang J, Freeman R, Lepault J, McDowall A (1982) Frozen aqueous suspensions. Ultramicroscopy 10: 55-61.
138. Sartori Blanc N, Studer D, Ruhl K, Dubochet J (1998) Electron beam-induced changes in vitreous sections of biological samples. J Microsc 192: 194-201.
139. Steinbrecht R, Müller M (1987) Freeze substitution and freeze-drying. Cryotechniques in Biological Electron Microscopy. Berlin: Springer Verlag. pp. 149-172.
140. Crowther RA, DeRosier DJ, Klug A (1970) The Reconstruction of a Three-Dimensional Structure from Projections and its Application to Electron Microscopy. Proceedings of the Royal Society of London. A. Mathematical and Physical Sciences 317: 319 -340.
141. Frank J (1989) Image analysis of single macromolecules. Electron Microsc. Rev 2: 53-74.
142. Van Heel M (1987) Angular reconstitution: a posteriori assignment of projection directions for 3D reconstruction. Ultramicroscopy 21: 111-123.
143. Koster A, Grimm R, Typke D, Hegerl R, Stoschek A, et al. (1997) Perspectives of molecular and cellular electron tomography. J.Struct.Biol. 120: 276-308.
144. Leis A, Rockel B, Andrees L, Baumeister W (2009) Visualizing cells at the nanoscale. Trends Biochem. Sci 34: 60-70.
145. Koster AJ, Chen H, Sedat JW, Agard DA (1992) Automated microscopy for electron tomography. Ultramicroscopy 46: 207-227.
146. McEwen BF, Radermacher M, Rieder CL, Frank J (1986) Tomographic three-dimensional reconstruction of cilia ultrastructure from thick sections. Proc. Natl. Acad. Sci. U.S.A 83: 9040-9044.
147. Frey TG, Mannella CA (2000) The internal structure of mitochondria. Trends Biochem. Sci 25: 319-324.
148. Geuze HJ, Murk JL, Stroobants AK, Griffith JM, Kleijmeer MJ, et al. (2003) Involvement of the endoplasmic reticulum in peroxisome formation. Mol. Biol. Cell 14: 2900-2907.
149. Beck M, Förster F, Ecke M, Plitzko JM, Melchior F, et al. (2004) Nuclear pore complex structure and dynamics revealed by cryoelectron tomography. Science 306: 1387-1390.
150. Mehlin H, Daneholt B, Skoglund U (1992) Translocation of a specific premessenger ribonucleoprotein particle through the nuclear pore studied with electron microscope tomography. Cell 69: 605-613.

151. Brandt F, Carlson L, Hartl FU, Baumeister W, Grünewald K (2010) The three-dimensional organization of polyribosomes in intact human cells. Mol. Cell 39: 560-569.
152. Ortiz JO, Förster F, Kürner J, Linaroudis AA, Baumeister W (2006) Mapping 70S ribosomes in intact cells by cryoelectron tomography and pattern recognition. J. Struct. Biol 156: 334-341.
153. Pierson J, Ziese U, Sani M, Peters PJ (2010) Exploring vitreous cryo-section-induced compression at the macromolecular level using electron cryo-tomography; 80S yeast ribosomes appear unaffected. J. Struct. Biol 173: 345-349.
154. Medalia O, Weber I, Frangakis AS, Nicastro D, Gerisch G, et al. (2002) Macromolecular architecture in eukaryotic cells visualized by cryoelectron tomography. Science 298: 1209-1213.
155. Snijder E, Siddell S, Gorbalenya A (2005) The order Nidovirales. Topley and Wilson's microbiology and microbial infections; Virology volume. London: Hodder Arnold, Vol. 10. pp. 390-404.
156. Bienz K, Egger D, Pfister T, Troxler M (1992) Structural and functional characterization of the poliovirus replication complex. J.Virol. 66: 2740-2747.
157. Novoa R, Calderita G, Arranz R, Fontana J, Granzow H, et al. (2005) Virus factories: associations of cell organelles for viral replication and morphogenesis. Biol.Cell 97: 147-172.
158. Kirkegaard K, Jackson W (2005) Topology of double-membraned vesicles and the opportunity for non-lytic release of cytoplasm. Autophagy 1: 182-184.
159. Ahlquist P (2006) Parallels among positive-strand RNA viruses, reverse-transcribing viruses and double-stranded RNA viruses. Nat.Rev.Microbiol. 4: 371-382.
160. Peiris J, Guan Y, Yuen K (2004) Severe acute respiratory syndrome. Nat.Med. 10: S88-S97.
161. Pyrc K, Berkhout B, van der Hoek L (2007) The novel human coronaviruses NL63 and HKU1. J.Virol. 81: 3051-3057.
162. Ziebuhr J (2004) Molecular biology of severe acute respiratory syndrome coronavirus. Curr.Opin. Microbiol. 7: 412-419.
163. Thiel V, Ivanov K, Putics A, Hertzig T, Schelle B, et al. (2003) Mechanisms and enzymes involved in SARS coronavirus genome expression. J.Gen.Virol. 84: 2305-2315.
164. Masters P (2006) The molecular biology of coronaviruses. Adv.Virus Res.: 193-292.
165. Kirkegaard K, Taylor M, Jackson W (2004) Cellular autophagy: Surrender, avoidance and subversion by microorganisms. Nat.Rev.Microbiol. 2: 301-314.
166. Clementz M, Kanjanahaluethai A, O'Brien T, Baker S (2008) Mutation in murine coronavirus replication protein nsp4 alters assembly of double membrane vesicles. Virology 375: 118-129.
167. Verheije M, Raaben M, Mari M, Te Lintelo E, Reggiori F, et al. (2008) Mouse hepatitis coronavirus RNA replication depends on GBF1-mediated ARF1 activation. PLoS Pathog. 4: e1000088.
168. Frey T, Perkins G, Ellisman M (2006) Electron tomography of membrane-bound cellular organelles. Annu.Rev.Biophys.Biomol.Struct. 35: 199-224.
169. Walther P, Ziegler A (2002) Freeze substitution of high-pressure frozen samples: the visibility of biological membranes is improved when the substitution medium contains water. J.Microsc. 208: 3-10.
170. Mackenzie J, Jones M, Westaway E (1999) Markers for trans-Golgi membranes and the intermediate compartment localize to induced membranes with distinct replication functions in flavivirus-infected cells. J.Virol. 73: 9555-9567.
171. Neuman B, Joseph J, Saikatendu K, Serrano P, Chatterjee A, et al. (2008) Proteomics analysis unravels the functional repertoire of coronavirus nonstructural protein 3. J.Virol. 82: 5279-5294.
172. Zhai Y, Sun F, Li X, Pang H, Xu X, et al. (2005) Insights into SARS-CoV transcription and replication from the structure of the nsp7-nsp8 hexadecamer. Nat.Struct.Mol.Biol. 12: 980-986.

173. Imbert I, Guillemot J, Bourhis J, Bussetta C, Coutard B, et al. (2006) A second, non-canonical RNA-dependent RNA polymerase in SARS coronavirus. EMBO J. 25: 4933-4942.
174. Sethna P, Hung S, Brian D (1989) Coronavirus subgenomic minus-strand RNAs and the potential for mRNA replicons. Proc.Natl.Acad.Sci.U.S.A. 86: 5626-5630.
175. Sawicki D, Wang T, Sawicki S (2001) The RNA structures engaged in replication and transcription of the A59 strain of mouse hepatitis virus. J.Gen.Virol. 82: 385-396.
176. Stollar B, Stollar V (1970) Immunofluorescent demonstration of double-stranded RNA in the cytoplasm of Sindbis virus-infected cells. Virology 42: 276-280.
177. Weber F, Wagner V, Rasmussen S, Hartmann R, Paludan S (2006) Double-stranded RNA is produced by positive-strand RNA viruses and DNA viruses but not in detectable amounts by negative-strand RNA viruses. J.Virol. 80: 5059-5064.
178. Targett-Adams P, Boulant S, McLauchlan J (2008) Visualization of double-stranded RNA in cells supporting hepatitis C virus RNA replication. J.Virol. 82:2182-95.
179. Schonborn J, Oberstrass J, Breyel E, Tittgen J, Schumacher J, et al. (1991) Monoclonal antibodies to double-stranded RNA as probes of RNA structure in crude nucleic acid extracts. Nucleic Acids Res. 19: 2993-3000.
180. Wileman T (2006) Aggresomes and autophagy generate sites for virus replication. Science 312: 875-878.
181. Bost A, Prentice E, Denison M (2001) Mouse hepatitis virus replicase protein complexes are translocated to sites of M protein accumulation in the ERGIC at late times of infection. Virology 285: 21-29.
182. Sparks J, Lu X, Denison M (2007) Genetic analysis of Murine hepatitis virus nsp4 in virus replication. J.Virol. 81: 12554-12563.
183. Kutik S, Guiard B, Meyer H, Wiedemann N, Pfanner N (2007) Cooperation of translocase complexes in mitochondrial protein import. J.Cell Biol. 179: 585-591.
184. Endo T, Yamamoto H, Esaki M (2003) Functional cooperation and separation of translocators in protein import into mitochondria, the double-membrane bounded organelles. J.Cell Sci 116: 3259-3267.
185. Egger D, Bienz K (2005) Intracellular location and translocation of silent and active poliovirus replication complexes. J.Gen.Virol. 86: 707-718.
186. Jackson W, Giddings T, Taylor M, Mulinyawe S, Rabinovitch M, et al. (2005) Subversion of cellular autophagosomal machinery by RNA viruses. PLoS Biol. 3: 861-871.
187. Miyanari Y, Atsuzawa K, Usuda N, Watashi K, Hishiki T, et al. (2007) The lipid droplet is an important organelle for hepatitis C virus production. Nat.Cell Biol. 9: 1089-1097.
188. van Hemert M, van den Worm S, Knoops K, Mommaas A, Gorbalenya A, et al. (2008) SARS-coronavirus replication/transcription complexes are membrane-enclosed and need a host factor for activity *in vitro*. PLoS Pathog. 4: e1000054.
189. Westaway E, Khromykh A, Mackenzie J (1999) Nascent flavivirus RNA colocalized in situ with double-stranded RNA in stable replication complexes. Virology 258: 108-117.
190. Versteeg G, Spaan W (2008) Host cell responses to coronavirus infections. Nidoviruses. Washington, D.C.: ASM Press. pp. 245-258.
191. Versteeg G, Bredenbeek P, van den Worm S, Spaan W (2007) Group 2 coronaviruses prevent immediate early interferon induction by protection of viral RNA from host cell recognition. Virology 361: 18-26.
192. Zhou H, Perlman S (2007) Mouse hepatitis virus does not induce Beta interferon synthesis and does not inhibit its induction by double-stranded RNA. J.Virol. 81: 568-574.

193. Roth-Cross J, Martinez-Sobrido L, Scott E, Garcia-Sastre A, Weiss S (2007) Inhibition of the alpha/beta interferon response by mouse hepatitis virus at multiple levels. J.Virol. 81: 7189-7199.
194. Kremer J, Mastronarde D, McIntosh J (1996) Computer visualization of three-dimensional image data using IMOD. J.Struct.Biol. 116: 71-76.
195. Martone M, Tran J, Wong W, Sargis J, Fong L, et al. (2008) The cell centered database project: an update on building community resources for managing and sharing 3D imaging data. J.Struct.Biol. 161: 220-231.
196. Frangakis A, Hegerl R (2001) Noise reduction in electron tomographic reconstructions using nonlinear anisotropic diffusion. J.Struct.Biol. 135: 250.
197. Perlman S, Netland J (2009) Coronaviruses post-SARS: update on replication and pathogenesis. Nat. Rev. Microbiol 7: 439-450.
198. Knoops K, Kikkert M, van den Worm S, Zevenhoven-Dobbe J, van der Meer Y, et al. (2008) SARS-coronavirus replication is supported by a reticulovesicular network of modified endoplasmic reticulum. PLoS Biol. 6: e226.
199. Egger D, Teterina N, Ehrenfeld E, Bienz K (2000) Formation of the poliovirus replication complex requires coupled viral translation, vesicle production, and viral RNA synthesis [In Process Citation]. J.Virol. 74: 6570-6580.
200. Gazina E, Mackenzie J, Gorrell R, Anderson D (2002) Differential requirements for COPI coats in formation of replication complexes among three genera of Picornaviridae. J.Virol. 76: 11113-11122.
201. Donaldson JG, Finazzi D, Klausner RD (1992) Brefeldin A inhibits Golgi membrane-catalysed exchange of guanine nucleotide onto ARF protein. Nature 360: 350-352.
202. Lippincott-Schwartz J, Yuan LC, Bonifacino JS, Klausner RD (1989) Rapid redistribution of Golgi proteins into the ER in cells treated with brefeldin A: evidence for membrane cycling from Golgi to ER. Cell 56: 801-813.
203. Mossessova E, Corpina RA, Goldberg J (2003) Crystal structure of ARF1*Sec7 complexed with Brefeldin A and its implications for the guanine nucleotide exchange mechanism. Mol. Cell 12: 1403-1411.
204. Orci L, Stamnes M, Ravazzola M, Amherdt M, Perrelet A, et al. (1997) Bidirectional transport by distinct populations of COPI-coated vesicles. Cell 90: 335-349.
205. Cuconati A, Molla A, Wimmer E (1998) Brefeldin A inhibits cell-free, de novo synthesis of poliovirus. J. Virol 72: 6456-6464.
206. Irurzun A, Perez L, Carrasco L (1992) Involvement of membrane traffic in the replication of poliovirus genomes: effects of brefeldin A. Virology 191: 166-175.
207. Maynell L, Kirkegaard K, Klymkowsky M (1992) Inhibition of poliovirus RNA synthesis by brefeldin A. J.Virol. 66: 1985-1994.
208. O'Donnell VK, Pacheco JM, Henry TM, Mason PW (2001) Subcellular distribution of the foot-and-mouth disease virus 3A protein in cells infected with viruses encoding wild-type and bovine-attenuated forms of 3A. Virology 287: 151-162.
209. Doedens J, Kirkegaard K (1995) Inhibition of cellular protein secretion by poliovirus proteins 2B and 3A. EMBO J. 14: 894-907.
210. Wessels E, Duijsings D, Lanke K, Melchers W, Jackson C, et al. (2007) Molecular determinants of the interaction between coxsackievirus protein 3A and guanine nucleotide exchange factor GBF1. J.Virol. 81: 5238-5245.
211. Wessels E, Duijsings D, Niu T, Neumann S, Oorschot V, et al. (2006) A viral protein that blocks Arf1-mediated COP-I assembly by inhibiting the guanine nucleotide exchange factor GBF1. Dev.Cell 11: 191-201.

212. Belov GA, Feng Q, Nikovics K, Jackson CL, Ehrenfeld E (2008) A critical role of a cellular membrane traffic protein in poliovirus RNA replication. PLoS Pathog 4: e1000216.
213. Görlich D, Prehn S, Hartmann E, Kalies KU, Rapoport TA (1992) A mammalian homolog of SEC61p and SECYp is associated with ribosomes and nascent polypeptides during translocation. Cell 71: 489-503.
214. Vasudevan C, Han W, Tan Y, Nie Y, Li D, et al. (1998) The distribution and translocation of the G protein ADP-ribosylation factor 1 in live cells is determined by its GTPase activity. J. Cell. Sci 111 (Pt 9): 1277-1285.
215. Zhang CJ, Rosenwald AG, Willingham MC, Skuntz S, Clark J, et al. (1994) Expression of a dominant allele of human ARF1 inhibits membrane traffic in vivo. J. Cell Biol 124: 289-300.
216. Dascher C, Balch WE (1994) Dominant inhibitory mutants of ARF1 block endoplasmic reticulum to Golgi transport and trigger disassembly of the Golgi apparatus. J. Biol. Chem 269: 1437-1448.
217. Dascher C, Matteson J, Balch WE (1994) Syntaxin 5 regulates endoplasmic reticulum to Golgi transport. J. Biol. Chem 269: 29363-29366.
218. Fujiwara T, Oda K, Yokota S, Takatsuki A, Ikehara Y (1988) Brefeldin A causes disassembly of the Golgi complex and accumulation of secretory proteins in the endoplasmic reticulum. J. Biol. Chem 263: 18545-18552.
219. Misumi Y, Misumi Y, Miki K, Takatsuki A, Tamura G, et al. (1986) Novel blockade by brefeldin A of intracellular transport of secretory proteins in cultured rat hepatocytes. J. Biol. Chem 261: 11398-11403.
220. Füllekrug J, Sönnichsen B, Schäfer U, Nguyen Van P, Söling HD, et al. (1997) Characterization of brefeldin A induced vesicular structures containing cycling proteins of the intermediate compartment/cis-Golgi network. FEBS Lett 404: 75-81.
221. Deitz SB, Dodd DA, Cooper S, Parham P, Kirkegaard K (2000) MHC I-dependent antigen presentation is inhibited by poliovirus protein 3A. Proc. Natl. Acad. Sci. U.S.A 97: 13790-13795.
222. Dodd DA, Giddings TH, Kirkegaard K (2001) Poliovirus 3A protein limits interleukin-6 (IL-6), IL-8, and beta interferon secretion during viral infection. J. Virol 75: 8158-8165.
223. Brabec-Zaruba M, Berka U, Blaas D, Fuchs R (2007) Induction of autophagy does not affect human rhinovirus type 2 production. J. Virol 81: 10815-10817.
224. Taylor MP, Kirkegaard K (2008) Potential subversion of autophagosomal pathway by picornaviruses. Autophagy 4: 286-289.
225. Wong J, Zhang J, Si X, Gao G, Mao I, et al. (2008) Autophagosome supports coxsackievirus B3 replication in host cells. J. Virol 82: 9143-9153.
226. Zhao Z, Thackray LB, Miller BC, Lynn TM, Becker MM, et al. (2007) Coronavirus replication does not require the autophagy gene ATG5. Autophagy 3: 581-585.
227. Voeltz GK, Prinz WA, Shibata Y, Rist JM, Rapoport TA (2006) A class of membrane proteins shaping the tubular endoplasmic reticulum. Cell 124: 573-586.
228. Tang W, Yang S, Wu B, Jheng J, Chen Y, et al. (2007) Reticulon 3 binds the 2C protein of enterovirus 71 and is required for viral replication. J. Biol. Chem 282: 5888-5898.
229. Vaux D, Tooze J, Fuller S (1990) Identification by anti-idiotypic antibodies of an intracellular membrane protein that recognizes a mammalian endoplasmic reticulum retention signal. Nature 345: 495-502.
230. Tang BL, Peter F, Krijnse-Locker J, Low SH, Griffiths G, et al. (1997) The mammalian homolog of yeast Sec13p is enriched in the intermediate compartment and is essential for protein transport from the endoplasmic reticulum to the Golgi apparatus. Mol. Cell. Biol 17: 256-266.

231. Laemmli U (1970) Cleavage of structural proteins during the assembly of the head of bacteriophage T4. Nature 227: 680-685.
232. Li Q, Lau A, Morris TJ, Guo L, Fordyce CB, et al. (2004) A syntaxin 1, Galpha(o), and N-type calcium channel complex at a presynaptic nerve terminal: analysis by quantitative immunocolocalization. J. Neurosci 24: 4070-4081.
233. te Velthuis A, Arnold J, Cameron C, van den Worm S, Snijder E (2010) The RNA polymerase activity of SARS-coronavirus nsp12 is primer dependent. Nucleic Acids Res. 38: 203-214.
234. Narayanan K, Huang C, Makino S (2008) SARS coronavirus accessory proteins. Virus Res 133: 113-121.
235. Ulasli M, Verheije MH, de Haan CAM, Reggiori F (2010) Qualitative and quantitative ultrastructural analysis of the membrane rearrangements induced by coronavirus. Cell. Microbiol 12: 844-861.
236. Carette J, Stuiver M, Van Lent J, Wellink J, Van Kammen A (2000) Cowpea mosaic virus infection induces a massive proliferation of endoplasmic reticulum but not Golgi membranes and is dependent on *de novo* membrane synthesis. J.Virol. 74: 6556-6563.
237. Miller D, Schwartz M, Dye B, Ahlquist P (2003) Engineered retargeting of viral RNA replication complexes to an alternative intracellular membrane. J.Virol. 77: 12193-12202.
238. Peranen J, Laakkonen P, Hyvonen M, Kaariainen L (1995) The alphavirus replicase protein nsP1 is membrane-associated and has affinity to endocytic organelles. Virology 208: 610-620.
239. Sawicki SG, Sawicki DL (1986) Coronavirus minus-strand RNA synthesis and effect of cycloheximide on coronavirus RNA synthesis. J. Virol 57: 328-334.
240. Knoops K, Swett-Tapia C, van den Worm SHE, Te Velthuis AJW, Koster AJ, et al. (2010) Integrity of the early secretory pathway promotes, but is not required for, severe acute respiratory syndrome coronavirus RNA synthesis and virus-induced remodeling of endoplasmic reticulum membranes. J. Virol 84: 833-846.
241. Puhka M, Vihinen H, Joensuu M, Jokitalo E (2007) Endoplasmic reticulum remains continuous and undergoes sheet-to-tubule transformation during cell division in mammalian cells. J. Cell Biol 179: 895-909.
242. den Boon JA, Diaz A, Ahlquist P (2010) Cytoplasmic viral replication complexes. Cell Host Microbe 8: 77-85.
243. Lee J, Marshall J, Bowden D (1994) Characterization of rubella virus replication complexes using antibodies to double-stranded RNA. Virology 200: 307-312.
244. Schwartz M, Chen J, Janda M, Sullivan M, den Boon J, et al. (2002) A positive-strand RNA virus replication complex parallels form and function of retrovirus capsids. Mol.Cell 9: 505-514.
245. Snijder E, Spaan W (2006) Arteriviruses. Fields Virology. Philadelphia, Pa.: Lippincott, Williams & Wilkins. pp. 1337-1355.
246. Fang Y, Snijder EJ (2010) The PRRSV replicase: exploring the multifunctionality of an intriguing set of nonstructural proteins. Virus Res 154: 61-76.
247. van Hemert M, de Wilde A, Gorbalenya A, Snijder E (2008) The in vitro RNA synthesizing activity of the isolated arterivirus replication/transcription complex is dependent on a host factor. J.Biol.Chem. 283: 16525-16536.
248. Manders E, Verbeek F, Aten J (1993) Measurement of co-localization of objects in dual color confocal images. Journal of Microscopy 169: 375-382.
249. Estes P, Cheville N (1970) The ultrastructure of vascular lesions in equine viral arteritis. Am.J.Pathol. 58: 235-253.
250. Wada R, Fukunaga Y, Kondo T, Kanemaru T (1995) Ultrastructure and immuno-cytochemistry of BHK-21 cells infected with a modified Bucyrus strain of equine arteritis virus. Arch.Virol. 140: 1173-1180.

251. Stueckemann J, Holth M, Swart W, Kowalchyk K, Smith M, et al. (1982) Replication of lactate dehydrogenase-elevating virus in macrophages. 2. mechanism of persistent infection in mice and cell culture. J.Gen.Virol. 59: 263-272.
252. Molenkamp R, van Tol H, Rozier B, van der Meer Y, Spaan W, et al. (2000) The arterivirus replicase is the only viral protein required for genome replication and subgenomic mRNA transcription. J.Gen. Virol. 81: 2491-2496.
253. Wassenaar A, Spaan W, Gorbalenya A, Snijder E (1997) Alternative proteolytic processing of the arterivirus replicase ORF1a polyprotein: evidence that NSP2 acts as a cofactor for the NSP4 serine protease. J.Virol. 71: 9313-9322.
254. Hinners I, Moschner J, Nolte N, Hille-Rehfeld A (1999) The orientation of membrane proteins determined in situ by immunofluorescence staining. Anal. Biochem 276: 1-7.
255. Schrodt S, Koch J, Tampé R (2006) Membrane topology of the transporter associated with antigen processing (TAP1) within an assembled functional peptide-loading complex. J. Biol. Chem 281: 6455-6462.
256. You HX, Lowe CR (1996) AFM Studies of Protein Adsorption: 2. Characterization of Immunoglobulin G Adsorption by Detergent Washing. Journal of Colloid and Interface Science 182: 586-601.
257. Leapman R, Aronova M (2007) Localizing specific elements bound to macromolecules by EFTEM. Methods Cell Biol. 79: 593-613.
258. Aronova MA, Kim YC, Harmon R, Sousa AA, Zhang G, et al. (2007) Three-dimensional elemental mapping of phosphorus by quantitative electron spectroscopic tomography (QuEST). J. Struct. Biol 160: 35-48.
259. Eskiw CH, Rapp A, Carter DRF, Cook PR (2008) RNA polymerase II activity is located on the surface of protein-rich transcription factories. J. Cell. Sci 121: 1999-2007.
260. Ahmed K, Li R, Bazett-Jones DP (2009) Electron spectroscopic imaging of the nuclear landscape. Methods Mol. Biol 464: 415-423.
261. Belin S, Hacot S, Daudignon L, Therizols G, Pourpe S, et al. (2010) Purification of ribosomes from human cell lines. Curr Protoc Cell Biol Chapter 3: Unit 3.40.
262. Svoboda D, Nielson A, Werber A, Higginson J (1962) An electron microscopic study of viral hepatitis in mice. Am. J. Pathol 41: 205-224.
263. Reggiori F, Monastyrska I, Verheije MH, Calì T, Ulasli M, et al. (2010) Coronaviruses Hijack the LC3-I-positive EDEMosomes, ER-derived vesicles exporting short-lived ERAD regulators, for replication. Cell Host Microbe 7: 500-508.
264. Zeegers J, van der Zeijst B, Horzinek M (1976) The structural proteins of equine arteritis virus. Virology 73: 200-205.
265. deVries A, Chirnside E, Horzinek M, Rottier P (1992) Structural proteins of equine arteritis virus. J.Virol. 66: 6294-6303.
266. Magnusson P, Hyllseth B, Marusyk H (1970) Morphological studies on equine arteritis virus. Arch. Gesamte Virusforsch. 30: 105-112.
267. Dea S, Sawyer N, Alain R, Athanasseous R (1995) Ultrastructural characteristics and morphogenesis of porcine reproductive and respiratory syndrome virus propagated in the highly permissive MARC-145 cell clone. Adv.Exp.Med.Biol. 380: 95-98.
268. Spilman MS, Welbon C, Nelson E, Dokland T (2009) Cryo-electron tomography of porcine reproductive and respiratory syndrome virus: organization of the nucleocapsid. J. Gen. Virol 90: 527-535.
269. Bamunusinghe D, Seo J, Rao ALN (2011) Subcellular localization and rearrangement of endoplasmic reticulum by brome mosaic virus capsid protein. J. Virol 85: 2953-2963.

270. Doll E, Bryans J, McCollum W, Crowe M (1957) Isolation of a filterable agent causing arteritis of horses and abortion by mares. Its differentiation from the equine abortion (influenza) virus. Cornell Vet. 47: 3-41.
271. Maclachlan N, Balasuriya U, Hedges J, Schweidler T, McCollum W, et al. (1998) Serologic response of horses to the structural proteins of equine arteritis virus. J.Vet.Diagn.Investig. 10: 229-236.
272. Mastronarde DN (2005) Automated electron microscope tomography using robust prediction of specimen movements. J. Struct. Biol 152: 36-51.
273. Ng DT, Brown JD, Walter P (1996) Signal sequences specify the targeting route to the endoplasmic reticulum membrane. J. Cell Biol 134: 269-278.
274. Meyer HA, Grau H, Kraft R, Kostka S, Prehn S, et al. (2000) Mammalian Sec61 is associated with Sec62 and Sec63. J. Biol. Chem 275: 14550-14557.
275. Mothes W, Heinrich SU, Graf R, Nilsson I, von Heijne G, et al. (1997) Molecular Mechanism of Membrane Protein Integration into the Endoplasmic Reticulum. Cell 89: 523-533.
276. Caliguiri L, Tamm I (1969) Membranous structures associated with translation and transcription of poliovirus RNA. Science 166: 885-886.
277. Roumiantzeff M, Summers DF, Maizel JV (1971) In vitro protein synthetic activity of membrane-bound poliovirus polyribosomes. Virology 44: 249-258.
278. Almsherqi ZA, McLachlan CS, Mossop P, Knoops K, Deng Y (2005) Direct template matching reveals a host subcellular membrane gyroid cubic structure that is associated with SARS virus. Redox Rep 10: 167-171.
279. Almsherqi ZA, Kohlwein SD, Deng Y (2006) Cubic membranes: a legend beyond the Flatland* of cell membrane organization. J. Cell Biol 173: 839-844.
280. Hu J, Shibata Y, Voss C, Shemesh T, Li Z, et al. (2008) Membrane proteins of the endoplasmic reticulum induce high-curvature tubules. Science 319: 1247-1250.
281. de Haan CAM, Reggiori F (2008) Are nidoviruses hijacking the autophagy machinery? Autophagy 4: 276-279.
282. Kanehara K, Kawaguchi S, Ng DTW (2007) The EDEM and Yos9p families of lectin-like ERAD factors. Semin. Cell Dev. Biol 18: 743-750.
283. Zuber C, Cormier JH, Guhl B, Santimaria R, Hebert DN, et al. (2007) EDEM1 reveals a quality control vesicular transport pathway out of the endoplasmic reticulum not involving the COPII exit sites. Proc. Natl. Acad. Sci. U.S.A 104: 4407-4412.
284. Calì T, Galli C, Olivari S, Molinari M (2008) Segregation and rapid turnover of EDEM1 by an autophagy-like mechanism modulates standard ERAD and folding activities. Biochem. Biophys. Res. Commun 371: 405-410.
285. Berger KL, Cooper JD, Heaton NS, Yoon R, Oakland TE, et al. (2009) Roles for endocytic trafficking and phosphatidylinositol 4-kinase III alpha in hepatitis C virus replication. Proc. Natl. Acad. Sci. U.S.A 106: 7577-7582.
286. Hsu N, Ilnytska O, Belov G, Santiana M, Chen Y, et al. (2010) Viral reorganization of the secretory pathway generates distinct organelles for RNA replication. Cell 141: 799-811.
287. Bergersen LH, Storm-Mathisen J, Gundersen V (2008) Immunogold quantification of amino acids and proteins in complex subcellular compartments. Nat. Protocols 3: 144-152.
288. Nilsson M, Malmgren H, Samiotaki M, Kwiatkowski M, Chowdhary BP, et al. (1994) Padlock probes: circularizing oligonucleotides for localized DNA detection. Science 265: 2085-2088.
289. Nilsson M, Antson DO, Barbany G, Landegren U (2001) RNA-templated DNA ligation for transcript analysis. Nucleic Acids Res 29: 578-581.

290. Lizardi PM, Huang X, Zhu Z, Bray-Ward P, Thomas DC, et al. (1998) Mutation detection and single-molecule counting using isothermal rolling-circle amplification. Nat. Genet 19: 225-232.
291. Thomas DC, Nardone GA, Randall SK (1999) Amplification of padlock probes for DNA diagnostics by cascade rolling circle amplification or the polymerase chain reaction. Arch. Pathol. Lab. Med 123: 1170-1176.
292. Landegren U, Nilsson M, Gullberg M, Söderberg O, Jarvius M, et al. (2004) Prospects for in situ analyses of individual and complexes of DNA, RNA, and protein molecules with padlock and proximity probes. Methods Cell Biol 75: 787-797.
293. van den Born E, Posthuma C, Knoops K, Snijder E (2007) An infectious recombinant equine arteritis virus expressing green fluorescent protein from its replicase gene. J.Gen.Virol. 88: 1196-1205.
294. van Driel LF, Valentijn JA, Valentijn KM, Koning RI, Koster AJ (2009) Tools for correlative cryo-fluorescence microscopy and cryo-electron tomography applied to whole mitochondria in human endothelial cells. Eur. J. Cell Biol 88: 669-684.
295. Agronskaia AV, Valentijn JA, van Driel LF, Schneijdenberg CTWM, Humbel BM, et al. (2008) Integrated fluorescence and transmission electron microscopy. J. Struct. Biol 164: 183-189.
296. Heintzmann R, Ficz G (2006) Breaking the resolution limit in light microscopy. Brief Funct Genomic Proteomic 5: 289-301.
297. Henriques R, Mhlanga MM (2009) PALM and STORM: what hides beyond the Rayleigh limit? Biotechnol J 4: 846-857.
298. Toomre D, Bewersdorf J (2010) A new wave of cellular imaging. Annu. Rev. Cell Dev. Biol 26: 285-314.

Summary

During the outbreak of the Severe Acute Respiratory Syndrome (SARS) in 2003, about 8000 people fell ill of which about 10% did not survive the infection. For about 4 months, the SARS outbreak had a profound effect on public life and the global economy. It was ultimately contained using quite traditional measures, like respiratory protection and quarantining of patients. Essentially there were no alternatives, since coronaviruses were relatively poorly studied and vaccines or antiviral drugs targeting this new virus were not available.

Positive-stranded RNA viruses, to which the SARS-coronavirus (SARS-CoV) belongs, replicate in the cytoplasm of infected host cells. Their replication complexes are commonly associated with modified host cell membranes. Membrane structures supporting viral RNA synthesis range from distinct spherular membrane invaginations to more elaborate webs of packed membranes and vesicles. Generally, their ultrastructure, morphogenesis, and exact role in viral replication remain to be defined.

Poorly characterized double-membrane vesicles (DMVs) were previously implicated in SARS-CoV RNA synthesis. To obtain more information about the 3-dimensional structure of coronavirus-induced membrane structures, electron tomography of cryofixed infected cells was applied in **chapter 2**. This analysis defines a unique reticulovesicular network (RVN) of modified endoplasmic reticulum that integrates convoluted membranes, numerous interconnected DMVs (diameter 200–300 nm), and "vesicle packets" apparently arising from DMV fusion. The convoluted membranes were most abundantly immunolabeled for viral replicase subunits. However, double-stranded RNA, presumably revealing the site of viral RNA synthesis, mainly localized to the DMV interior and was enclosed by a double membrane. Since connections between the DMV interior and cytosol could not be discerned, the analysis raises several questions about the mechanism of DMV formation and the actual site of SARS-CoV RNA synthesis. The data described in chapter 2 document the extensive virus-induced reorganization of host cell membranes into a network that is used to organize viral replication and possibly hide replicating RNA from antiviral defense mechanisms.

In **chapter 3**, it was investigated how the early secretory pathway interacts with the RVN and the viral replication/transcription complex (RTC) that is anchored to it. When the secretory pathway was disrupted by brefeldin A (BFA) treatment shortly after the start of infection, RVN formation and viral RTC activity were not blocked and continued up to 11 h post infection, although RNA synthesis was reduced by about 80%. *In vitro* RTC assays, using membrane fractions from infected cells, demonstrated that BFA does not directly interfere with the activity of the viral RNA-synthesizing enzymes. Confocal microscopy studies showed that early secretory pathway components are not associated with SARS-CoV-induced replication sites, although our studies revealed that infection induces a remarkable redistribution of the translocon subunit Sec61α. Ultrastructural studies, including electron tomography,

revealed that the formation of the RVN and all its previously documented features can occur in the presence of BFA, despite differences in volume and morphology of the network. We therefore conclude that early secretory pathway proteins do not play a direct role in RVN morphogenesis or functionality of the SARS-CoV RTC. The BFA-induced disruption of ER integrity and functionality probably affects the overall quality of the membrane scaffold that is needed to support the viral RTC and/or the availability of specific host factors, which in turn compromises viral RNA synthesis.

Translation of the viral RNA genome produces the replicase polyproteins that direct RNA synthesis. Although it is generally accepted that viral RNA synthesis initially depends on the same RNA template, it was unknown which effect translation inhibition has on the functionality of the coronavirus RTC and development of the RVN. Therefore, in **chapter 4**, the effect of translation inhibition on the RNA synthesis of SARS-CoV and mouse hepatitis virus was studied by using cycloheximide and puromycin. Both inhibitors prevented the usual exponential increase in viral RNA synthesis, with immunofluorescence and electron microscopy indicating that RVN development came to a standstill. Nevertheless, limited RNA synthesis was supported, implying that continued translation is not an absolute requirement and suggesting a direct link between RVN formation and accumulation of coronavirus proteins.

Also the replicase proteins of the arteriviruses are associated with unusual double-membrane vesicles (DMVs; diameter ~100 nm), which were previously proposed to derive from the endoplasmic reticulum (ER). Using advanced electron microscopic techniques, including electron tomography and electron spectroscopic imaging, an in-depth ultrastructural analysis of cells infected with the prototypic arterivirus equine arteritis virus (EAV) was performed in **chapter 5**. It was established that the outer membranes of EAV-induced DMVs are interconnected with each other and the ER, thus forming a reticulovesicular network that – to a certain extent – resembles membrane structures accommodating the RNA synthesis of the very distantly related coronaviruses. A clear and striking parallel between coronavirus and arterivirus DMVs is the accumulation in their interior cavity of double-stranded RNA, the presumed intermediate of viral RNA synthesis. However, openings connecting DMV interior and cytosol were only rarely observed, and likely represented fixation or staining artifacts. Also semi-permeabilization and nuclease digestion experiments suggested that the interior of EAV-induced DMVs is inaccessible from the cytosol, implying that the double-stranded RNA is compartmentalized by membranes. As a novel approach to visualize and quantify the RNA content of viral replication structures, we explored electron spectroscopic imaging of DMVs, which revealed the presence of an RNA amount equaling up to a few dozen copies of the EAV genome. Finally, we visualized a peculiar network of EAV nucleocapsid protein-containing protein sheets and tubules, which appears intertwined with the RVN. This potential intermediate in nucleocapsid formation suggests that arterivirus RNA synthesis and virion assembly are coordinated in intracellular space.

Despite significant morphological differences between the replication networks induced by SARS-CoV and EAV, it seems that RVN formation is a common property of cells infected with nidoviruses. Together with biochemical studies of the viral enzyme complex, our ultrastructural description of this replication network will aid to further dissect the early stages of the nidovirus life cycle and its virus-host interactions.

Samenvatting

Tijdens de Severe Acute Respiratory Syndrome (SARS) epidemie van 2003 werden ongeveer 8000 mensen ziek, waarvan circa 10% de infectie niet overleefden. Gedurende ongeveer 4 maanden had de SARS-uitbraak een diepgaand effect op het openbare leven en de mondiale economie. De nieuwe ziekte werd uiteindelijk onder controle gebracht met behulp van een combinatie van traditionele maatregelen, zoals adembescherming en quarantaine van patiënten. In essentie waren er geen alternatieven, aangezien coronavirussen voorheen slechts beperkt bestudeerd waren en vaccins of antivirale middelen tegen dit nieuwe virus niet beschikbaar waren.

Virussen met een positiefstrengig RNA genoom, waartoe o.a. het SARS-coronavirus (SARS-CoV) behoort, vermenigvuldigen zich in het cytoplasma van de geïnfecteerde gastheercel. De assemblage van hun replicatiecomplexen gaat gepaard met de modificatie van membranen in de gastheercel. Deze door het virus geïnduceerde structuren, waarvan men aanneemt dat ze de virale RNA synthese faciliteren, variëren van relatief simpele membraaninvaginaties tot meer uitgebreide netwerken van onderling verbonden membranen en blaasjes. De ultrastructuur en morfogenese van deze membraanveranderingen, en hun exacte rol in de virale replicatie, zijn nog grotendeels onbekend.

Eerder was gesuggereerd dat blaasjes met een dubbele membraan (double-membrane vesicles; DMVs) betrokken zouden zijn bij de RNA synthese van SARS-CoV. Om meer inzicht te krijgen in de 3-dimensionale structuur van deze coronavirus-geïnduceerde membraanveranderingen werd in **hoofdstuk 2** elektronen tomografie toegepast op geïnfecteerde cellen. Deze analyse liet zien dat SARS-CoV een uniek reticulovesiculair netwerk (RVN) van gemodificeerd endoplasmatisch reticulum (ER) induceert dat bestaat uit "in elkaar gedraaide" membranen (convoluted membranes; CM), talrijke onderling verbonden DMVs (diameter 200-300 nm), en "gebundelde blaasjes" (vesicles packets; VP), die kennelijk ontstaan ten gevolge van DMV fusie. Kwantitatief bekeken bevatten de CM de meeste virale replicase eiwitten, maar het dubbelstrengs RNA, de veronderstelde intermediair in de virale RNA synthese, bevond zich voornamelijk binnenin de DMVs, en was dus omgeven door de dubbele membraan. Omdat er geen openingen konden worden aangetoond die de inhoud van DMV en cytosol verbinden, werpt deze analyse een aantal vragen op over het mechanisme van DMV biogenese en de daadwerkelijke plek van SARS-CoV RNA synthese. Samengevat beschrijft hoofdstuk 2 de virus-geïnduceerde reorganisatie van gastheercelmembranen tot een netwerk dat mogelijk wordt gebruikt om de virale replicatie te coördineren en eventueel te verbergen voor antivirale afweermechanismen.

In **hoofdstuk 3** werd onderzocht in hoeverre het RVN en het daaraan verankerde virale replicatie en transcriptie complex (RTC) afhankelijk zijn van de COPII-gemedieerde transport mechanisme. Wanneer, tijdens het begin van de infectie, de COPII-gemedieerde transport

werden verstoord door brefeldine A (BFA) behandeling, werden RVN vorming en virale RTC activiteit niet geblokkeerd en kon tot tenminste 11 uur na infectie RNA synthese worden gemeten, hoewel verminderd tot ongeveer 20% van het normale niveau. *In vitro* RTC experimenten uitgevoerd met behulp van membraanfracties die waren geïsoleerd uit geïnfecteerde cellen toonden aan dat BFA geen rechtstreeks effect heeft op de activiteit van de virale RNA synthetiserende enzymen. Confocale microscopie toonde aan dat onderdelen van COPII-gemedieerde transport mechanisme niet zijn geassocieerd met het SARS-CoV-geïnduceerde RVN. Wel bleek uit deze experimenten dat SARS-CoV infectie een opmerkelijke herverdeling veroorzaakt van de translocon-subunit Sec61α. Uit ultrastructurele studies, waaronder elektronen tomografie, bleek dat de vorming van het RVN en al de bovengenoemde onderdelen mogelijk is in de aanwezigheid van BFA, ondanks verschillen in volume en morfologie van het netwerk. Dit suggereert dat de membraancompartimenten en eiwitten aan het begin van de cellulaire secretieroute geen directe rol spelen in de SARS-CoV RVN morfogenese dan wel RTC functionaliteit. De verstoring van ER stabiliteit en functionaliteit door BFA behandeling beïnvloeden waarschijnlijk de kwaliteit van de membranen die nodig zijn om het virale RTC te ondersteunen en/of de beschikbaarheid van specifieke gastheerfactoren, hetgeen vervolgens de virale RNA synthese verstoort.

Translatie van het virale RNA genoom leidt tot de productie van replicase polyproteinen die vervolgens de RNA synthese aansturen. Hoewel het duidelijk was dat voor virale RNA synthese initieel dezelfde RNA matrijs gebruikt wordt, was het onbekend welk effect translatieremming heeft op de functionaliteit van het RTC en de ontwikkeling van het RVN. Daartoe werd in **hoofdstuk 4** het effect van de translatieremmers cycloheximide en puromycine op de RNA synthese van SARS-CoV en muizen hepatitis virus (MHV) gemeten. Beide remmers voorkwamen de gebruikelijke exponentiële stijging van virale RNA synthese. Immunofluorescentie en elektronen microscopie lieten zien dat daarmee ook de RVN ontwikkeling tot stilstand kwam. Toch was er nog beperkte RNA synthese meetbaar, hetgeen impliceert dat translatie geen absolute vereiste is en dat er een directe link bestaat tussen RVN formatie en de ophoping van coronavirus eiwitten.

Ook de replicase eiwitten van arterivirusen zijn geassocieerd met DMVs (diameter ~100 nm), waarvan al eerder werd aangenomen dat ze hun oorsprong vinden in het ER. Met behulp van geavanceerde elektronenmicroscopische technieken, waaronder elektronen tomografie en spectroscopische beeldvorming, is in **hoofdstuk 5** een uitgebreide ultrastructurele analyse uitgevoerd op cellen die geïnfecteerd waren met het prototype arterivirus, equine arteritis virus (EAV). Vastgesteld werd dat de buitenste membranen van de door EAV geïnduceerde DMVs onderling verbonden zijn en tevens verbonden zijn met het ER. Hiermee lijkt het door arterivirussen gevormde RVN - tot op zekere hoogte – op de membraanveranderingen geïnduceerd door hun verre verwanten, de coronavirussen. Een duidelijke en opvallende overeenkomst tussen coronavirus en arterivirus DMVs is de ophoping van dubbelstrengs RNA in het interieur. Er werden opnieuw slechts sporadisch (mogelijke) verbindingen tussen

DMV interieur en cytosol waargenomen. Om te onderzoeken of deze het gevolg waren van fixatie- of kleuringartefacten werden semi-permeabilisatie en nuclease-digestie experimenten uitgevoerd. Deze suggereerden dat het interieur van de door EAV geïnduceerde DMVs niet toegankelijk is vanaf het cytosol, wat impliceert dat het dubbelstrengs RNA volledig is ingesloten door membranen. Als een nieuwe benadering voor visualisatie en kwantificering van de RNA inhoud van virale replicatiestructuren werd elektronen spectroscopische beeldvorming van DMVs gebruikt. Daaruit bleek dat DMVs een hoeveelheid RNA bevatten die kan oplopen tot een paar dozijn kopieën van het EAV genoom. Tot slot werd een uniek netwerk van EAV nucleocapside eiwit waargenomen dat bestaat uit eiwitvlakken en –buizen. Dit netwerk lijkt verweven te zijn met het RVN en is een potentiële intermediair in nucleocapsidevorming die suggereert dat arterivirus RNA synthese en virus assemblage plaatselijk worden gecoördineerd in de intracellulaire ruimte.

Ondanks de aanzienlijke morfologische verschillen tussen de door SARS-CoV en EAV geïnduceerde membraannetwerken, blijkt dat RVN-vorming een gemeenschappelijke eigenschap is van cellen die geïnfecteerd zijn met nidovirussen. Samen met de biochemische studies naar het actieve virale enzymcomplex zal de ultrastructurele beschrijving van dit replicatienetwerk helpen om de vroege stadia van de nidovirus levenscyclus en relevante virus-gastheer interacties verder te ontleden.

Curriculum vitae

Kèvin Knoops is geboren in Heerlen op 3 juli 1980. In 1998 behaalde hij zijn gymnasium diploma aan Rolduc, te Kerkrade. In hetzelfde jaar begon hij zijn studie biologie in Groningen en specialiseerde zich in elektronen en confocale microscopie onder begeleiding van Prof. Marten Veenhuis (Groningen), Prof. Masako Osumi (Tokyo, Japan) en Prof. Sepp Kohlwein (Graz, Oostenrijk). In 2004 studeerde Kèvin af in het vakgebied eukaryote microbiologie met het predicaat "*met zeer veel genoegen*". In hetzelfde jaar begon hij aan zijn promotieonderzoek in het Leids Universitair Medisch Centrum (LUMC) waar hij onderzoek verrichtte naar de architectuur van de membraanveranderingen die gevormd worden door nidovirussen, waartoe ook het SARS-coronavirus behoort. Het onderzoek werd uitgevoerd bij de sectie Moleculaire Virologie (afdeling Medische Microbiologie) van Prof. Eric Snijder en de sectie Ultrastructurele en Moleculaire Beeldvorming van Dr. Henk Koerten en, sinds 2005, Prof. Bram Koster, waarbij Dr. Mieke Mommaas optrad als directe begeleidster en co-promotor. Ondersteund door een EMBO fellowship startte Kèvin in 2010 zijn eerste postdoc project in het laboratorium van Dr. Christiane Schaffitzel aan het Europees Moleculair Biologisch Laboratorium (EMBL) in Grenoble (Frankrijk), waar hij de dynamiek van translocatie en membraaneiwitten bestudeert.

Awards

4th Annual Research Award (2010)
Animation of the year 2009
BioMed Central & Biology Image Library

Kiem award (2009)
Best first publication written by young microbiologist
Dutch Society of (Medical) Microbiology

List of publications

Knoops, K., Bárcena, M., Limpens, R.W.A.L., Koster, A.J., Mommaas, A.M., and Snijder, E.J. (submitted for publication) Ultrastructural characterization of arterivirus replication structures: Reshaping the endoplasmic reticulum to accommodate viral RNA synthesis.

van den Worm, S.H.E., **Knoops, K.**, Zevenhoven-Dobbe, J.C., Beugeling, C., van der Meer, Y., Mommaas, A.M., and Snijder, E.J. (2011) Development and RNA-synthesizing activity of coronavirus replication structures in the absence of protein synthesis. *Journal of Virology* (in press)

Knoops, K., Swett-Tapia, C., van den Worm, S.H., Te Velthuis, A.J., Koster, A.J., Mommaas, A.M., Snijder, E.J., and Kikkert, M. (2010) Integrity of the early secretory pathway promotes, but is not required for, severe acute respiratory syndrome coronavirus RNA synthesis and virus-induced remodeling of endoplasmic reticulum membranes. *Journal of Virology* 84(2):833-46.

Knoops, K., Kikkert, M., van den Worm, S.H., Zevenhoven-Dobbe, J.C., van der Meer, Y., Koster, A.J., Mommaas, A.M. & Snijder, E.J. (2008) SARS-coronavirus replication is supported by a reticulovesicular network of modified endoplasmic reticulum. *PLoS Biology* 16;6(9):e226.

van Hemert, M.J., van den Worm, S.H., **Knoops, K.**, Mommaas, A.M., Gorbalenya, A.E., and Snijder, E.J. (2008) SARS-coronavirus replication/transcription complexes are membrane-protected and need a host factor for activity in vitro. *PLoS Pathogens* 2;4(5):e1000054.

van Driel, L.F., **Knoops, K.**, Koster, A.J., and Valentijn, J.A. (2008) Fluorescent labeling of resin-embedded sections for correlative electron microscopy using tomography-based contrast enhancement. *Journal of Structural Biology* 161(3):372-83.

van den Born, E., Posthuma, C.C., **Knoops, K.**, and Snijder, E.J. (2007) An infectious recombinant equine arteritis virus expressing green fluorescent protein from its replicase gene. *Journal of General Virology* 88(Pt 4):1196-205.

Almsherqi, Z.A., McLachlan, C.S., Mossop, P., **Knoops, K.**, and Deng, Y. (2005) Direct template matching reveals a host subcellular membrane gyroid cubic structure that is associated with SARS virus. *Redox Report* 10(3):167-71.

Komduur, J.A., Bellu, A.R., **Knoops, K.**, van der Klei, I.J., and Veenhuis, M. (2004) Cold-inducible selective degradation of peroxisomes in Hansenula polymorpha. *FEMS Yeast Research* 5(3):281-5.